

1-1-1981

An investigation of flow characteristics in radial nozzle cascades.

Gholam R. Hashemi

Follow this and additional works at: <http://preserve.lehigh.edu/etd>



Part of the [Mechanical Engineering Commons](#)

Recommended Citation

Hashemi, Gholam R., "An investigation of flow characteristics in radial nozzle cascades." (1981). *Theses and Dissertations*. Paper 2423.

This Thesis is brought to you for free and open access by Lehigh Preserve. It has been accepted for inclusion in Theses and Dissertations by an authorized administrator of Lehigh Preserve. For more information, please contact preserve@lehigh.edu.

AN INVESTIGATION OF FLOW CHARACTERISTICS
IN RADIAL NOZZLE CASCADES

by

Gholam R. Hashemi

A Thesis
Presented to the Graduate Committee
of Lehigh University
in Candidacy for the Degree of
Master of Science
in
Mechanical Engineering

Lehigh University

1982

ProQuest Number: EP76699

All rights reserved

INFORMATION TO ALL USERS

The quality of this reproduction is dependent upon the quality of the copy submitted.

In the unlikely event that the author did not send a complete manuscript and there are missing pages, these will be noted. Also, if material had to be removed, a note will indicate the deletion.



ProQuest EP76699

Published by ProQuest LLC (2015). Copyright of the Dissertation is held by the Author.

All rights reserved.

This work is protected against unauthorized copying under Title 17, United States Code
Microform Edition © ProQuest LLC.

ProQuest LLC.
789 East Eisenhower Parkway
P.O. Box 1346
Ann Arbor, MI 48106 - 1346

CERTIFICATE OF APPROVAL

This thesis is accepted and approved in partial fulfillment of the requirements for the degree of Master of Science in Mechanical Engineering.

Dec. 9 1982
(date)

Professor in Charge

Chairman of the Department

ACKNOWLEDGMENTS:

The author thanks his parents who provided invaluable guidance and support throughout his education.

The author extends his deepest gratitude to Dr. Jerzy Owczarek, his advisor, who gave him the opportunity to undertake this investigation as his thesis work assignment, and whose support and cooperation made this thesis possible.

He would also like to express his thanks to the Air Products and Chemicals, Inc. for financial support of this investigation. Helpful suggestions and encouragement received from Messrs. R. Filippi and R. Lemak are deeply appreciated.

TABLE OF CONTENTS

	<u>Page No.</u>
Certificate of Approval	ii
Acknowledgments	iii
List of Figures	vi
List of Tables	xv
Nomenclature	xvi
Abstract	1
I Introduction	3
II Test Objectives	12
III Description of Test Rigs	14
3-A. Main Test Rig	14
3-B. Optical Test Rig	17
3-C. Modifications to the Test Rig	18
IV Description of Test Procedure	21
V Test Results from the Main Test Rig	23
VI Secondary Flow Visualization within the Main Test Rig	25
VII Test Results from Optical Test Rig	26
VIII Analysis of Test Results	27
Conclusions	34
References	123
Appendix A. Analysis of the Flow in the Vaneless Space Following the Nozzle Vanes	125
Appendix B. Sample of Calculations and Uncertainties of Test Results	133

(Table of Contents - cont.)

	<u>Page No.</u>
Appendix C. Sample of Intermediate Test Results	141
Biography of Author	172

LIST OF FIGURES

	<u>Page No.</u>
Figure 1. Line Diagram of the Test Setup	35
Figure 2. Drawing of Orifice	36
Figure 3. Photograph of Steel Test Rig - Side View	37
Figure 4. Photograph of Steel Test Rig - Front View	38
Figure 5. Photograph of Probe Holder and Probes	39
Figure 6. Photograph of Nozzles, Shroud and Collector	40
Figure 7. Photograph of Nozzles and Probe Holder	41
Figure 8. Drawing of the Main Test Rig	42
Figure 9. Drawing of the Vane	43
Figure 10. Variation of Brass Protractor Angle with Nozzle Setting Angle	44
Figure 11. Variation of Brass Protractor Angle with Nozzle Throat Width	45
Figure 12. Drawing of the Probe Holder (original and modified design)	46
Figure 13. Drawing of the Plexiglass Disk	47
Figure 14. Drawing of the Shroud (original and modified design)	48
Figure 15. Photograph of the Optical Test Rig (front view)	49
Figure 16. Photograph of the Inside of the Optical Test Rig	50
Figure 17. Photograph of the Optical Test Rig (back view)	51
Figure 18. The Optical Test Rig	52

(List of Figures - cont.)

	<u>Page No.</u>
Figure 19. Photograph of the Guide Vanes	53
Figure 20. Drawing of the Guide Vane Attachment	54
Figure 21. Drawing of the Swirl-Removing Vanes	55
Figure 22. Probe with Protractor	56
Figure 23. Probe Protractor Calibration Setup	57
Figure 24. Test Data Sheet for Main Test Rig	58
Figure 25. Measured Variation of the Flow Angle with Radius Ratio, r/r_{TE} , for Three Nozzle Setting Angles 15, 20, and 25 Degrees. Supply Pressure 19.26 PSIA, Nozzle Width 0.148 in.	59
Figure 26. Measured Variation of the Flow Angle with Radius Ratio, r/r_{TE} , for Three Nozzle Setting Angles 15, 20, and 25 Degrees. Supply Pressure 19.13 PSIA, Nozzle Width 0.200 in.	60
Figure 27. Measured Variation of the Flow Angle with Radius Ratio, r/r_{TE} , for Three Nozzle Setting Angles 15, 20, and 25 Degrees. Supply Pressure 24.35 PSIA, Nozzle Width 0.148 in.	61
Figure 28. Measured Variation of the Flow Angle with Radius Ratio, r/r_{TE} , for Three Nozzle Setting Angles 15, 20, and 25 Degrees. Supply Pressure 24.44 PSIA, Nozzle Width 0.200 in.	62
Figure 29. Variation of the Flow Velocity with Radius Ratio, r/r_{TE} , for Three Nozzle Setting Angles 15, 20, and 25 Degrees. Supply Pressure 19.13 PSIA, Nozzle Width 0.200 in.	63

(List of Figures - cont.)

	<u>Page No.</u>
Figure 19. Photograph of the Guide Vanes	53
Figure 20. Drawing of the Guide Vane Attachment	54
Figure 21. Drawing of the Swirl-Removing Vanes	55
Figure 22. Probe with Protractor	56
Figure 23. Probe Protractor Calibration Setup	57
Figure 24. Test Data Sheet for Main Test Rig	58
Figure 25. Measured Variation of the Flow Angle with Radius Ratio, r/r_{TE} , for Three Nozzle Setting Angles 15, 20, and 25 Degrees. Supply Pressure 19.26 PSIA, Nozzle Width 0.148 in.	59
Figure 26. Measured Variation of the Flow Angle with Radius Ratio, r/r_{TE} , for Three Nozzle Setting Angles 15, 20, and 25 Degrees. Supply Pressure 19.13 PSIA, Nozzle Width 0.200 in.	60
Figure 27. Measured Variation of the Flow Angle with Radius Ratio, r/r_{TE} , for Three Nozzle Setting Angles 15, 20, and 25 Degrees. Supply Pressure 24.35 PSIA, Nozzle Width 0.148 in.	61
Figure 28. Measured Variation of the Flow Angle with Radius Ratio, r/r_{TE} , for Three Nozzle Setting Angles 15, 20, and 25 Degrees. Supply Pressure 24.44 PSIA, Nozzle Width 0.200 in.	62
Figure 29. Variation of the Flow Velocity with Radius Ratio, r/r_{TE} , for Three Nozzle Setting Angles 15, 20, and 25 Degrees. Supply Pressure 19.13 PSIA, Nozzle Width 0.200 in.	63

(List of Figures - cont.)

	<u>Page No.</u>
Figure 30. Variation of the Flow Velocity with Radius Ratio, r/r_{TE} , for Three Nozzle Setting Angles 15, 20, and 25 Degrees. Supply Pressure 19.26 PSIA, Nozzle Width 0.148 in.	64
Figure 31. Variation of the Flow Velocity with Radius Ratio, r/r_{TE} , for Three Nozzle Setting Angles 15, 20, and 25 Degrees. Supply Pressure 24.35 PSIA, Nozzle Width 0.148 in.	65
Figure 32. Variation of the Flow Velocity with Radius Ratio, r/r_{TE} , for Three Nozzle Setting Angles 15, 20, and 25 Degrees. Supply Pressure 24.44 PSIA, Nozzle Width 0.200 in.	66
Figure 33. Variation of the Mach Number with Radius Ratio, r/r_{TE} , for Three Nozzle Setting Angles 15, 20, and 25 Degrees. Supply Pressure 24.35 PSIA, Nozzle Width 0.148 in.	67
Figure 34. Variation of the Mach Number with Radius Ratio, r/r_{TE} , for Three Nozzle Setting Angles 15, 20, and 25 Degrees. Supply Pressure 24.44 PSIA, Nozzle Width 0.200 in.	68
Figure 35. Variation of the Mach Number with Radius Ratio, r/r_{TE} , for Three Nozzle Setting Angles 15, 20, and 25 Degrees. Supply Pressure 19.13 PSIA, Nozzle Width 0.200 in.	69
Figure 36. Variation of the Mach Number with Radius Ratio, r/r_{TE} , for Three Nozzle Setting Angles 15, 20, and 25 Degrees. Supply Pressure 19.26 PSIA, Nozzle Width 0.148 in.	70

(List of Figures - cont.)

Page No.

Figure 37.	Variation of the Loss Coefficient, e , with Radius Ratio, r/r_{TE} , for Three Nozzle Trailing Edge Angles 15, 20, and 25 Degrees. Supply Pressure 24.44 PSIA, Nozzle Width 0.200 in.	71
Figure 38.	Variation of the Loss Coefficient, e , with Radius Ratio, r/r_{TE} , for Three Nozzle Trailing Edge Angles 15, 20, and 25 Degrees. Supply Pressure 24.35 PSIA, Nozzle Width 0.148 in.	72
Figure 39.	Variation of the Loss Coefficient, e , with Radius Ratio, r/r_{TE} , for Three Nozzle Trailing Edge Angles 15, 20, and 25 Degrees. Supply Pressure 19.13 PSIA, Nozzle Width 0.200 in.	73
Figure 40.	Variation of the Loss Coefficient, e , with Radius Ratio, r/r_{TE} , for Three Nozzle Setting Angles 15, 20, and 25 Degrees. Supply Pressure 19.26 PSIA, Nozzle Width 0.148 in.	74
Figure 41.	Variation of the Loss Coefficient, γ_N , with Radius Ratio, r/r_{TE} , for Three Nozzle Setting Angles 15, 20, and 25 Degrees. Supply Pressure 24.35 PSIA, Nozzle Width 0.148 in.	75
Figure 42.	Variation of the Loss Coefficient, γ_N , with Radius Ratio, r/r_{TE} , for Three Nozzle Setting Angles 15, 20, and 25 Degrees. Supply Pressure 24.44 PSIA, Nozzle Width 0.200 in.	76
Figure 43.	Variation of the Loss Coefficient, γ_N , with Radius Ratio, r/r_{TE} , for Three Nozzle Setting Angles 15, 20, and 25 Degrees. Supply Pressure 19.26 PSIA, Nozzle Width 0.148 in.	77

(List of Figures - cont.)

Page No.

Figure 44.	Variation of the Loss Coefficient, Y_N , with Radius Ratio, r/r_{TE} , for Three Nozzle Setting Angles 15, 20, and 25 Degrees. Supply Pressure 19.13 PSIA, Nozzle Width 0.200 in.	78
Figure 45.	Variation of the Loss Coefficient, Y_N , with Reynolds Number, Re_{DH} , for Probe Location No. 1.	79
Figure 46.	Variation of the Loss Coefficient, Y_N , with Reynolds Number, Re_ℓ , for Probe Location No. 1.	80
Figure 47.	Variation of the Loss Coefficient, Y_N , with Reynolds Number, Re_H , for Probe Location No. 1.	81
Figure 48.	Variation of the Loss Coefficient, ξ , with Reynolds Number, Re_{DH} , for Probe Location No. 1.	82
Figure 49.	Variation of the Loss Coefficient, ξ , with Reynolds Number, Re_ℓ , for Probe Location No. 1.	83
Figure 50.	Variation of the Loss Coefficient, ξ , with Reynolds Number, Re_H , for Probe Location No. 1.	84
Figure 51.	Variation of the Loss Coefficient, Y_N , with Reynolds Number, Re_{DH} , for Probe Location No. 2.	85
Figure 52.	Variation of the Loss Coefficient, Y_N , with Reynolds Number, Re_ℓ , for Probe Location No. 2.	86
Figure 53.	Variation of the Loss Coefficient, Y_N , with Reynolds Number, Re_H , for Probe Location No. 2.	87

(List of Figures - cont.)

	<u>Page No.</u>
Figure 54. Variation of the Loss Coefficient, ξ , with Reynolds Number, Re_{DH} , for Probe Location No. 2.	88
Figure 55. Variation of the Loss Coefficient, ξ , with Reynolds Number, Re_λ , for Probe Location No. 2.	89
Figure 56. Variation of the Loss Coefficient, ξ , with Reynolds Number, Re_H , for Probe Location No. 2.	90
Figure 57. Variation of the Loss Coefficient, γ_N , with Reynolds Number, Re_{DH} , for Probe Location No. 3.	91
Figure 58. Variation of the Loss Coefficient, γ_N , with Reynolds Number, Re_λ , for Probe Location No. 3.	92
Figure 59. Variation of the Loss Coefficient, γ_N , with Reynolds Number, Re_H , for Probe Location No. 3.	93
Figure 60. Variation of the Loss Coefficient, ξ , with Reynolds Number, Re_{DH} , for Probe Location No. 3.	94
Figure 61. Variation of the Loss Coefficient, ξ , with Reynolds Number, Re_λ , for Probe Location No. 3.	95
Figure 62. Variation of the Loss Coefficient, ξ , with Reynolds Number, Re_H , for Probe Location No. 3.	96
Figure 63. Variation of the Flow Angle, θ_M , Obtained from Mass Flow Rate Calculation with Radius Ratio, r/r_{TE} , for Low Pressure Test.	97

(List of Figures - cont.)

	<u>Page No.</u>
Figure 64. Variation of the Flow Angle, θ_M , Obtained from Mass Flow Rate Calculations with Radius Ratio, r/r_{TE} , for High Pressure Test.	98
Figure 65. Variation of the Flow Angle, θ_M , with the Reynolds Number, Re_{DH} , for Probe Location No. 1.	99
Figure 66. Variation of the Flow Angle, θ_M , with the Reynolds Number, Re_H , for Probe Location No. 1.	100
Figure 67. Variation of the Flow Angle, θ_M , with the Reynolds Number, Re_{DH} , for Probe Location No. 2.	101
Figure 68. Variation of the Flow Angle, θ_M , with the Reynolds Number, Re_H , for Probe Location No. 2.	102
Figure 69. Variation of the Flow Angle, θ_M , with the Reynolds Number, Re_{DH} , for Probe Location No. 3.	103
Figure 70. Variation of the Flow Angle, θ_M , with the Reynolds Number, Re_H , for Probe Location No. 3.	104
Figure 71. Variation of the Specific Angular Momentum, rV_θ , with Radius Ratio, r/r_{TE} , for the Low Pressure Test.	105
Figure 72. Variation of the Specific Angular Momentum, rV_θ , with Radius Ratio, r/r_{TE} , for the High Pressure Test.	106
Figure 73. Photograph of Flow Pattern on Probe Holder and Shroud Walls for Nozzle Height 0.148 in. Supply Pressure 9.3 IN-HG, Nozzle Angle 25 Degrees.	107

(List of Figures - cont.)

	<u>Page No.</u>
Figure 74. Photograph of Flow Pattern on Probe Holder and Shroud Walls for Nozzle Height 0.148 in. Supply Pressure 9.3 IN-HG, Nozzle Angle 20 Degrees.	108
Figure 75. Photograph of Flow Pattern on Probe Holder and Shroud Walls for Nozzle Height 0.148 in. Supply Pressure 9.3 IN-HG, Nozzle Angle 15 Degrees.	109
Figure 76. Photograph of Flow Pattern on Probe Holder and Shroud Walls for Nozzle Height 0.148 in. Supply Pressure 9.3 IN-HG, Nozzle Angle 10 Degrees.	110
Figure 77. Photograph of Flow Pattern on Probe Holder and Shroud Walls for Nozzle Height 0.200 in. Supply Pressure 9.3 IN-HG, Nozzle Angle 25 Degrees.	111
Figure 78. Photograph of Flow Pattern on Probe Holder and Shroud Walls for Nozzle Height 0.200 in. Supply Pressure 9.3 IN-HG, Nozzle Angle 20 Degrees.	112
Figure 79. Photograph of Flow Pattern on Probe Holder and Shroud Walls for Nozzle Height 0.200 in. Supply Pressure 9.3 IN-HG, Nozzle Angle 15 Degrees.	113
Figure 80. Photograph of Flow Pattern on Probe Holder and Shroud Walls for Nozzle Height 0.200 in. Supply Pressure 9.3 IN-HG, Nozzle Angle 10 Degrees.	114
Figure 81. Photograph of Flow Pattern on Probe Holder and Shroud Walls for Nozzle Height 0.148 in. Supply Pressure 20 IN-HG, Nozzle Angle 25 Degrees, and Without the Guide Vanes.	115

(List of Figures - cont.)

	<u>Page No.</u>
Figure 82. Photograph of Flow Pattern on Probe Holder and Shroud Walls for Nozzle Height 0.148 in. Supply Pressure 20 IN-HG, Nozzle Angle 15 Degrees, and Without the Guide Vanes.	116
Figure 83. Photograph of Flow Pattern on Probe Holder and Shroud Walls for Nozzle Height 0.148 in. Supply Pressure 20 IN-HG, Nozzle Angle 25 Degrees, and With the Guide Vanes.	117
Figure 84. Photograph of Flow Pattern on Probe Holder and Shroud Walls for Nozzle Height 0.148 in. Supply Pressure 20 IN-HG, Nozzle Angle 15 Degrees, and With the Guide Vanes.	118

LIST OF TABLES

	<u>Page No.</u>
Table No. 1 Variation of the Trailing Edge Angles with the Brass Protractor Angle	119
Table No. 2 Variation of the Throat Widths with the Brass Protractor Angle	120
Table No. 3 Optical Test Rig Results for Nozzle Trailing Edge Angle 8 Degrees	121
Table No. 4 Optical Test Rig Results for Nozzle Trailing Edge Angle 18 Degrees	121
Table No. 5 Optical Test Rig Results for Nozzle Trailing Edge Angle 28 Degrees.	122

NOMENCLATURE

Symbols

a	speed of sound
C_F	friction coefficient
D_H	hydraulic diameter
e	loss coefficient $(P_{SUP} - P_T)/P_{SUP}$
ℓ	chord
h	enthalpy
H	blade thickness or height
M	Mach number
P_T	total pressure
P_{SUP}	supply pressure
P, P_1, P_2, P_3, P_4	static pressures
P_{atm}	atmospheric pressure
r	radius
R	gas constant
r_{TE}	trailing edge radius
ReD_H	Reynolds number based on hydraulic diameter
Re_H	Reynolds number based on blade height
Re_ℓ	Reynolds number based on chord
T	temperature
T_{SUP}	supply temperature
T_t	total temperature

(Nomenclature - cont.)

T_{atm}	atmospheric temperature
U	peripheral speed
V	flow velocity
V_r	radial component of flow velocity
V_θ	tangential component of flow velocity
γ_N	loss coefficient $(P_{sup} - P_T) / (P_T - P)$

Greek Symbols

ρ	density
α_{TE}	nozzle trailing edge angle
θ	flow angle
θ_M	flow angle obtained from mass flow rate
Q	velocity coefficient
ξ	isentropic loss coefficient

Subscripts

2	nozzle exit condition
s	isentropic condition
TE	trailing edge

ABSTRACT

A study was made of flow characteristics of an adjustable nozzle cascade of a radial-inflow turbine. Nozzles of two different heights were tested at three trailing edge angles and two supply pressures. The test data show that for the low pressure test, the loss coefficient at three different radial locations varied from about 0.035 to 0.12 for nozzle height of 0.200 in. and from about 0.05 to 0.24 for the nozzle height of 0.148 in. For the high pressure test the results show that the loss coefficient for the nozzle height 0.200 in. varied from about 0.02 to 0.08 and for the nozzle height 0.148 in. from 0.06 to 0.14, depending on radius.

The flow angles at three different radial locations were obtained using the mass flow rate. For the low pressure test, the flow angles for probe location no. 1 varied from 21 to 28 degrees for different nozzle heights and setting angles. The range of flow angles for probe location no. 2 under the same conditions as probe no. 1 was from 23 to 30 degrees and for probe no. 3 this range was from 25 to 35 degrees. For the high pressure test, the results indicate that the range of the flow angles for probe location no. 1 was from 25 to 37 degrees, for probe location no. 2 it was from 28 to 39 degrees, and for probe location no. 3 it was from 30 to 44 degrees. In general, the results

show that as the Reynolds number, Re_H , increases from 2.4×10^4 to 4.7×10^4 the flow angles increase and the loss coefficients decrease.

I. INTRODUCTION

The radial flow turbine has had a long history of development since 150 years ago, when the first commercial hydraulic turbine (C-1830) was developed by a French engineer, Fourneyron. His system was of the radial-outflow type. In 1847 a radial-inflow type of hydraulic turbine was built by Francis and Boyden in the U.S.A. The amount of work that one can get from a radial-inflow turbine depends on the difference between the product of tangential component of flow velocity and rotor speed, UV_θ , at entry and exit of rotor. To have the positive work the product of UV_θ at the entry to the rotor must be greater than at rotor exit. This can be achieved by producing large component of tangential flow velocity at rotor entry and allowing little or no swirl in the exit absolute flow. The large component of tangential velocity $V_\theta = V \cos\theta$ can be obtained by either large mass flow rate or small flow angle at rotor entry. To achieve these goals, one needs to know the conditions of the flow after the nozzles. The purpose of this investigation was to obtain a better understanding of the flow downstream of a nozzle cascade of a radial-inflow turbine for different supply pressures, nozzle heights, and nozzle trailing edge angles. The losses in a radial-inflow turbine can be divided into nozzle passage loss, (profile and wall losses), rotor incidence loss, rotor passage

loss, rotor discharge loss, and wheel disk friction loss. In this investigation the nozzle passage loss and the flow angle variation downstream of a cascade of radial nozzle vanes, have been studied.

The enthalpy loss coefficient which normally includes the inlet scroll losses is defined as:

$$\xi = (h_2 - h_{2S}) / \frac{1}{2} v_2^2 \quad (1)$$

The loss coefficient can be expressed in terms of the velocity coefficient

$$Q = \frac{v_2}{v_{2S}} \quad (2)$$

Since

$$h_0 = h_2 + \frac{1}{2} v_2^2 = h_{2S} + \frac{1}{2} v_{2S}^2 \quad (3)$$

and

$$h_2 - h_{2S} = \frac{1}{2} (v_{2S}^2 - v_2^2) \quad (4)$$

we can write

$$h_2 - h_{2S} = \frac{1}{2} v_{2S}^2 (1 - Q^2) \quad (5)$$

Substituting Equation 5 into Equation 1 gives

$$\xi = \frac{1}{Q^2} - 1 \quad (6)$$

The stagnation pressure loss coefficient is defined as follows:

$$Y_N = (P_{o_1} - P_{o_2}) / (P_{o_2} - P_2) \quad (7)$$

The loss coefficient Y_N can be related to ξ by

$$Y_N \approx (1 + \frac{1}{2} \gamma M_2^2) \xi \quad (8)$$

Literature Survey

Literature survey has been done to be able to compare the results of this investigation to other similar investigations. This survey shows that little is known about the losses in radial-inflow nozzle cascades. In 1952 Balje made an attempt to calculate the nozzle loss using friction coefficient for a flat plate in a paper discussing a method of computing performance characteristics of radial-inflow turbine, [1]. In 1960 Mizumachi published his test results (experimental and analytical) [2]. He used an air test rig which had a radial-inflow nozzle cascade followed by another radial cascade of vanes. The purpose of the second cascade of vanes was to remove most of the swirl from the flow. The nozzle flow angle was determined from the flow rate, calculated nozzle exit velocity, and the angular momentum of the air. Tests were made on six straight nozzle cascades, having 16 or 20 blades and also on a special curved nozzle cascade. The height and the chord of the nozzle vanes were 26 mm and 67.5 mm respectively. (The aspect ratio of the nozzle vane was $H/l = 0.385$). The trailing edge radii of the nozzles were in the range of 135 to 144.2 mm, and the throats were in the 7.30 to 15.09 mm range.

Mizumachi's test results show that the flow angle at nozzle exit could be correlated by equation

$$\theta = 0.92 \sin^{-1}(t/S) \quad (9)$$

where t is throat and S is the pitch of a two-dimensional nozzle cascade obtained by transformation of the nozzles tested. The range of angle $\sin^{-1}(t/s)$ was between 5.2° to 15.8° . The nozzle total loss coefficient, ξ , which includes the end walls and profile friction losses, and the secondary loss was found to decrease from about 0.12 to 0.07 as the Reynolds number, Re_λ , increased from 1.5×10^5 to 4×10^5 for all nozzle cascades except for the nozzle cascade having small trailing edge angle of about 5.2° . For this cascade the loss coefficient, ξ , was about 0.15 in the Reynolds number, Re_λ , range from 2×10^5 to 5×10^5 . It dropped to 0.11 in the range of 5×10^5 to 6×10^5 .

In 1959, Knoernschild proposed that the ratio of the tangential component of the flow velocity downstream of the nozzles can be correlated as follows [3]:

$$\frac{V_\theta}{V_{\theta TE}} = \left(\frac{r_{TE}}{r} \right)^{0.9} \quad (10)$$

In 1963, Hiett and Johnston reported on tests of three radial-inflow turbines, [4]. Turbine A had tip width of 0.5 in., turbine B $5/16$ in. and turbine C $3/16$ in. There were seventeen nozzle blades having aspect ratios of approximately 0.38, 0.24, and 0.14. The trailing edge of the nozzle cascade was located on a 5.5 in.

diameter circle, and the trailing edge pitch/chord ratio was 0.75. The flow angles for three different nozzle trailing edge angles, 10° , 20° , and 30° were obtained by calculation of the mass flow rate. In order to investigate the effect of incidence angle on the performance of the nozzles, two tests were run with the inlet scroll of turbine A and with turbine B. This configuration was called the AB build. The results show that for three turbines A, B, and C and for nozzle trailing edge angle 20° , the incidence angle for turbines A and B was 15° . It was 9° for turbine C. The results for the turbine B show that for three different nozzle trailing edge angles 10° , 20° , and 30° the incidence angles were 8° , 15° , and 21° respectively, and, for turbine build AB for nozzle trailing edge angles 20° and 30° the incidence angles were in order of 2° and 10° . For the nozzle trailing edge angle of 20° , the loss coefficient, Y_N , was higher in turbine A than C. It varied from 0.04 to 0.07. When the nozzle trailing edge angles were 20° , the flow angle at a radius of 5 in. for three turbines A, B, and C was 21.3° , 22.3° and 22° , respectively. The loss coefficients for turbine B for three different nozzle trailing edge angles 10° , 20° , and 30° were 0.05, 0.05, and 0.07 respectively. The flow angles at radius of 5 in. for the turbine B tested at three nozzle trailing edge angles 10° , 20° , and 30° were 13.1° , 22.3° , and 31.3° . For

turbine build AB, the results show that for two nozzle trailing edge angles 20° , and 30° the loss coefficients were the same and equal to 0.03 but the flow angles at radius of 5 in. were 22.6 and 32.2 for two nozzle trailing edges angles 20° , and 30° , respectively.

The Reynolds number based on the flow velocity at nozzle exit and the turbine tip widths was approximately in the range of 0.5 to 2.2×10^5 . The results show that the nozzle pressure loss coefficient is dependent on the incidence angle to the cascade and on the nozzle trailing edge angle. The flow angles 0.5 in. downstream of the nozzle were found to be 1.3° to 3.1° larger than the nozzle trailing edge angles. Hiett and Johnston have found that the measured flow angles at nozzle exit corresponded closely to those obtained from the sine rule.

In 1966, Rodgers [5] reported that for small incidence angles the following equation for the total nozzle loss coefficient could be used. For $1.0 > r/r_{TE} > 0.91$

$$\xi = \frac{0.05}{(Re_H)^{0.2}} \left[\frac{3\cot\theta}{S/\lambda} + \frac{S\sin\theta}{H} \right] \quad (11)$$

where S is the nozzle pitch, λ is the chord and H is the nozzle height. The Reynolds number is based on the flow velocity at nozzle exit.

In 1973, Benson and Jackson [6] reported that the flow angle in the interspace between nozzle cascade and rotors of a radial-inflow water turbine model was affected not only by the flow rate but also by the turbine rotor speed. Their results showed that the flow angle downstream of a nozzle cascade having nozzle trailing edge angle 15.4° in general at first decreased with radius and subsequently started to increase. At a radius ratio, r/r_{TE} , of 0.95 the flow angle was between 43° and 30° , depending on the test condition. It was constant in the radius ratio range from about 0.88 to about 0.75. Subsequently, it started to increase.

In 1967, Khalid, Tabakoff, and Hamed [7] reported on their experimental and theoretical studies of losses in nozzles of radial-inflow turbines. They concluded that for the thin long curved nozzle blades used the nozzle total loss coefficient depends on the nozzle trailing edge angle, Mach number, and the boundary layer profile parameters. Their results are presented in form of graphs and maps.

In 1980 Fairbanks presented results of experiments and analysis of the deviation angles at the exit of a radial nozzle cascade [8]. The results showed that for very thin nozzle trailing edge angles with aspect ratio $H/\lambda \approx 0.26$ the mean flow angle at nozzle exit was about 30° for the nozzle trailing edge angle of

27°. The flow angle at the exit from the nozzles was determined using total pressure probes located at various angles downstream of the nozzles. The mass-flow averaged values of the total loss coefficient ranged from 0.033 to 0.0414 for lowest and highest mass flow rate respectively. No values of the Reynolds number are given.

II. TEST OBJECTIVES

The objectives of the test were to obtain the total pressure loss characteristics and the average flow angles downstream of a set of 13 nozzle vanes of a radial inflow turbine. The results were to be obtained for three different nozzle trailing edge angles and for two different blade heights. The original plans called for the tests to be made at an average flow Mach number at the nozzle throats of about 0.2, 0.5, 0.7 and 1.0 and at trailing edge angles of 10°, 15°, and 20°. The blade heights were selected to be 0.148 in. and 0.200 in. During the test program a flow instability, known as the "vortex whistle", appeared. This flow instability, which affected the total pressure readings, limited the flow Mach numbers and the vane trailing edge angles at which tests could be run. The vortex whistle appeared at small trailing edge angles at sufficiently high supply pressures. Its appearance could be delayed only by inserting a set of guide vanes to remove most of the swirl component of the flow. These guide vanes were placed near the exit of the vaneless space downstream of the nozzles. More detailed description of the vortex whistle phenomenon is given in Section IV. As a result of the limitation on the test conditions imposed by the vortex whistle, the objectives were modified and the tests were run for the two selected blade heights of 0.200 in. and 0.148 in. at

the trailing edge angles of 15° , 20° , and 25° and at the flow
Mach numbers at nozzle throats of about 0.2 and 0.4.

III. DESCRIPTION OF TEST SET UP

Figure 1 shows the line diagram of the test set up. A Richmond Engineering Co. type MFG. No. K-41372TK15 tank was used at inlet to which air was supplied by a compressor at 80 psig. The mass flow rate of air was measured by a standard orifice with flange pressure taps which were connected to a U-tube manometer filled with water for the tests at a Mach number about 0.2 and with a fluid having specific gravity 2.95 for the tests at a Mach number of 0.4. Figure 2 shows the drawing of the orifice mounted between flanges. A Fisher type 99-901 control valve was used to control the air pressure in the 2 in. diameter PVC pipe leading to the test rig. Experiments were run on two different test rigs, the main test rig and the optical test rig.

3-A The Main Test Rig

The main test rig was designed and manufactured by the Air Products and Chemicals, Inc. Figures 3, 4, 5, 6 and 7 show photographs of the rig. The three important components of the steel test rig were: the nozzle vanes, the probe holder, and the shroud. Figure 8 shows the drawing of the steel test rig and its components.

The Nozzle Vanes

The main test rig was designed with 13 nozzles. Figure 7 shows a photograph of the nozzles. A drawing of the nozzle vanes is shown in Figure 9.

The nozzle vanes could be rotated about controllly-located shafts so that their trailing edge angles could be changed. The trailing edge angle adjustment was accomplished with the aid of a linkage shown in Figure 8. To set the trailing edge angle of the vanes, a bar with an indicator and a brass protractor were used. By moving the bar and reading the brass protractor angle, one could set the desired trailing edge angle of the vanes. The bar and the brass protractor can be seen in Figure 5. Figure 10 shows a plot of the variation of the brass protractor angles with the trailing edge angle of the vanes and table 1 shows the values of plotted points. The throat widths between the nozzle vanes were measured for different trailing edge angles and the results are presented in table 2 and in graphical form in Figure 11. In the experiments, two sets of nozzle vanes were used both having identical profiles but different heights. The vane heights were 0.200 in. and 0.148 in.

The Probe Holder

The probe holder can be seen in the photographs shown in Figures 5 and 7. A drawing of the probe holder is shown in Figure 12. The probe holder was connected to the steel test rig by a steel collar and four bolts which can be seen in Figure 5.

The total pressures were measured by three probes at three different radii, 1.44 in., 1.28 in., and 1.03 in. The static pressures were measured by three pressure taps which were provided in the probe holder at the same radii. By loosening the steel collar one could rotate the probe holder from zero to 360 degrees. (The test data were taken for 40 degree arcs at five degree intervals.)

Rotation of the probe holder was accomplished by using a steel rod which was located at the center of the probe holder. This rod can be seen in Figure 5. A circular plexiglass disk attached to the steel rod, was provided with radial indicator lines at probe locations to facilitate measurement of the flow angles. It can be seen in Figure 5. Figure 13 shows a drawing of the circular plexiglas disk.

The Shroud

Figures 6 and 14 show a photograph and a drawing of the shroud, respectively. The shroud was movable in and out with

the aid of four jack bolts. Movement of the shroud was needed to ensure that the vanes were touching the shroud and pressing against the steel front casing plate.

3-B the Optical Test Rig

The optical test rig was designed with an idea to observe the formation of shock waves, if they existed, at nozzle exits for large pressure ratios across the nozzles. In addition, it allowed us to measure the pressure distribution of air in one nozzle passage. Figures 15, 16 and 17 show photographs of the optical test rig, and Figure 18 shows the drawing of the rig. The optical test rig had six vanes of 0.200 in. height with the same shape as those which were used in the main test rig. The nozzle vanes were designed so that they could be set at three different trailing edge angles of 8°, 18° and 28°. The rest of the flow passage was blocked by a ring segment made of plexiglass. Figure 16 shows the ring segment and the location of the eight pressure taps of 1/32 in. diameter which were used to measure the static pressure in one nozzle passage. A window was provided in the optical test rig to allow optical measurements to be made. That window can be seen in the photograph shown in Figure 15.

3-C Modifications to the Steel Test Rig

The following modifications were made to the test rig:

1-Modifications to the Shroud and the Probe Holder

The modifications to probe holder and shroud are shown in Figures 12 and 14, respectively. The reason for the modification of the probe holder was to decrease its tip in size. The shroud was modified to increase its exit flow area and to make it of uniform cross section.

2-Modification to the Attachment Plate of the Steel Rod

A new plexiglass attachment disk was designed to facilitate precise measurement of the flow angles and of the spanwise distances of the probe from the shroud. The drawing of the disk is shown in Figure 13.

3-The Guide Vanes

To remove the vortex whistle as much as possible a set of 18 guide vanes was designed to make the flow of air more radial in the vaneless space near the exit. A photograph and two drawings of the guide vanes are shown in Figures 19, 20, and 21, respectively.

IV. DESCRIPTION OF THE MEASUREMENT EQUIPMENT

In the tests, measurements were made of the static and total pressures, the mass flow rate and the temperatures. A Meriam Instrument Co. Type W, model 30KH80 mercury manometer was used to measure the static and supply pressures. Differences between the supply pressure and the total pressures were measured by three U-tube water manometers. Each manometer had a safety valve to prevent escape of water from the manometers into the main test rig. The temperatures of air were measured by two thermocouples, one located at a point 20 in. upstream of the flow orifice, and the other in the collector of the main test rig.

The mass flow rate of air was measured by an orifice having 1.145 in. diameter. The static pressure at the upstream tap of the orifice was measured by a gage. The pressure difference across the orifice plate was measured by a U-tube manometer filled with water for the low pressure test and with a manometer fluid having specific gravity of 2.95 for the high pressure test. A sample of the mass flow rate calculation is shown in Appendix B.

The total pressures were measured using three cobra probes at three different locations, as shown in Figure 13. A drawing of a probe which was used in experiments is shown in Figure 22. Each probe had a protractor rigidly attached to measure the flow angle. These probes could be used up to the flow Mach number

of 0.7 and pitch angles smaller than 5 degrees. Each probe was made of three small tubes. The middle tube was used to measure the total pressure at the time when the side tubes were reading the same pressure.

Calibration of the protractor of the probes was performed using a steel pipe as shown in Figure 23. The calibration procedure was as follows: To get the zero of a protractor lined up with the head of its probe, a probe was placed inside of the steel pipe. The side tubes of the probe were connected to a U-tube manometer and the middle tube was blocked by a plastic cover. Air flow was introduced into the steel pipe, and the probe rotated until side tubes were reading the same pressure. At this time the protractor of the probe was rotated (without rotating probe) until the zero of the protractor and a sharp edge located on the steel pipe were matched. Then the protractor was tightened to the probe and the calibration process was completed. Three U-tube water manometers with safety valves were used to balance the pressures in the side tubes of the three probes. These manometers were made of glass tubes (O.D.=0.6 cm) which could take high pressure.

V. DESCRIPTION OF TEST PROCEDURE

Two series of tests were made on the main test rig. One series corresponded to a flow Mach number at nozzle exits about 0.2, and the other corresponded to the flow Mach number of about 0.4. The tests on the steel test rig included measurement of the total and static pressures, flow rates, and flow angles corresponding to nozzle trailing edge angles of 15°, 20° and 20°. Test data were obtained for two sets of nozzles having heights of 0.148 in., and 0.200 in. The measurements were made using three pressure probes at spanwise probe locations corresponding to approximately 12.5%, 25%, 50%, 75% and 87.5% of nozzle heights. The pressure measurements were made with each probe over 40 degrees traverse angles, every five degrees.

Figure 24 shows the test data sheet used. The test procedure consisted of the following steps:

1. The control valve was set to give required supply pressure (P_{SUP}) and the flow orifice manometer was read.
2. The three pressure probes were set at the selected spanwise location.
3. The probe holder was rotated to zero circumferential traverse angle position.
4. The safety valves of the water manometers were opened.
(Three water manometers were used for balancing the probes, and

three more for measuring the difference between the supply pressure and the total pressures.)

5. The PVC valves No. 1 and 2, shown in Figure 1, were opened to let the air flow to the system. At this time a check for leakages was made.

6. After a couple of minutes, probes were balanced at the maximum total pressure reading by using water manometers.

7. After balancing of the probes was finished, the static pressures (P_S), probe angles (α) and the differences between the supply and total pressures ($P_{SUP} - P_{TOTAL}$) were measured.

8. Next, the probe holder was rotated five degrees and new test data obtained as before.

9. The same procedure was followed for the remaining circumferential position until a 40° arc was traversed.

10. After the last traverse angle reading was recorded, the flow valve was closed. The probes were moved to new spanwise locations, and the test procedure repeated.

The same steps were followed for other trailing edge angle settings and for the other set of vanes.

VI. TEST RESULTS FROM THE MAIN TEST RIG

A sample of test results corresponding to selected values of spanwise locations, nozzle trailing edge angles and supply pressure is given in Appendix C. The data shown includes the measured flow angle, the static-to-total pressure ratio, the dimensionless total pressure loss coefficient $(P_{SUP} - P_T)/P_{SUP}$, and the computed flow velocities and flow Mach numbers, for various circumferential and spanwise probe locations for the nozzle trailing edge angle of 25 degrees. The nozzle height in these tests was 0.200 in. and the throat Mach number was about 0.2. The test points correspond to the three pressure probes used.

Calculation of the flow velocities and the flow Mach numbers was done on a computer. The test results obtained were averaged using the flow-weighting technique. The results are shown in Figures from 25 to 44.

Figures 25, 26, 27 and 28 show the variation of the flow angle with the radius ratio, r/r_{TE} , for three nozzle setting angles of 15°, 20° and 25° for the low pressure test ($P_{SUP} = 19.26$ psia) and the high pressure test ($P_{SUP} = 24.4$ psia), and two nozzle heights 0.148 in. and 0.200 in. Figures 29, 30, 31 and 32 show the variation of the flow velocity, Figures 33, 34, 35 and 36 show the variation of the Mach number, Figures 37, 38, 39 and 40 show the variation of the $(P_{SUP} - P_{TOTAL})/(P_{SUP})$.

Finally, the variation of the loss coefficients,
 $(P_{SUP} - P_{TOTAL}) / (P_{TOTAL} - P_{STATIC})$, with the radius ratio, r/r_{TE} ,
are shown in Figures 41, 42, 43 and 44.

VI. SECONDARY FLOW VISUALIZATION IN THE MAIN TEST RIG

The flow visualization in the main test rig was obtained by using drawing paper which was attached to the shroud and the probe holder walls and covered uniformly with a mixture of oil and fine graphite powder. Air was allowed to flow through the nozzle cascade for five minutes. Then the paper was removed and photographed. Figures 73 to 80 show the photographs of the patterns of air on the walls of the nozzle cascade for two nozzle heights 0.200 in. and 0.148 in., and for three nozzle trailing edge angles 10, 15, 20 and 25 degrees, for the low pressure test conditions. For the high pressure test the flow visualization was done only for the nozzle height 0.148 in. and for two nozzle trailing edge angles 15 and 25 degrees. These flow visualization tests were run with and without swirl-removing guide vanes. Figures 81, 82, 83, and 84 show the photographs of the patterns of air on the walls of the nozzle cascade for the high pressure test.

VII. TEST RESULTS FROM THE OPTICAL TEST RIG

The test results obtained on the optical test rig are shown in Tables 3, 4 and 5. These results were obtained for three different trailing edge angles 8° , 18° , and 28° , for the vanes having height of 0.200 in., and for five supply pressures. For each supply pressure four static pressures were measured close to the exit opening of the optical test rig. From the pressure ratios of static pressures to supply pressures, flow Mach numbers downstream of nozzle throats were calculated. The pressure taps were located at radii 2.09 in., 1.98 in., 1.875 in., and 1.81 in. They correspond to locations No. 1, 2, 3 and 4.

VIII. ANALYSIS OF TEST DATA

The variation of the measured flow angle with the radius ratio, r/r_{TE} , is shown in Figures 25, 26, 27 and 28. For the low pressure test and for the two sets of vanes used, the results show that the flow angles tend, in general, to decrease as the r/r_{TE} ratio decreases. For the high pressure test, the results show that the flow angles are approximately constant with the r/r_{TE} ratio. The experimentally-determined flow angles using the cobra probe are not considered to be correct. The reason for it is the fact that two side pressure tubes of the cobra probe are at different radii at all flow angles except at 90° (radial flow), and the static pressure depends on radius. The flow angles in the test rig were of the order of 30° .

Since the flow angles could not be obtained from the cobra probe measurements, it was decided to calculate them using the mass flow rate, determined with the orifice, and the flow velocities. The flow velocities were determined using the total pressure readings, obtained from the cobra probe, which were considered to be reliable, and the static pressures measured using wall taps. The average flow velocities for each probe location were obtained by flow-weighing. The flow angles determined using the measured mass flow rate, θ_M , are plotted against the radius ratio, r/r_{TE} , in Figures 63 and 64. The values of the flow

angles corresponding to the trailing edges of the nozzle vanes were obtained using extrapolated values of the flow velocity and density. These figures show that the flow angles increase from probe no. 1 to probe no. 3. It decreases from the trailing edges to the probe no. 1 for the nozzle height 0.20 in. for the low pressure and the high pressure tests, and increases for the nozzle height 0.148 in. for the low pressure test and decreases for the high pressure test. A decrease of the flow angle from the trailing edge can be explained by the effect of the vane trailing edge thicknesses. For each trailing edge angle the values of θ_M for H=0.200 in are above the values for H=0.148 in.

The effect of the Reynolds number based on hydraulic diameter of the nozzle throat passage, Re_{DH} , on the flow angles for three probe locations are shown in Figures 65, 67, and 69. Figures 66, 68, and 70 show the effect of the Reynolds number based on nozzle vane height, Re_H , on the flow angles for three probe locations. Figures 65, 67 and 69 show that the flow angles, θ_M , increase as the Reynolds number, Re_{DH} , increases from 3.15×10^4 to 7×10^4 . Figures 66, 68, and 70 show that the flow angles, θ_M , also increase as Reynolds number, R_H , increases from 2.25×10^4 to 5.35×10^4 .

The variations of the angular momentum per unit mass, rV_θ , with the radius ratio, r/r_{TE} , for the low pressure and high pressure tests using flow angles from the mass flow rate calculations are

shown in Figures 71 and 72. These figures show that the term rv_θ decreases as the radius ratio, r/r_{TE} , decreases. This is because the angular momentum of the fluid decreases as a result of friction. The results show that the flow in the vaneless space is not a free vortex flow in which $rv_\theta = \text{constant}$. The values of the term rv_θ are larger for the nozzle vane height (H) of 0.148 in. than for the nozzle vane height 0.200 in. This is so because for the same supply pressure, the flow velocity for $H=0.148$ in. is larger than for $H=0.200$ in. For the smaller nozzle trailing edge angles, the values of rv_θ are larger than for the larger trailing edge angles mainly because the corresponding flow angles are smaller.

The variations of the flow velocities with radius ratio, r/r_{TE} , show that, as expected, the velocities increase as radius ratio, r/r_{TE} , decreases. Figures 29, 30, 31 and 32 show that the flow velocity increases as nozzle vane height decreases from 0.2 in. to 0.148 in. It can be also seen that the flow velocities are higher for smaller trailing edge angle. The only exception is for the test points corresponding to $\alpha_{TE} = 15^\circ$, $H = 0.200$ in and $M_{TE} \approx 0.2$. It appears that these test results should be disregarded.

The variations of the loss coefficients, $\gamma_N = (P_{SUP} - P_T) / (P_T - P_{STATIC})$ and $\xi = [(h-his)/\frac{1}{2} \rho v^2] \approx \gamma_N / (1 + \frac{\gamma M^2}{2})$ with the Reynolds number

based on hydraulic diameter of the nozzle throat passage, R_{DH} , nozzle vane height, Re_H , and nozzle vane chord are shown in Figures 45 to 62 for the three probe locations. These figures show that the values of the loss coefficients, γ_N and ξ are higher for the nozzle vane height of 0.148 in. than 0.200 in. As Reynolds number increases the loss coefficients decrease for the nozzle height of 0.200 in. at all three probe locations. For the nozzle height 0.148 in. the losses increase with increasing Reynolds number for $r = 1.44$ in. They decrease at the other probe locations. The values of the Re_λ are greater than the values of Re_{DH} and Re_H . The values of the Reynolds number, Re_λ , are about 1.8×10^5 for the nozzle height 0.200 in. and 2.25×10^5 for nozzle height 0.148 in. for the low pressure test. For the high pressure test, the values of the Reynolds number, Re_λ , are about 3.6×10^5 for nozzle vane height 0.200 in., and 4.2×10^5 for nozzle height 0.148 in. For the three nozzle trailing edge angles, 15, 20, and 25 degrees the values of the loss coefficients are closer to each other for nozzle height 0.200 in. than 0.148 in.

Figures 73 to 84 show the flow patterns on the probe holder and shroud walls. Clearly visible are the secondary flows in the form of leading-edge vortices, and the direction of the incoming flow to the cascade. The wall traces show that the inlet angle to the cascade varied circumferentially and, as a result,

some leading edge vortex traces differed considerably from each other. The photographs show that in radial inflow cascade with incoming flow direction varying from radial to that of zero incidence angle, as a result of a strong radial pressure gradient, the nozzle passage vortices are either very weak or entirely absent and the upstream-facing pressure side legs of the leading edge vortices in general do not meet the suction sides of the adjacent blades. Figure 80 shows that for small nozzle trailing edge angles the vortex legs forming on the suction side of the blades are swept by the radial pressure gradient away from the blades. At the same time the vortex legs forming on the pressure side of the blades are pressed against the blade side walls and leave the blades at the trailing edges. Thus they form a spiral of well-defined traces (of counter-rotating vortices) which converge to the small exit radius. This phenomenon is more visible in photograph of nozzle height 0.200 in. Figures 81 and 82 show that for the high pressure test the phenomenon causing the vortex whistle interferes with the leading edge vortex, making it difficult to see them on the traces. The effect of the vortex whistle phenomenon is stronger for small nozzle trailing edge angles than for large ones. This can be seen in Figure 82, where for the nozzle trailing edge of 15 degrees and no guide vanes, the paper on the probe holder wall was torn by the vortex.

A comparison of the test results with those of Mizumachi [2] shows that for the probe location no. 1 the loss coefficient, ξ , is smaller than Mizumachi's average values by about 0.05 for the low pressure test and about 0.025 for the high pressure test. Mizumachi's loss coefficients do not include the effects of the vaneless space. In addition, his nozzles had high aspect ratio. As a result, his loss coefficients appear to be too high.

The angular momentum variation shown in Figure 71 shows that for the nozzle trailing edge of 15° and nozzle height 0.148 in. the term, $rv_{\theta TE}$, is about 9 (ft^2/sec) greater than the value obtained from Equation 10. In general, the experimental results show that the term, $rv_{\theta TE}$, decreases with decreasing radius much faster than Equation 10 predicts.

A comparison of the loss coefficient, ξ , with Equation 11 shows that for the probe location no. 1 and the low pressure test, for the nozzle vane height 0.200 in. the loss coefficients, ξ , are 0.121, 0.097, and 0.082. The corresponding measured results shown in Figure 50 are 0.035, 0.05, and 0.034. These losses are for the nozzle trailing edge angles 15° , 20° , and 25° , respectively. A comparison of the loss coefficients which are obtained from Equation 11 with those from this experiment shows that Equation 11 predicts always higher losses.

The loss coefficients, ξ , of Hiett and Johnston correspond to somewhat higher Reynolds numbers than those covered in these tests. Their values are lower than those determined in this investigation.

IX. CONCLUSIONS

This study showed that the flow in the vaneless space downstream of nozzles of a radial-inflow turbine is not uniform. It also showed that, in the test rig used, the incidence angles around the nozzle vanes varies from blade to blade. The loss coefficients generally decrease as the Reynolds number increases, and the losses are greater for blade height 0.148 in. than 0.200 in.

The flow angles for the nozzle height 0.200 in. and the low pressure test increase from probe no. 1 to probe no. 3 and decrease from the trailing edge radius to probe no. 1. For nozzle height 0.148 in. and the low pressure test the flow angle always increases as the radius ratio, r/r_{TE} , decreases from the trailing edge to the probe location no. 3. The high pressure test results show that the flow angle increases from probe no. 1 to probe no. 3 and decreases from the trailing edge to probe no. 1 for both nozzle heights 0.200 and 0.148 in. The results also show that, in general, the flow angles increase as the Reynolds number increases and as the nozzle height increases. In addition, it was found that, in general, the loss coefficients decrease as the Reynolds number increases and as the nozzle height increases.

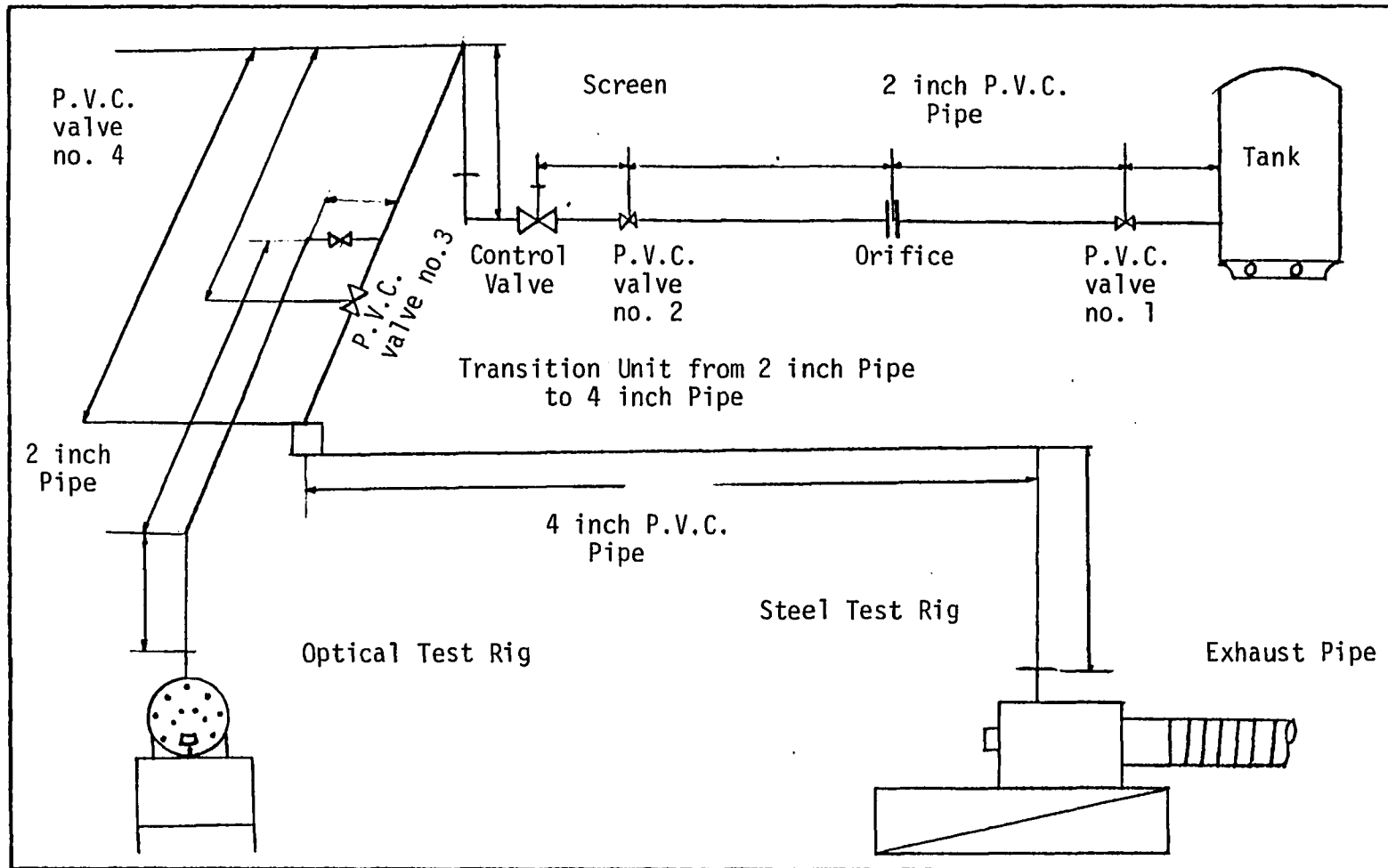


FIG. 1 Line diagram of the test setup.

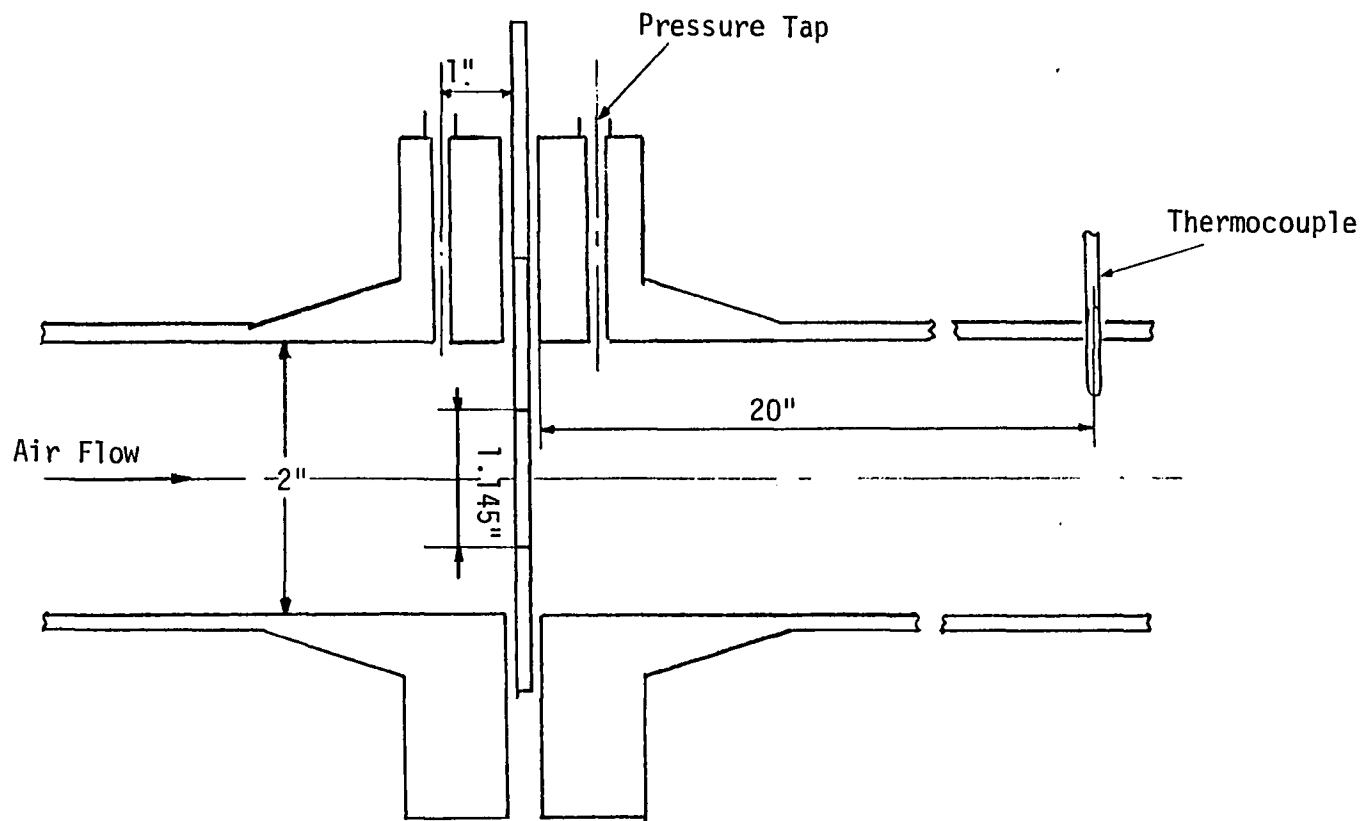


FIG. 2 Drawing of orifice with flange taps

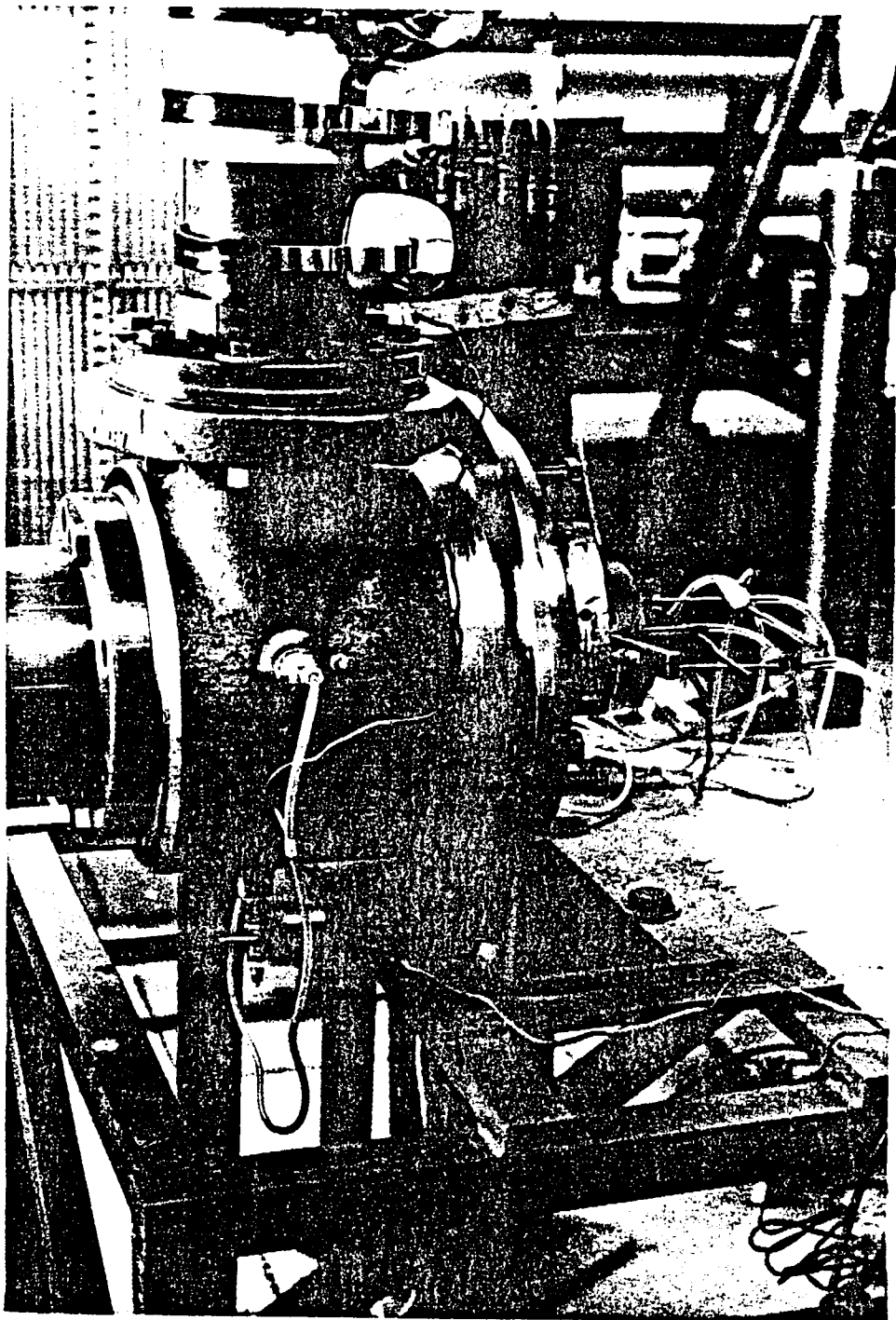


FIG. 3 Picture of steel test rig from side view.

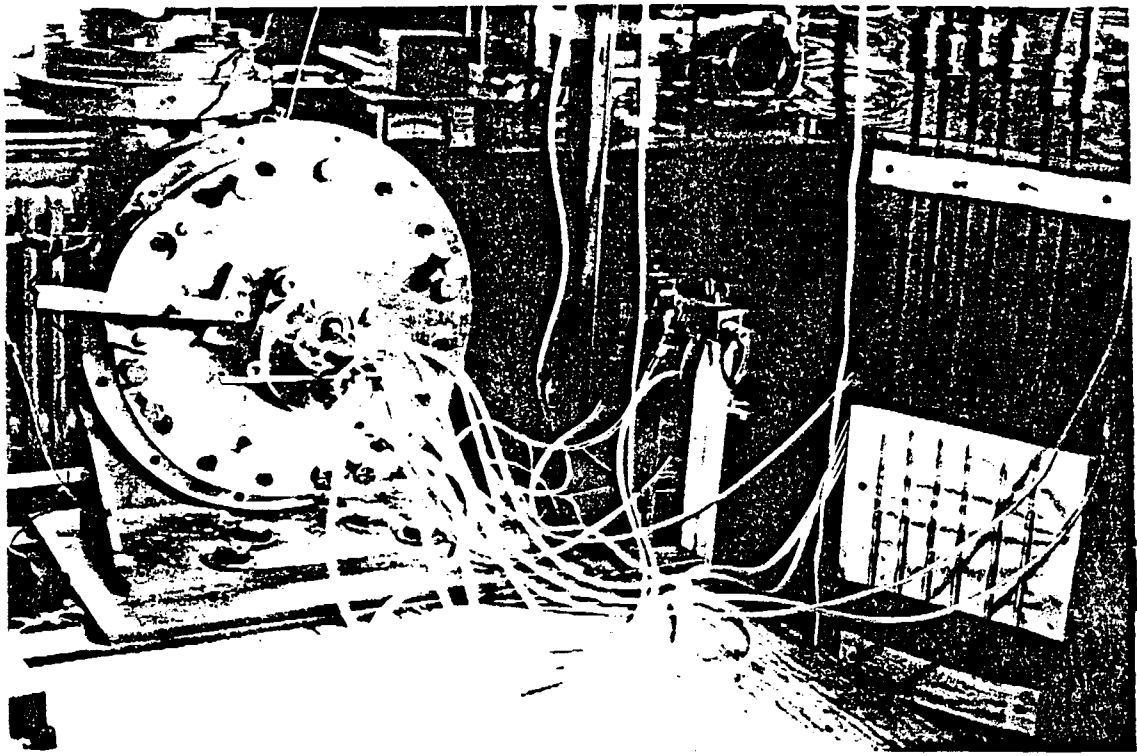


FIG. 4 Picture of steel test rig from front view.

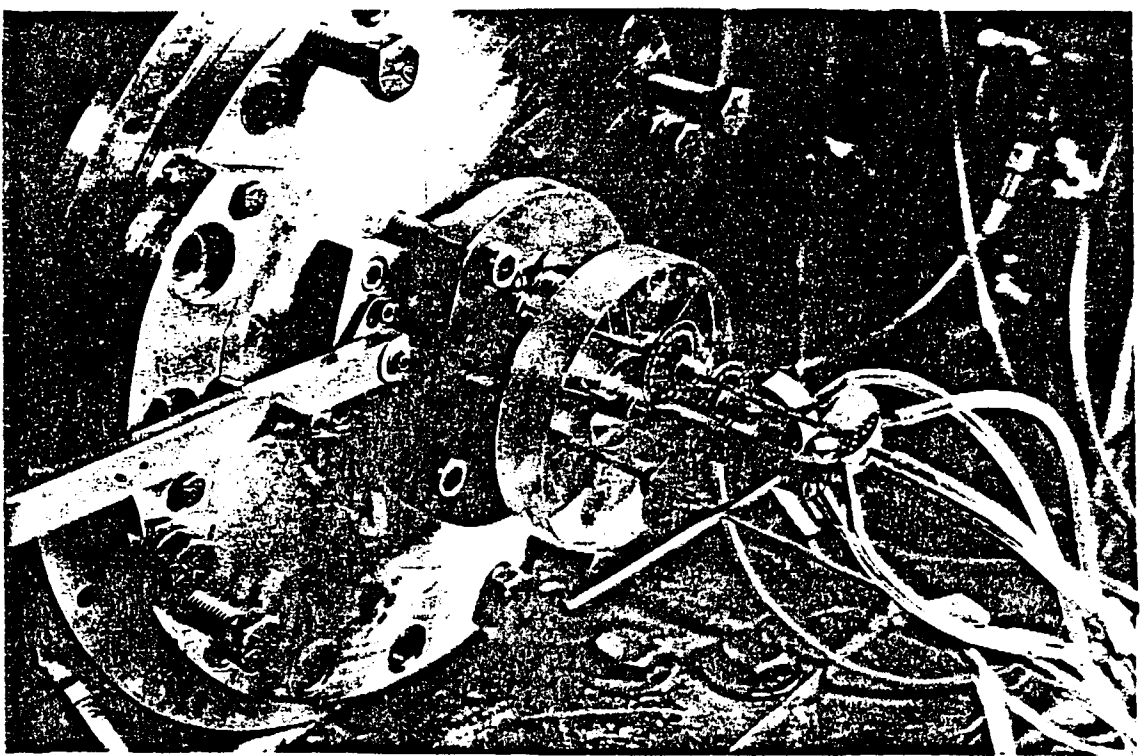


Fig. 5 Picture of probe holder and probes.

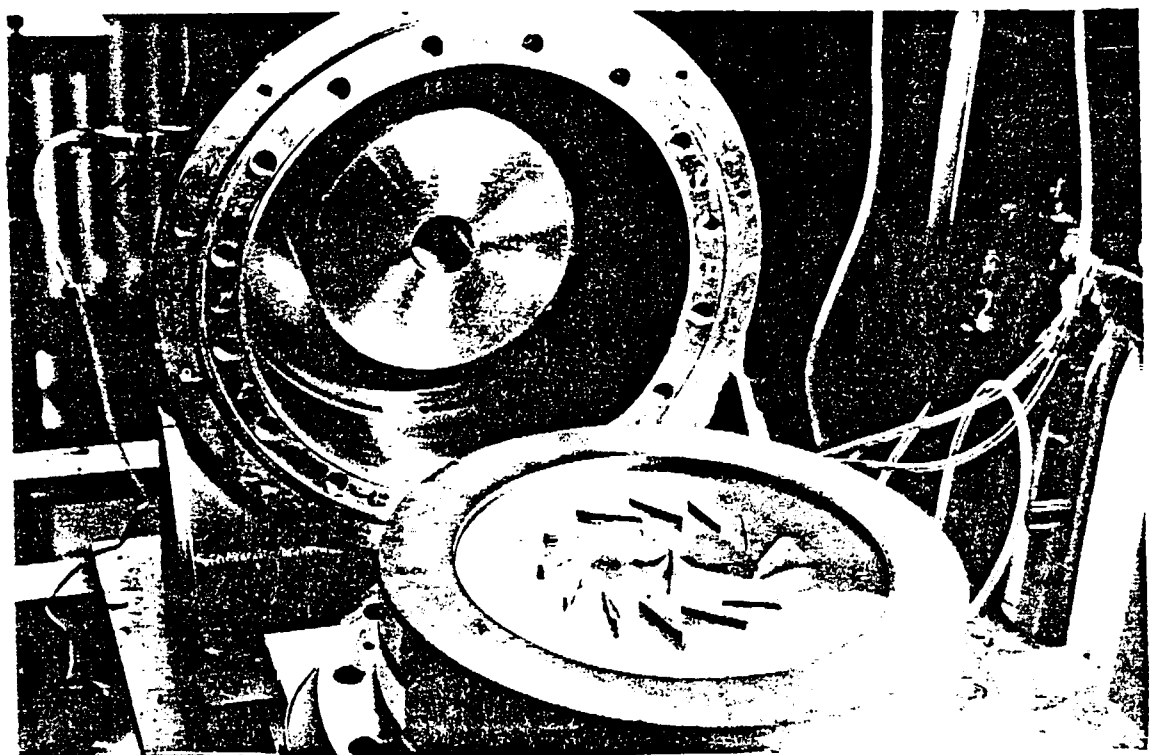


FIG. 6 Picture of nozzles and shroud (inside look of steel test rig)



FIG. 7 Nozzle assembly and inside look of probe holder

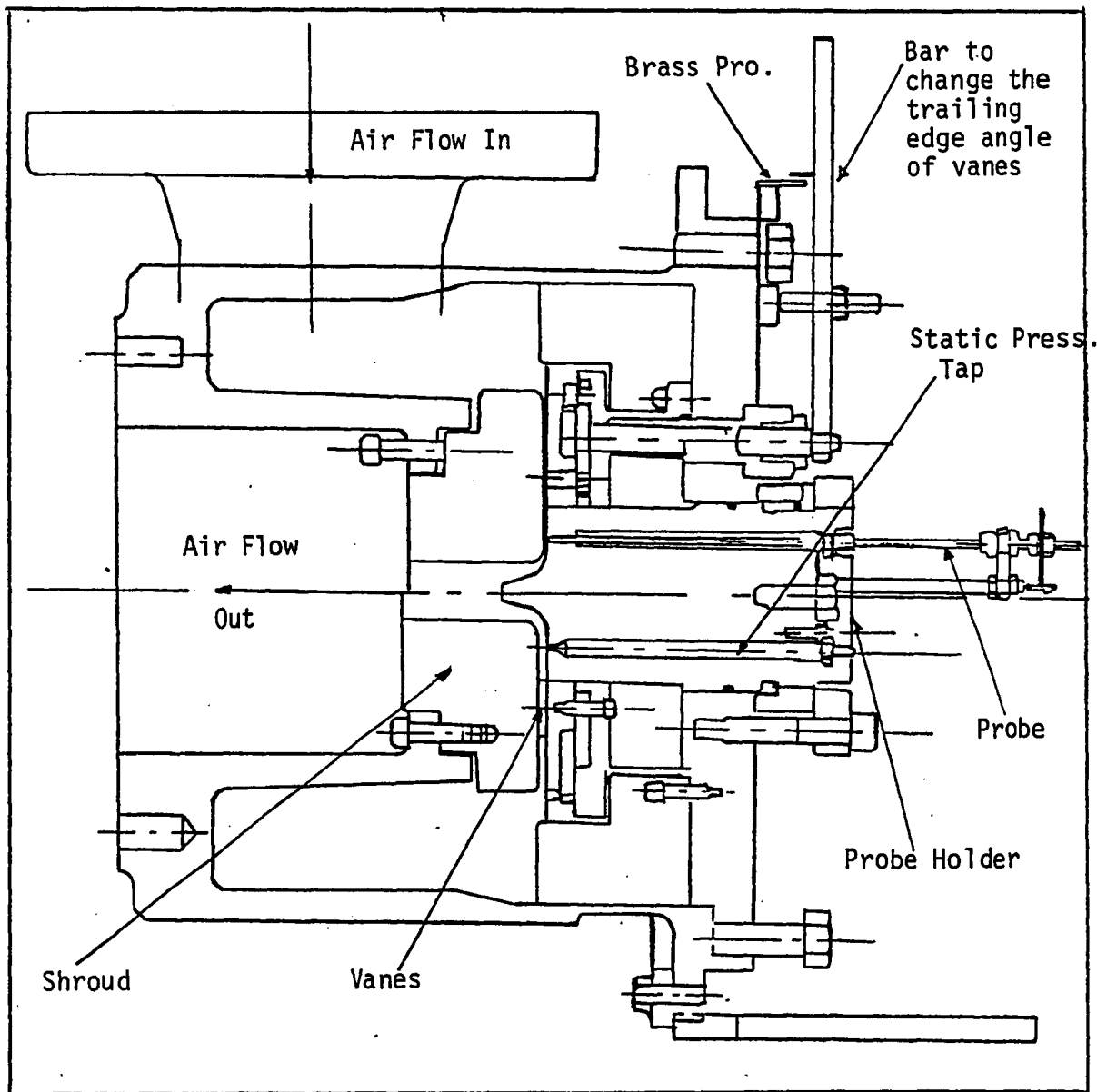


FIG. 8 Drawing of the main test rig.

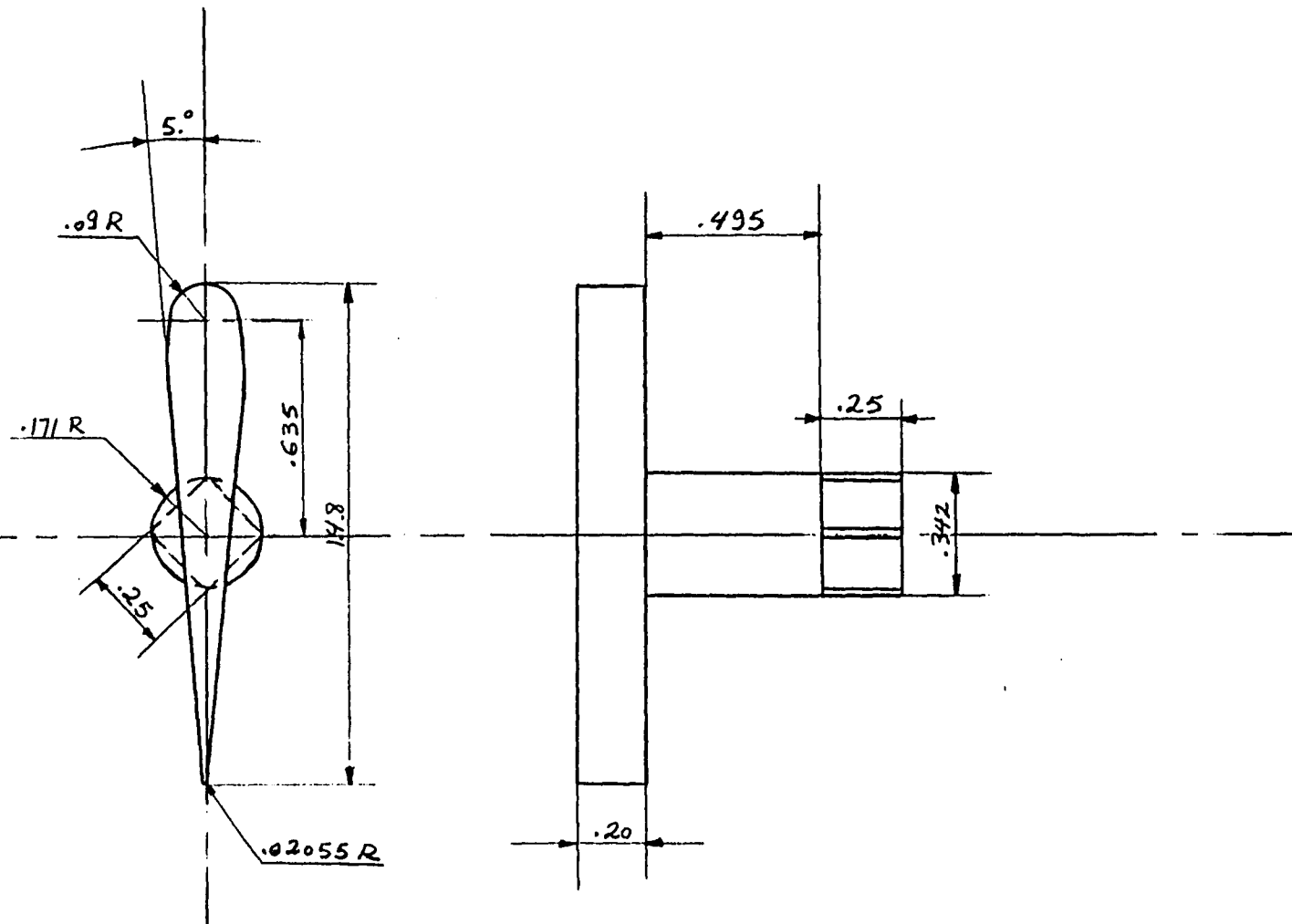


FIG. 9 Drawing of one vane with width .2 in.

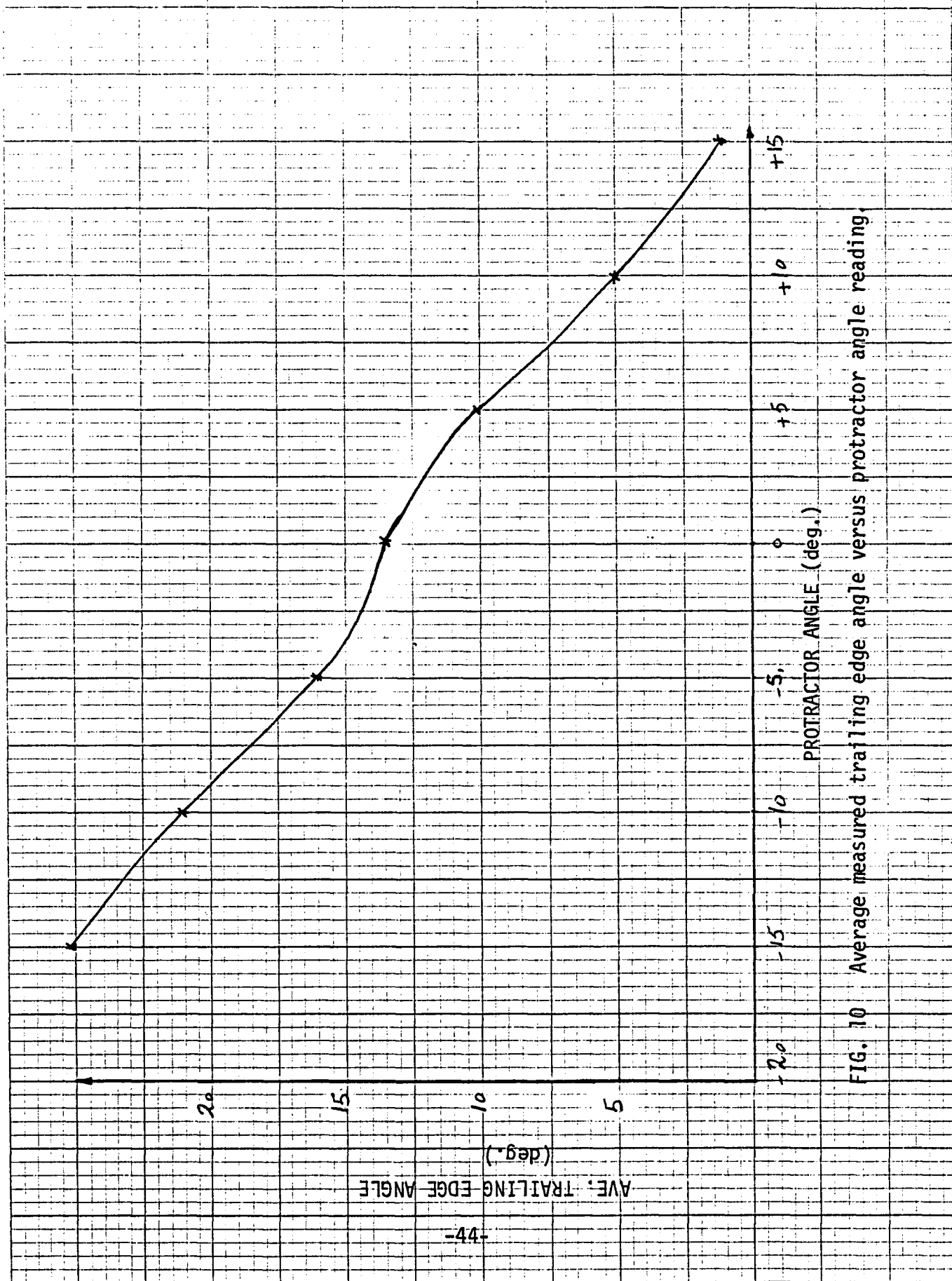


FIG. 10 Average measured trailing edge angle versus protractor angle reading.

AVE. TRAILING EDGE ANGLE

(deg.)

20

15

10

5

-4

-20

-15

-10

-5

0

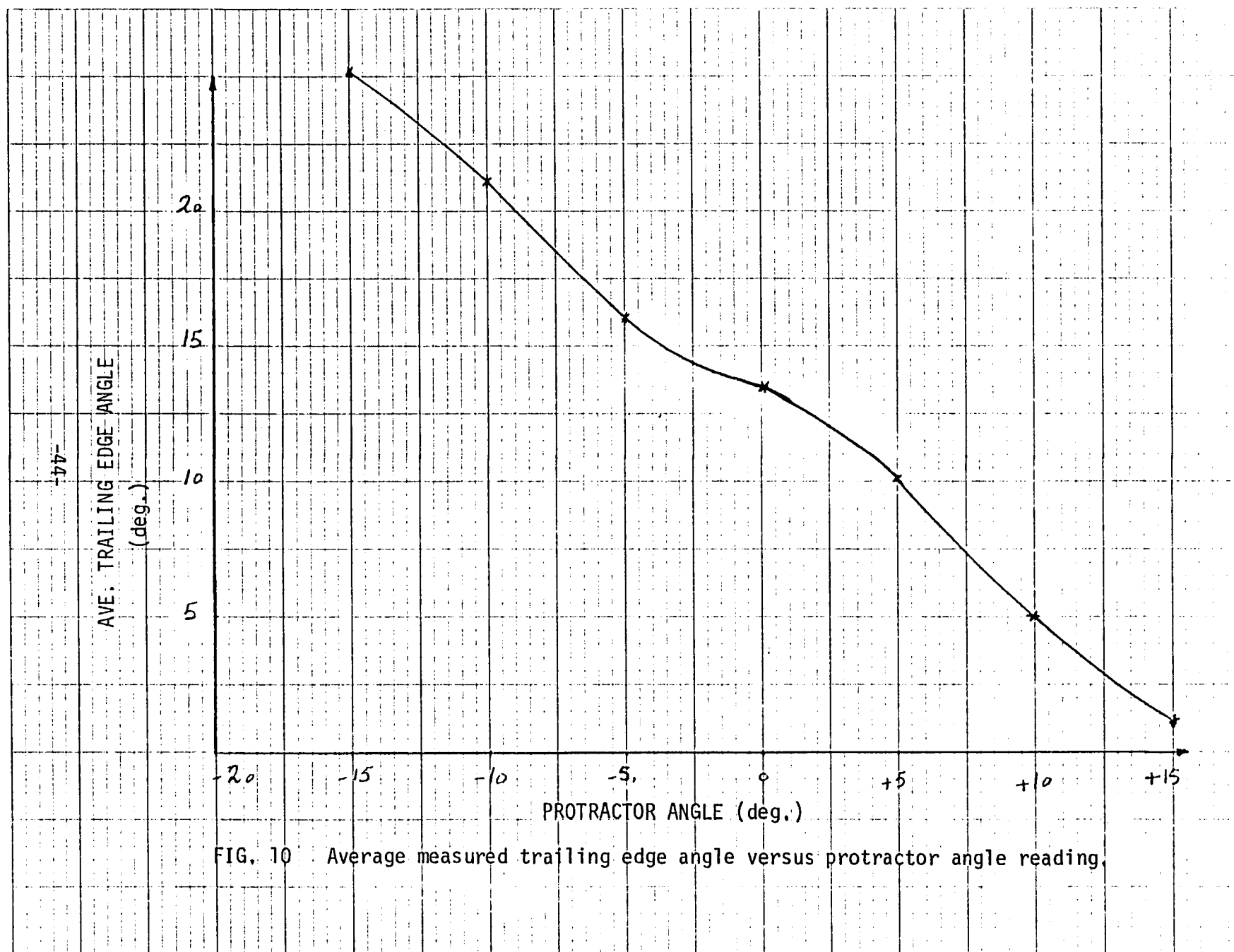
+5

+10

+15

PROTRACTOR ANGLE (deg.)

FIG. 10 Average measured trailing edge angle versus protractor angle reading.



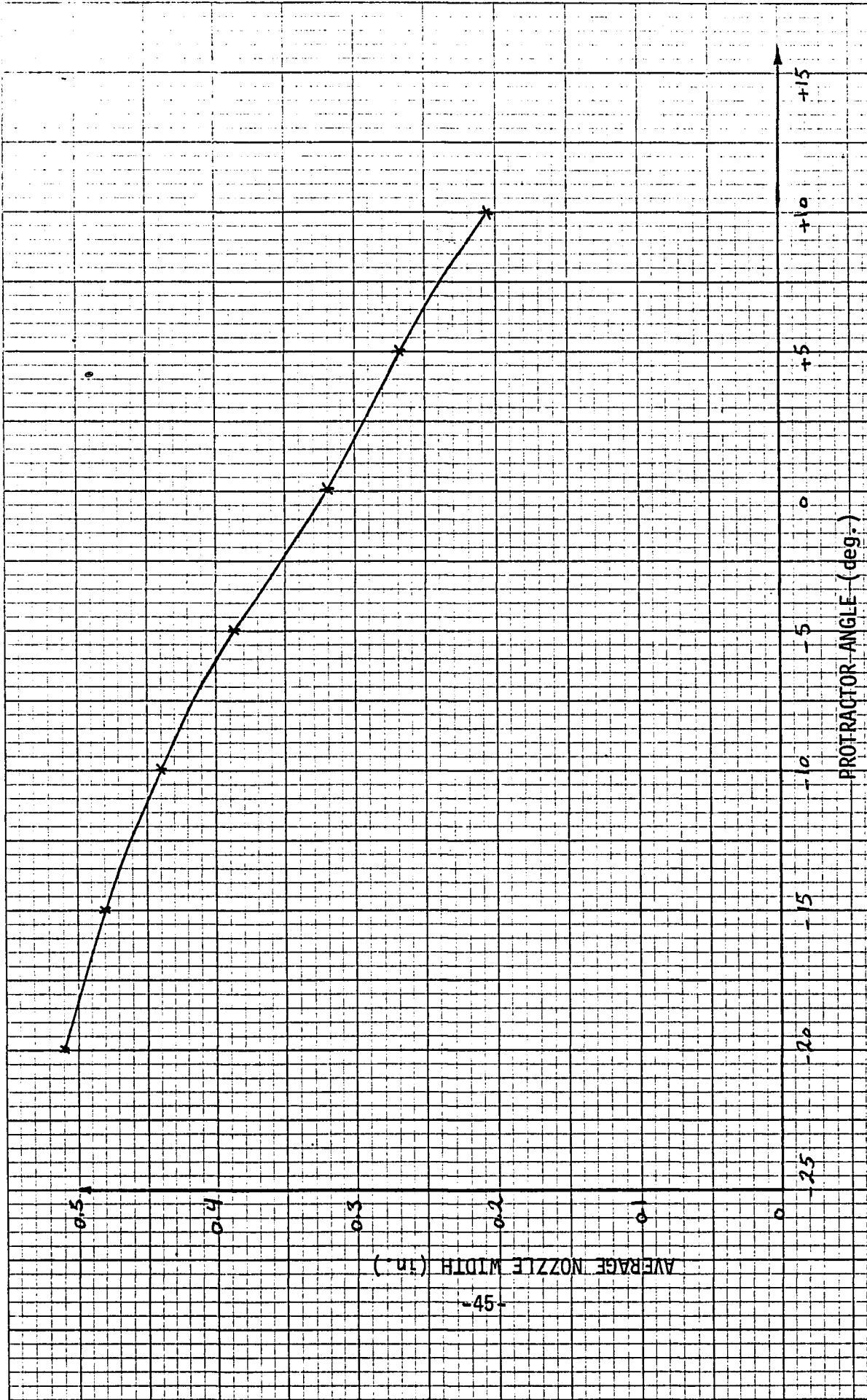


FIG. 11 Average measured throat width versus protractor angle reading.



FIG. 11 Average measured throat width versus protractor angle reading,

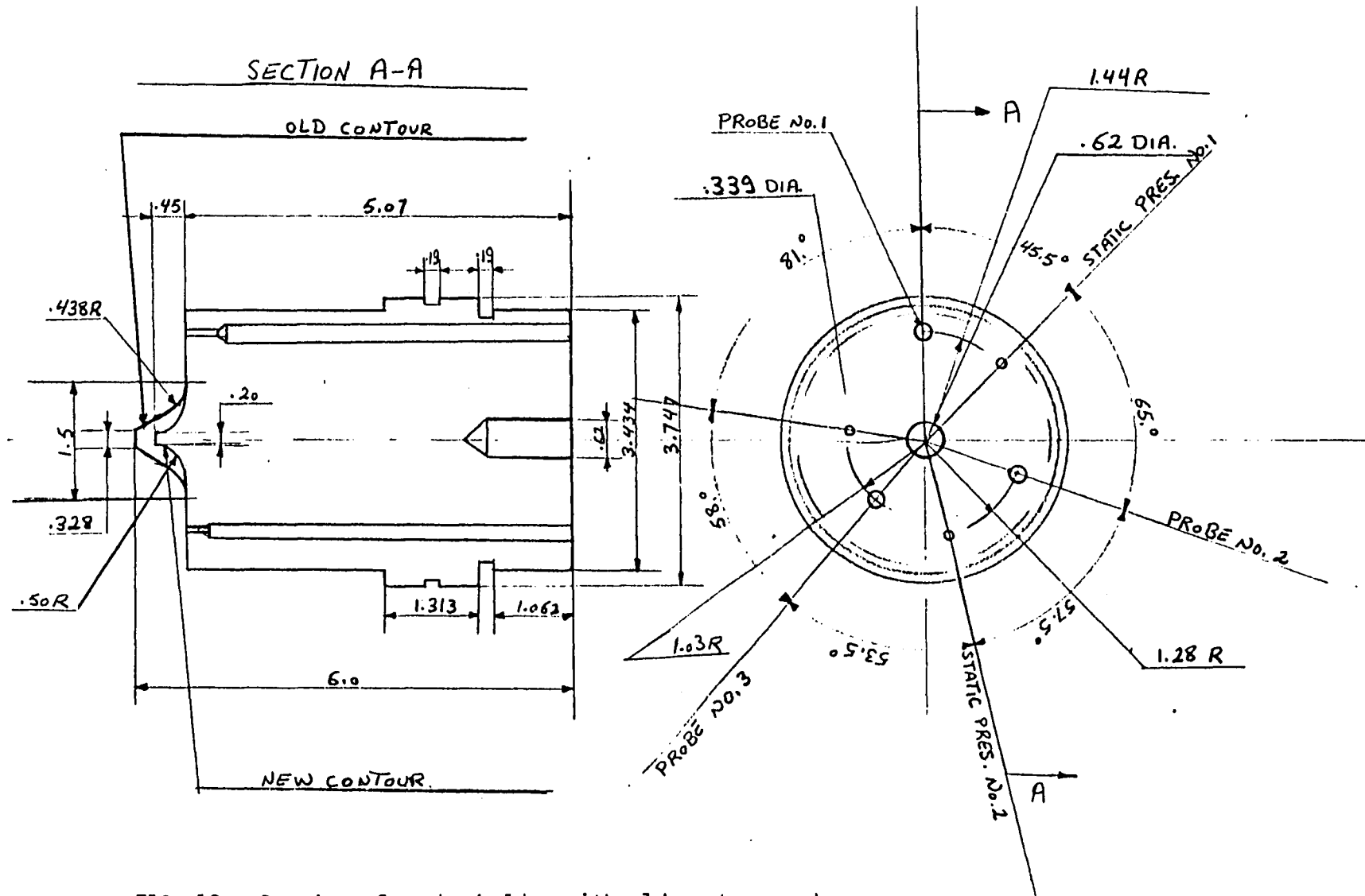


FIG. 12 - Drawing of probe holder with old contour and new one.

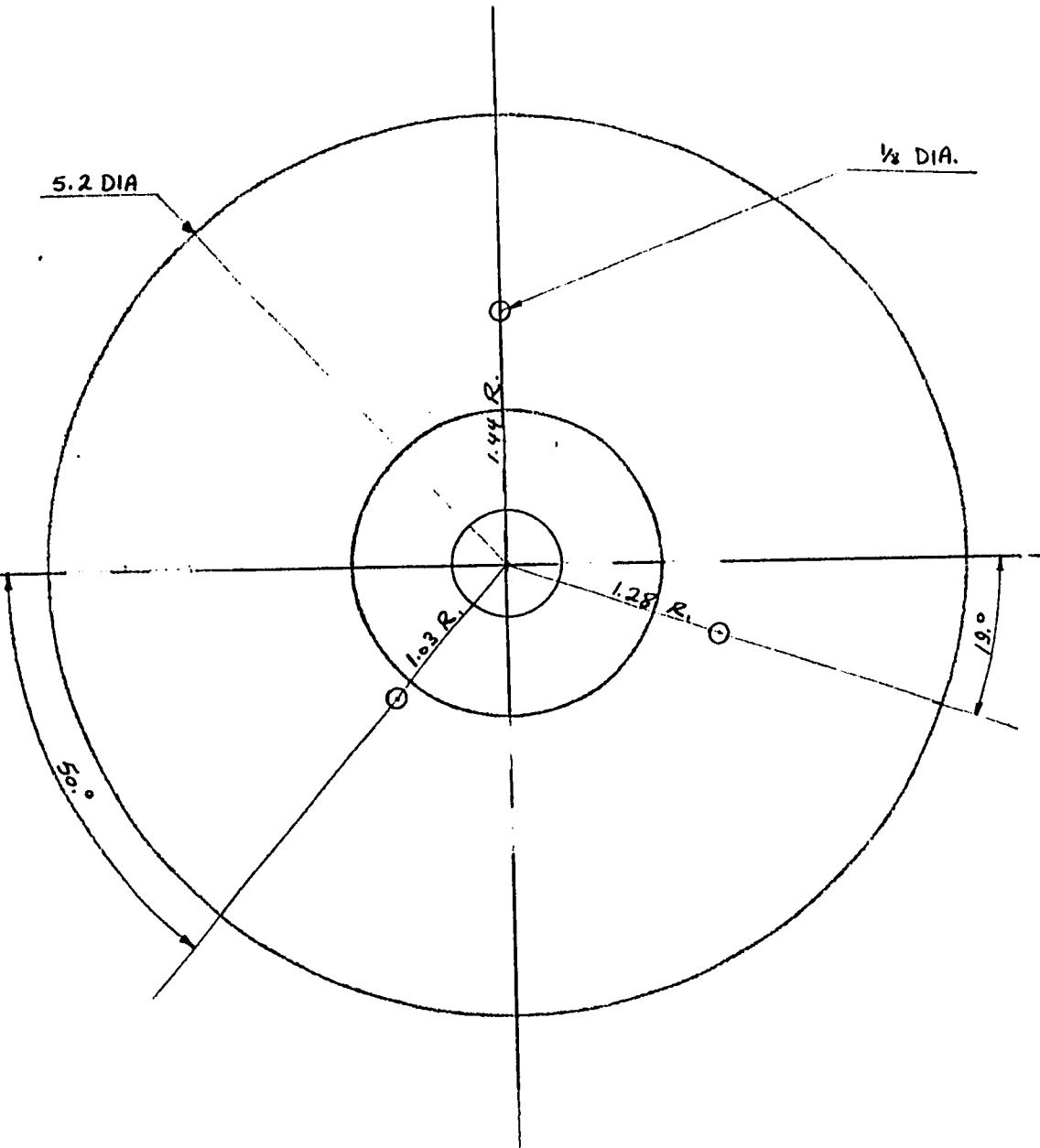
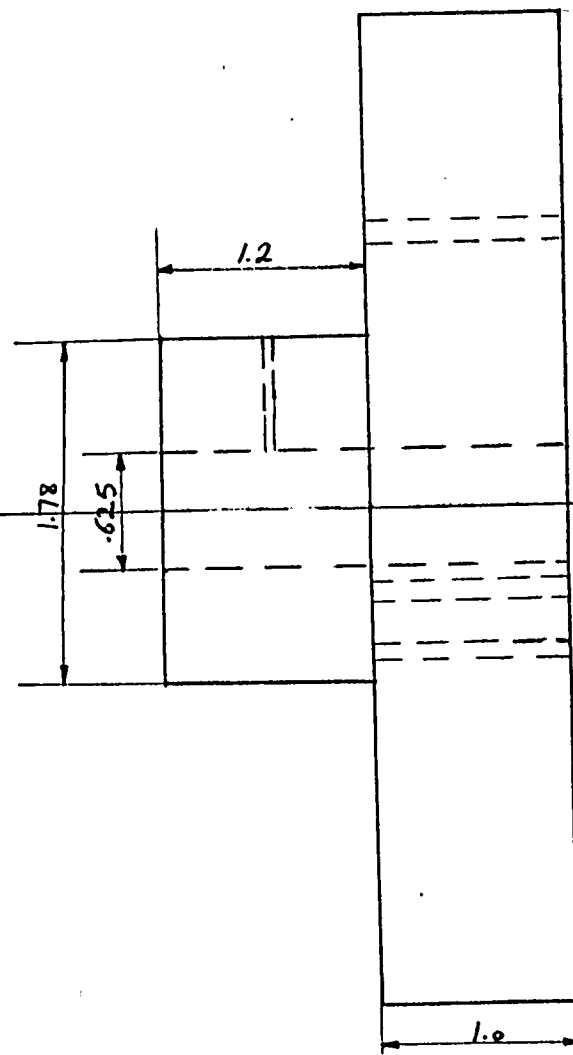


FIG. 13 - Drawing of the plexiglass disk.

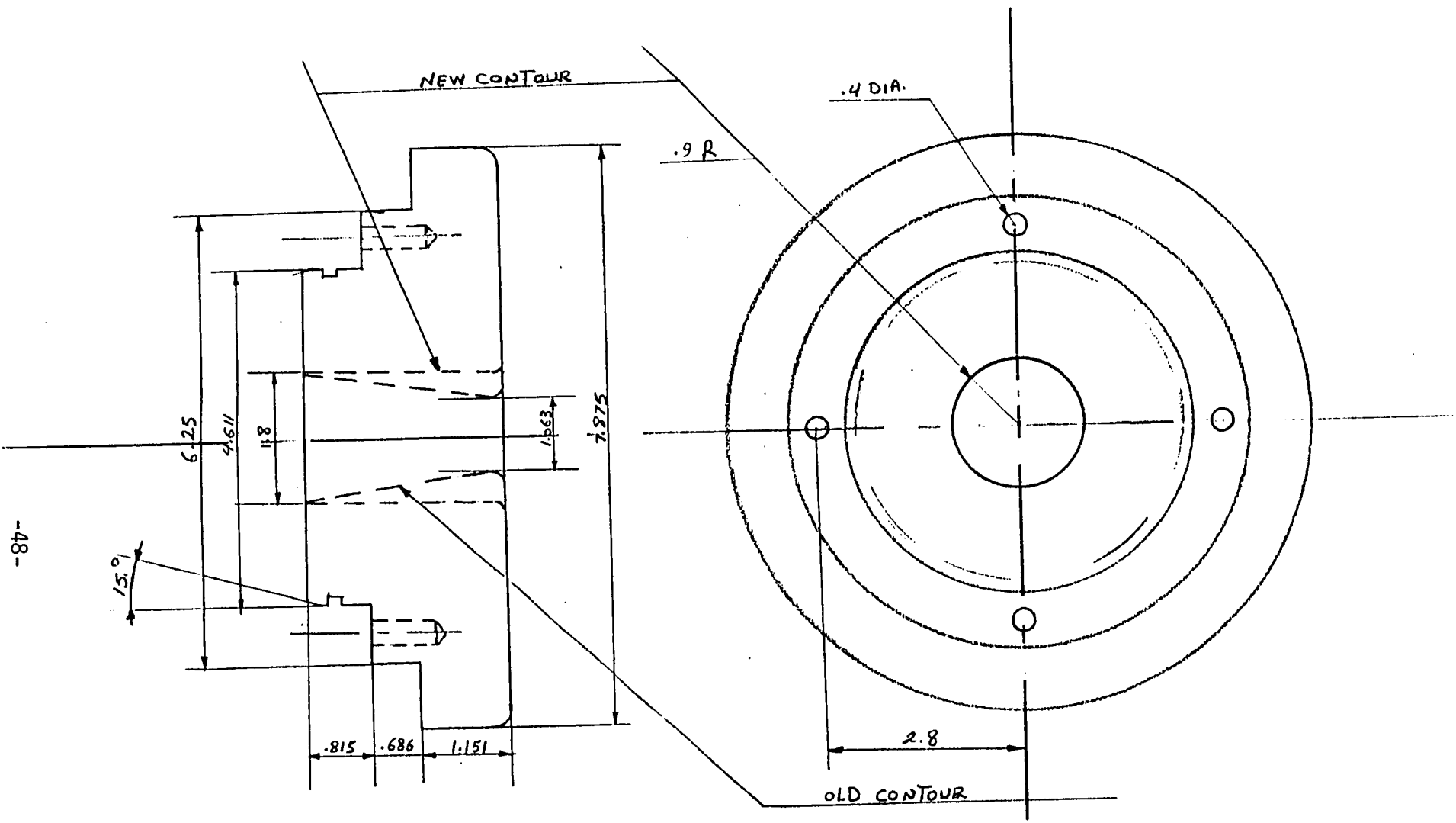


FIG. 14 Drawing of shroud with old contour and new contour

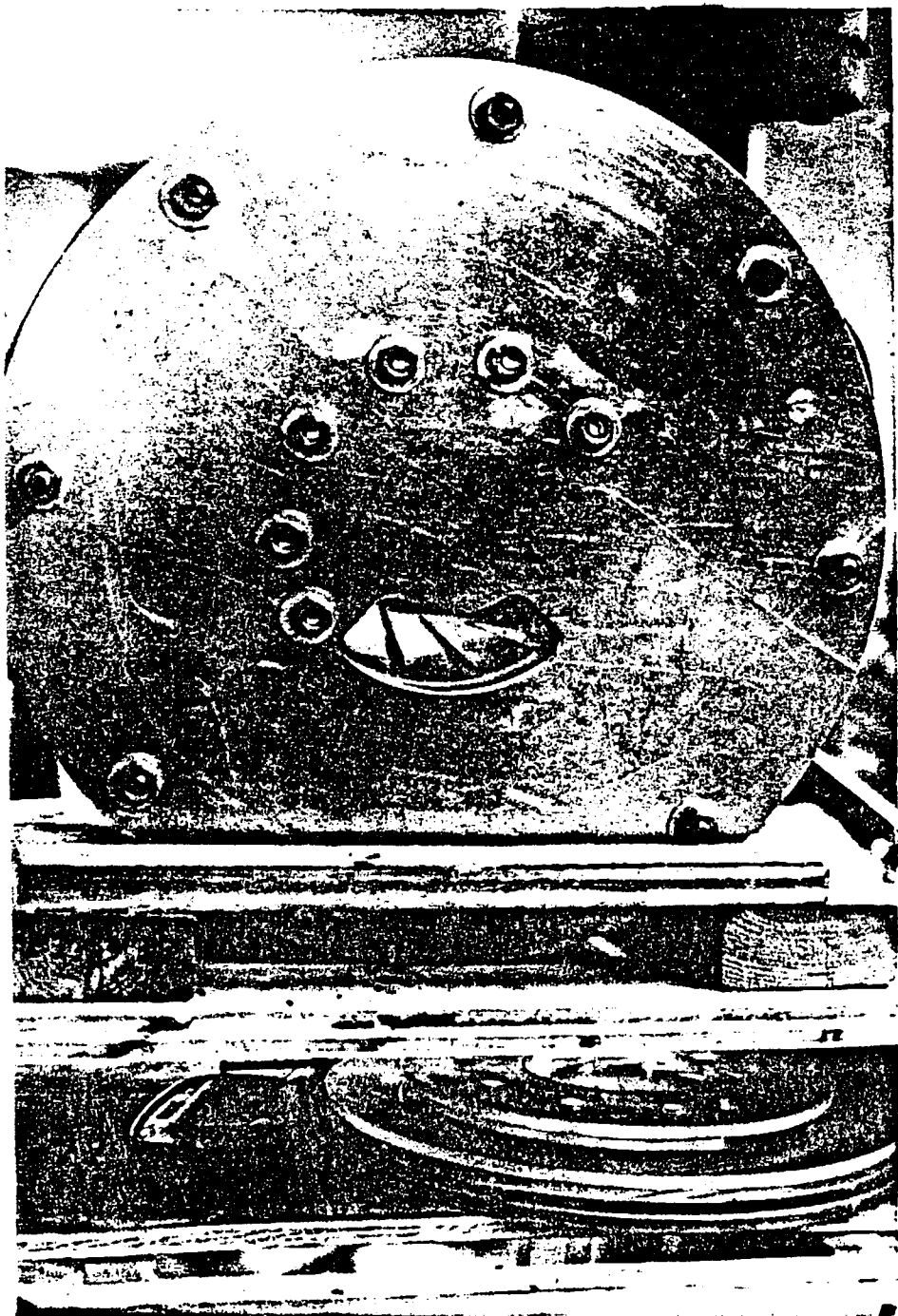


FIG. 15 Photograph of optical test rig from outside view.

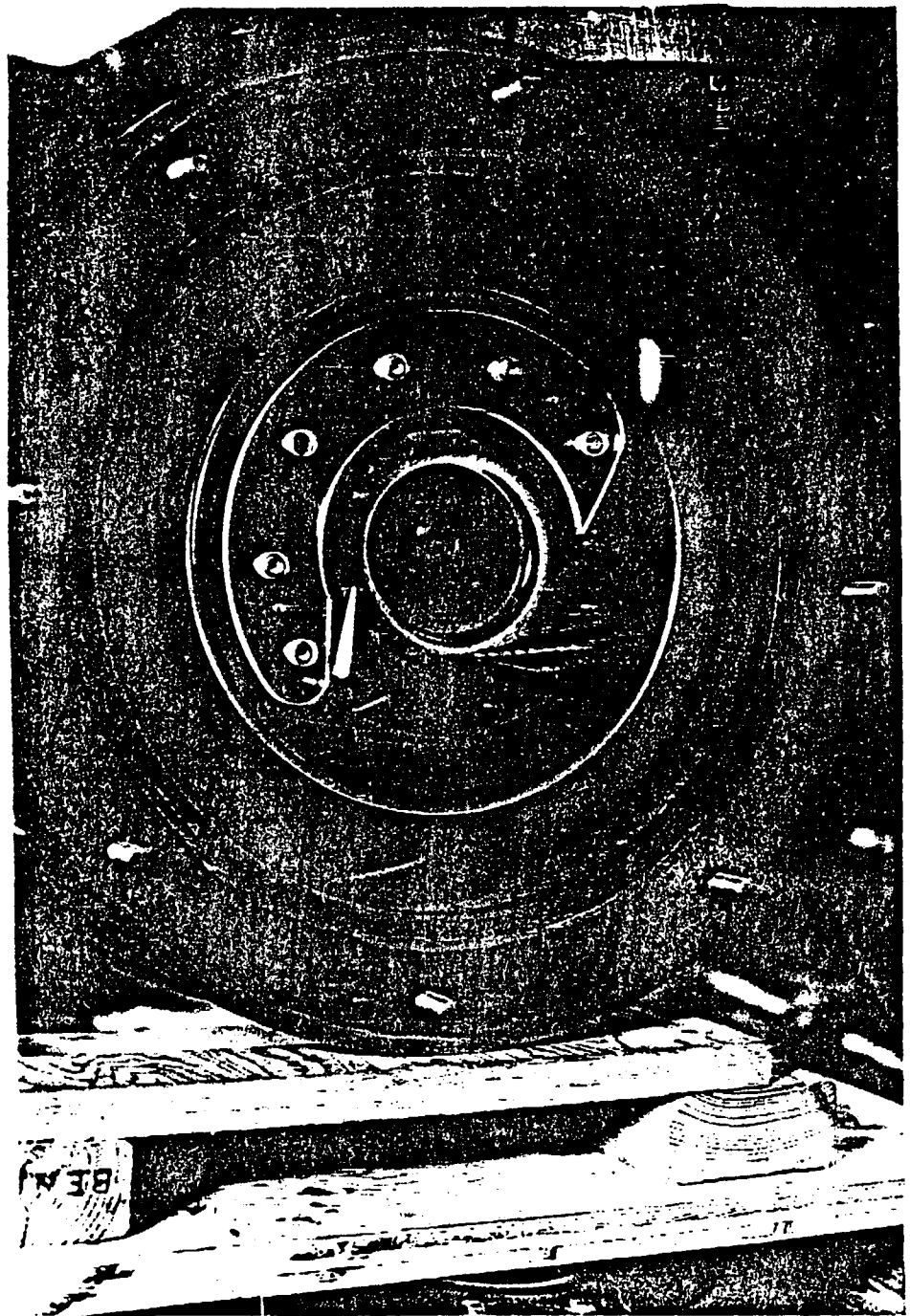


FIG. 16 Photograph of optical test rig from inside.

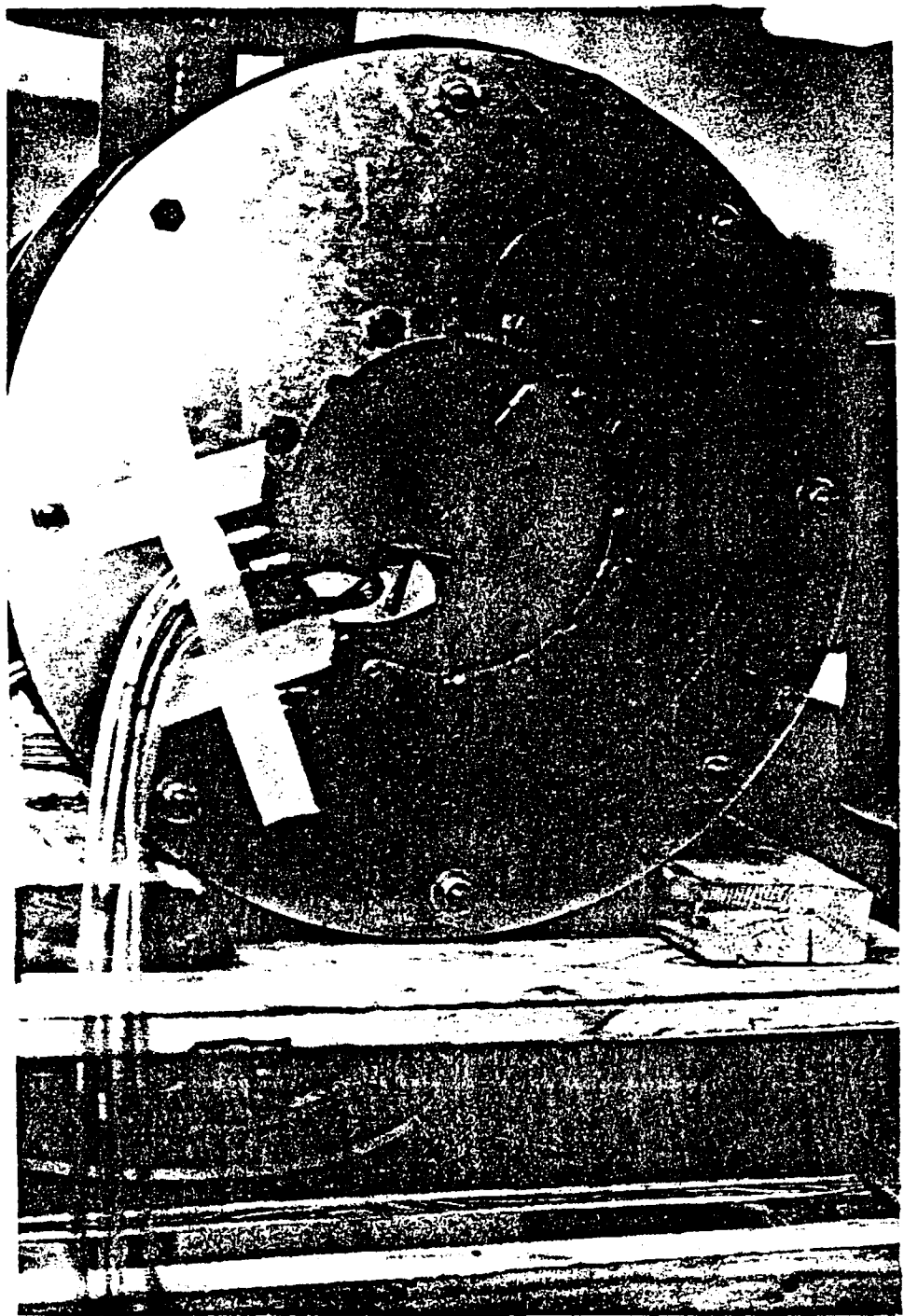


FIG. 17 Picture of optical test rig from outside view.

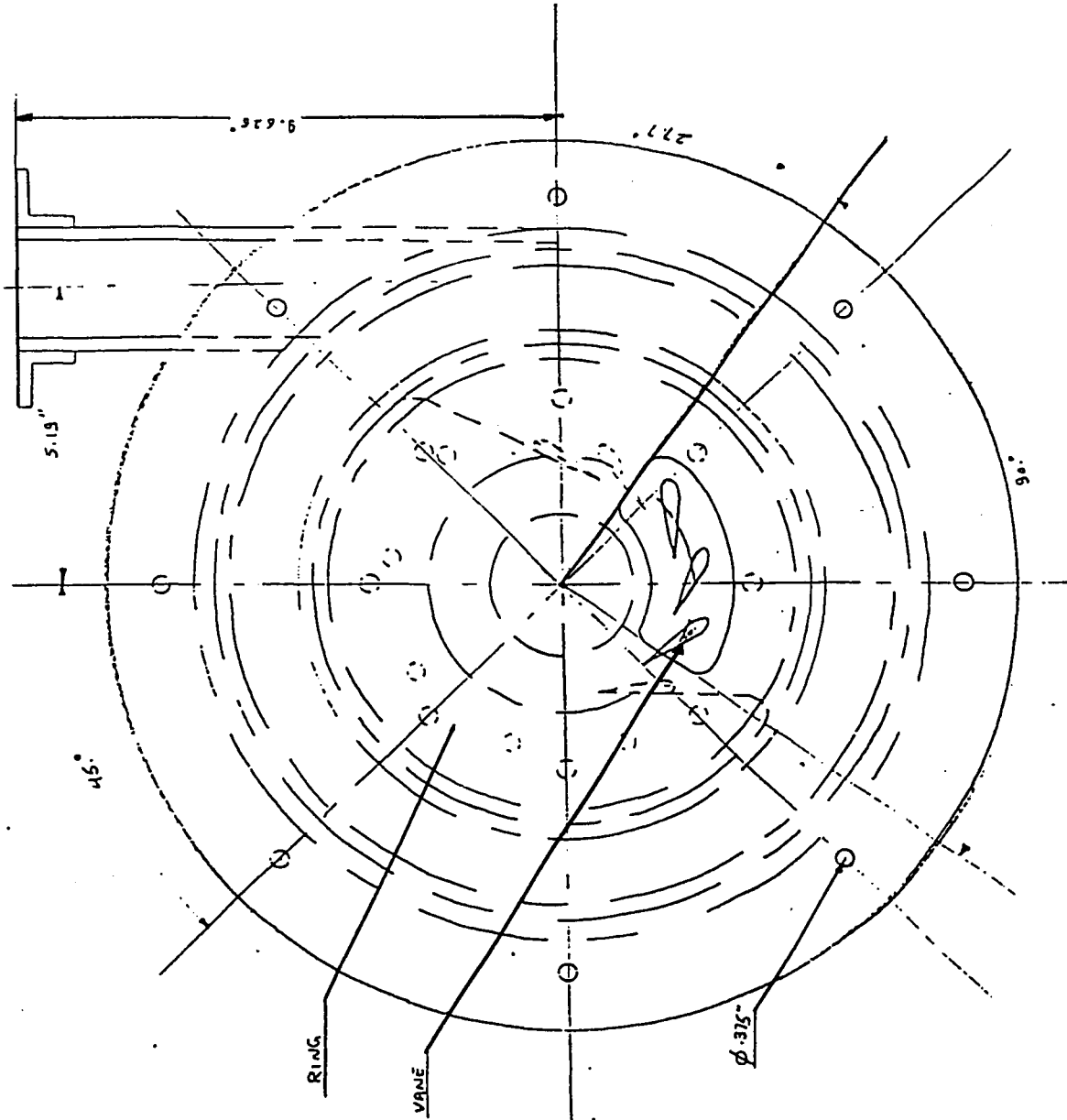
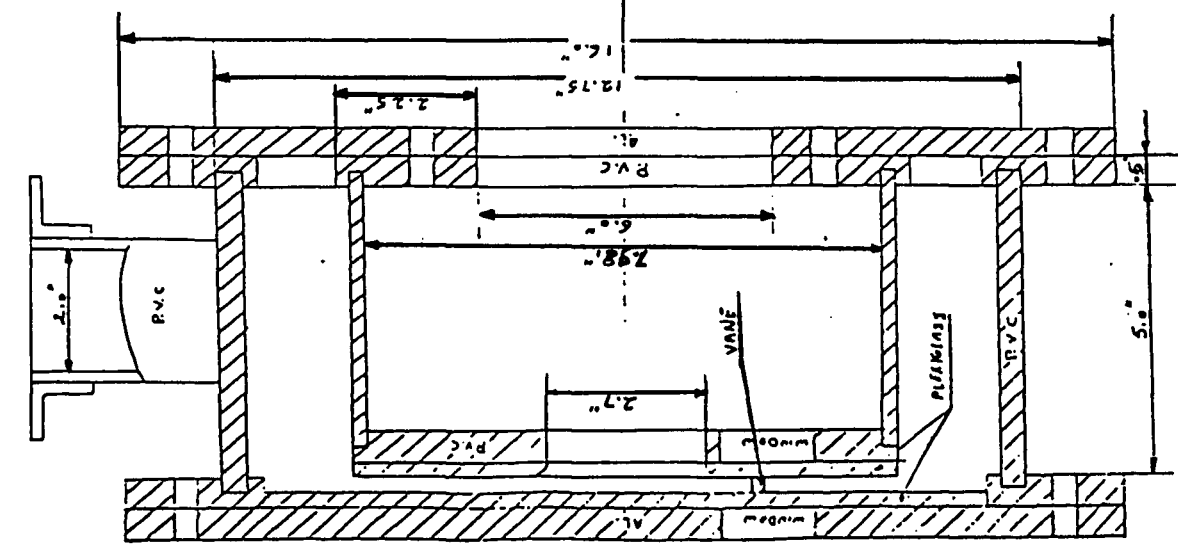


FIG. 18 Drawing of optical test rig.

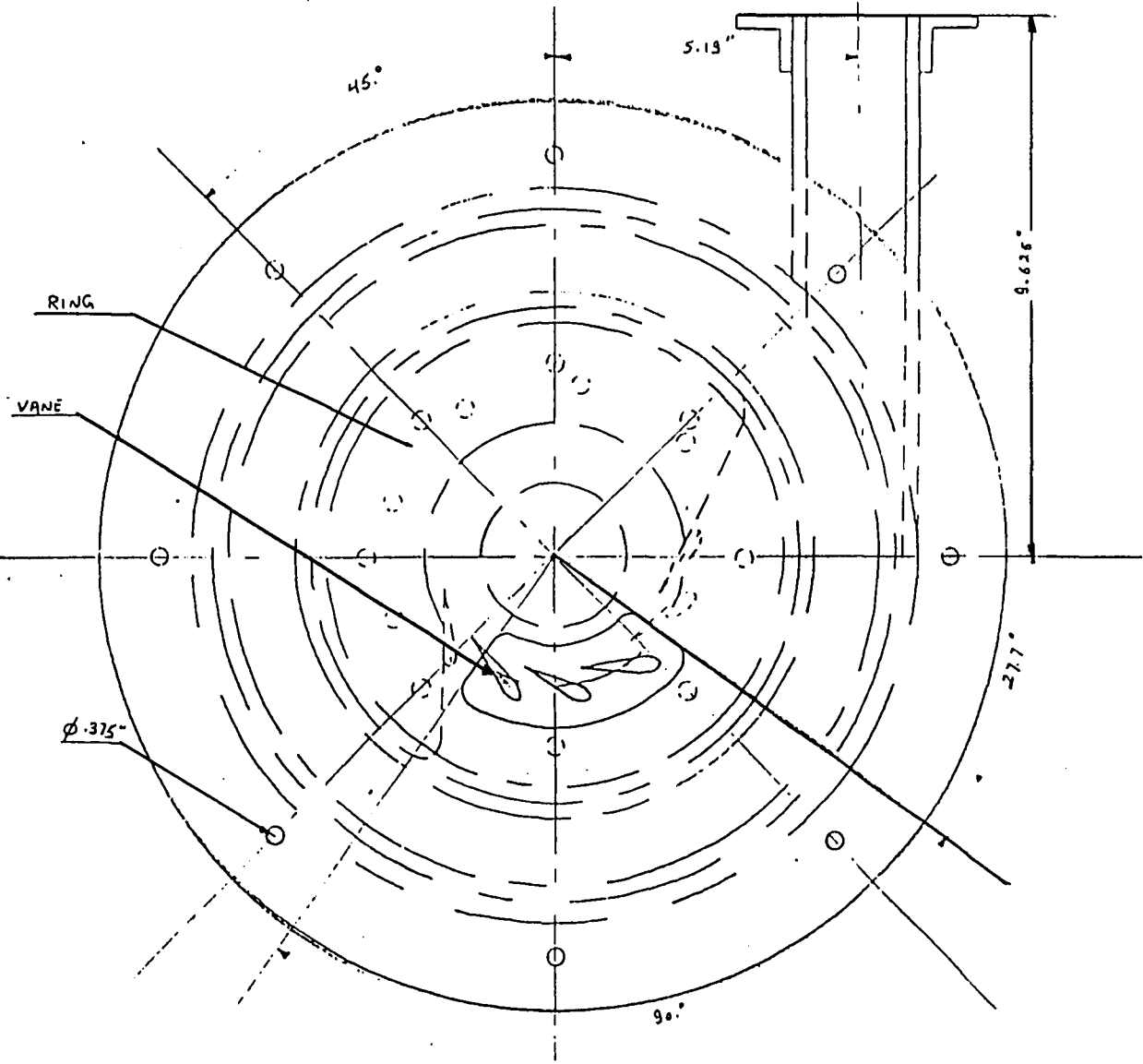
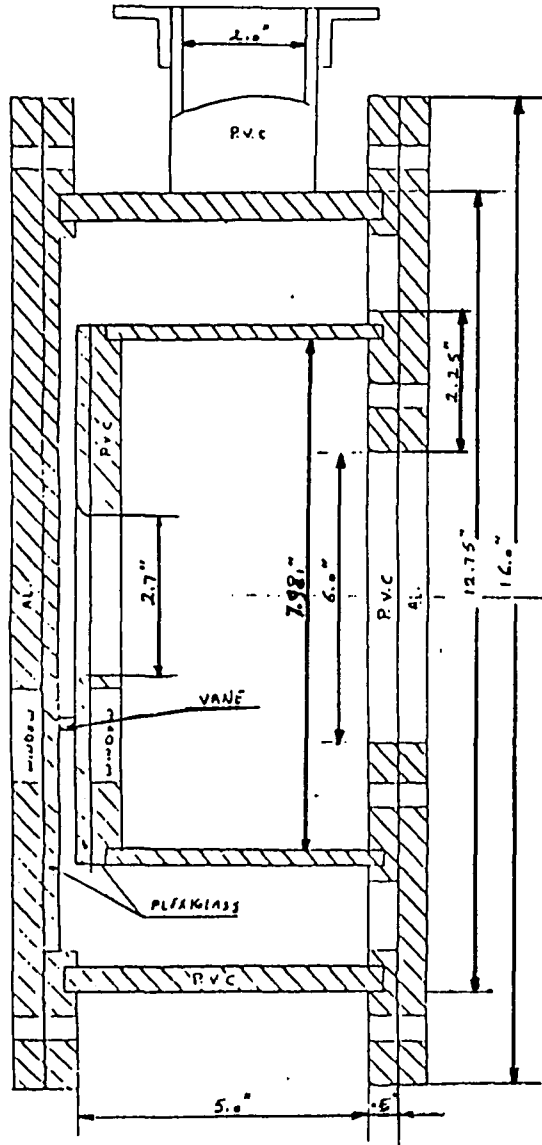


FIG. 18 Drawing of optical test rig.

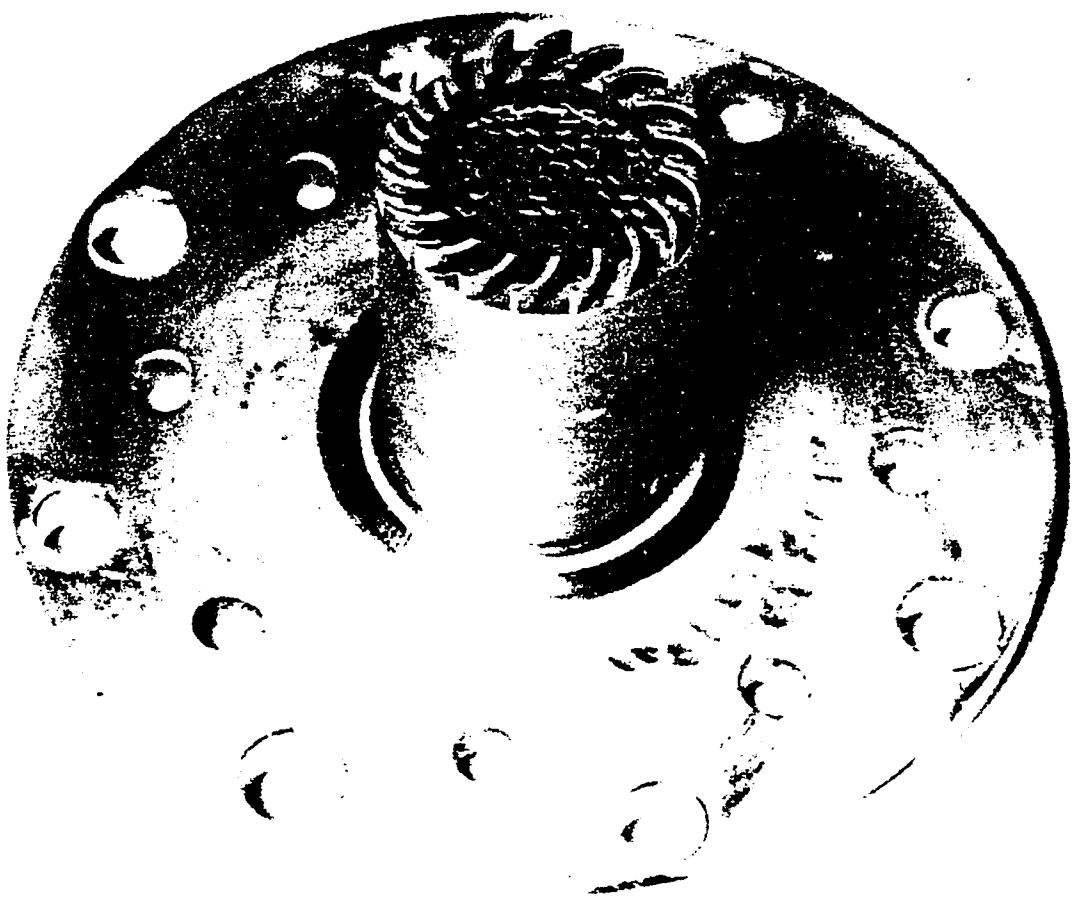


FIG. 19 - Picture of swirller with 18 vanes and flow straightener.

-54-

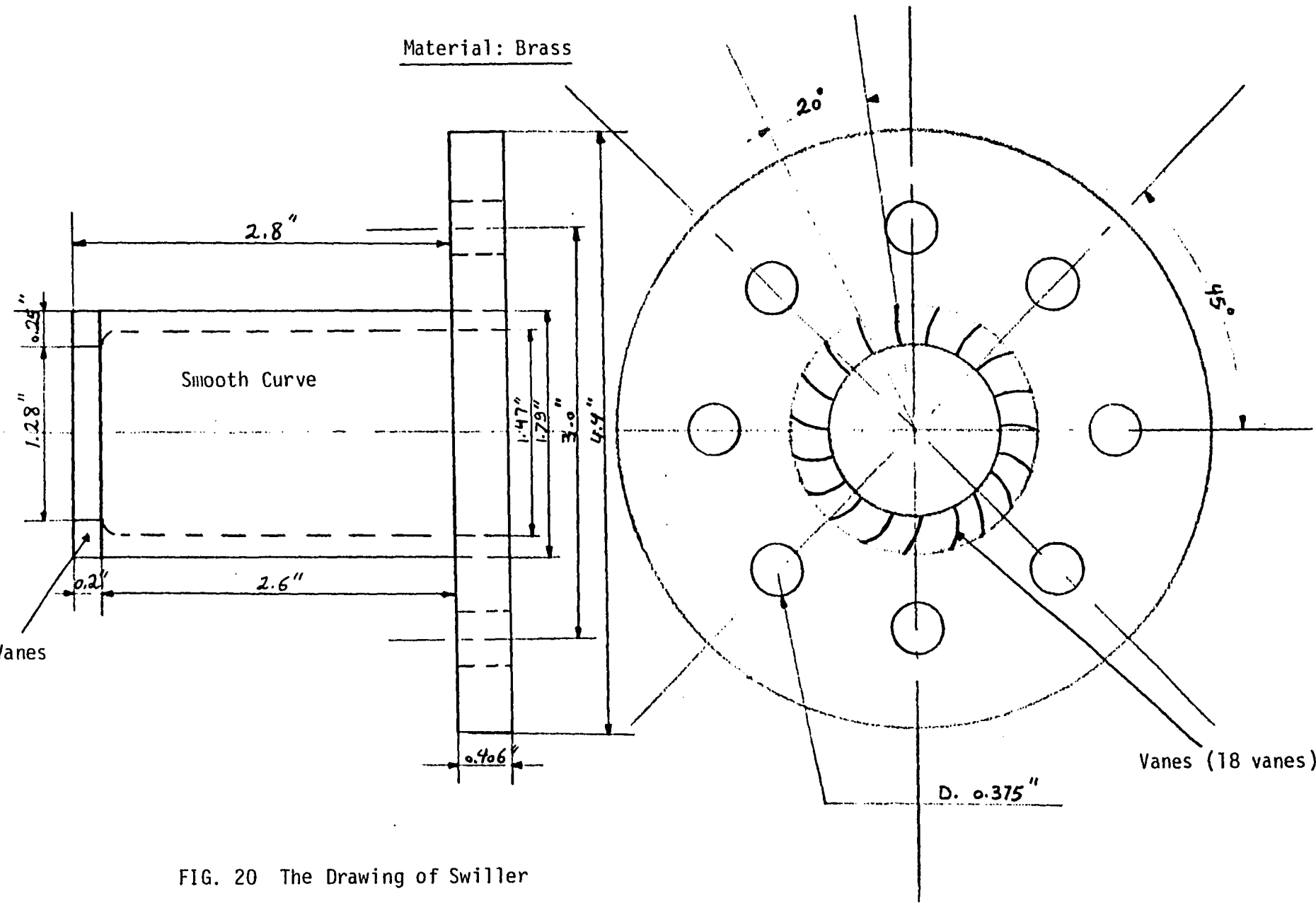


FIG. 20 The Drawing of Swiller

-55-

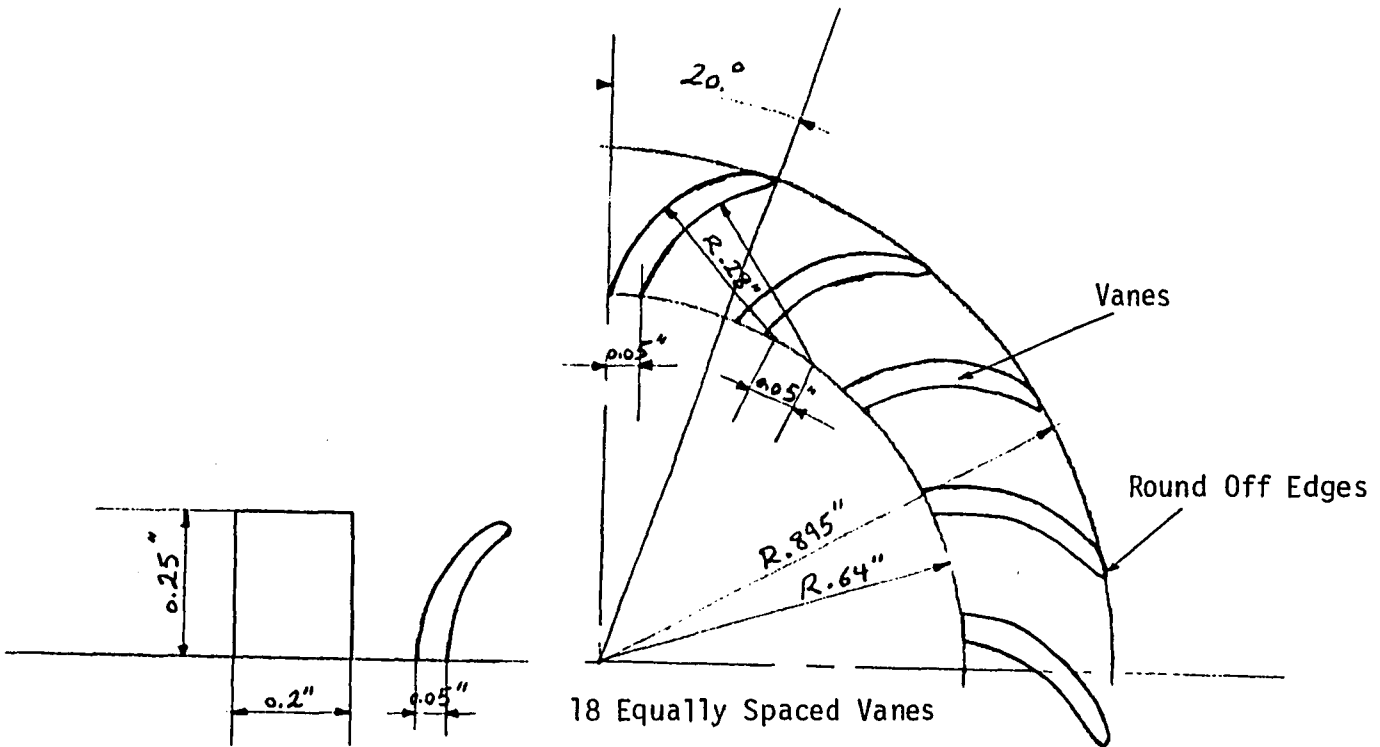


FIG. 21 The Drawing of Vanes Setting for 18 Vanes

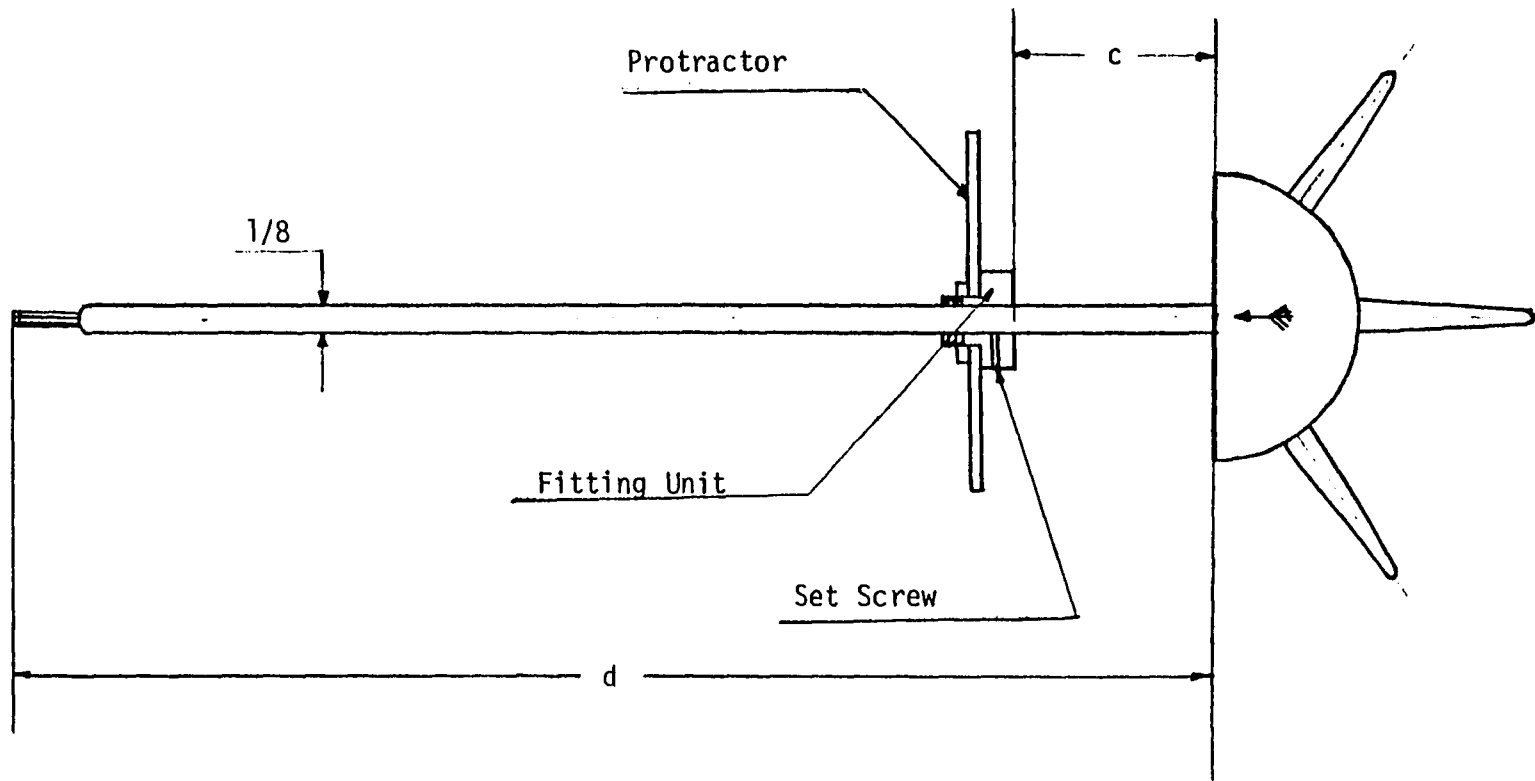


FIG. 22 Drawing of probe with protractor

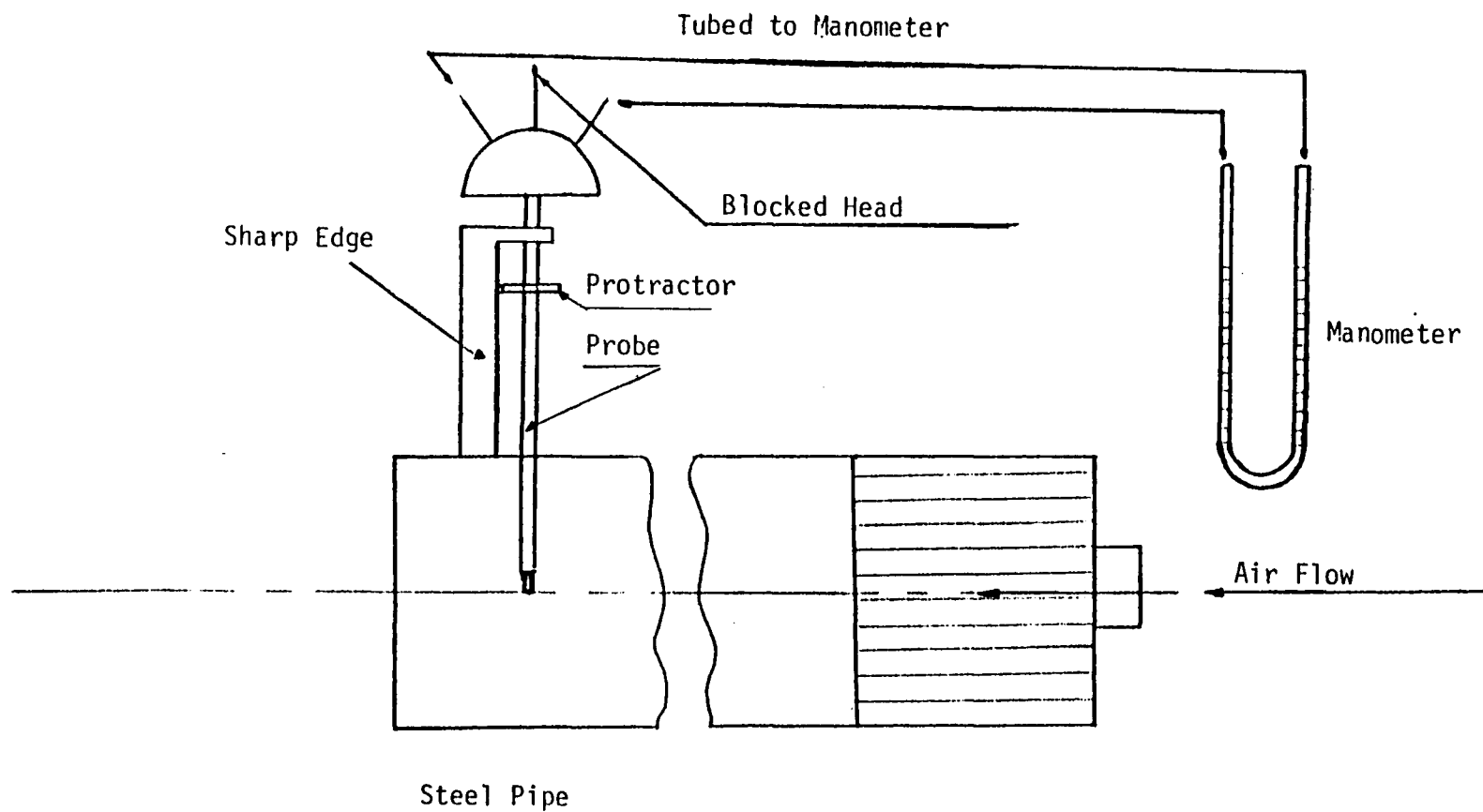


FIG. 23 Probe protractor calibration setup.

NOZZLE WIDTH	IN.	PRESS. OF ORIFICE P_1	PSIG	DATE:
NOZZLE ANGLE	DEG.	FLOW ORIFICE ΔP	IN-S.G.=	SUPPLY TEMP. T_{SUP} °F
PROTRACTOR ANGLE	DEG.	TEM. OF ORIFICE T_1	°F	P_{ATM} IN-HG
FLOW ORIFICE DIA.	IN.	SUPPLY PRESS. P_{SUP}	IN-HG	T_{ATM} °F

STATIC AND TOTAL TRAVERSES

FLOW ANGLE, θ , MEASURED FROM RADIAL DIRECTION

SPANWISE PROBE LOCATION: % OF NOZZLE WIDTH MEASURED FROM SHROUD

-58

CIRC. ANGLE	P(IN-HG)			P _{SUP} -P _T (IN-H ₂ O)			θ(DEG.)			NOTES
	1	2	3	1	2	3	1	2	3	
0										
5										
10										
15										
20										
25										
30										
35										
40										

FIG. 24 Test data sheet
for main test rig.

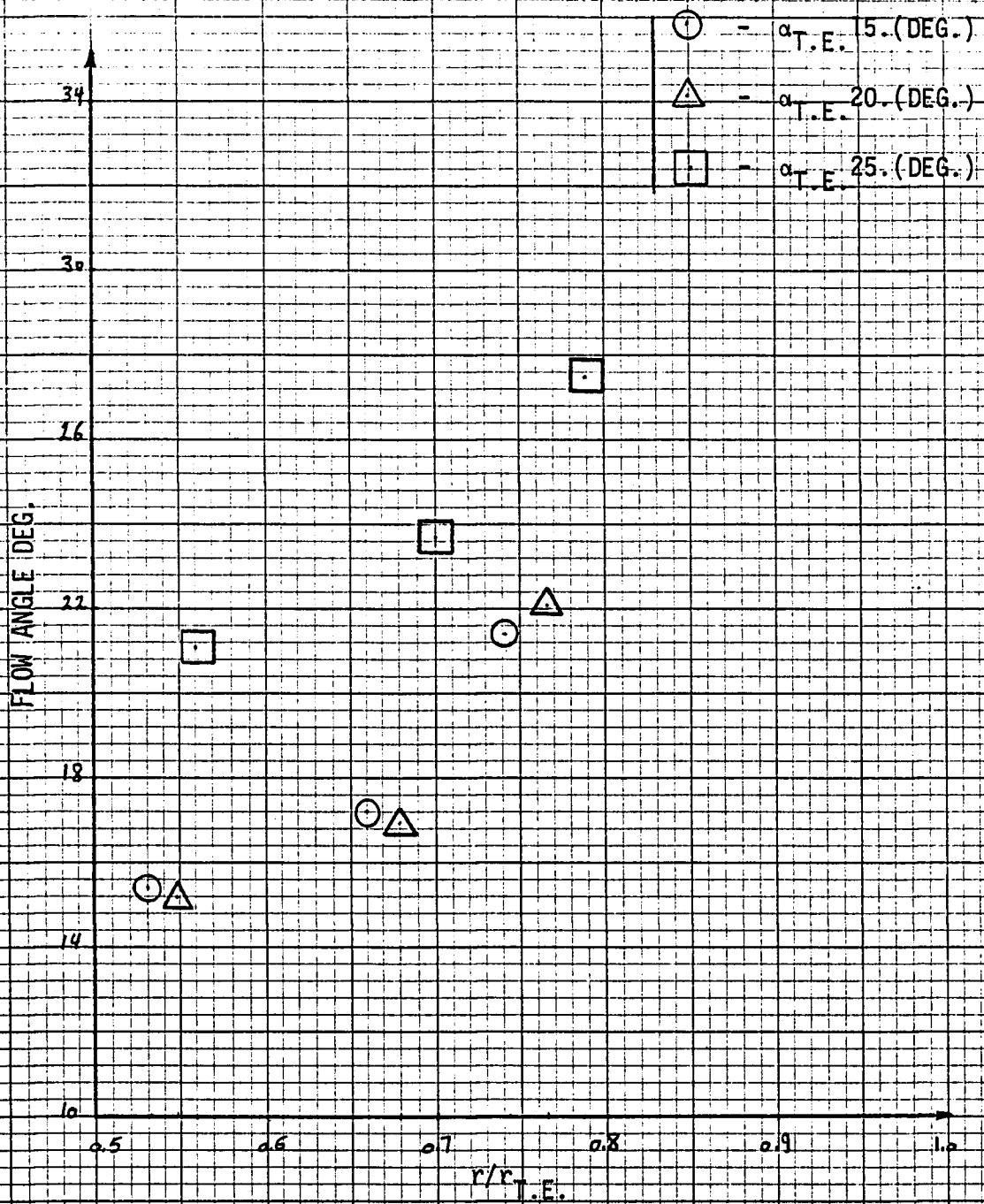


FIG. 25. Variation of the flow angle with radius ratio for three nozzle setting angles, 15., 20., and 25. deg., supply pressure 19.26 psia, nozzle width 0.148 in.

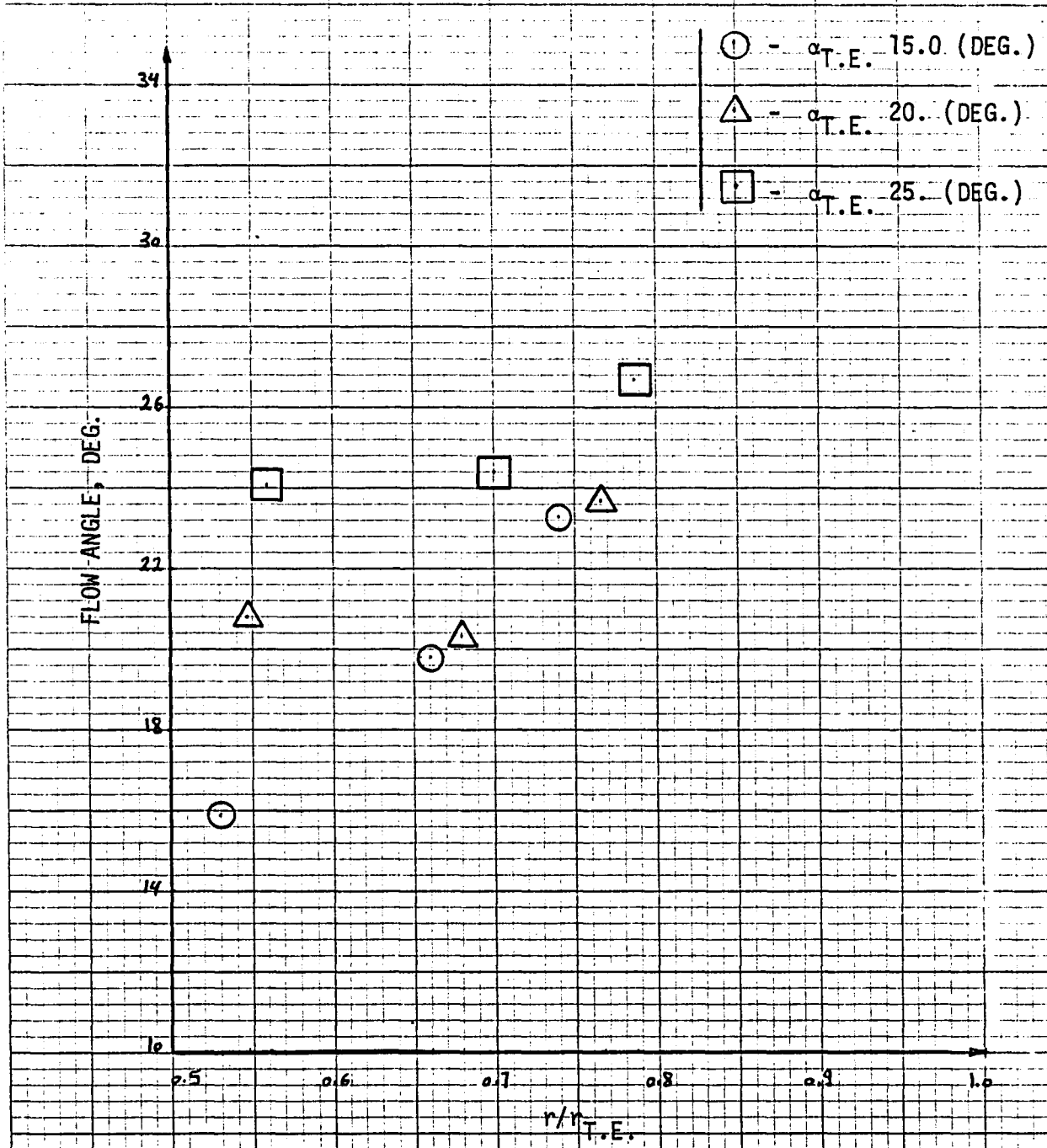


FIG. 26 Variation of the flow angle with radius ratio for three nozzle setting angles, 15., 20., and 25. Deg., supply pressure 19.13 psia, nozzle width 0.200 in.

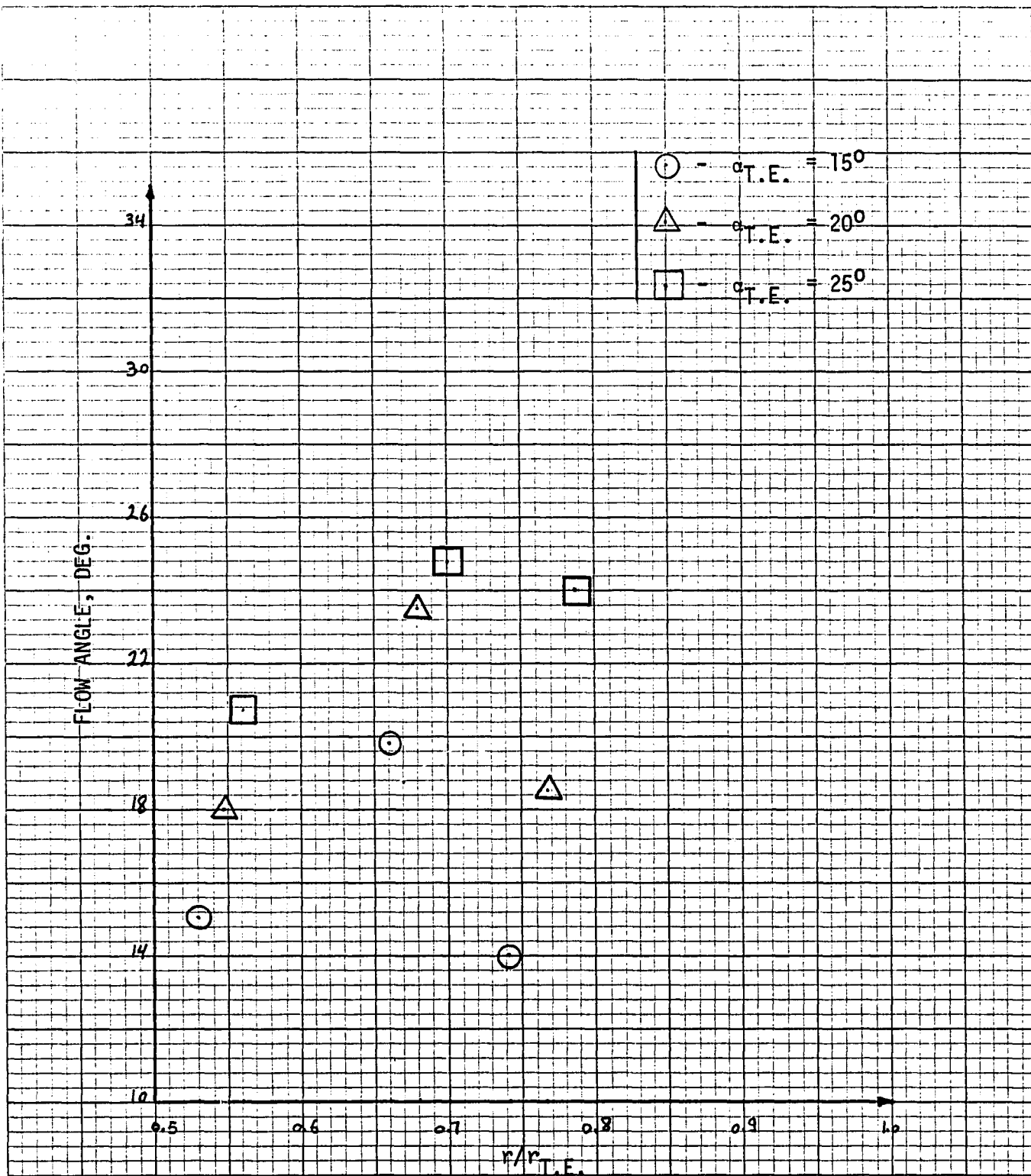


FIG. 27 Variation of the flow angle with radius ratio for three nozzle setting angles, 15., 20., and 25. Deg., supply pressure 24,35 psia, nozzle width 0.148 in.

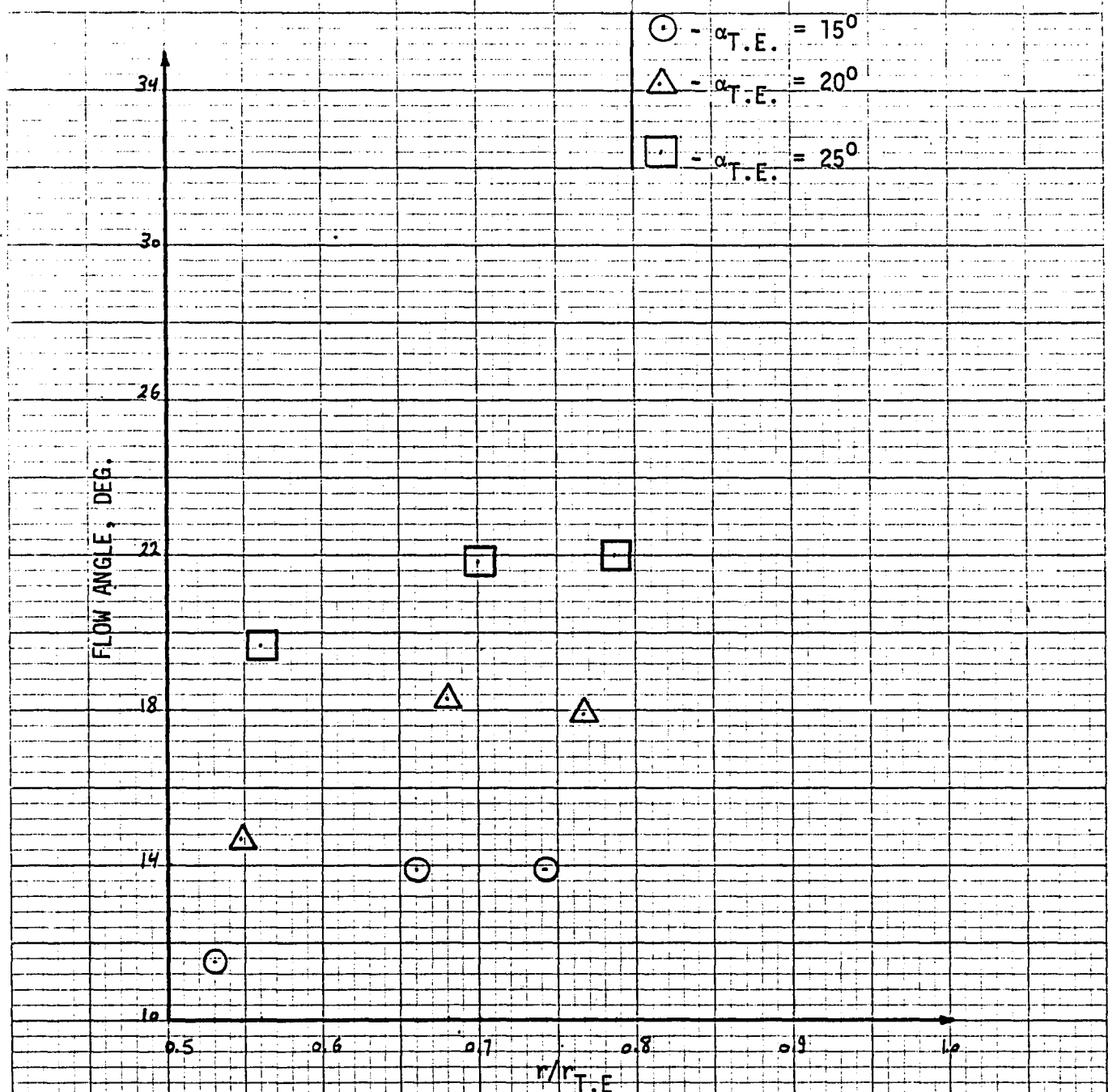


FIG. 28 Variation of the flow angle with radius ratio for three nozzle setting angles, 15., 20., and 25. Deg., supply pressure 24.44 psia, nozzle width 0.200 in.

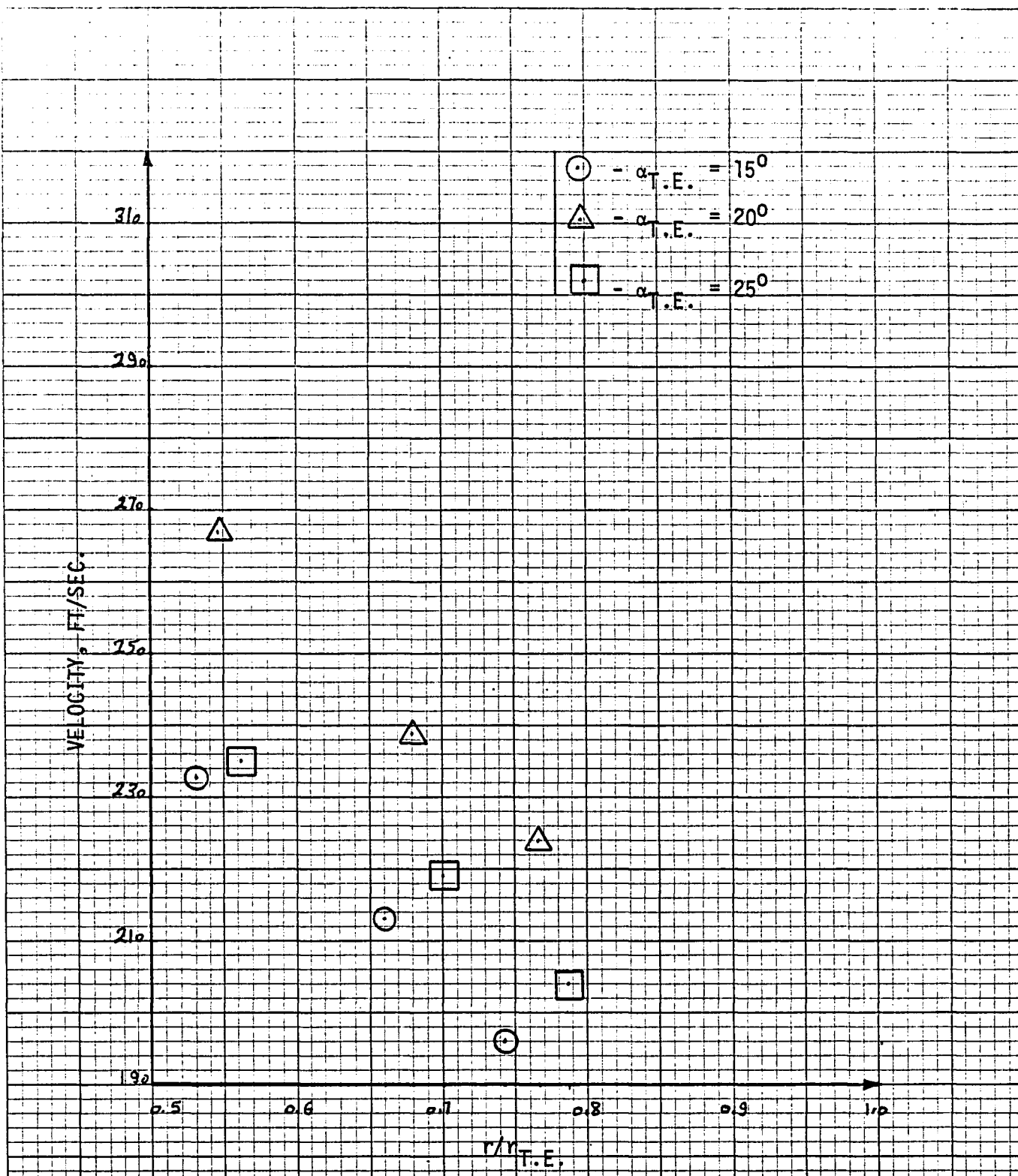


FIG. 29 Variation of the flow velocity with radius ratio for three nozzle setting angles, 15., 20., and 25. deg., supply pressure 19.13 psia, nozzle width 0.200 in.

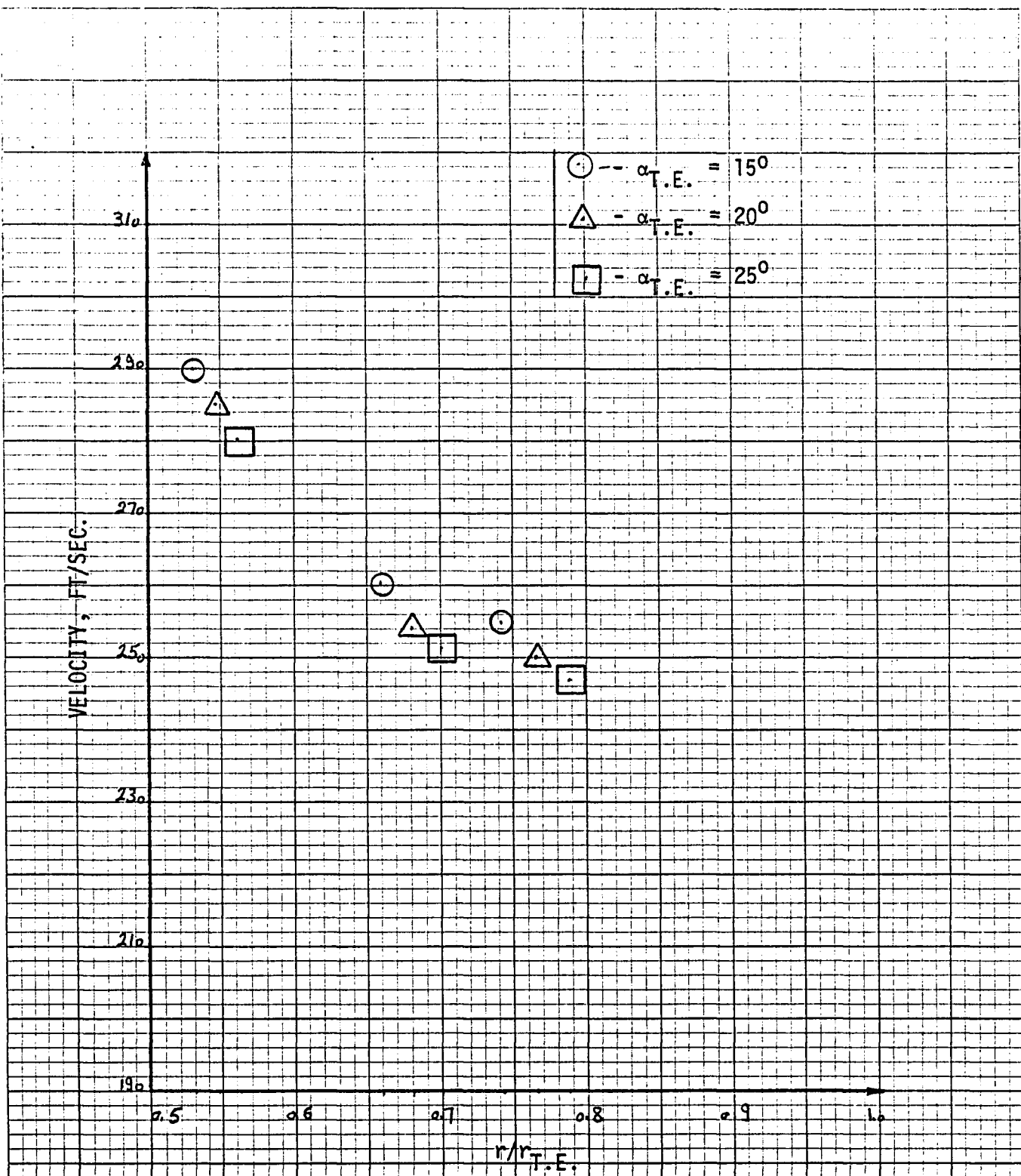


FIG. 30. Variation of the flow velocity with radius ratio for three nozzle setting angles, 15., 20., and 25. deg., supply pressure 19.26 psia, nozzle width 0.148 in.

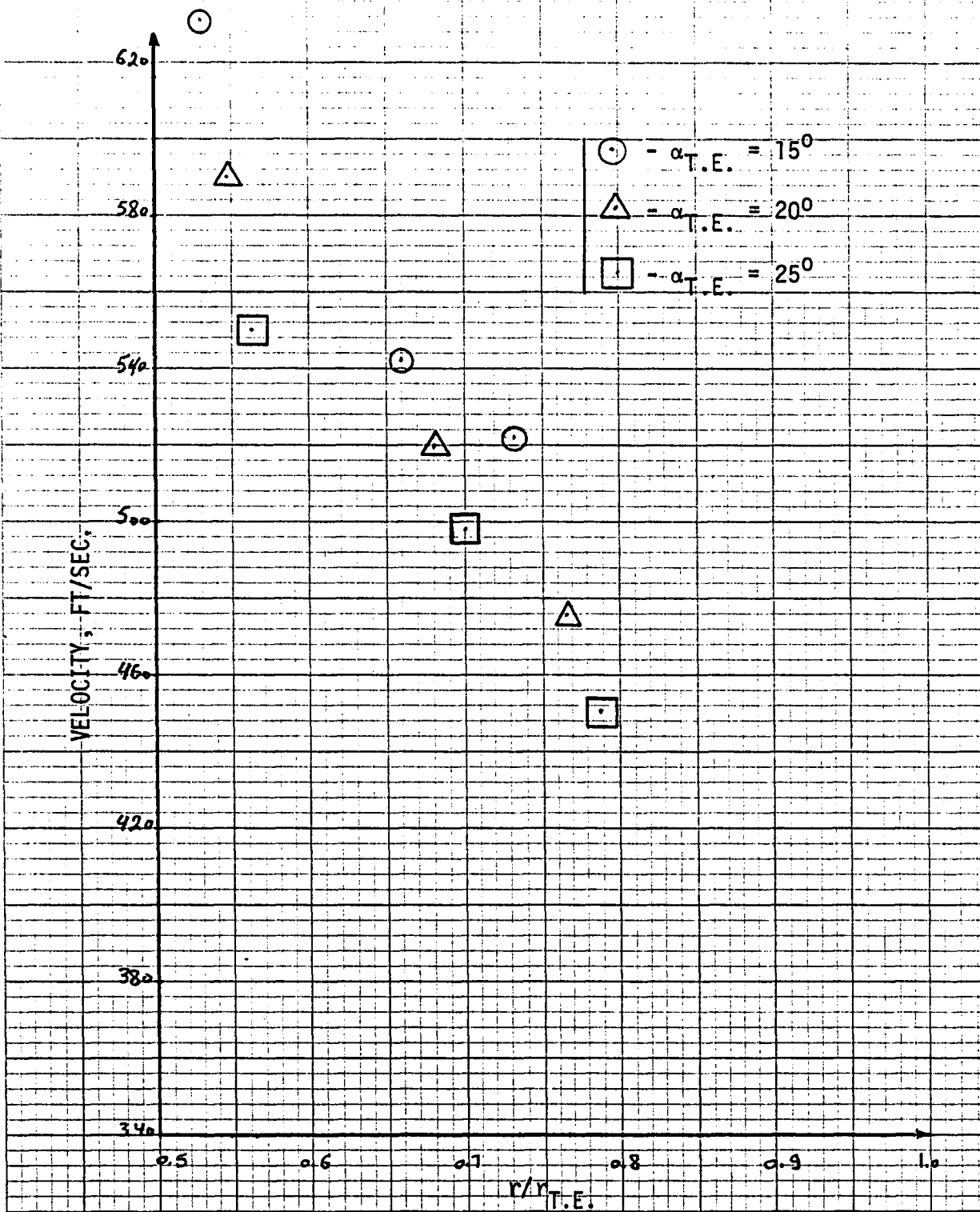


FIG. 31 Variation of the flow velocity with radius ratio for three nozzle setting angles, 15., 20., and 25. deg., supply pressure 24.35 psia, nozzle width 0.148 in.

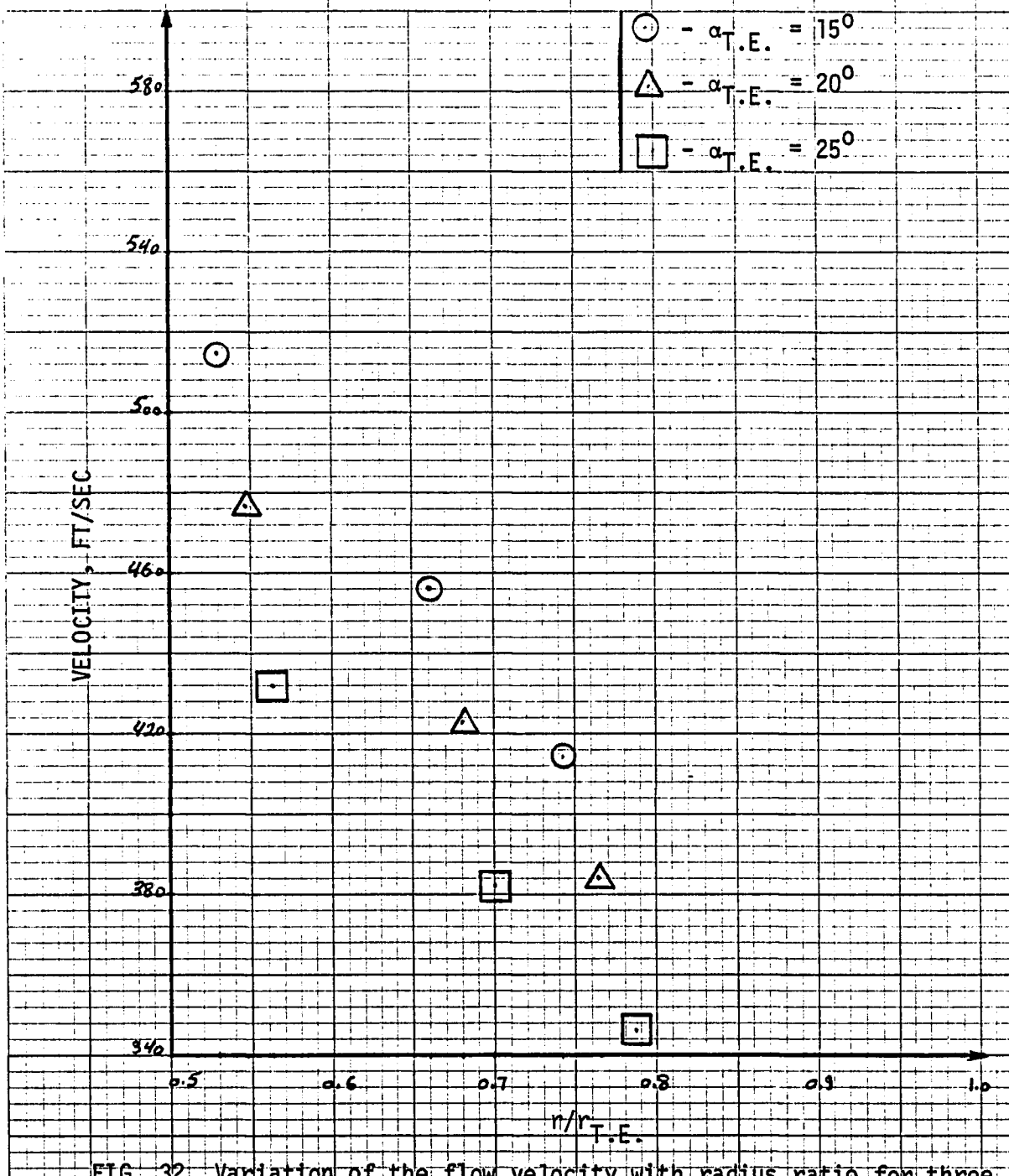


FIG. 32 Variation of the flow velocity with radius ratio for three nozzle setting angles, 15., 20., and 25. deg., supply pressure 24.44 psia, nozzle width 0.200 in.

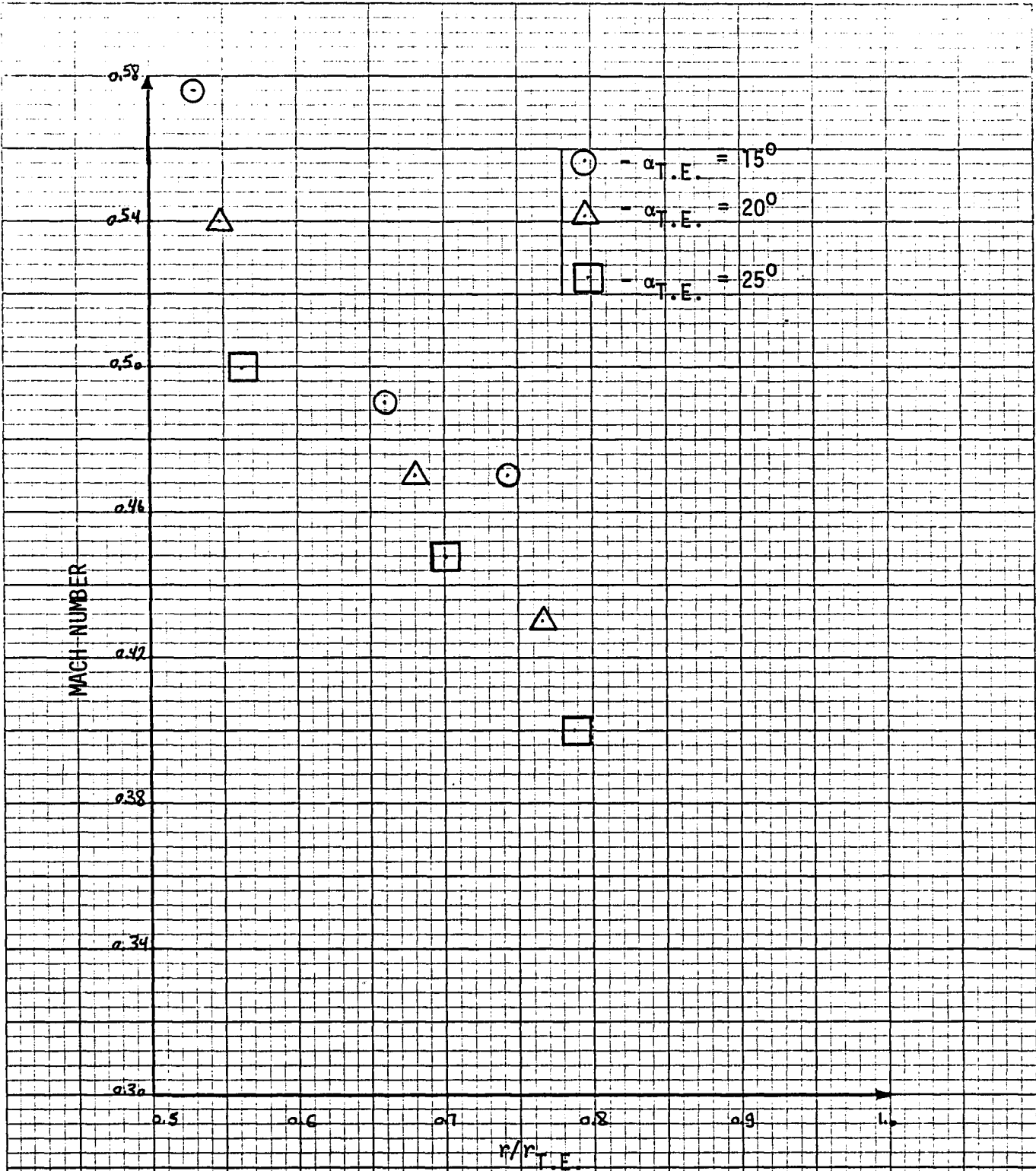


FIG. 33. Variation of the Mach number with radius ratio for three nozzle setting angles, 15., 20., and 25. deg., supply pressure 24.35 psia, nozzle width 0.148 in.

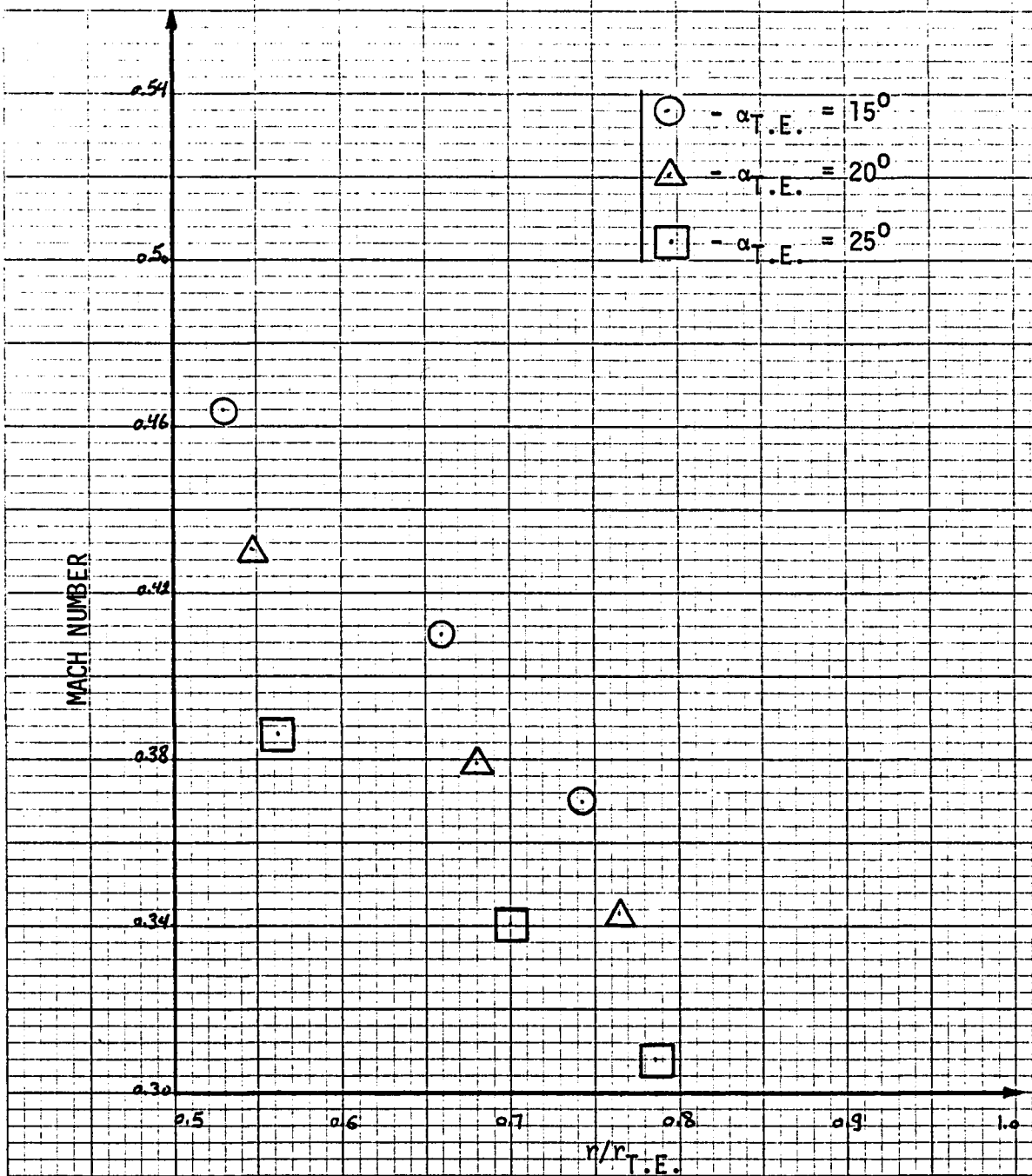


FIG. 34 Variation of the Mach number with radius ratio for three nozzle setting angles 15., 20., and 25. deg., supply pressure 24.44 psia, nozzle width 0.200 in.

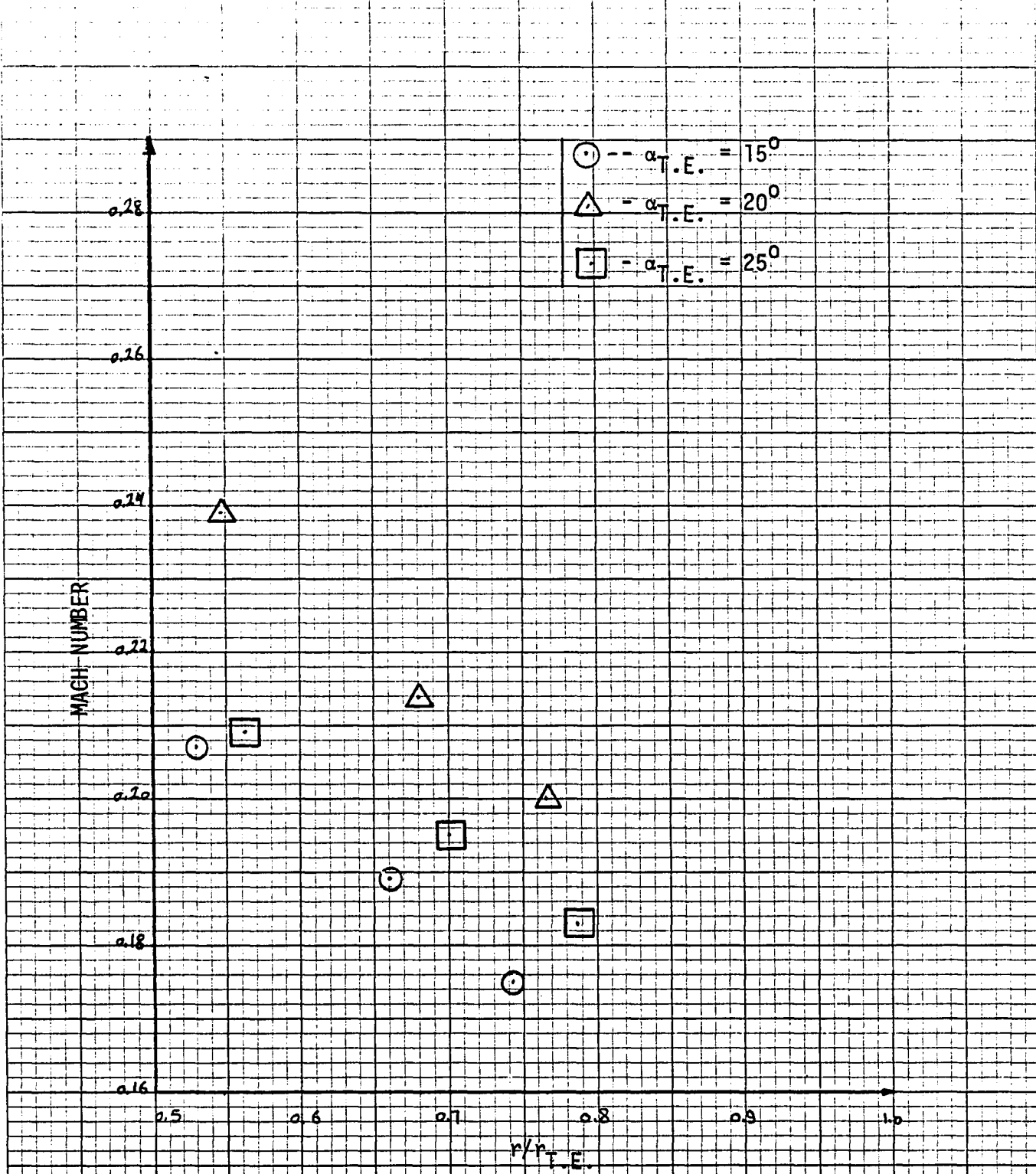


FIG. 35 Variation of the Mach number with radius ratio for three nozzle setting angles, 15., 20., and 25. deg., supply pressure 19.13 psia, nozzle width 0.200 in.

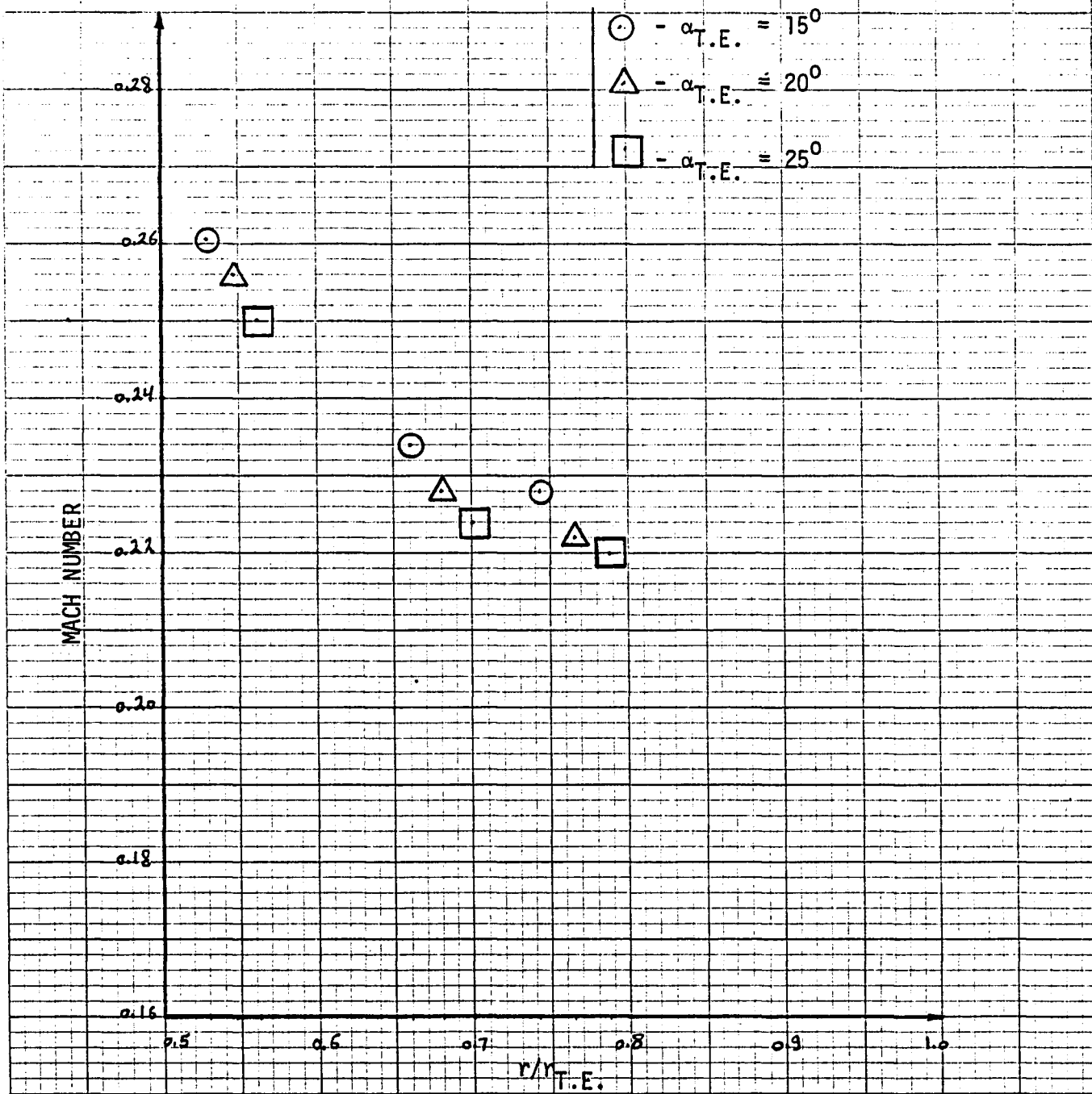


FIG. 36 Variation of the Mach number with radius ratio for three nozzle setting angles 15., 20., and 25. deg., supply pressure 19.26 psia, nozzle width 0.148 in.

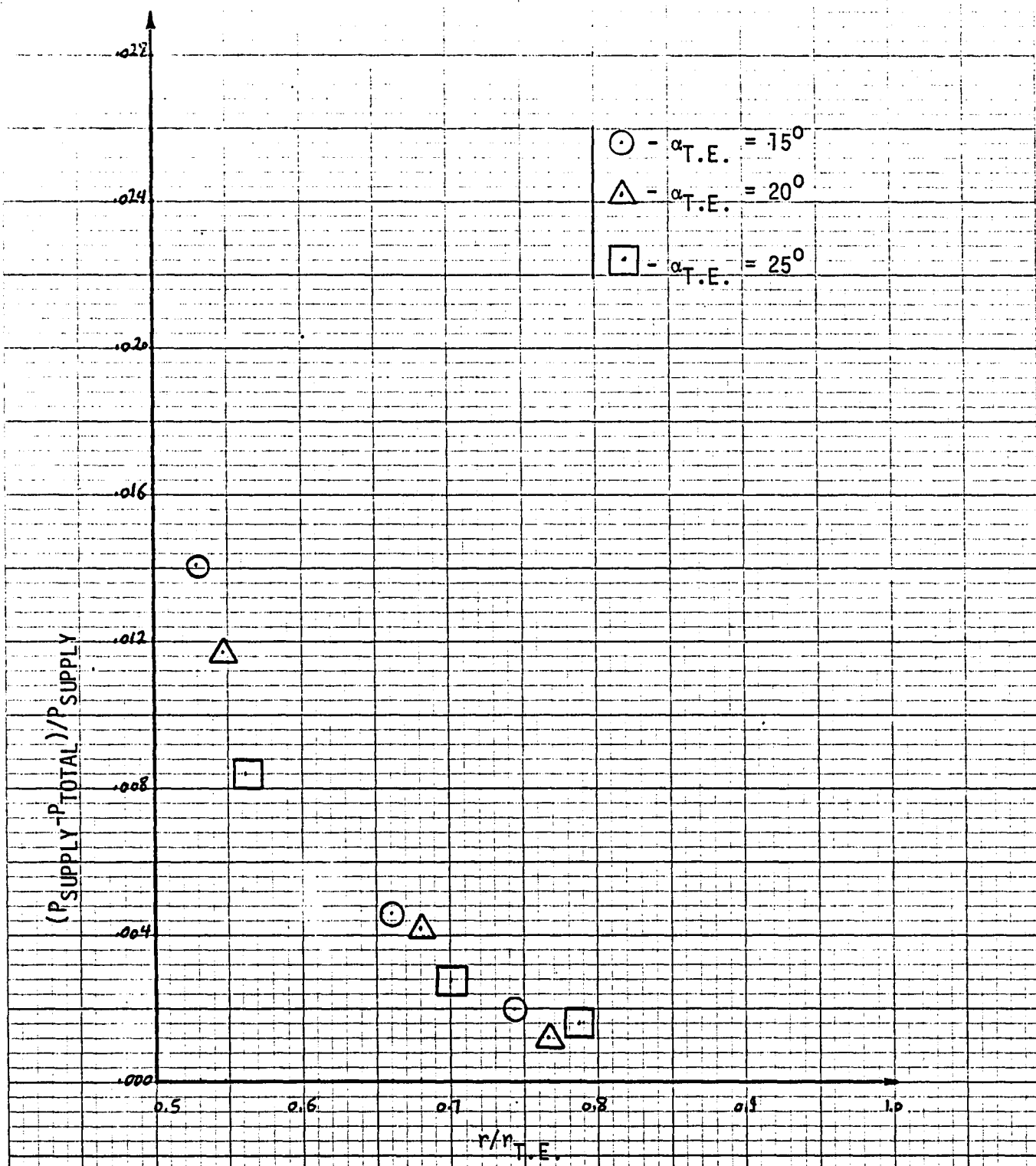


FIG. 37 Variation of the loss coefficient with radius ratio for three nozzle setting angles 15., 20., and 25. deg., supply pressure 24.44 psia, nozzle width 0.200 in.

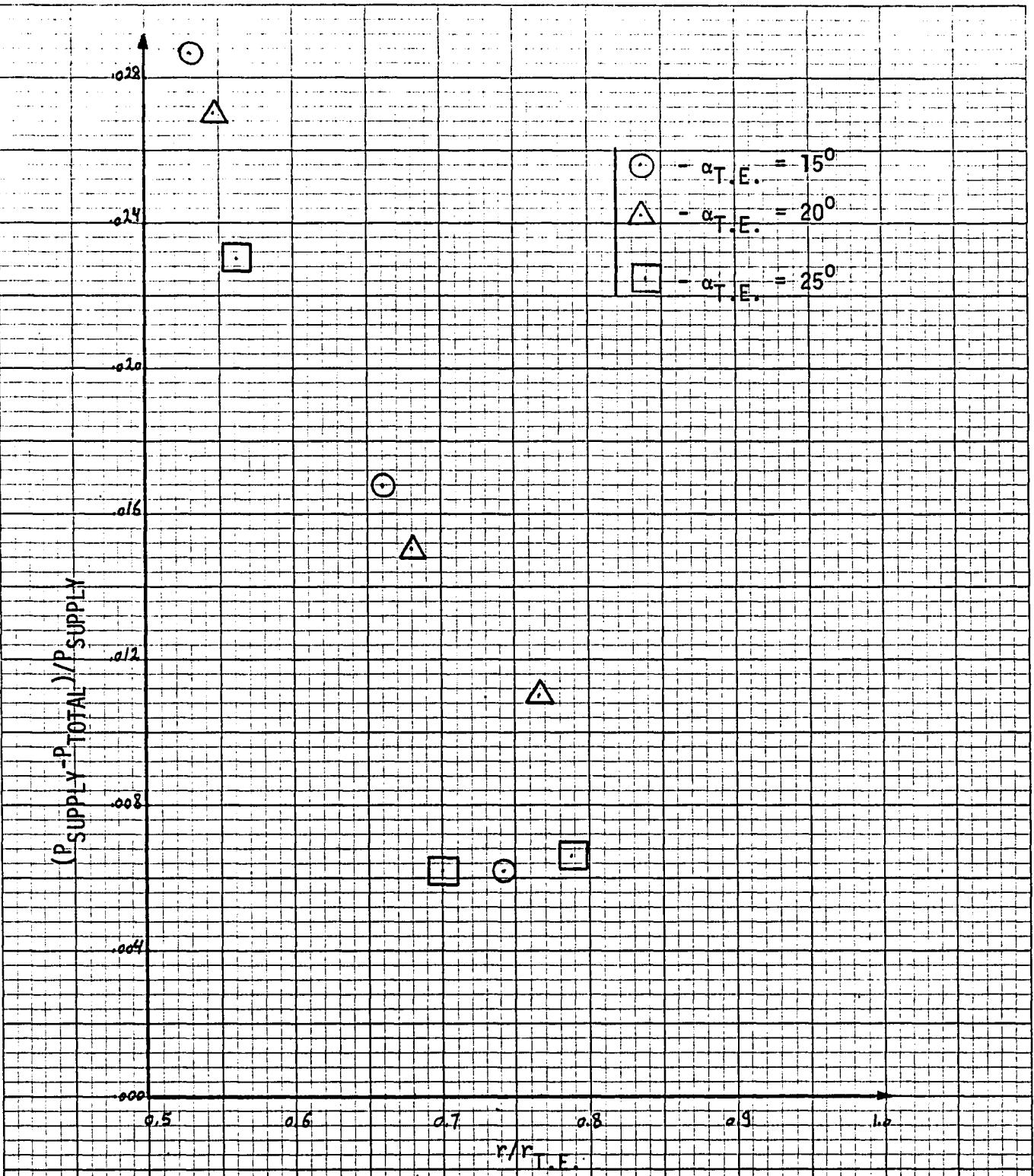


FIG. 38 Variation of the loss coefficient with radius ratio for three nozzle setting angles 15, 20, and 25 deg., supply pressure 24.35 psia, nozzle width 0.148 in.

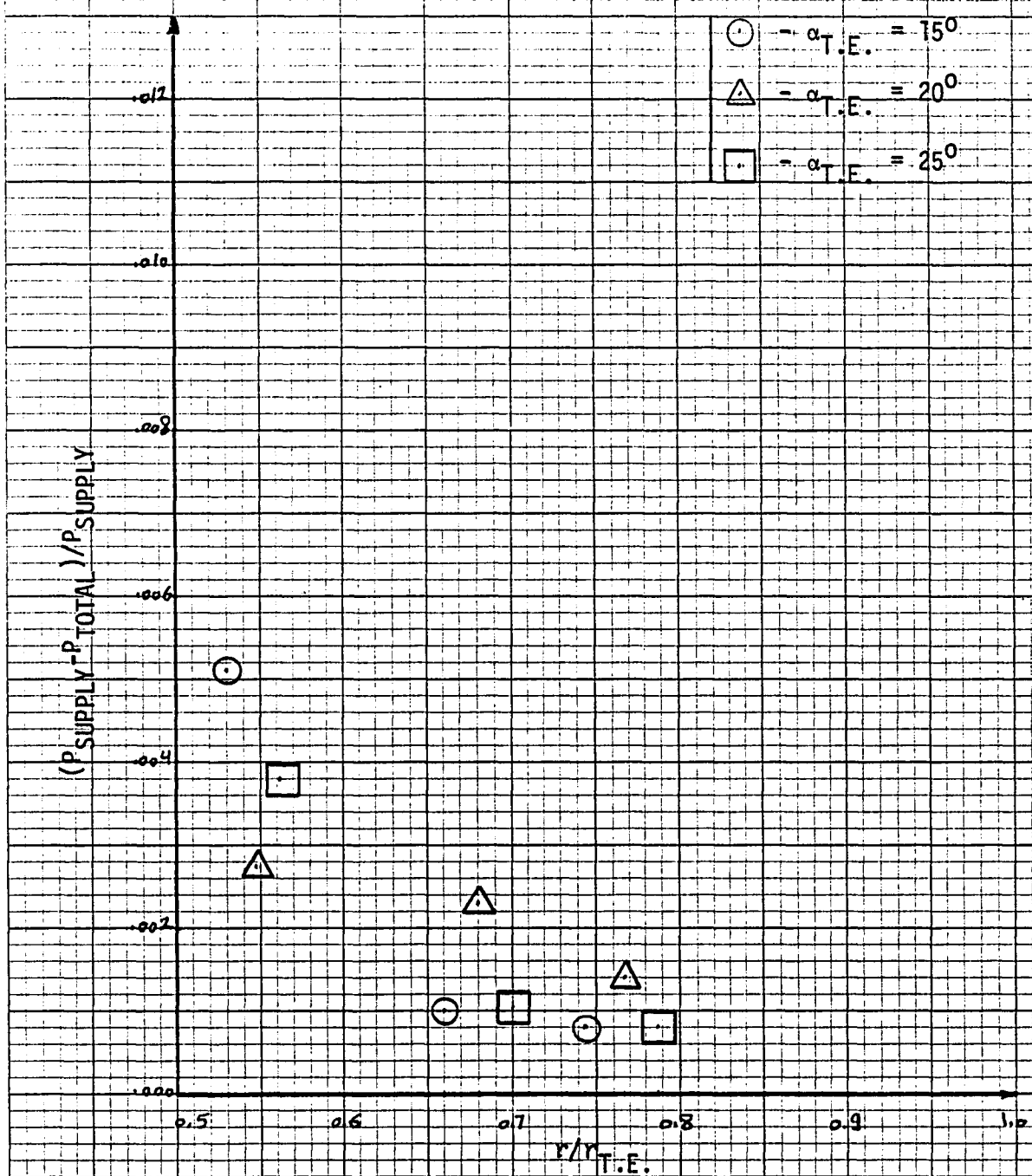


FIG. 39 Variation of the loss coefficient with radius ratio for three nozzle setting angles, 15., 20., and 25. deg., supply pressure 19.13 p.s.i., nozzle width 0.200 in.

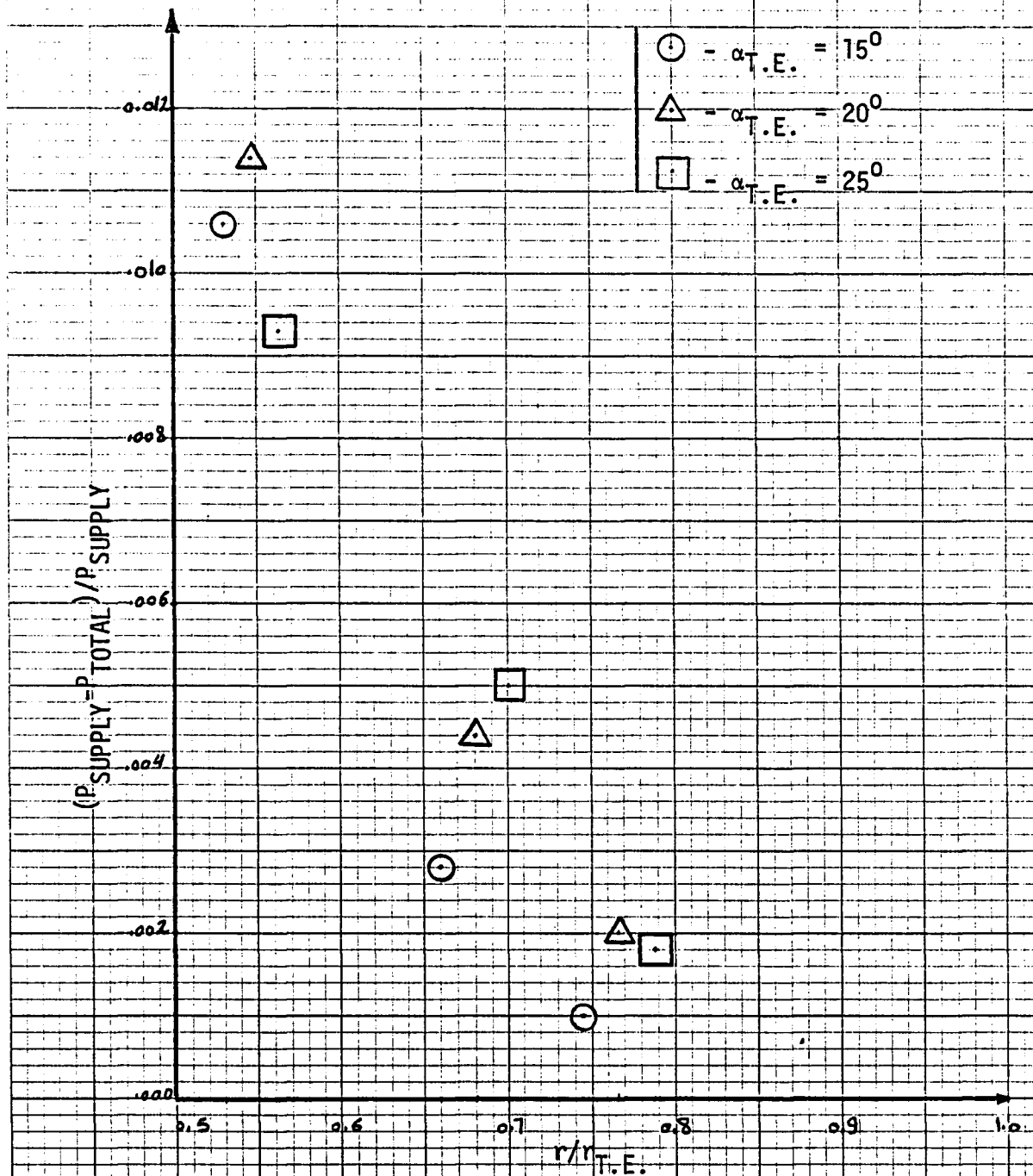


FIG. 40 Variation of the loss coefficient with radius ratio for three nozzle setting angles, 15., 20., and 25. deg., supply pressure 19.26 psia, nozzle width 0.148 in.

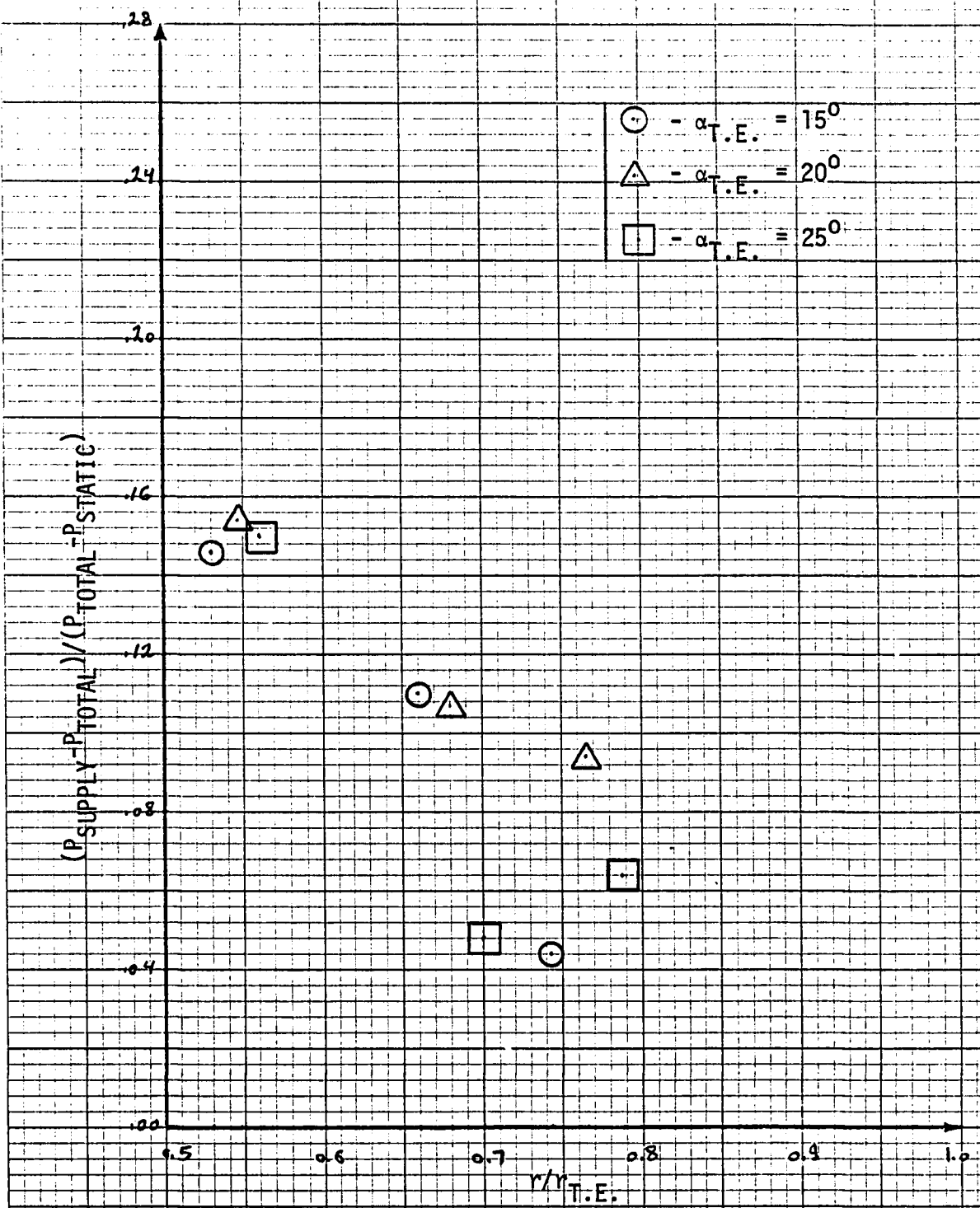


FIG. 41 Variation of the loss coefficient with radius ratio for three nozzle setting angles, 15., 20., and 25. deg., supply pressure 24.35 psia, nozzle width 0.148 in.

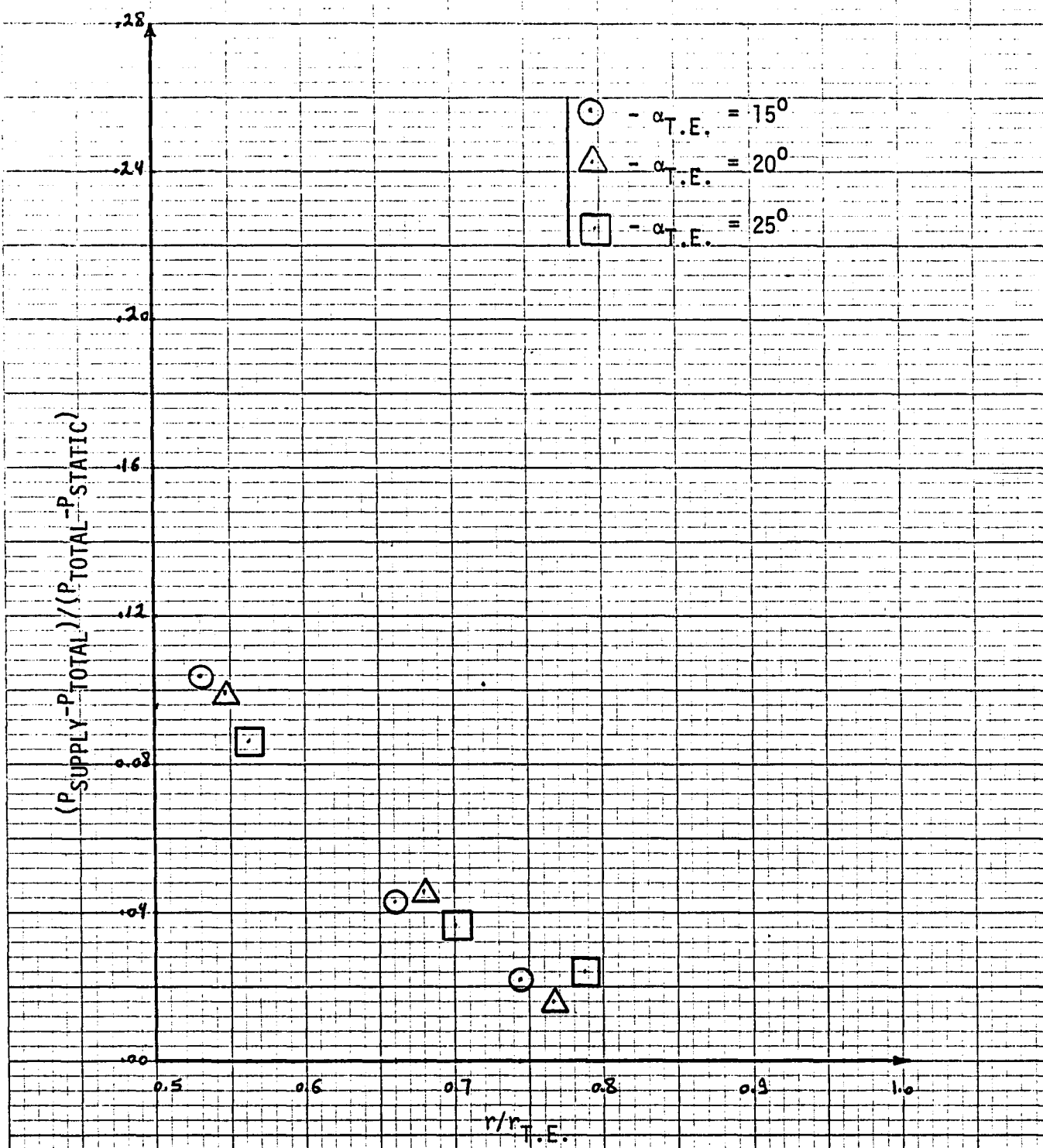


FIG. 42 Variation of the loss coefficient with radius ratio for three nozzle setting angles, 15., 20., and 25. deg., supply pressure 24.44 psia, nozzle width 0.200 in.

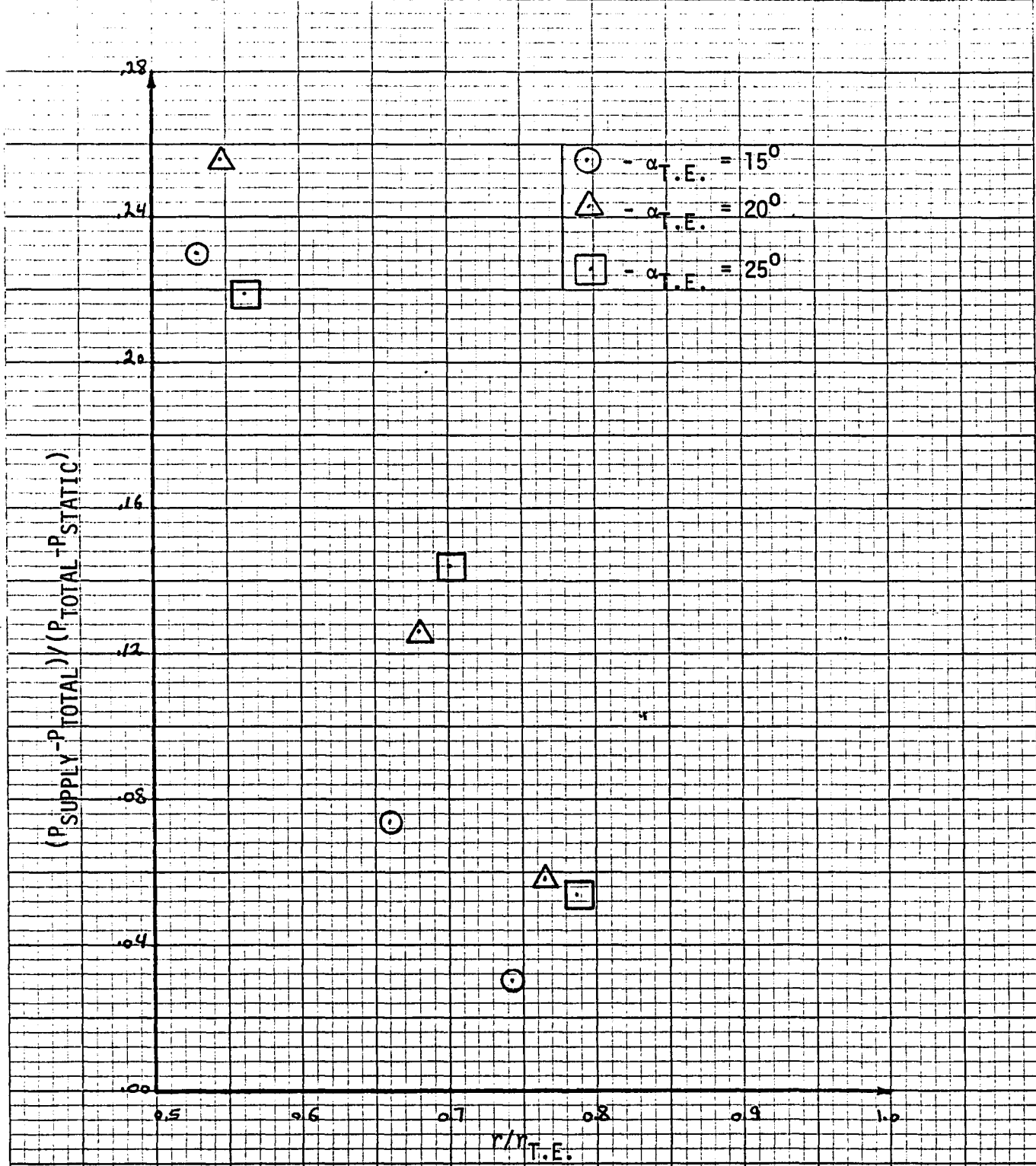


FIG. 43 Variation of the loss coefficient with radius ratio for three nozzle setting angles, 15., 20., and 25. deg., supply pressure 19.26 psia, nozzle width 0.148 in.

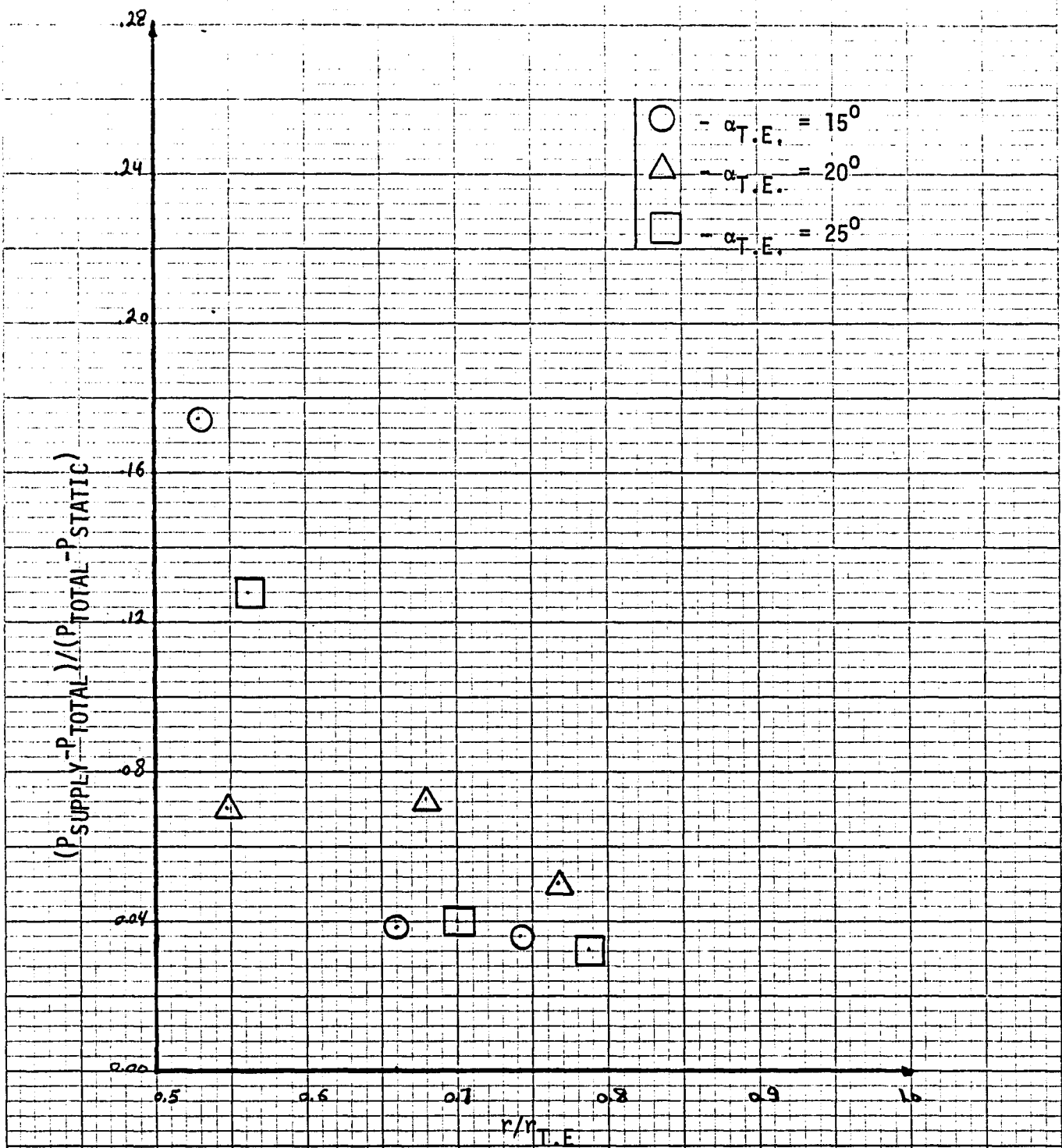


FIG. 44. Variation of the loss coefficient with radius ratio for three nozzle setting angles, 15., 20., and 25. deg., supply pressure 19.13 psia, nozzle width 0.200 in.

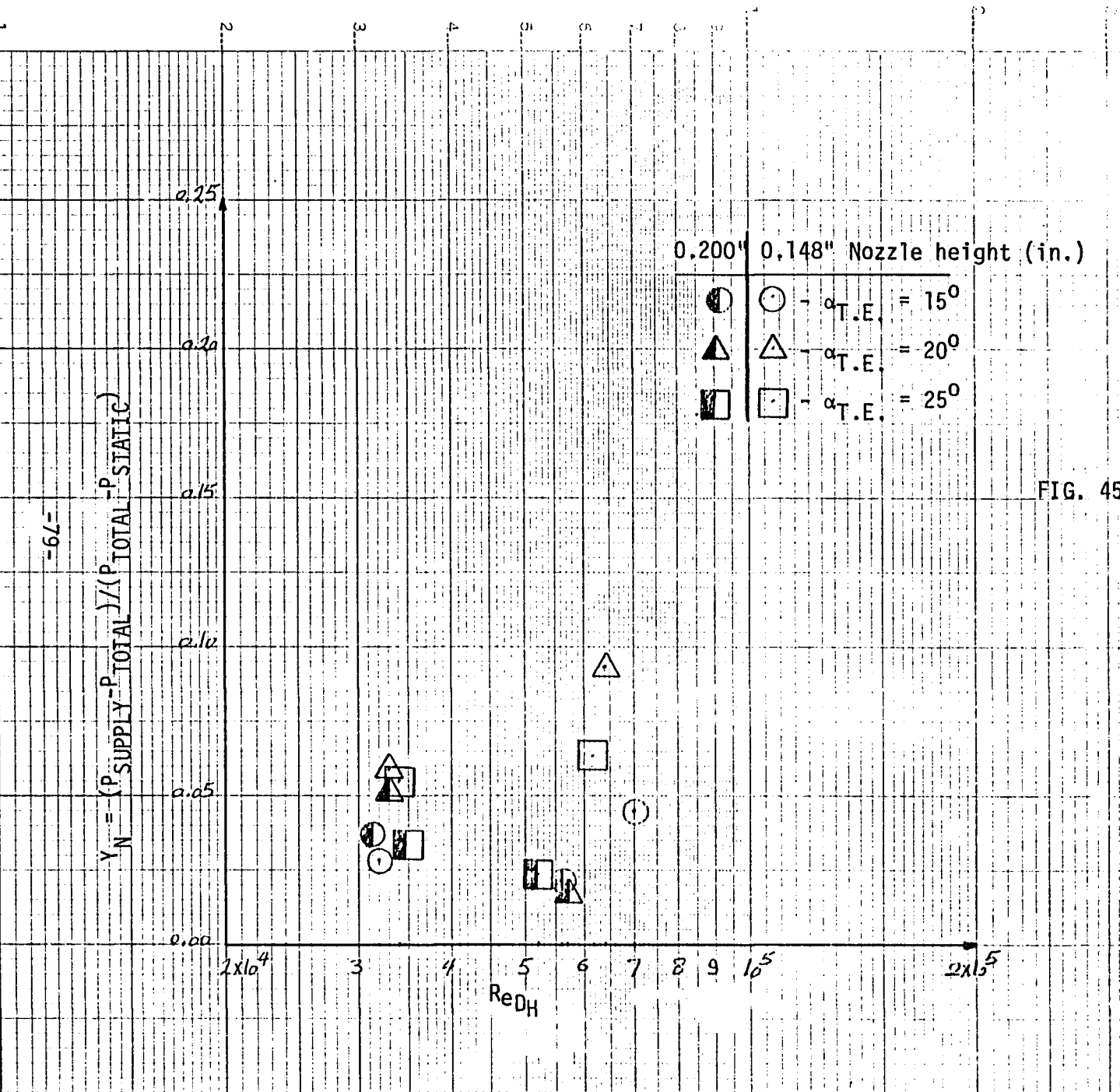


FIG. 45 Variation of the loss coefficient, Y_N , with Reynolds no. based on hydraulic diameter for three nozzle setting angles, 15., 20., and 25. deg. and two nozzle vane widths 0.200 and 0.148 in. at probe no. 1 located at radius 1.44 in.

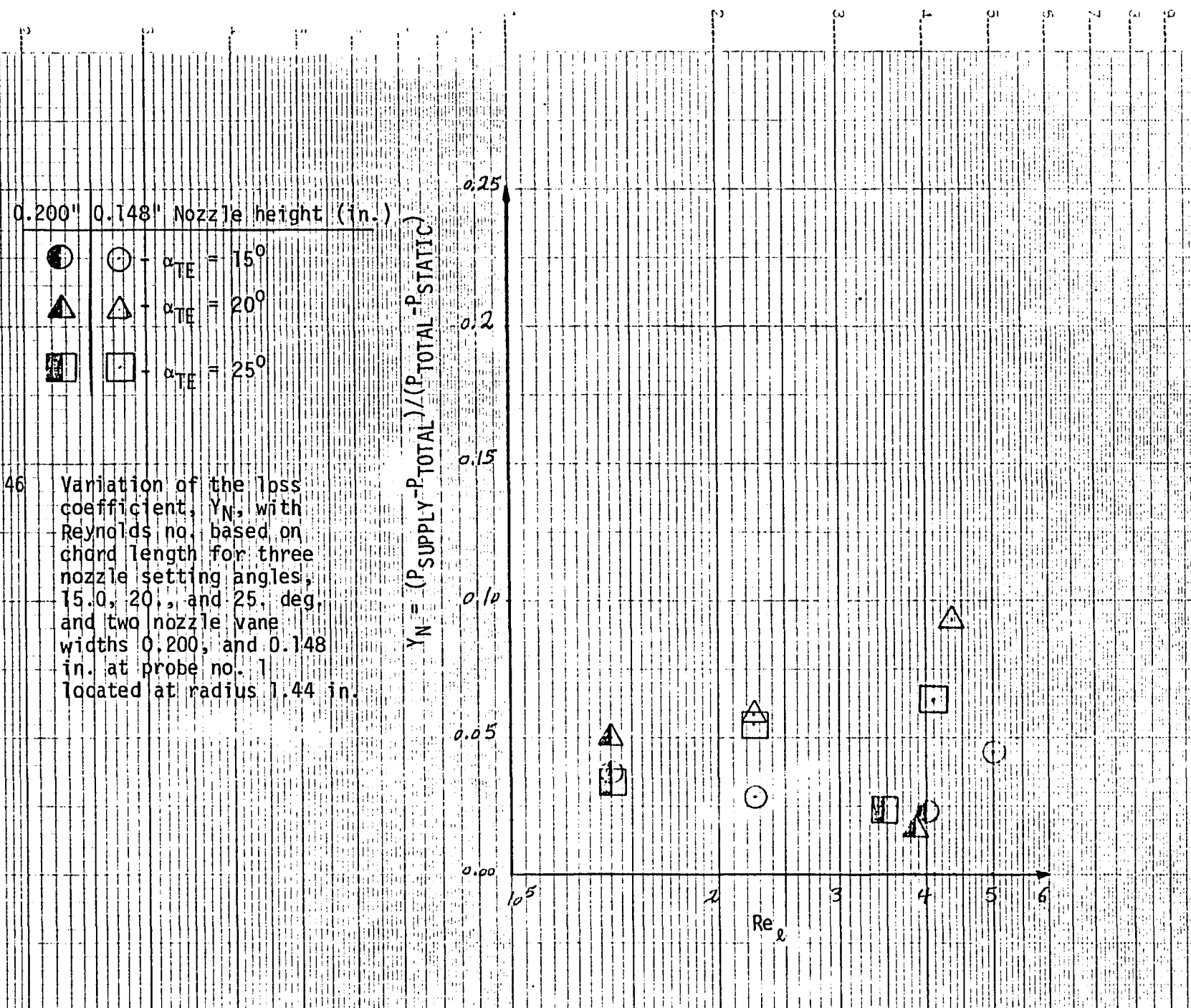


FIG. 46 Variation of the loss coefficient, N , with Reynolds no. based on chord length for three nozzle setting angles, 15.0, 20., and 25. deg, and two nozzle vane widths 0.200, and 0.148 in. at probe no. 1 located at radius 1.44 in.

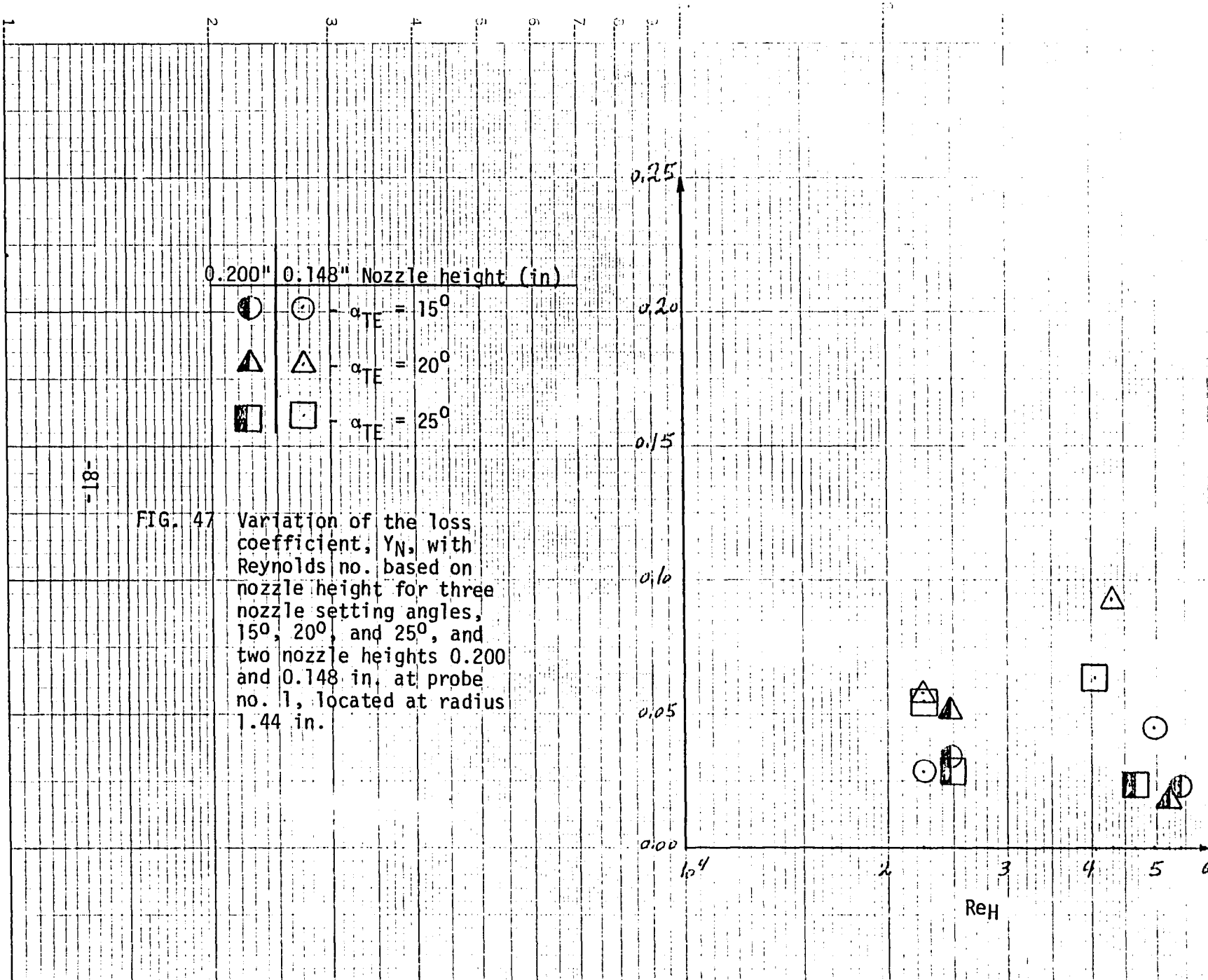
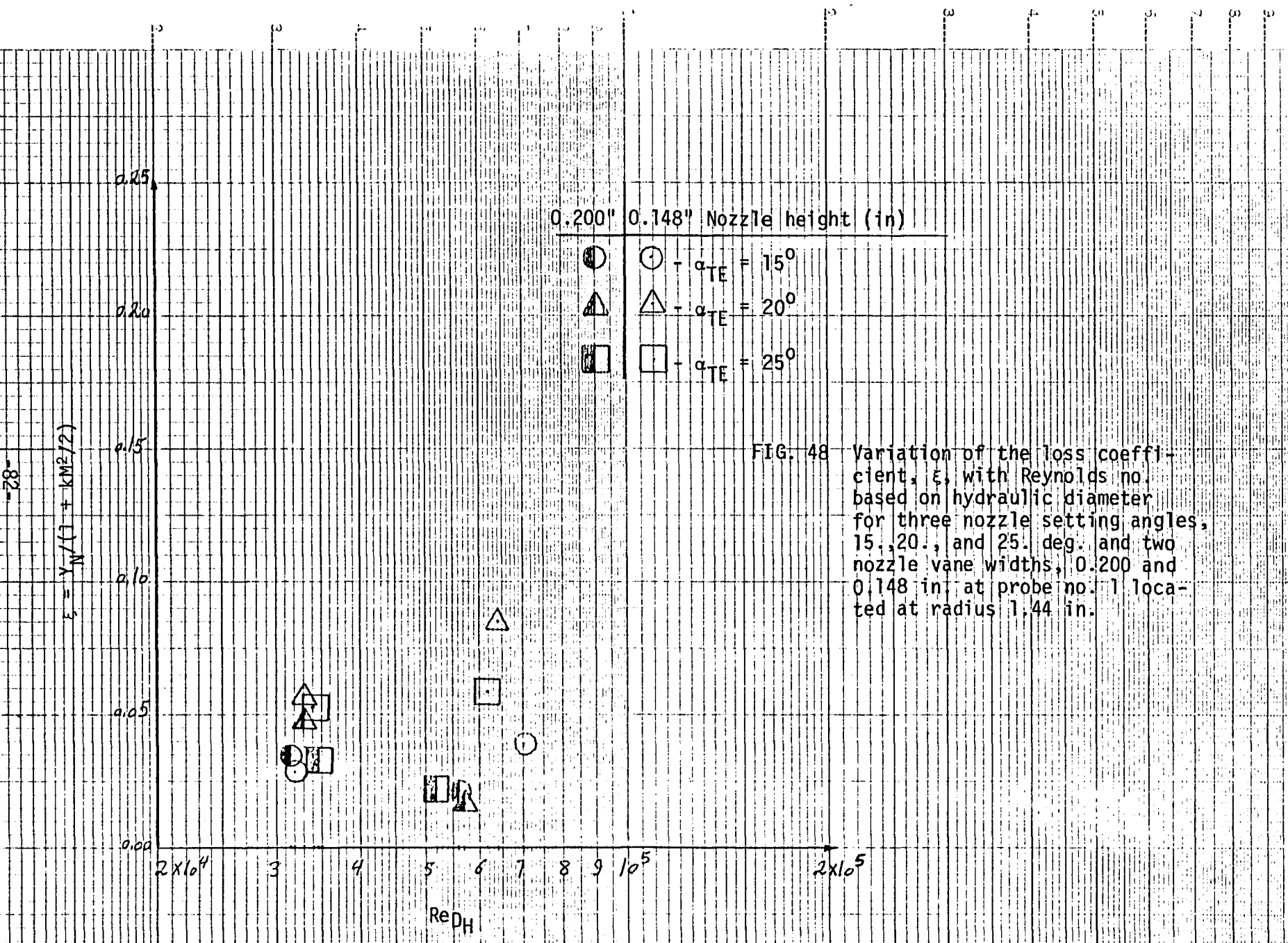


FIG. 47 Variation of the loss coefficient, Y_N , with Reynolds no. based on nozzle height for three nozzle setting angles, 15° , 20° , and 25° , and two nozzle heights 0.200 and 0.148 in. at probe no. 1, located at radius 1.44 in.



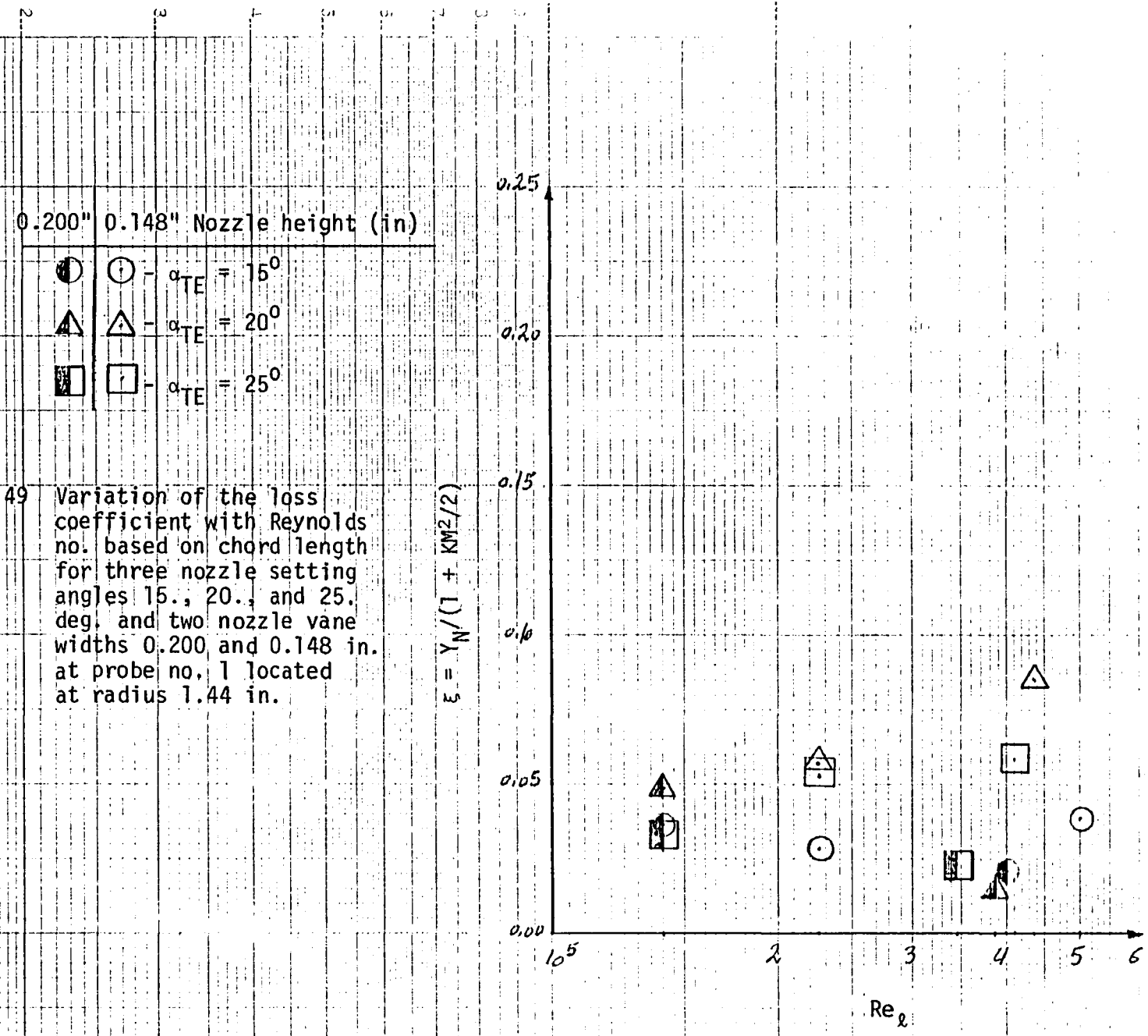
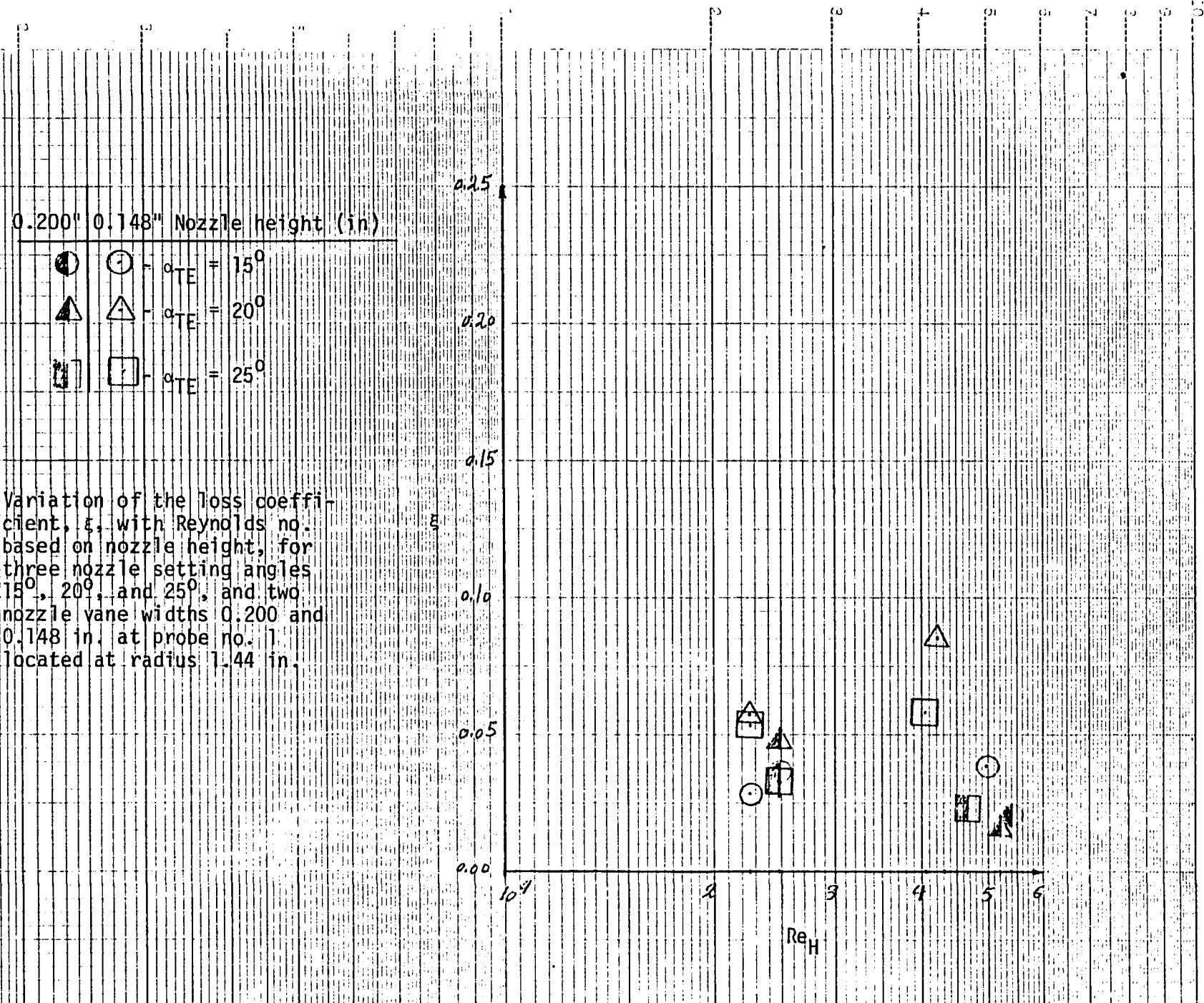


FIG. 49 Variation of the loss coefficient with Reynolds no. based on chord length for three nozzle setting angles 15., 20., and 25. deg. and two nozzle vane widths 0.200 and 0.148 in. at probe no. 1 located at radius 1.44 in.



-84- FIG. 50 Variation of the loss coefficient, ξ , with Reynolds no. based on nozzle height, for three nozzle setting angles 15° , 20° , and 25° , and two nozzle vane widths 0.200 and 0.148 in. at probe no. 1 located at radius 1.44 in.

$$Y_N = \frac{(P_{SUPPLY} - P_{TOTAL}) / (P_{TOTAL} - P_{STATIC})}{}$$

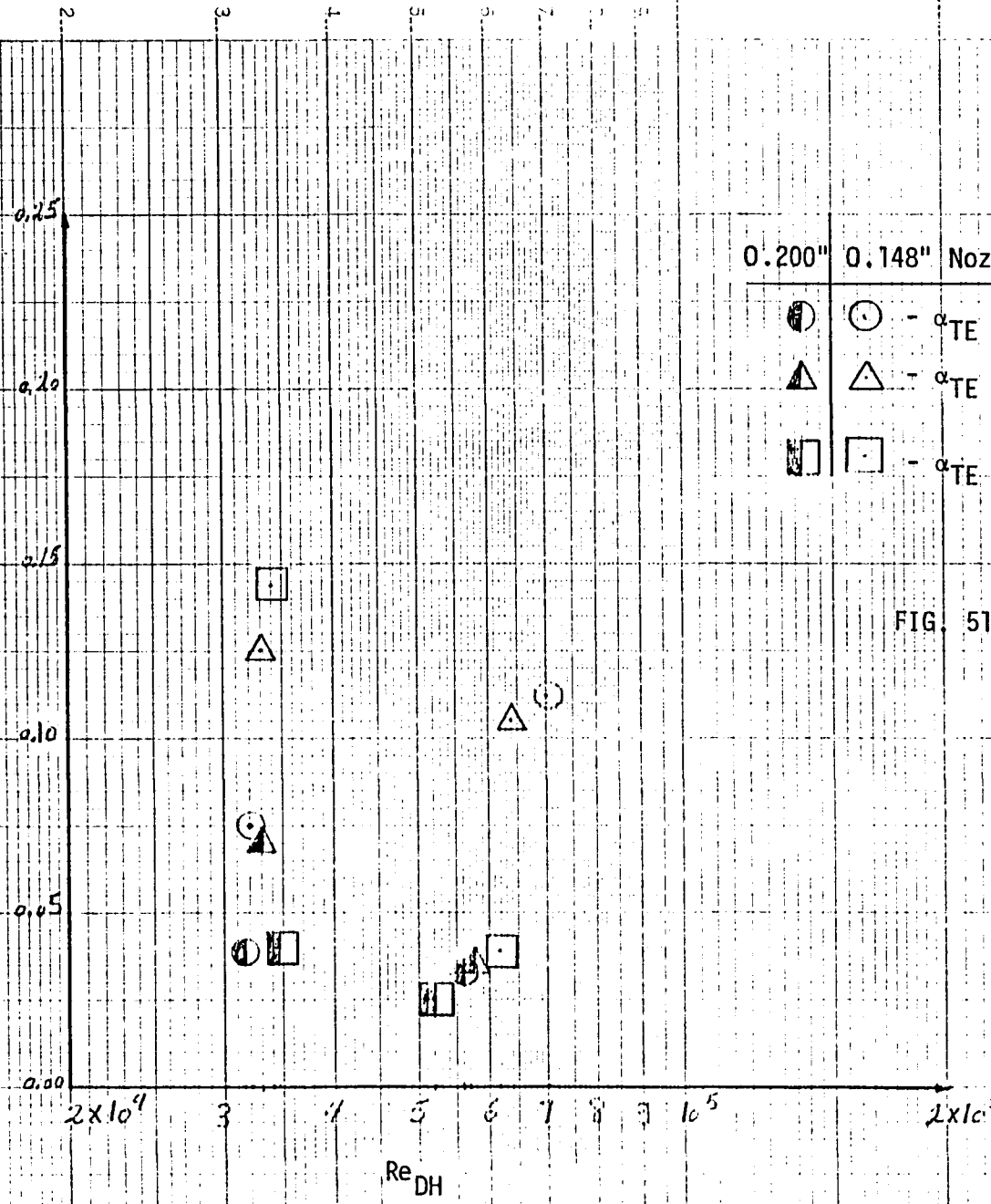


FIG. 51 Variation of the loss coefficient, Y_N , with Reynolds no.

based on hydraulic diameter
for three nozzle setting angles
 15° , 20° , and 25° . deg. and two
nozzle vane widths, 0.200 and
0.148 in. at probe no. 2 located
at radius 1.28 in.

0.200" 0.148" Nozzle height (in.)

- \bullet - $\alpha_{TE} = 15^\circ$
- Δ - $\alpha_{TE} = 20^\circ$
- \square - $\alpha_{TE} = 25^\circ$

$$N = \frac{\text{SUPPLY TOTAL} / P_{\text{TOTAL}}}{P_{\text{STALL}}}$$

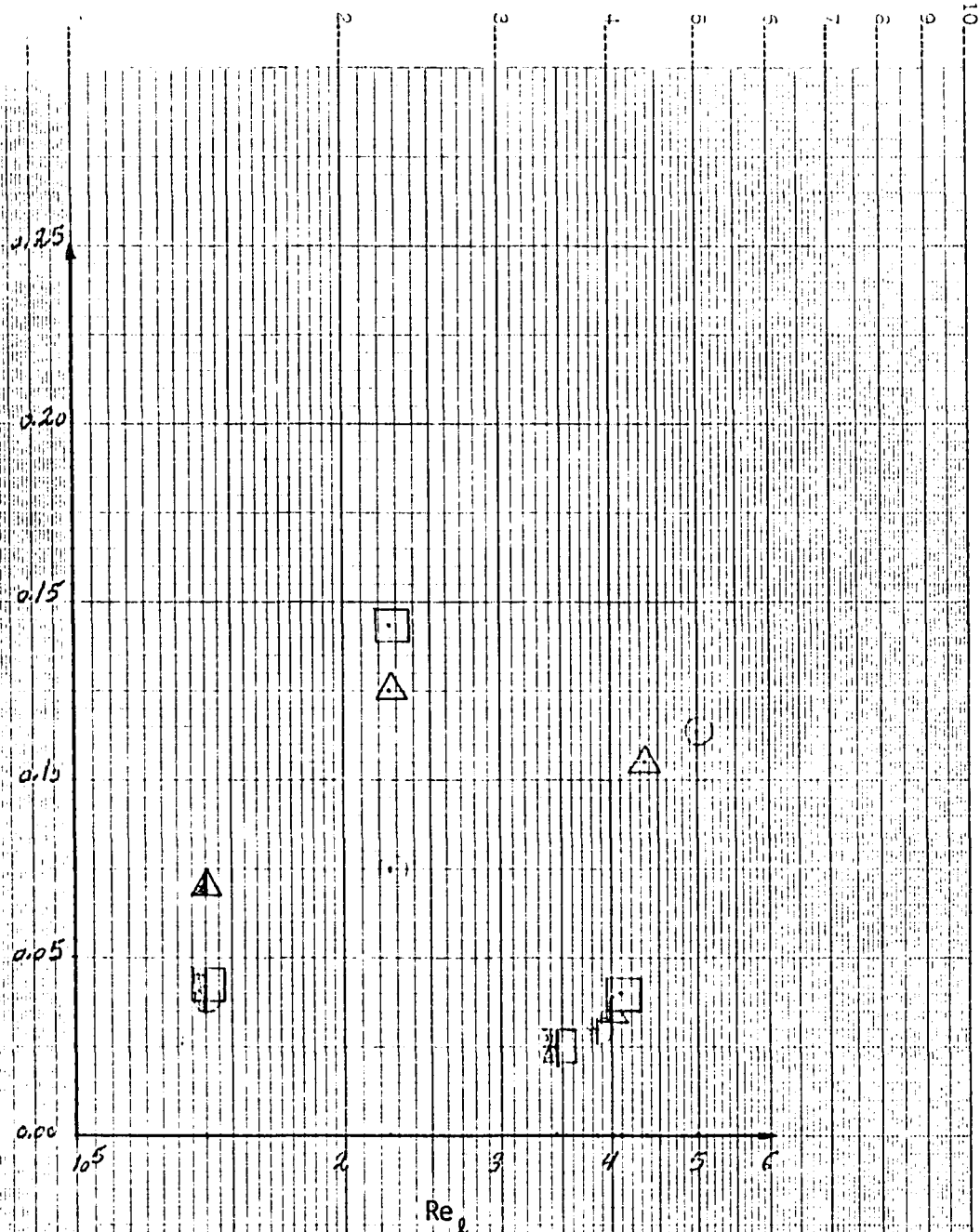


FIG. 52 Variation of the loss coefficient, N , with Reynolds no., based on chord length for three nozzle setting angles, 15., 20., and 25. deg. and two nozzle vane widths 0.200 and 0.148 in. at probe no. 2 located at radius 1.28 in.

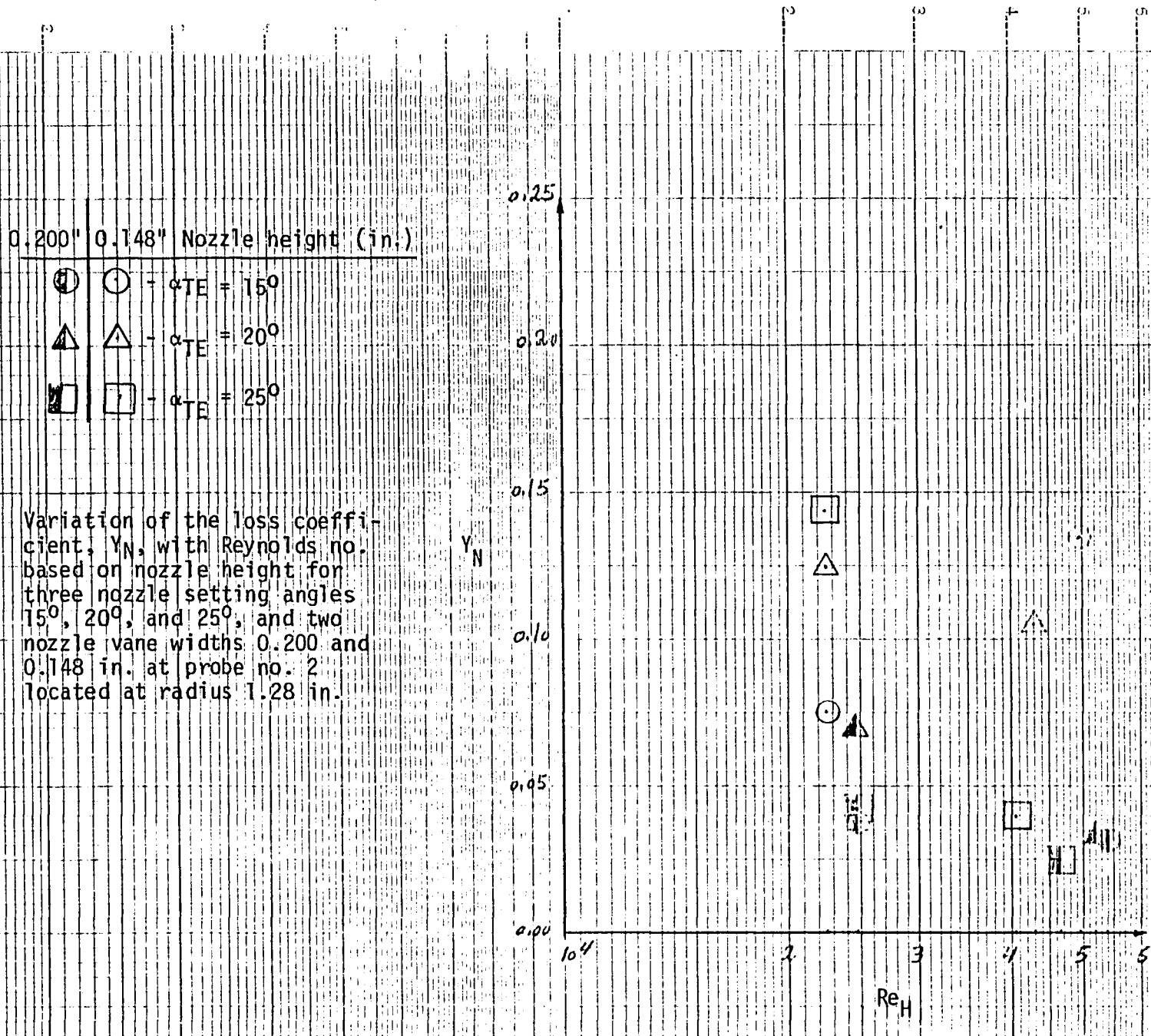
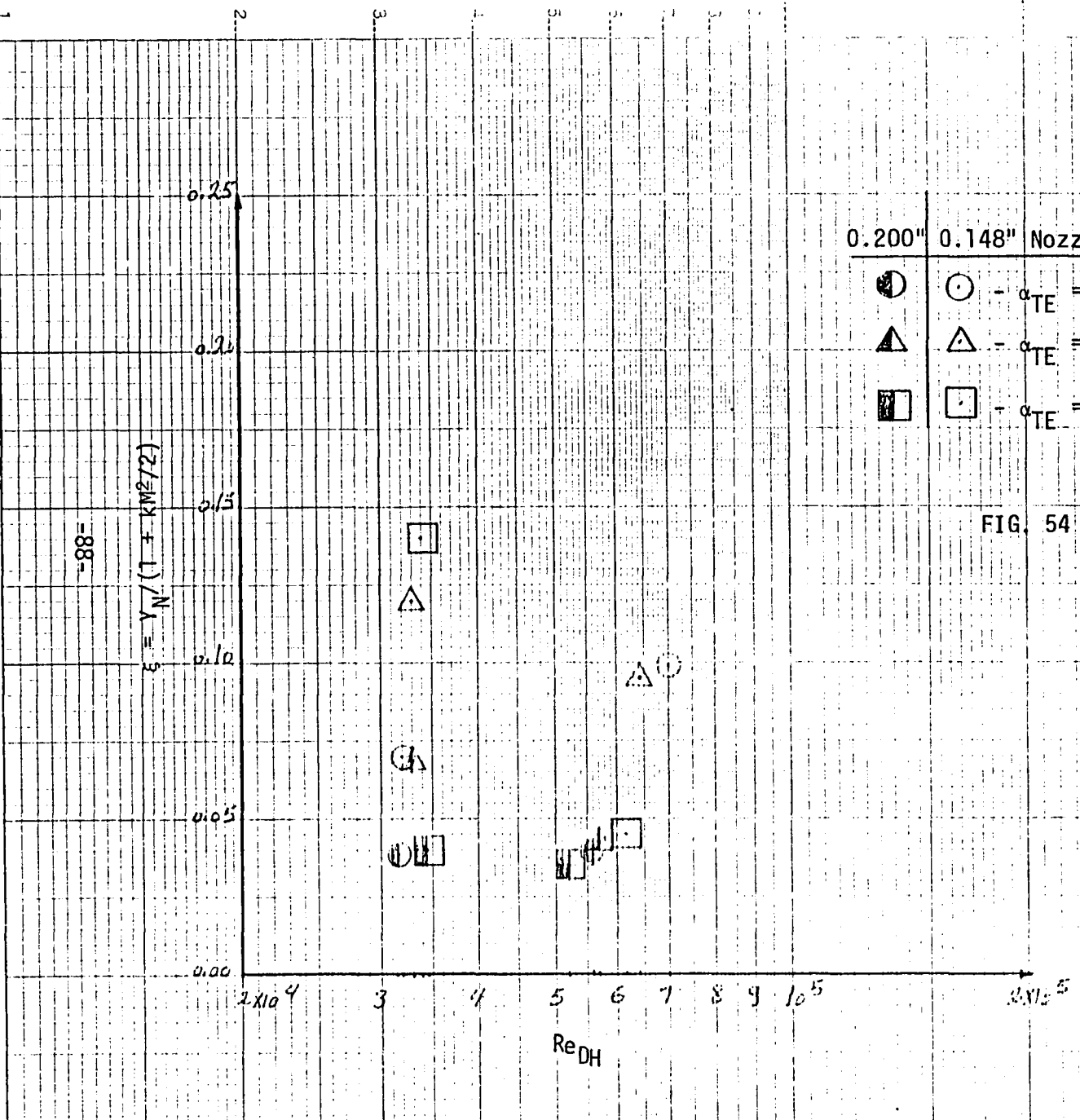


FIG. 53 Variation of the loss coefficient, Y_N , with Reynolds no. based on nozzle height for three nozzle setting angles 15° , 20° , and 25° , and two nozzle vane widths 0.200 and 0.148 in. at probe no. 2 located at radius 1.28 in.



0.200" 0.148" Nozzle height (in.)

(\circ) - $\alpha_{TE} = 15^\circ$
 (\triangle) - $\alpha_{TE} = 20^\circ$
 (\square) - $\alpha_{TE} = 25^\circ$

FIG. 54 Variation of the loss coefficient, ξ , with Reynolds number based on hydraulic diameter for three nozzle setting angles 15., 20., and 25. deg. and two nozzle vane widths 0.200 and 0.148 in. at probe no. 2 located at radius 1.28 in.

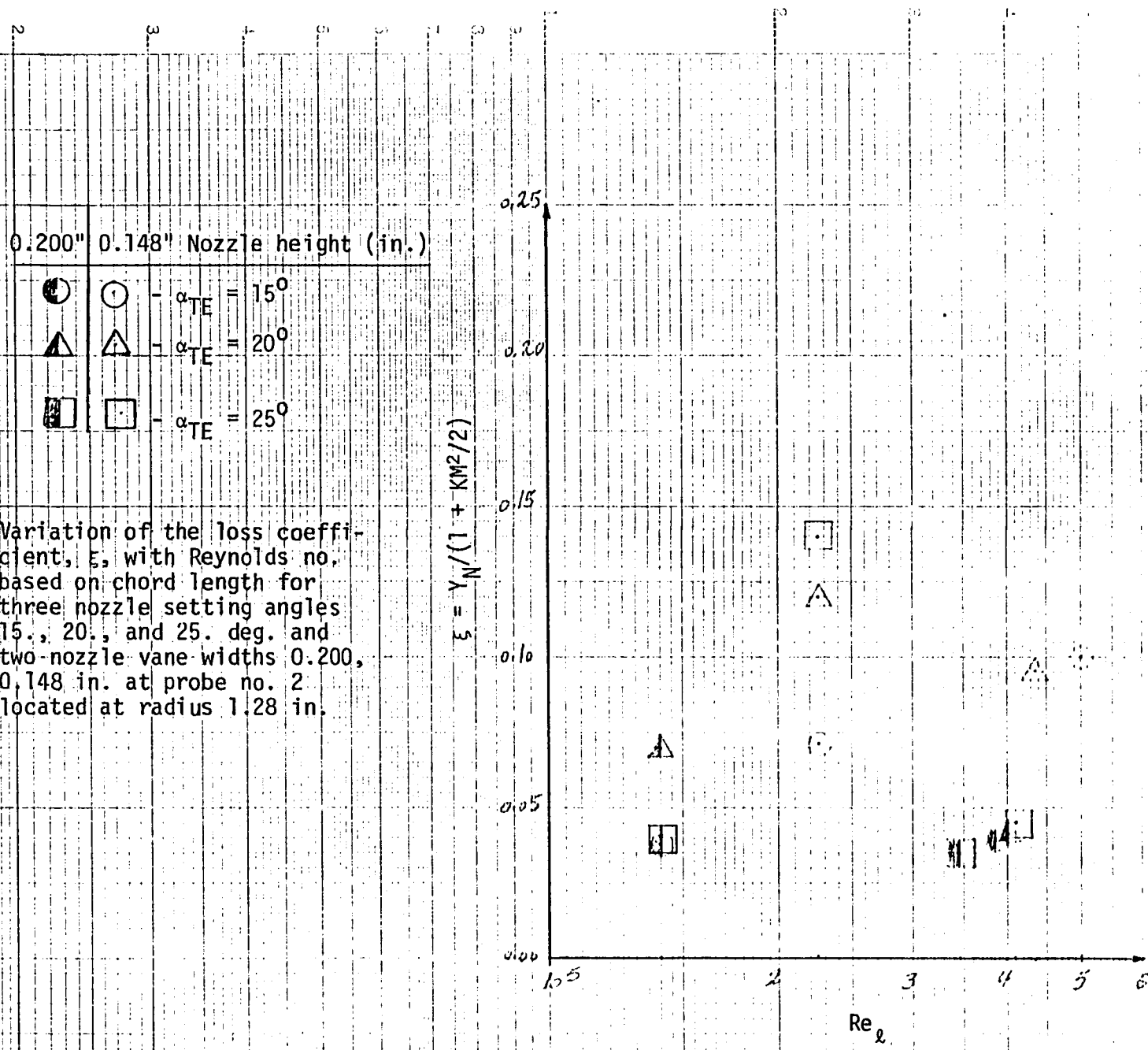


FIG. 55 Variation of the loss coefficient, ξ , with Reynolds no., based on chord length for three nozzle setting angles 15., 20., and 25. deg. and two-nozzle vane widths 0.200, 0.148 in. at probe no. 2 located at radius 1.28 in.

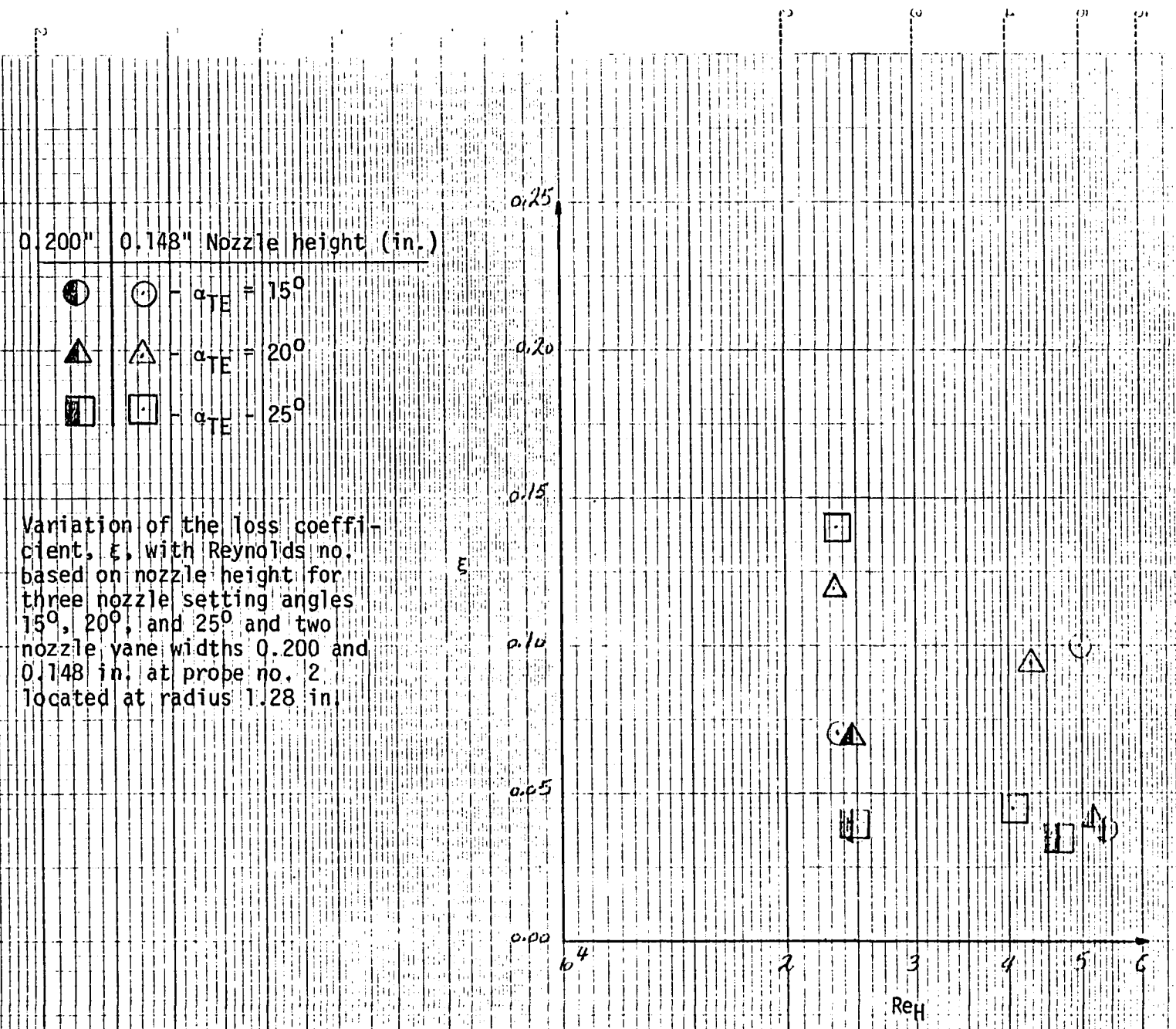


FIG. 56 Variation of the loss coefficient, ξ , with Reynolds no., based on nozzle height for three nozzle setting angles 15° , 20° , and 25° and two nozzle vane widths 0.200 and 0.148 in. at probe no. 2 located at radius 1.28 in.

-90-

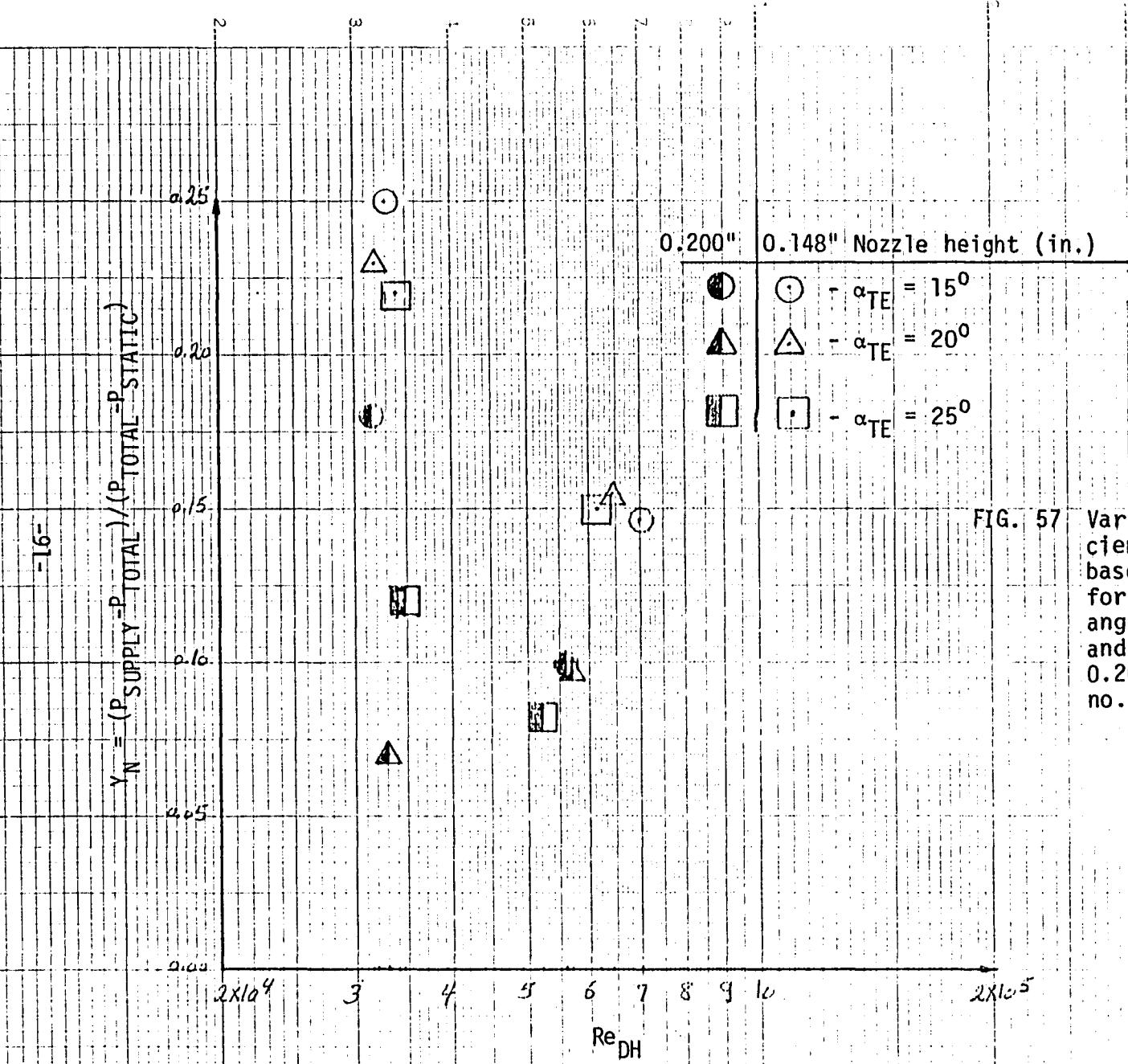
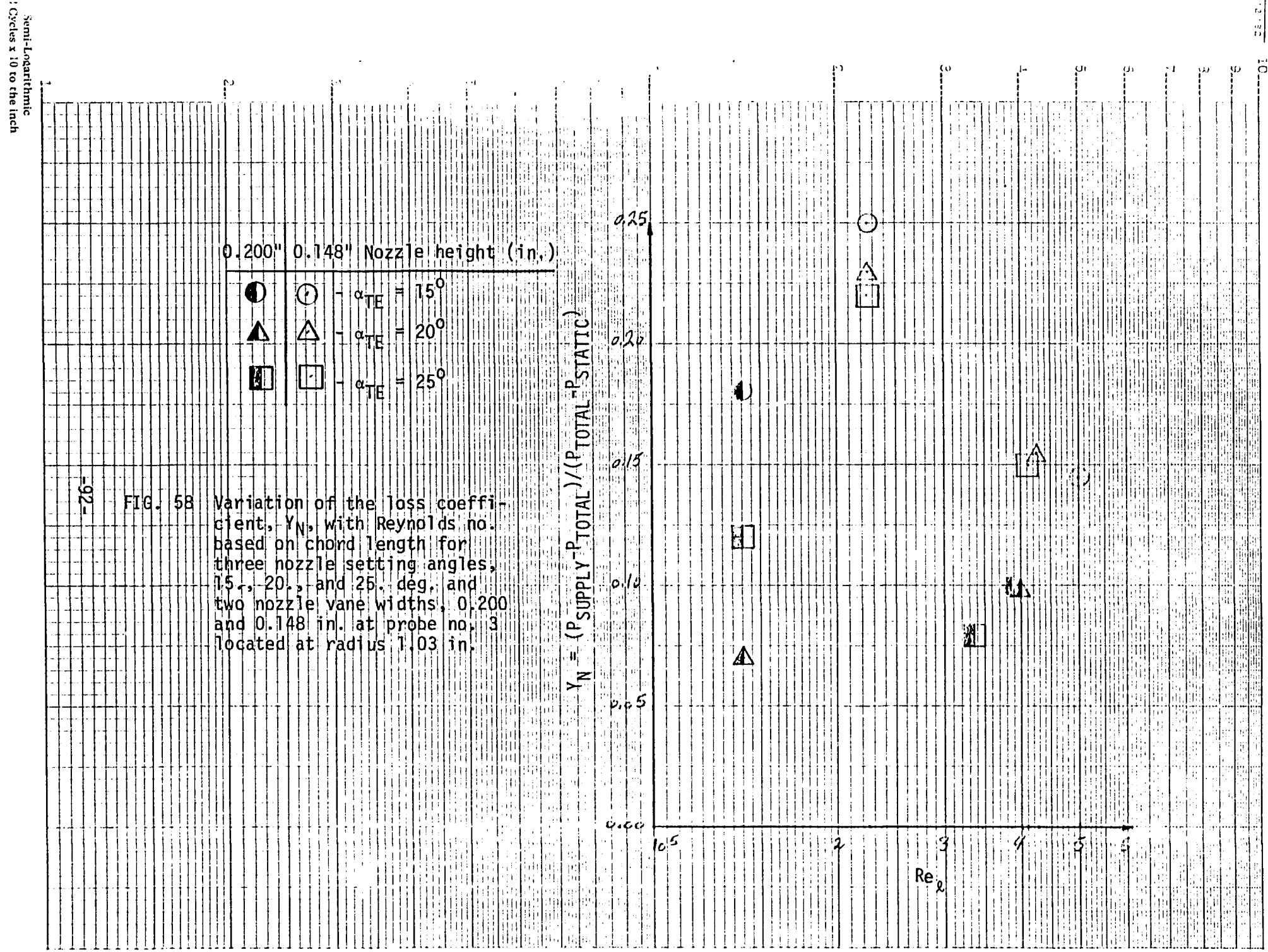


FIG. 57

Variation of the loss coefficient, Y_N , with Reynolds no. based on hydraulic diameter for three nozzle setting angles, 15., 20. and 25. deg. and two nozzle vane widths 0.200 and 0.148 in., at probe no. 3 located at radius 1.03 in.



-92- FIG. 58 Variation of the loss coefficient, Y_N , with Reynolds no. based on chord length for three nozzle setting angles, 15°, 20°, and 25° deg., and two nozzle vane widths, 0.200 and 0.148 in. at probe no. 3 located at radius 1.03 in.

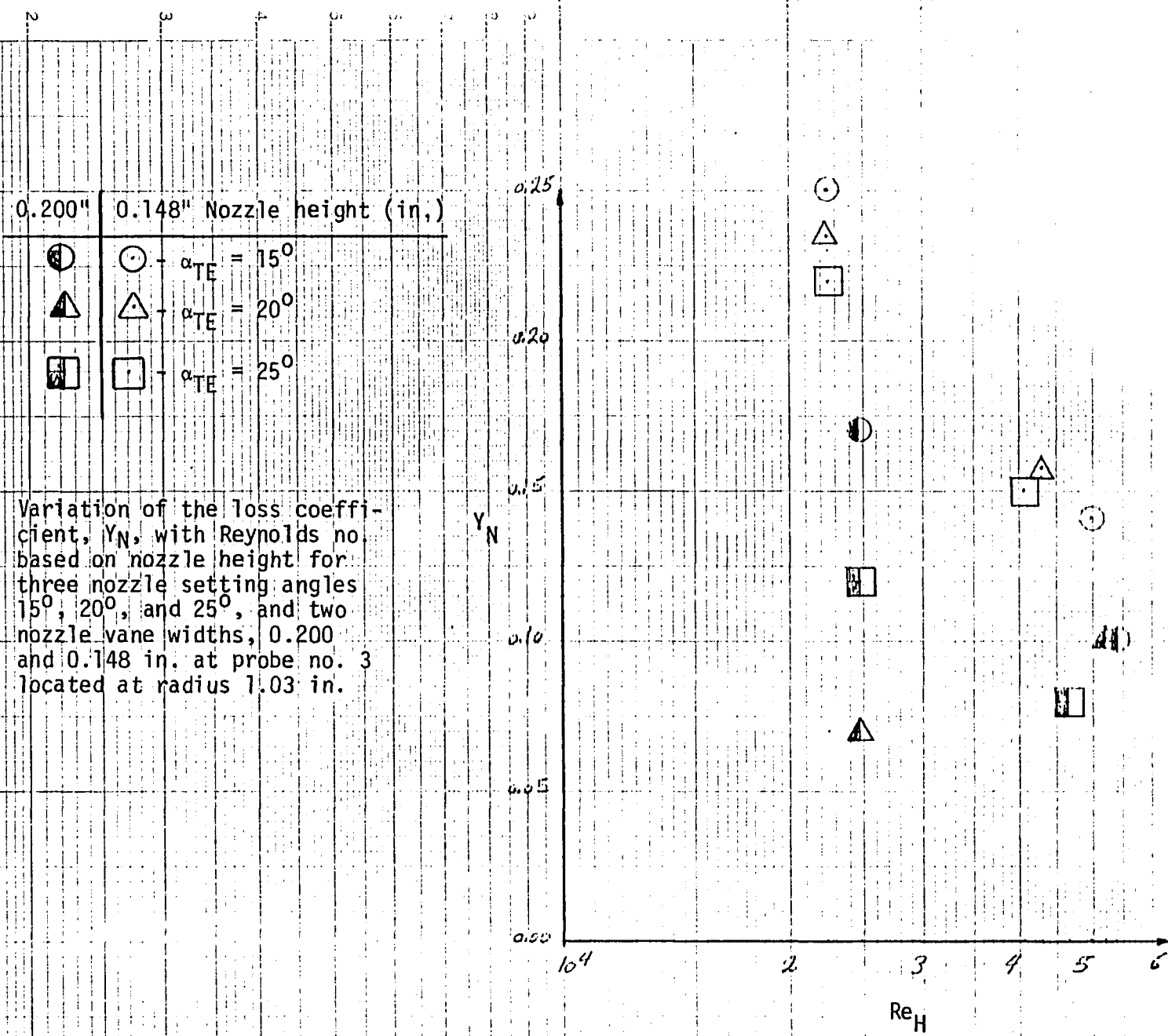


FIG. 59 Variation of the loss coefficient, Y_N , with Reynolds no based on nozzle height for three nozzle setting angles 15° , 20° , and 25° , and two nozzle vane widths, 0.200 and 0.148 in. at probe no. 3 located at radius 1.03 in.

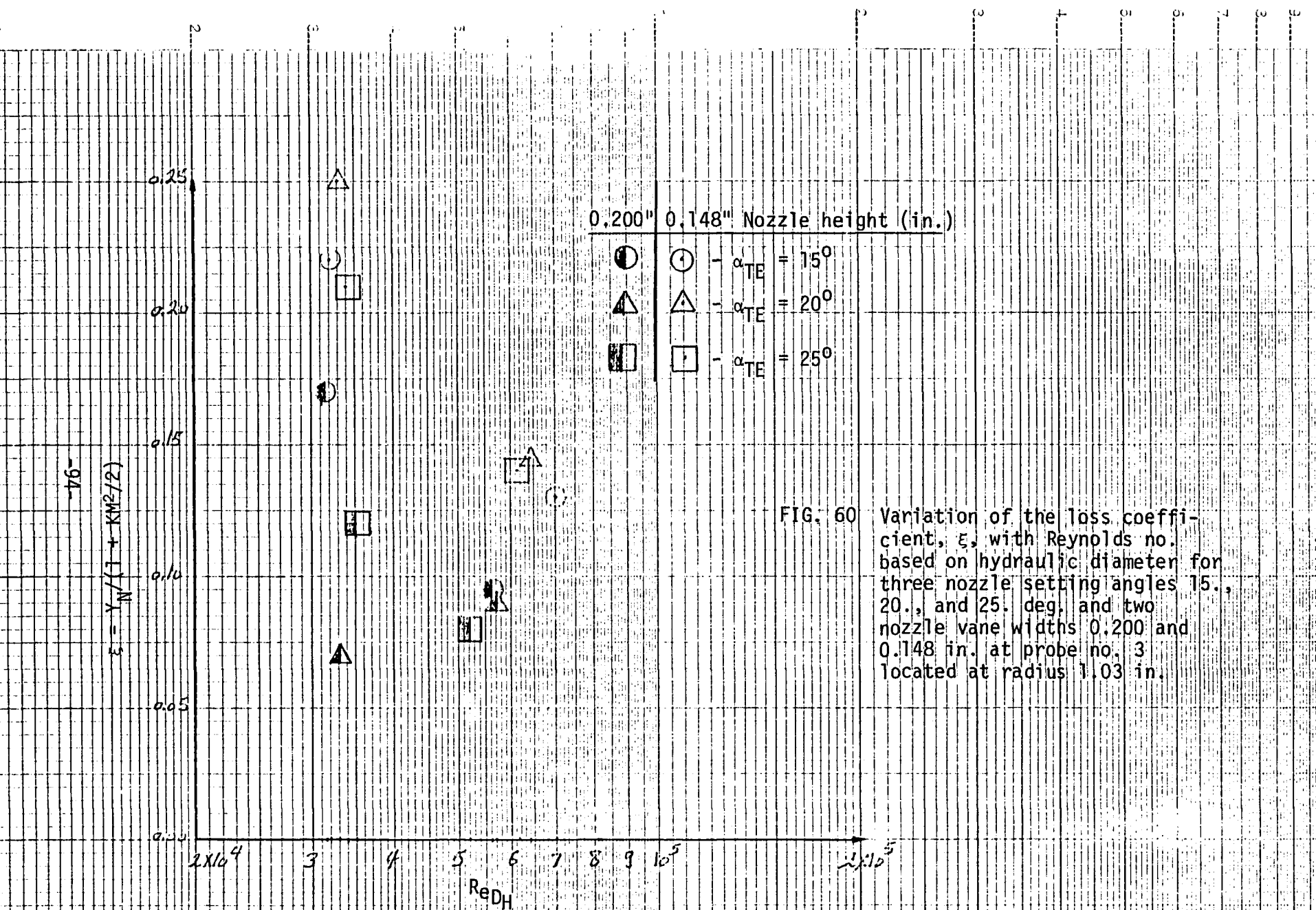


FIG. 60 Variation of the loss coefficient, ξ , with Reynolds no. based on hydraulic diameter for three nozzle setting angles 15., 20., and 25. deg. and two nozzle vane widths 0.200 and 0.148 in. at probe no. 3 located at radius 1.03 in.

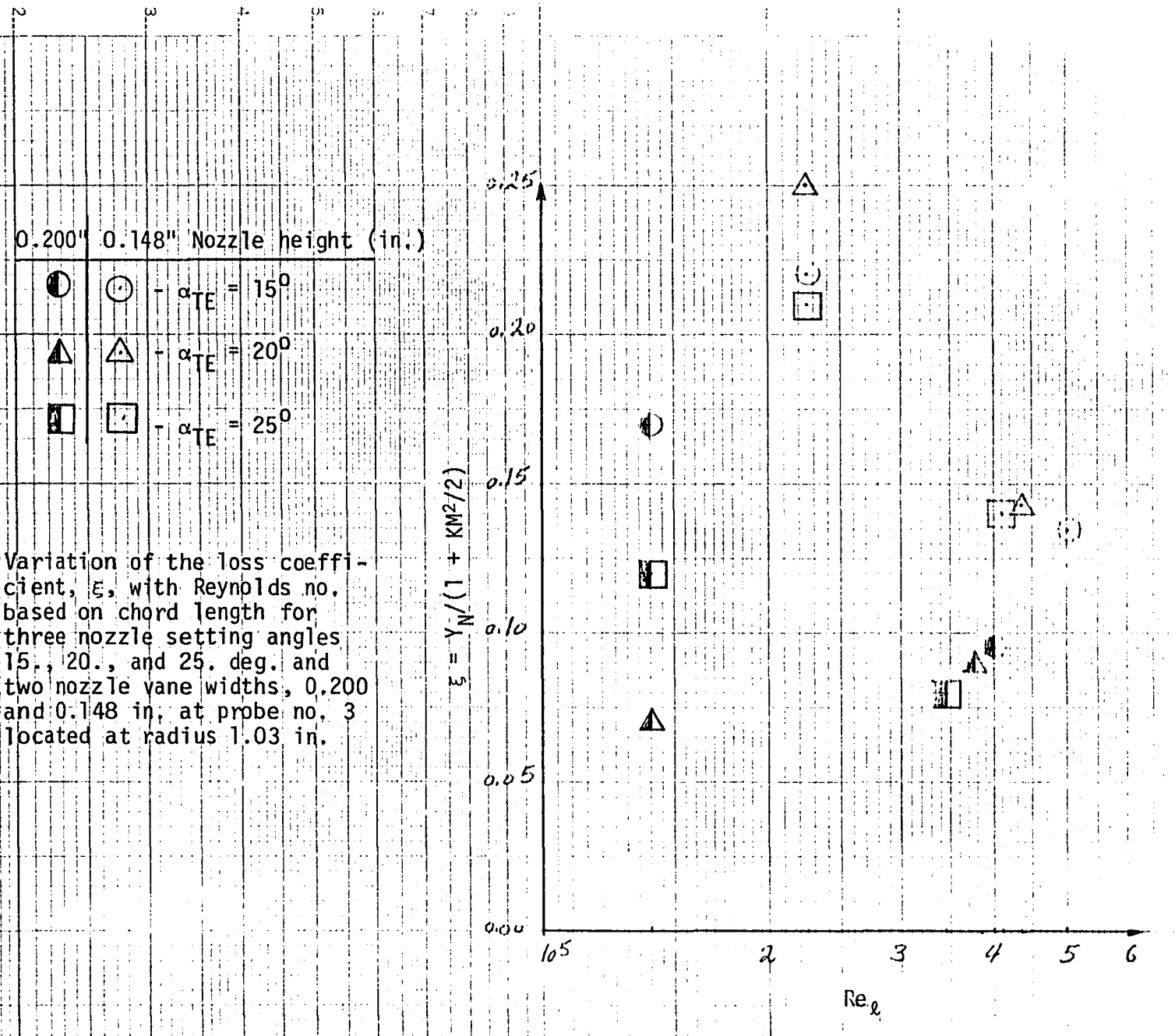


FIG. 61 Variation of the loss coefficient, ξ , with Reynolds no. based on chord length for three nozzle setting angles 15., 20., and 25. deg. and two nozzle vane widths, 0.200 and 0.148 in, at probe no. 3 located at radius 1.03 in.

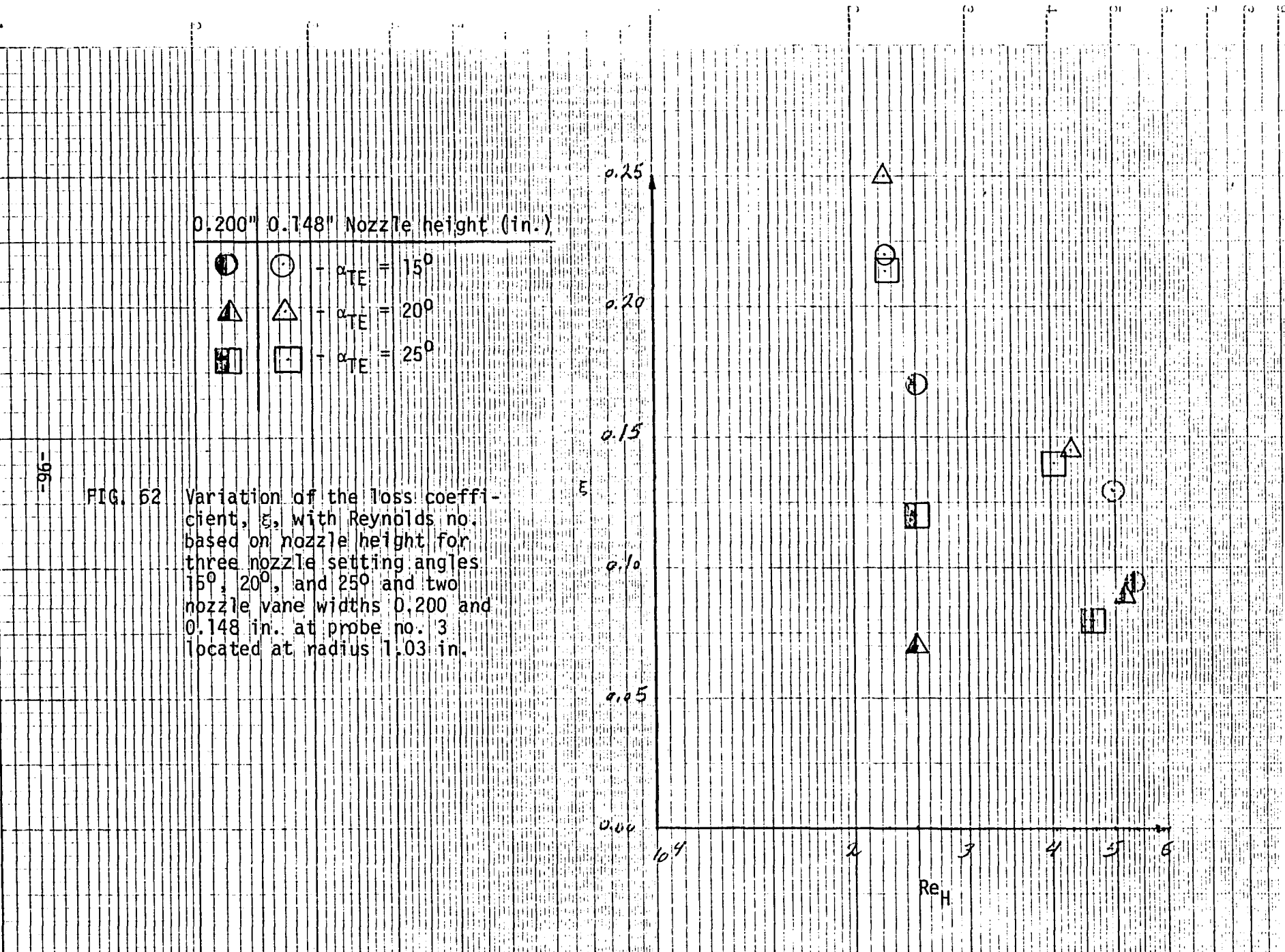


FIG. 62 Variation of the loss coefficient, ϵ , with Reynolds no. based on nozzle height for three nozzle setting angles 15° , 20° , and 25° and two nozzle vane widths 0.200 and 0.148 in. at probe no. 3 located at radius 1.03 in.

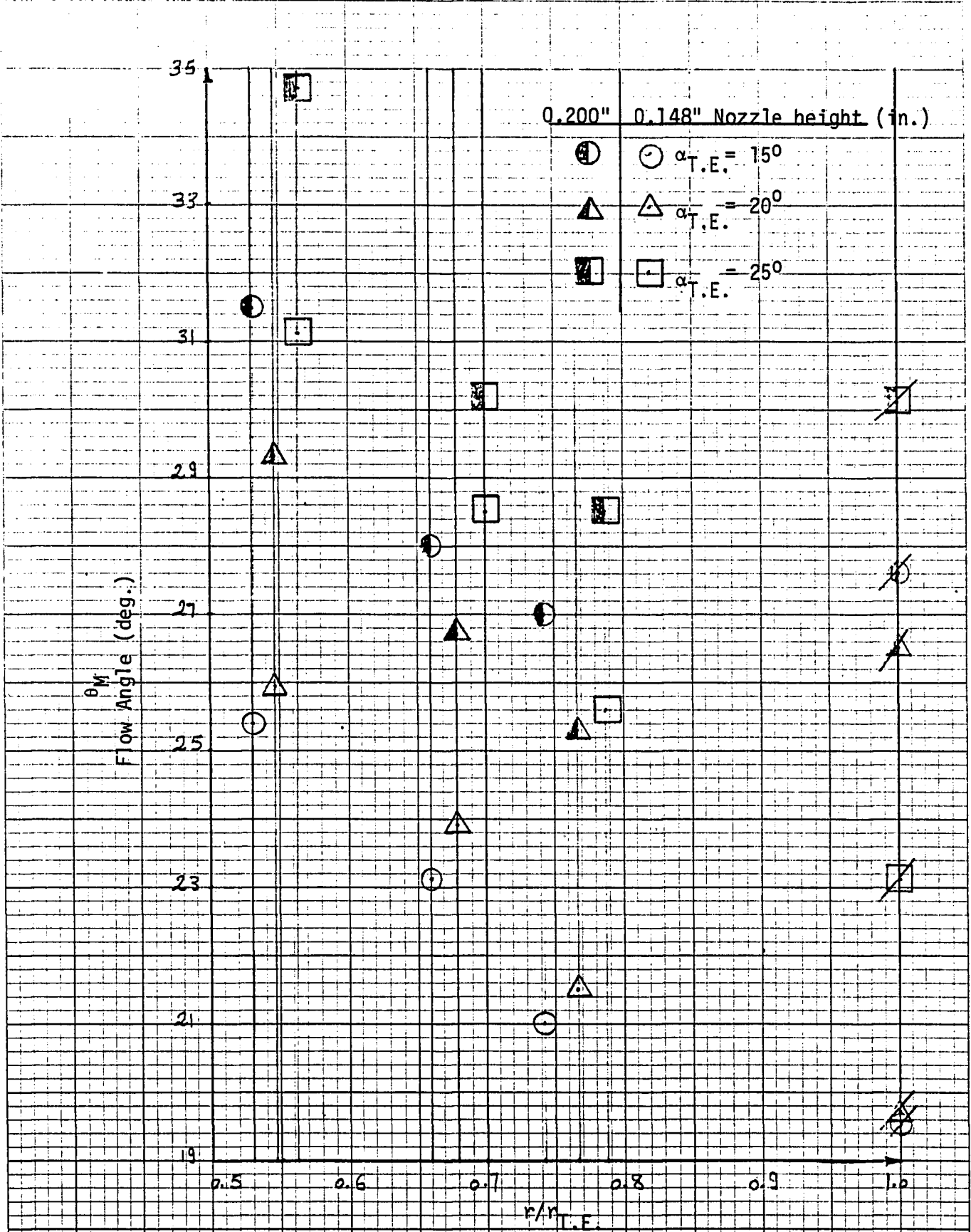


FIG. 63 Variation of the flow angle obtained from mass flow rate calculation with radius ratio for low press. test.

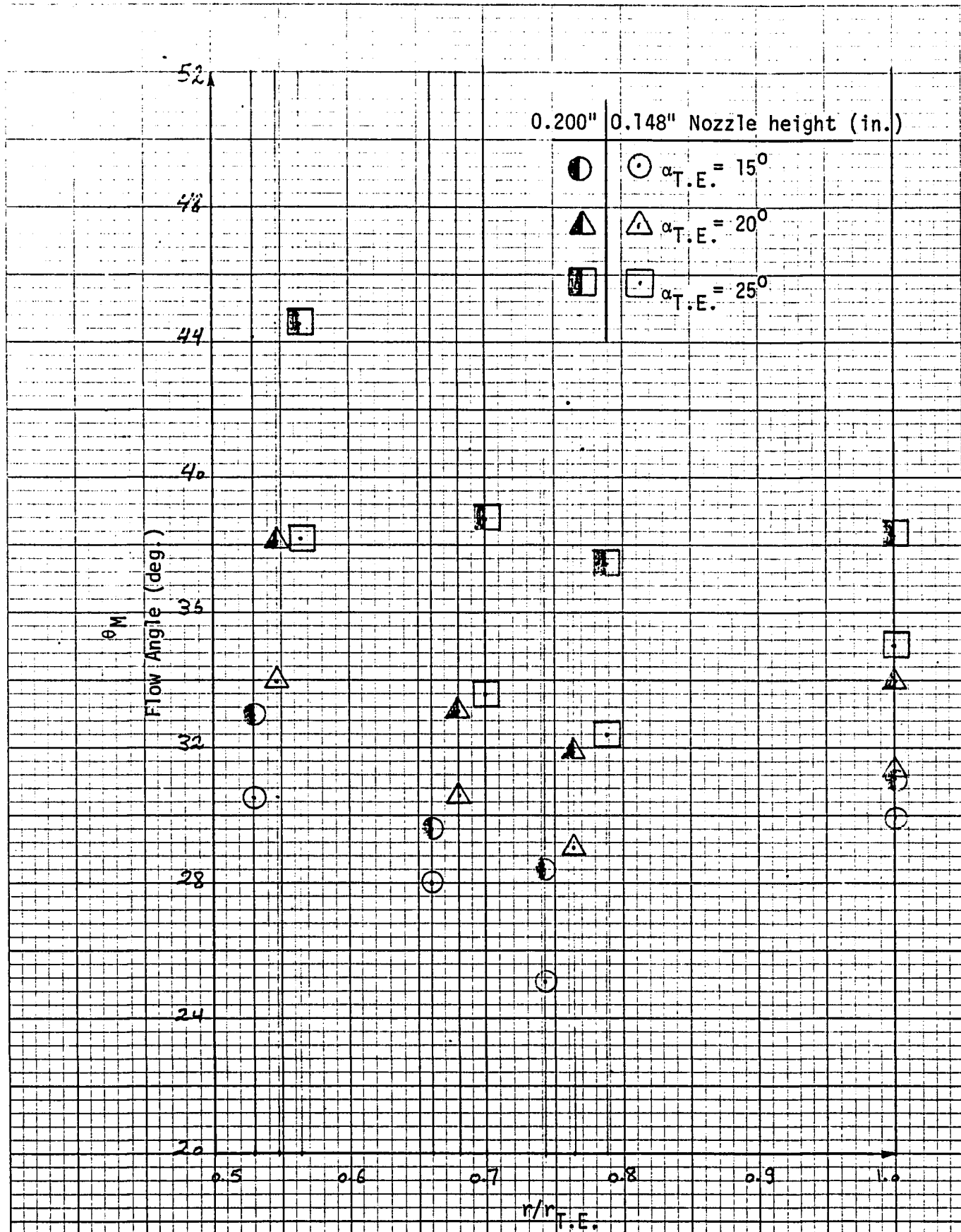


FIG. 64 Variation of the flow angle obtained from mass flow rate calculation with radius ratio for high press. test.

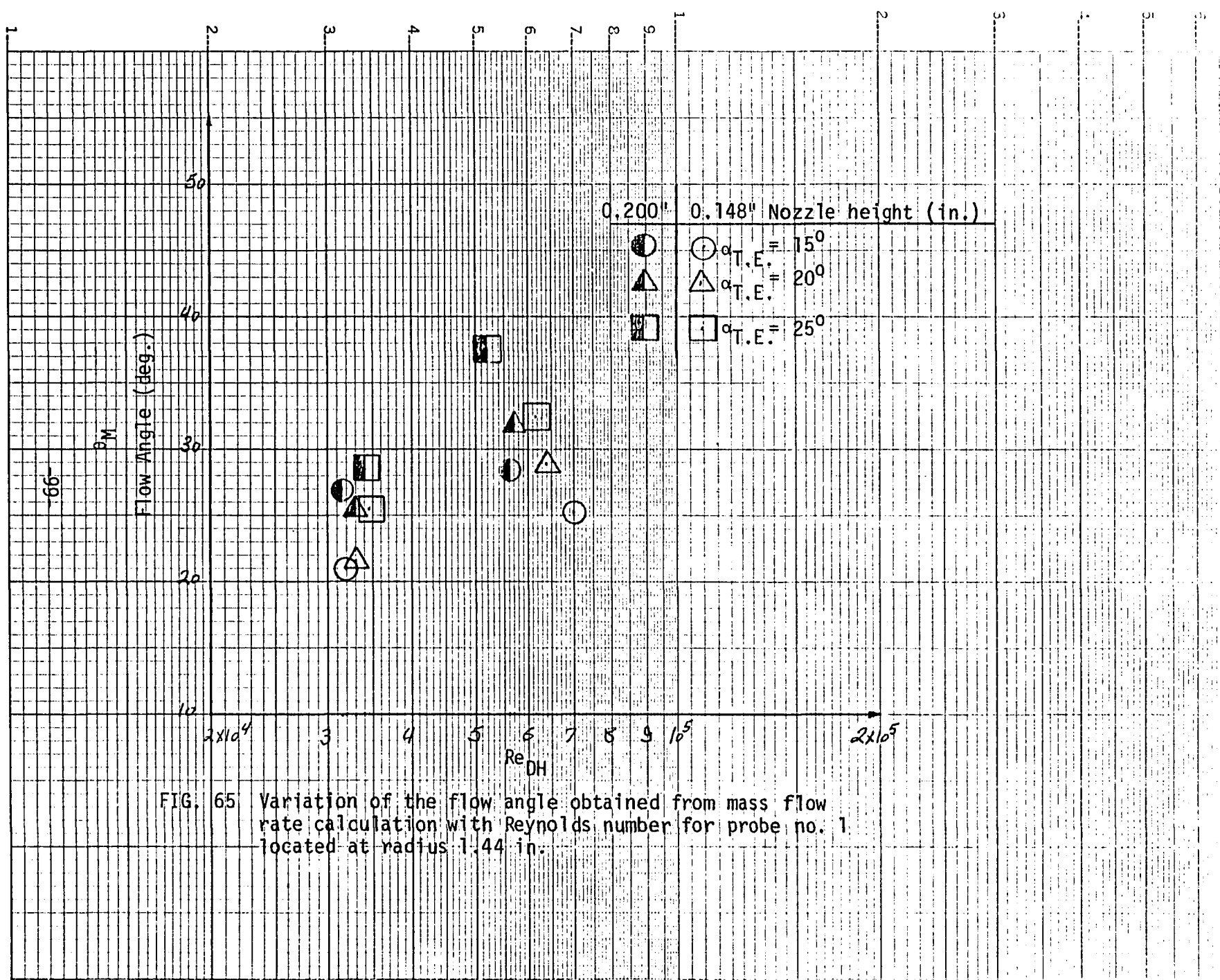


FIG. 65 Variation of the flow angle obtained from mass flow rate calculation with Reynolds number for probe no. 1 located at radius 1.44 in.

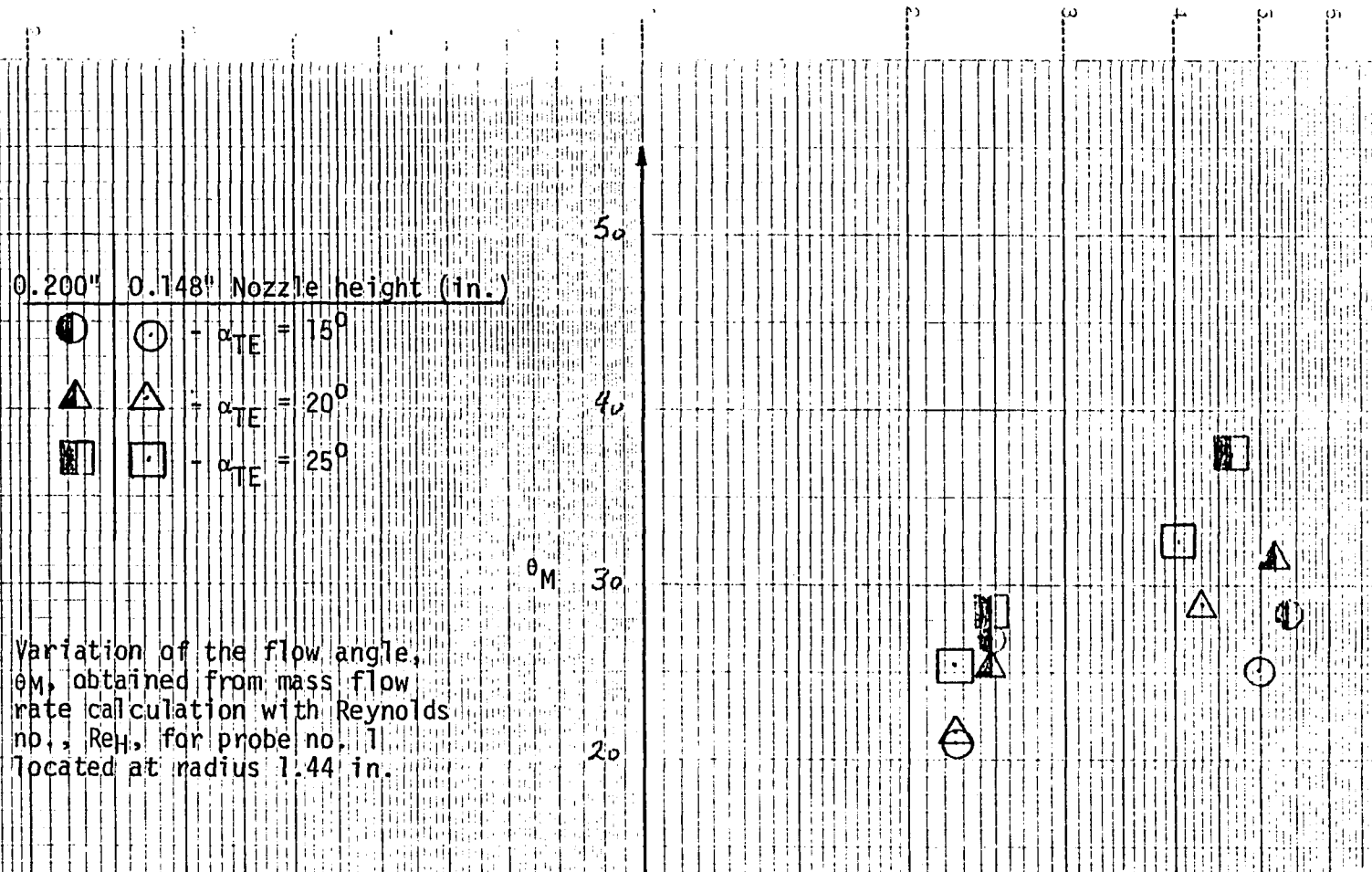


FIG. 66 Variation of the flow angle, θ_M , obtained from mass flow rate calculation with Reynolds no., Re_H , for probe no. 1 located at radius 1.44 in.

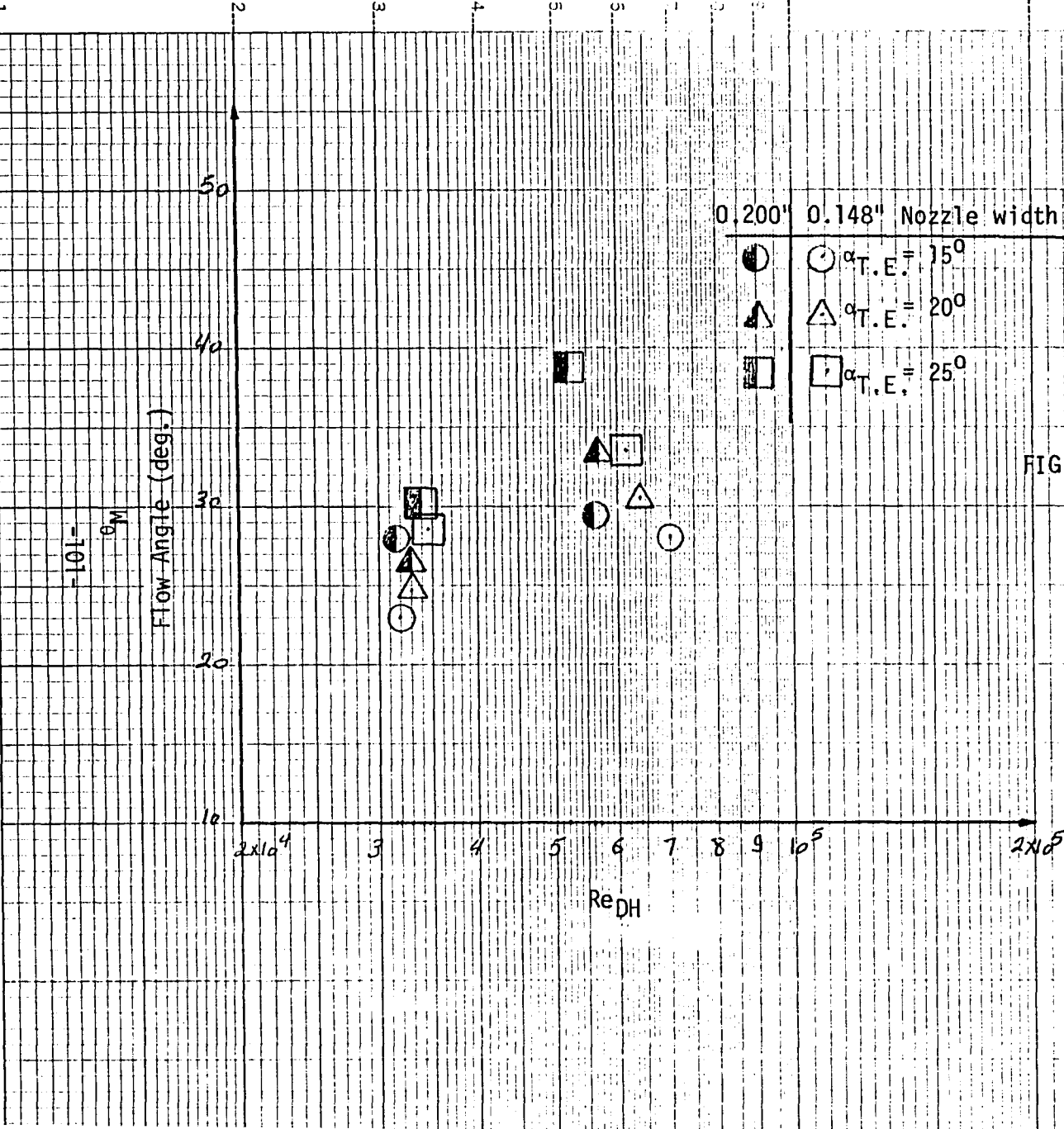


FIG. 67 Variation of the flow angle obtained from mass flow rate calculation with Reynolds number for probe no. 2 located at radius 1.28 in.

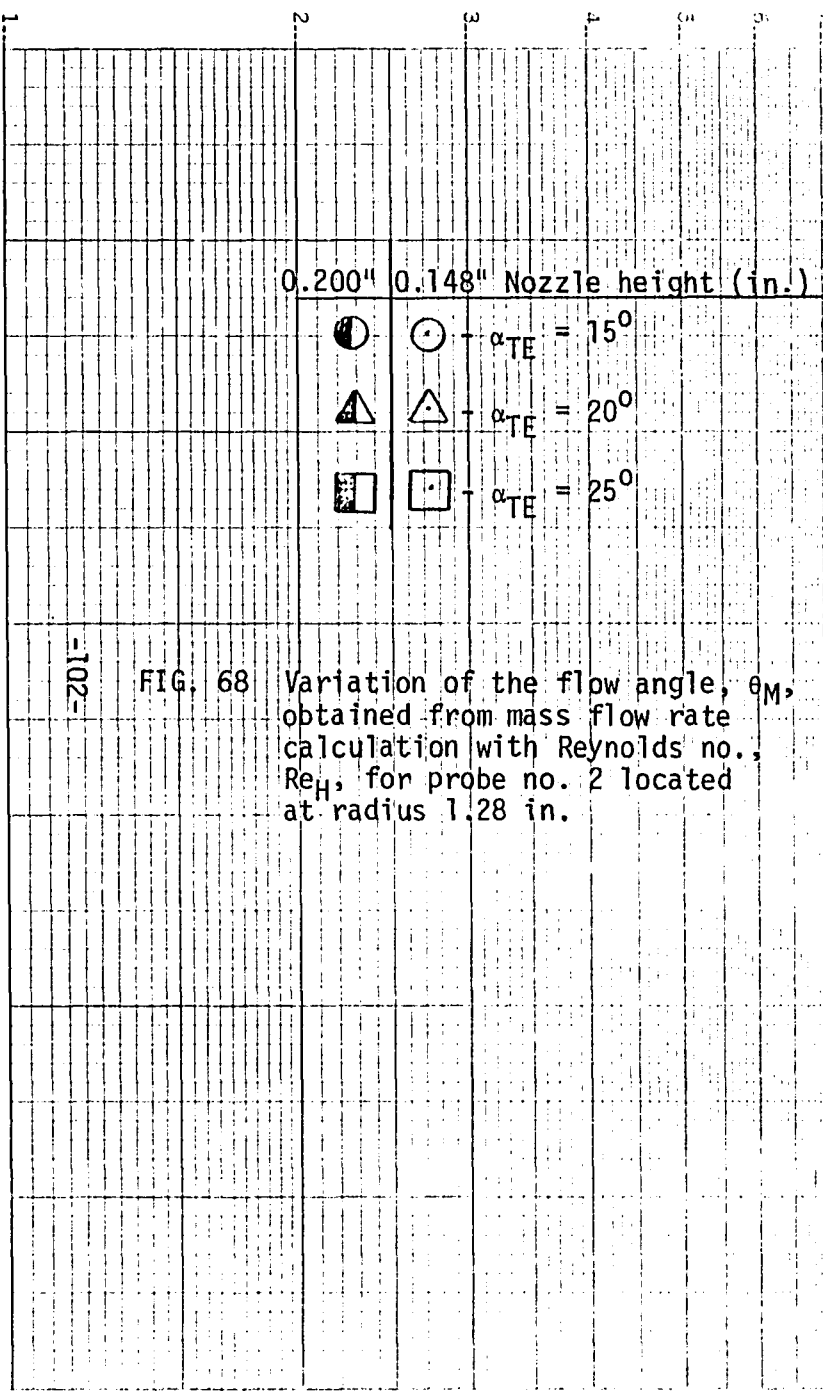
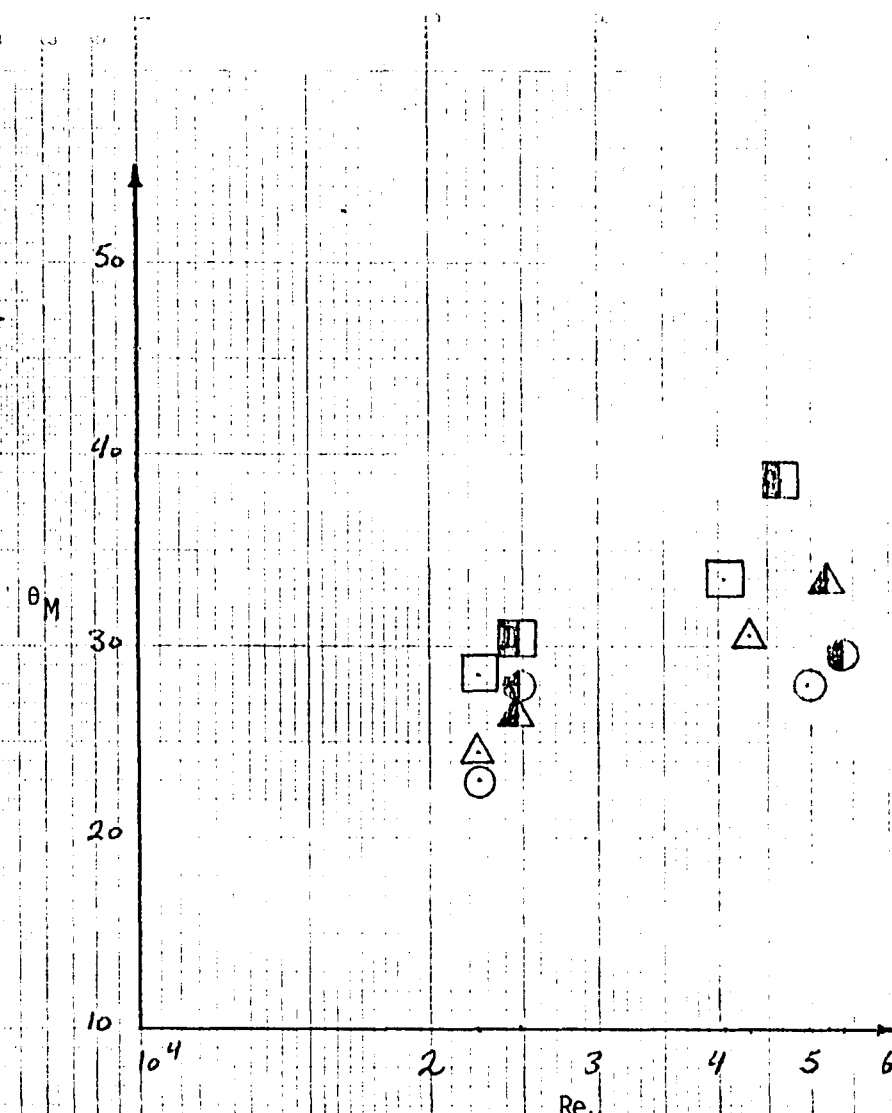


FIG. 68 Variation of the flow angle, θ_M , obtained from mass flow rate calculation with Reynolds no., Re_H , for probe no. 2 located at radius 1.28 in.



1

2

3

4

5

6

7

8

9

10

11

12

13

14

15

16

17

18

19

20

21

22

23

24

25

26

27

28

29

30

31

32

33

34

35

36

50

40

30

20

10

1×10^4

3

4

5

6

7

8

9

10

10^5

2×10^5

Re_{DH}

(deg.)

M_∞

-103-

0.200" 0.148" Nozzle height (in.)

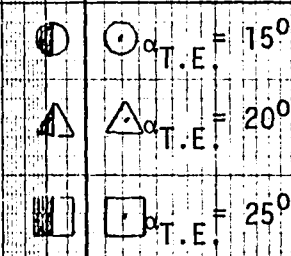


FIG. 69

Variation of the flow angle obtained from mass flow rate calculation with Reynolds number for probe no. 3 located at radius 1.03 in.

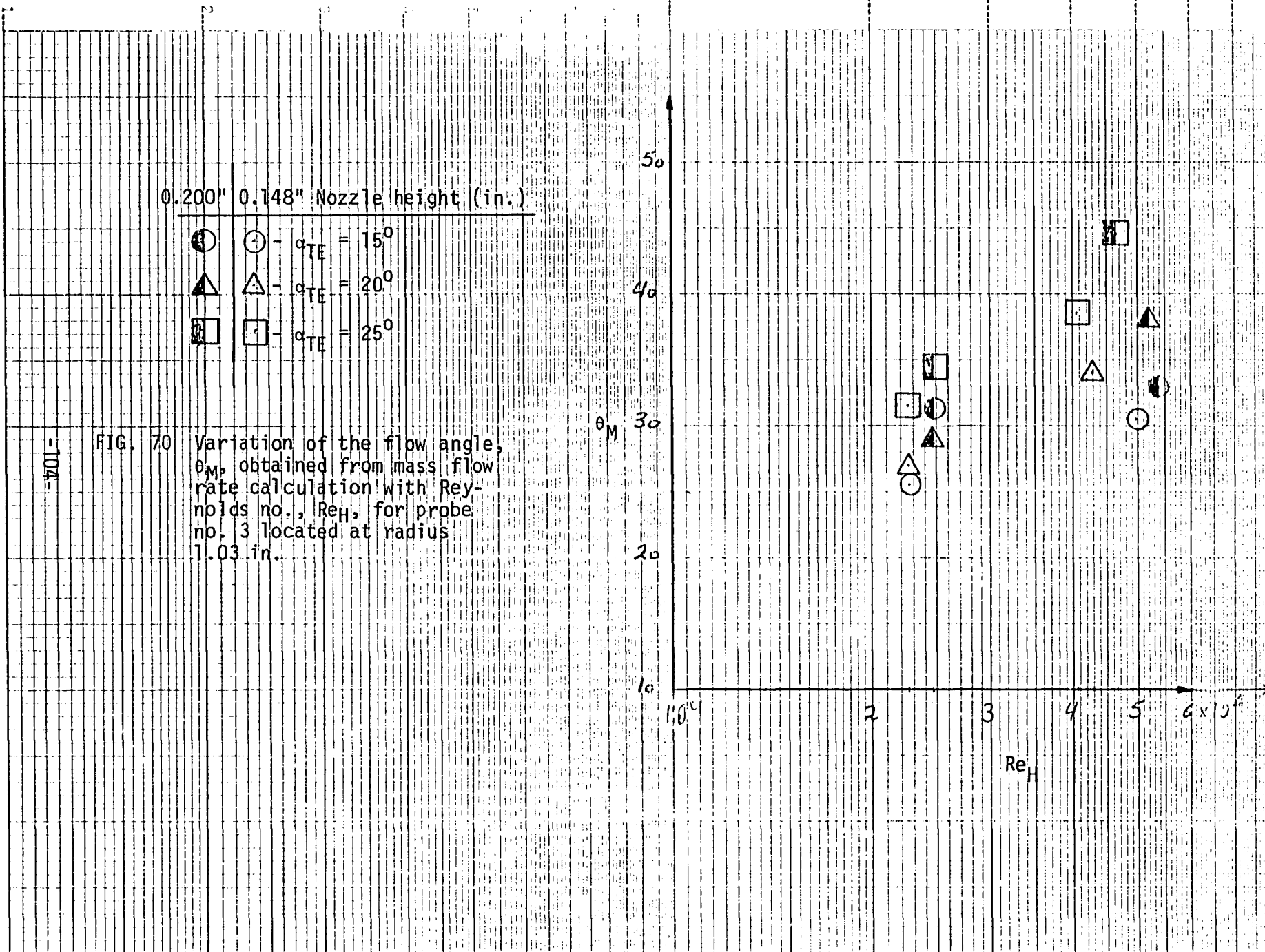


FIG. 70 Variation of the flow angle, θ_M , obtained from mass flow rate calculation with Reynolds no., Re_H , for probe no. 3 located at radius 1.03 in.

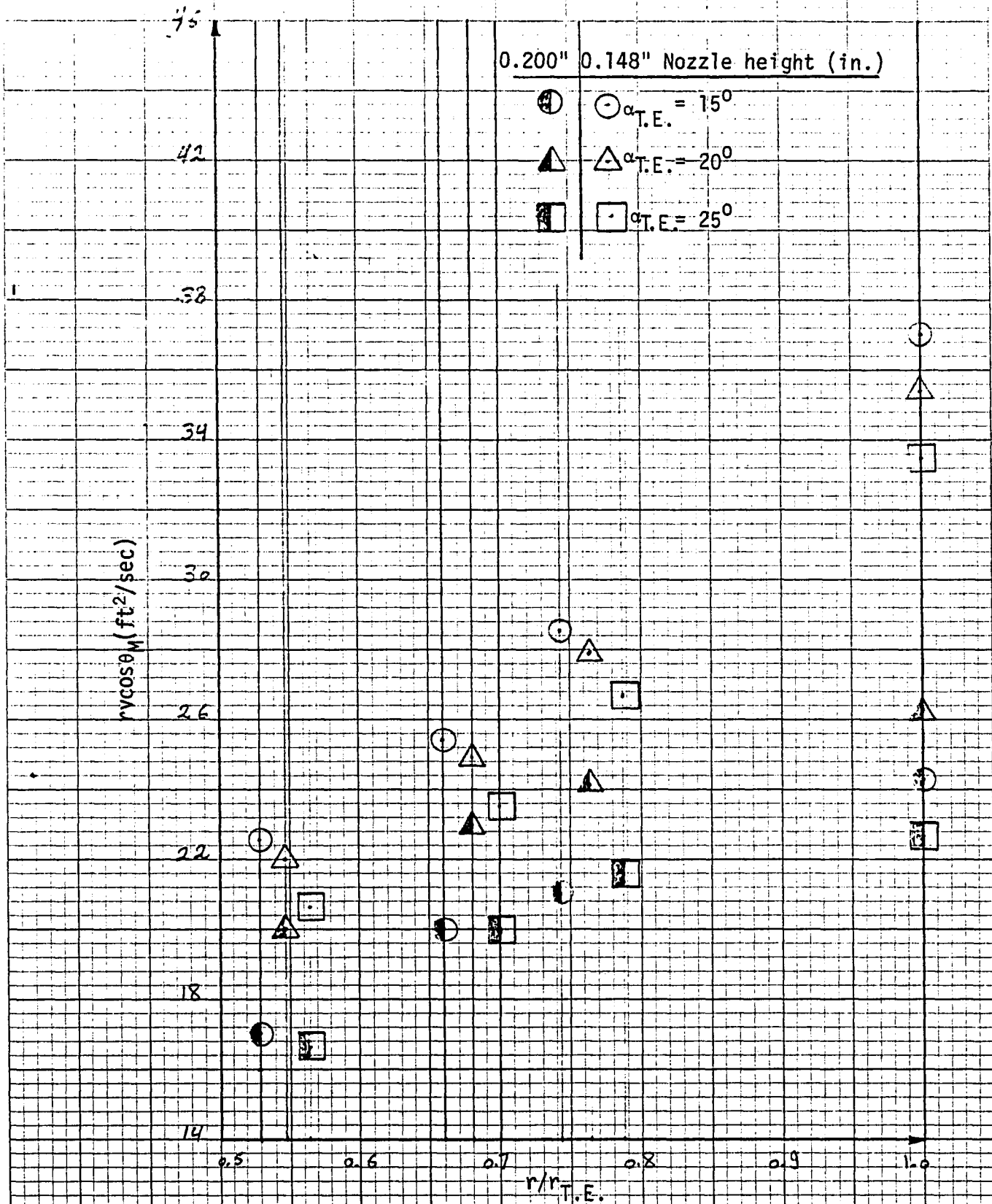


FIG. 71 Variation of the $r/cos \theta_M$ obtained from mass flow rate calculation with radius ratio for low press.

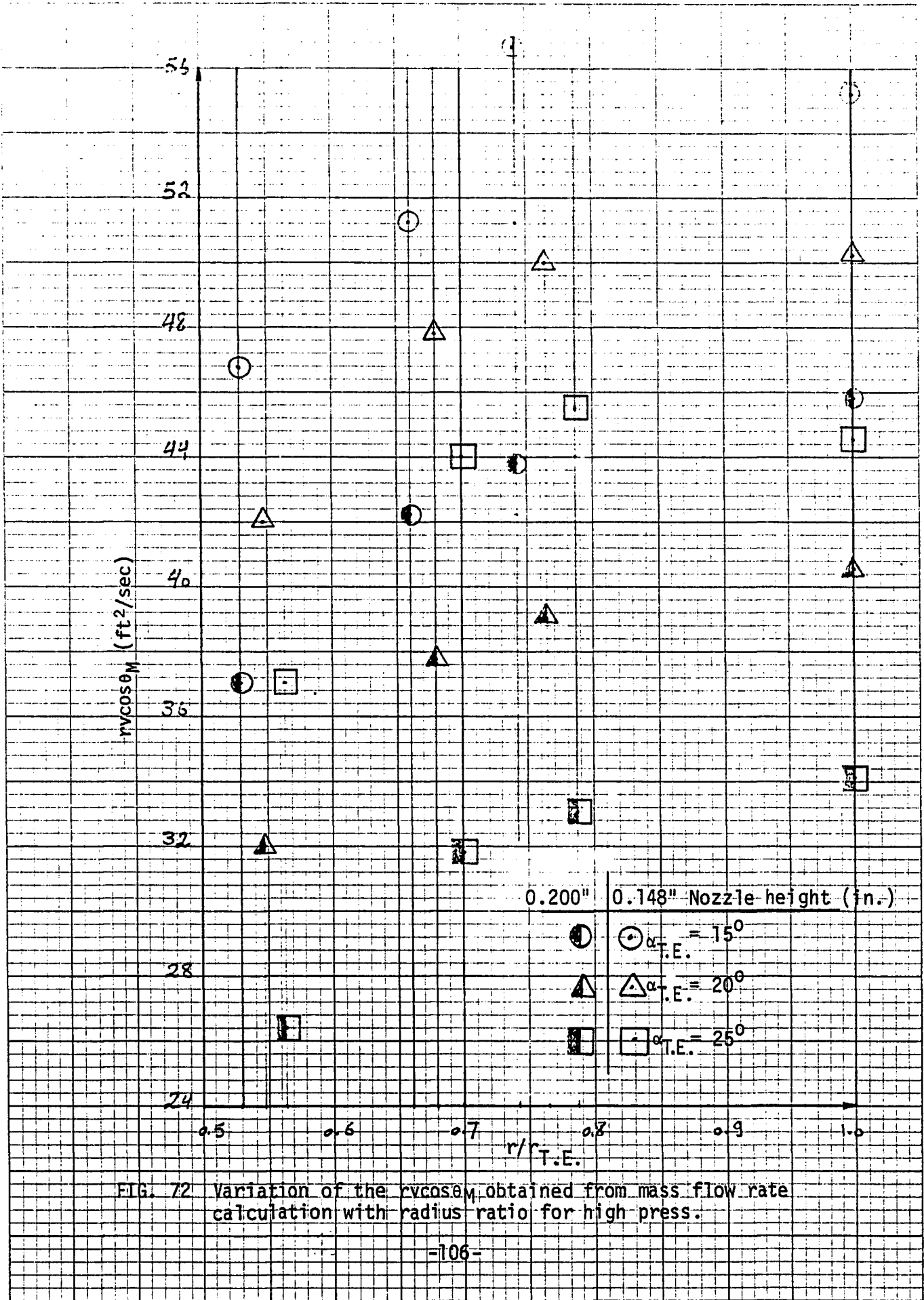
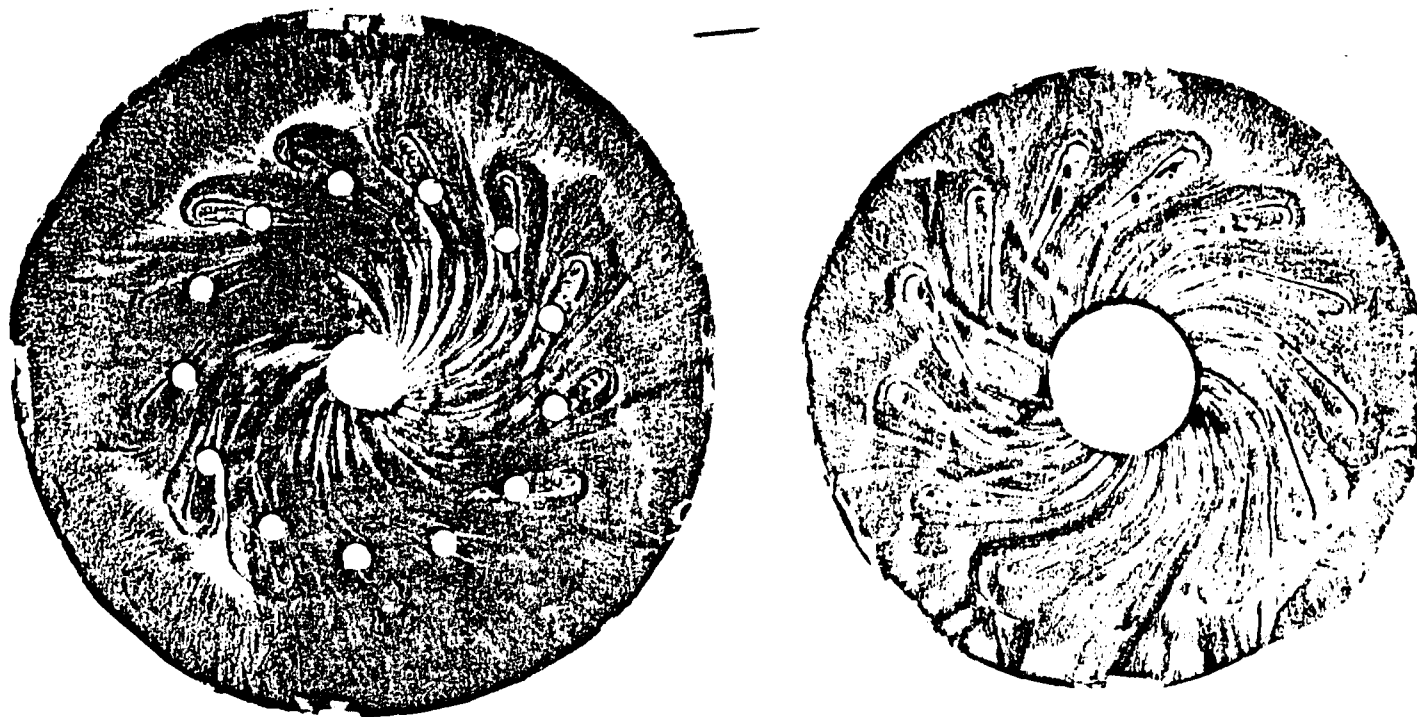


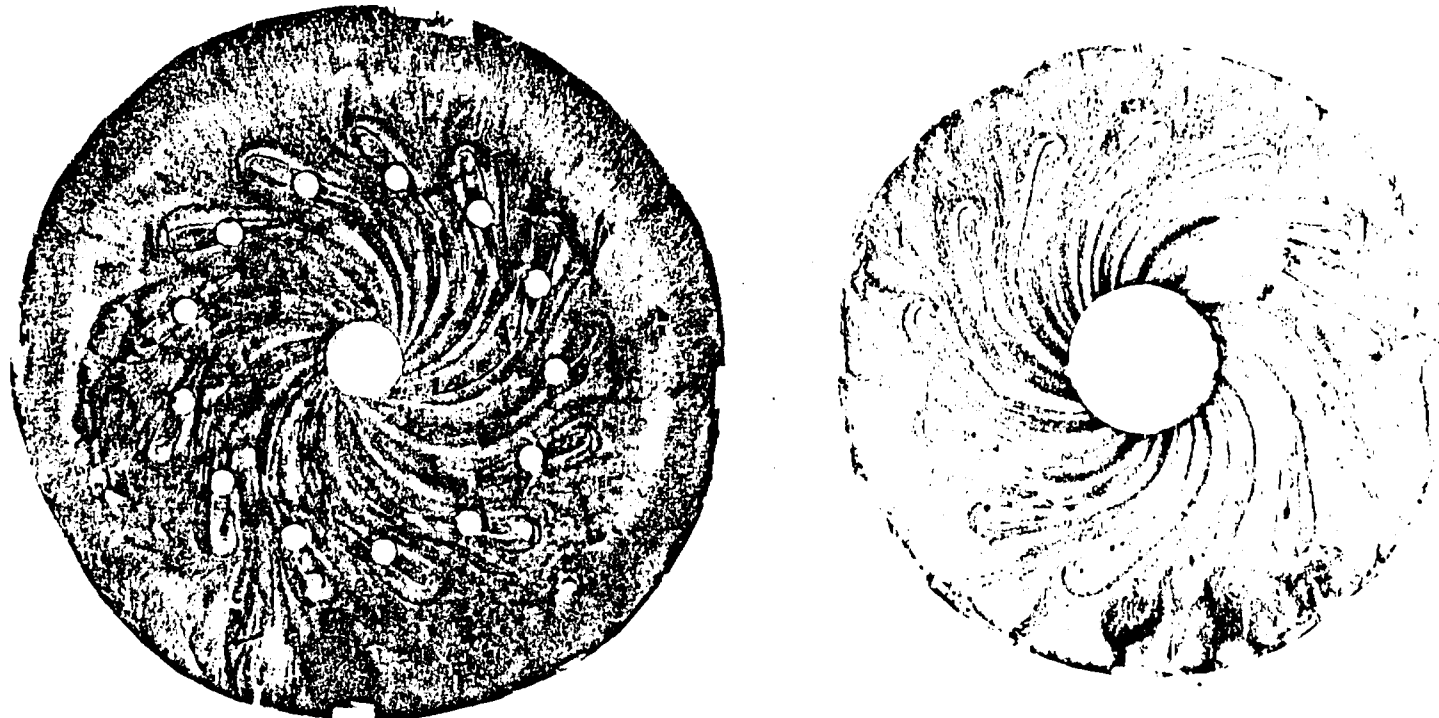
FIG. 72 Variation of the $rvcose_M$ obtained from mass flow rate calculation with radius ratio for high press.



A

B

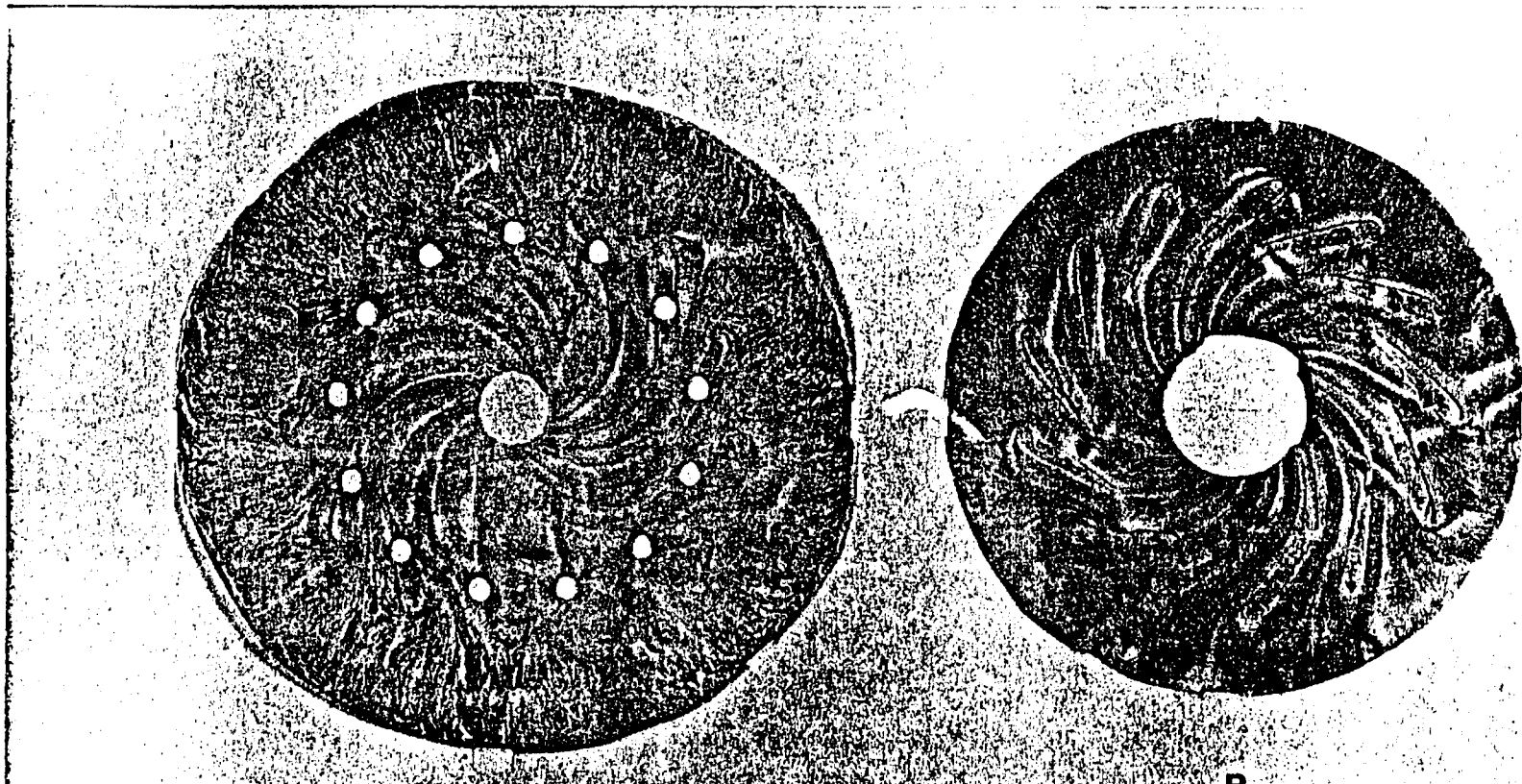
FIGURE 73 .FLOW PATTERNS IN THE TEST RIG VISUALIZED
USING LAMP BLACK AND OIL. NOZZLE ANGLE 25 DEG;
NOZZLE HEIGHT 0.148 IN. PSUPPLY 9.3 IN-HG,
A—PROBE HOLDER
B—SHROUD



A

B

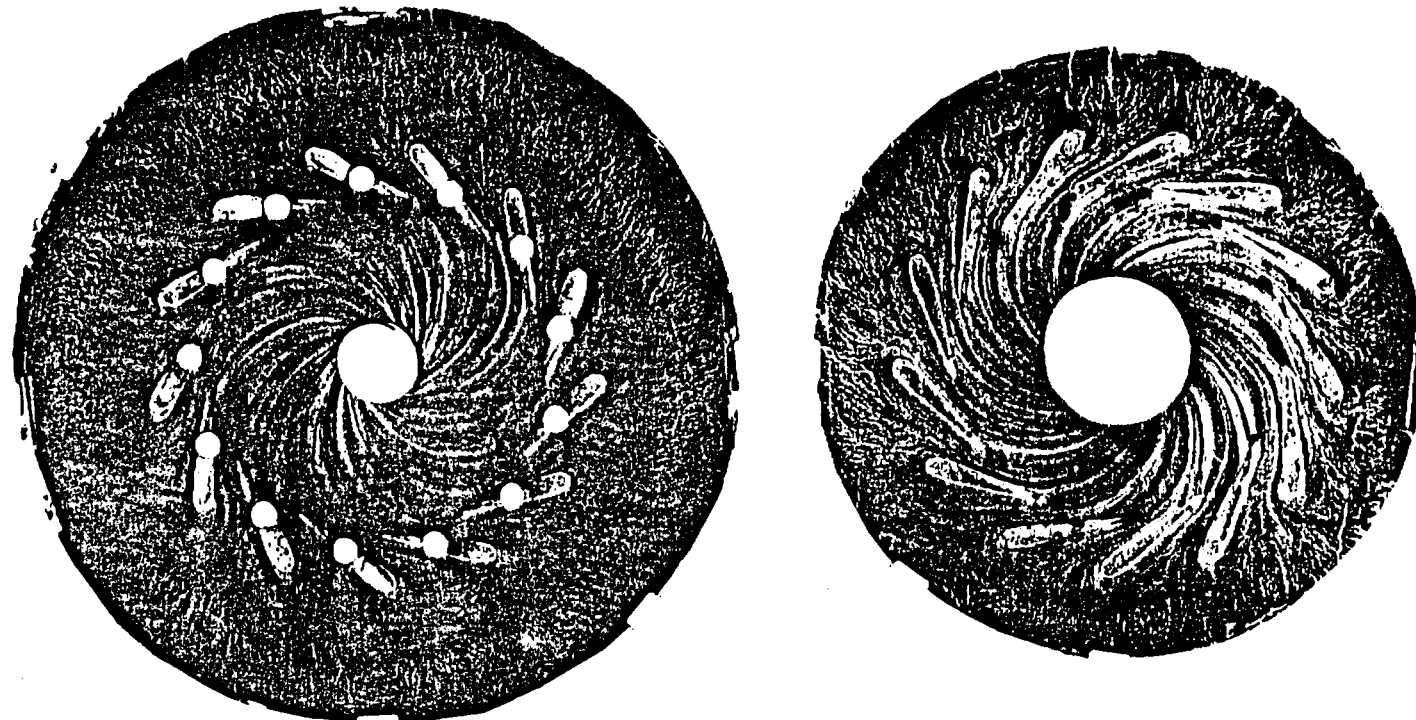
FIGURE 74 .FLOW PATTERNS IN THE TEST RIG VISUALIZED
USING LAMP BLACK AND OIL.NOZZLE ANGLE 20 DEG;
NOZZLE HEIGHT 0.148 IN.PSUPPLY 9.3 IN-HG,
A—PROBE HOLDER
B—SHROUD



A

B

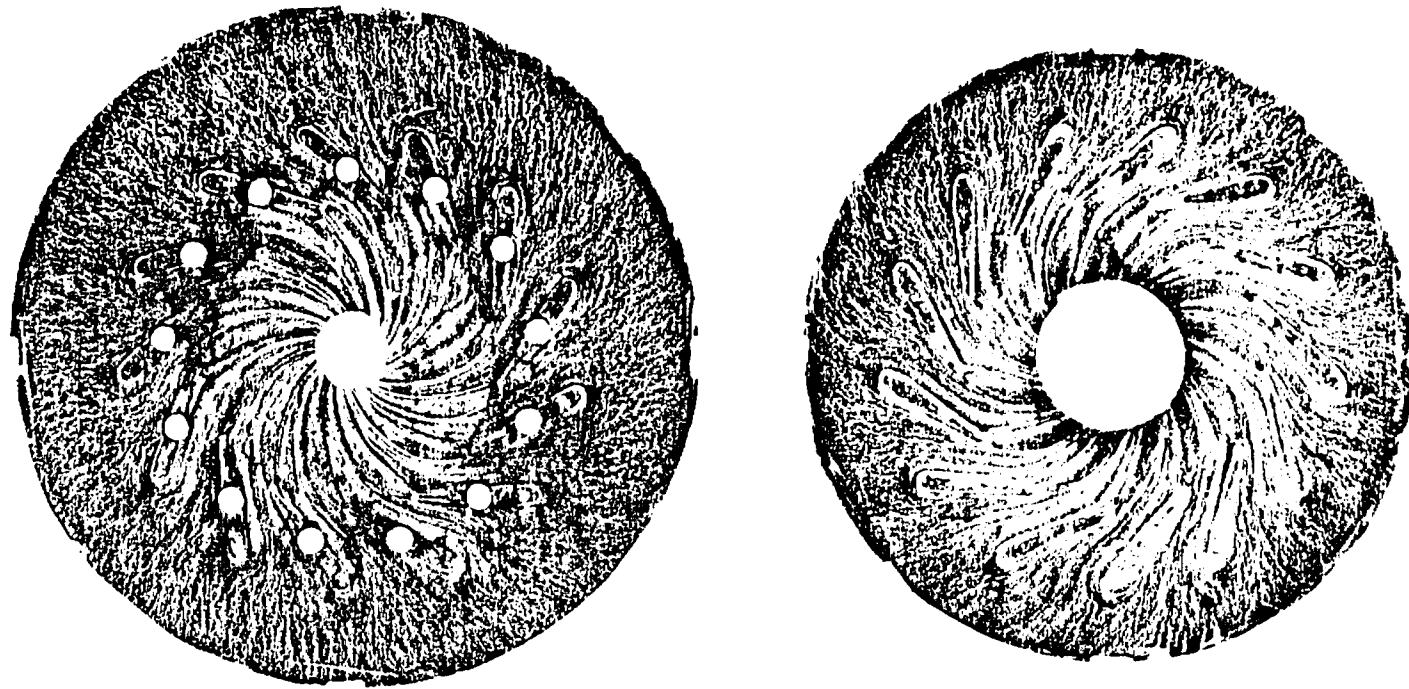
FIGURE 75. FLOW PATTERNS IN THE TEST RIG VISUALIZED
USING LAMP BLACK AND OIL. NOZZLE ANGLE 15 DEG;
NOZZLE HEIGHT 0.148 IN. IPSUPPLY 9.3 IN-HG,
A—PROBE HOLDER
B—SHROUD



A

B

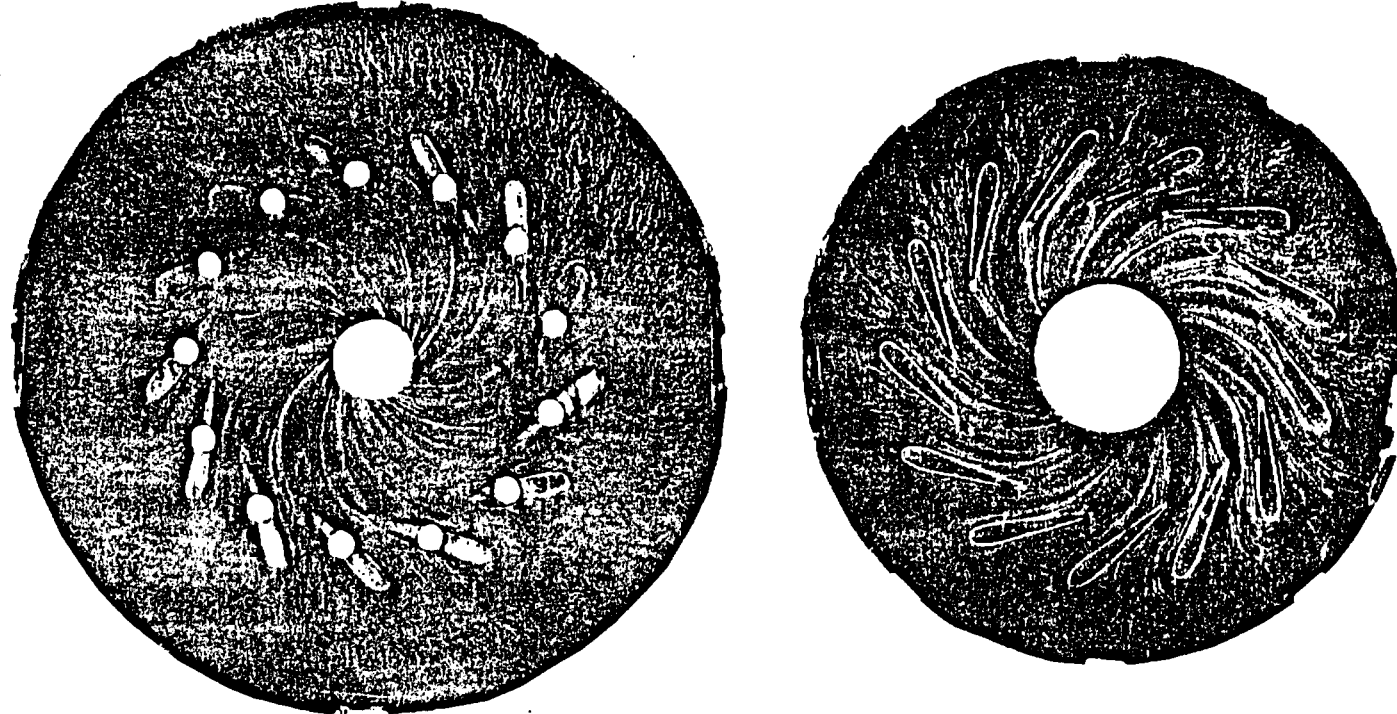
FIGURE 76 . FLOW PATTERNS IN THE TEST RIG VISUALIZED
USING LAMP BLACK AND OIL. NOZZLE ANGLE 10° DEG;
NOZZLE HEIGHT 0.148 IN. PSUPPLY 9.3 IN-HG,
A—PROBE HOLDER
B—SHROUD



A

B

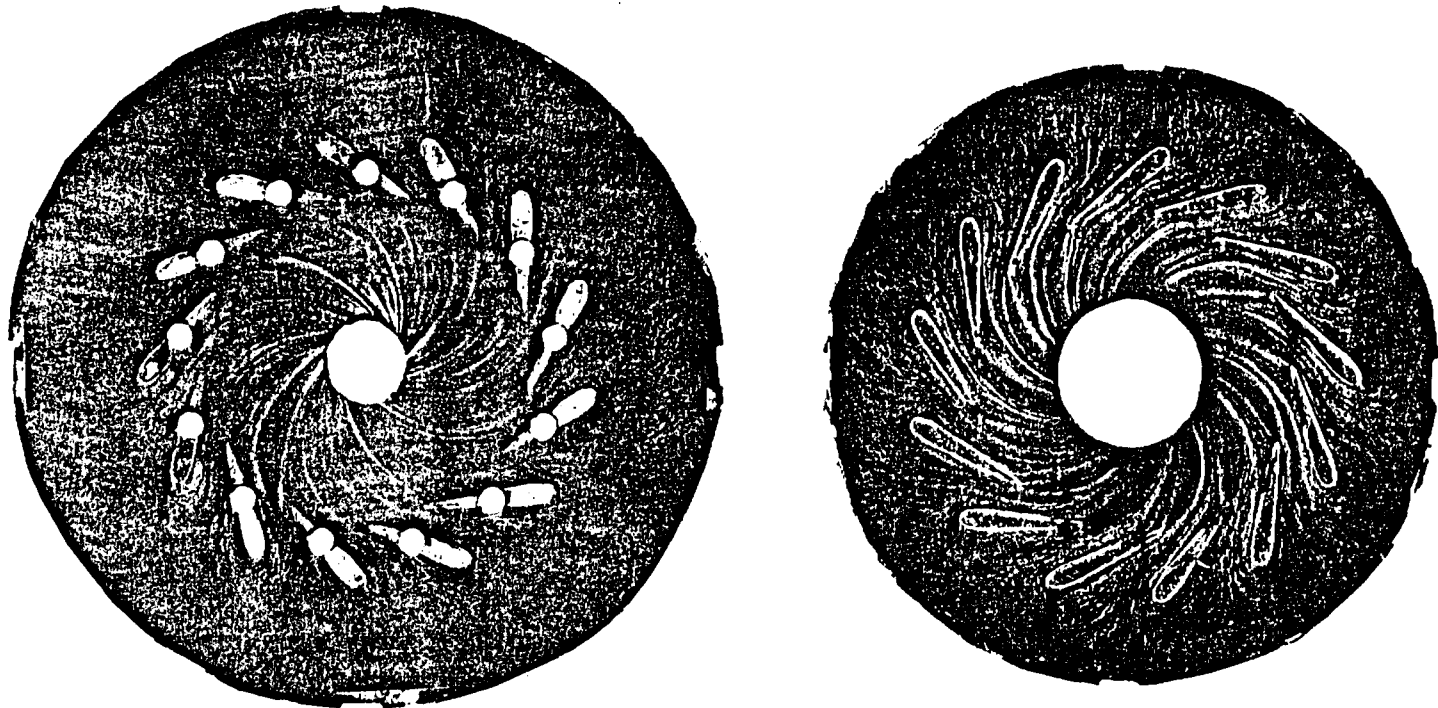
FIGURE 77 .FLOW PATTERNS IN THE TEST RIG WHEN USED
USING LAMP BLACK AND OIL. NOZZLE ANGLE 25 DEG,
NOZZLE HEIGHT 0.20 IN. PSUPPLY 9.3 IN-LB/G.
A--PROBE HOLDER
B--SHROUD



A

B

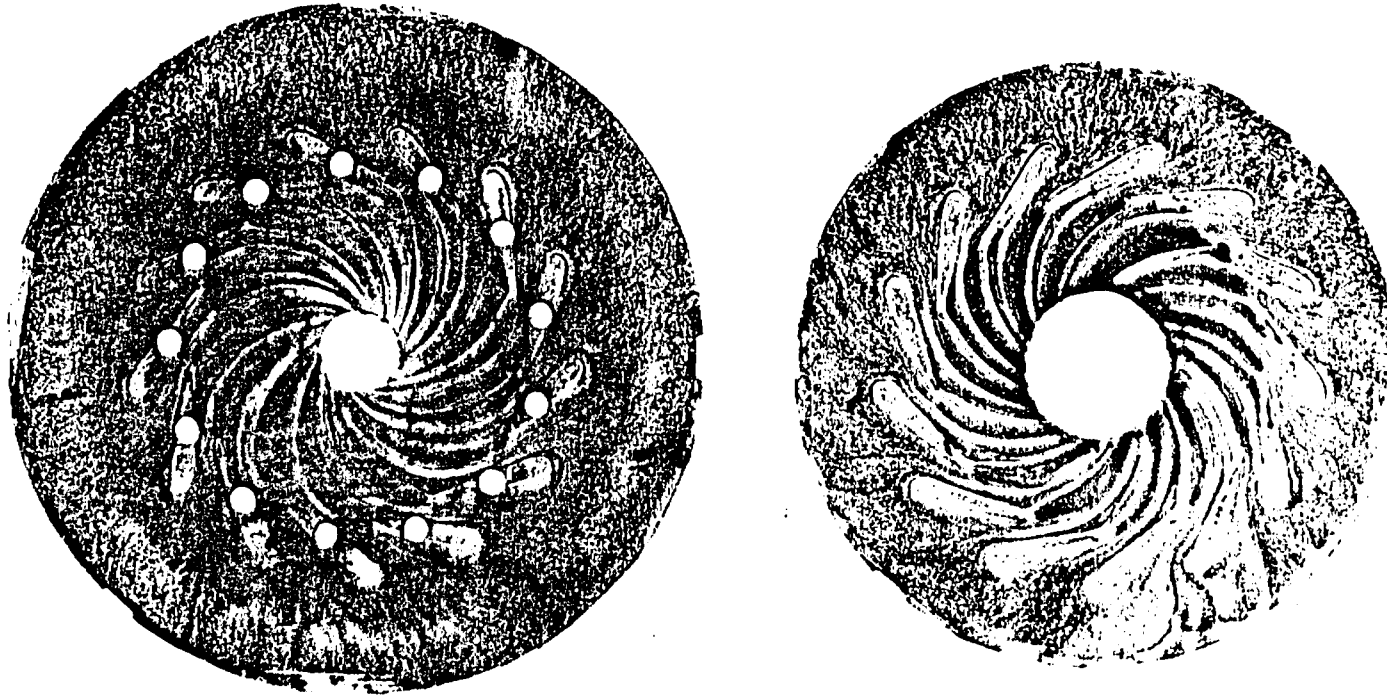
FIGURE 78 .FLOW PATTERNS IN THE TEST RIG VISUALIZED
USING LAMP BLACK AND OIL. NOZZLE ANGLE 20 DEG;
NOZZLE HEIGHT 0.20 IN. PSUPPLY 9.3 IN-HG,
A—PROBE HOLDER
B—SHROUD



A

B

FIGURE 79 .FLOW PATTERNS IN THE TEST RIG VISUALIZED
USING LAMP BLACK AND OIL. NOZZLE ANGLE 15 DEG;
NOZZLE HEIGHT 0.20 IN. PSUPPLY 9.3 IN-HG,
A—PROBE HOLDER
B—SHROUD



A

B

FIGURE 80 .FLOW PATTERNS IN THE TEST RIG VISUALIZED
USING LAMP BLACK AND OIL. NOZZLE ANGLE 10 DEG;
NOZZLE HEIGHT 0.20 IN. PSUPPLY 9.3 IN-HG,
A—PROBE HOLDER
B—SHROUD

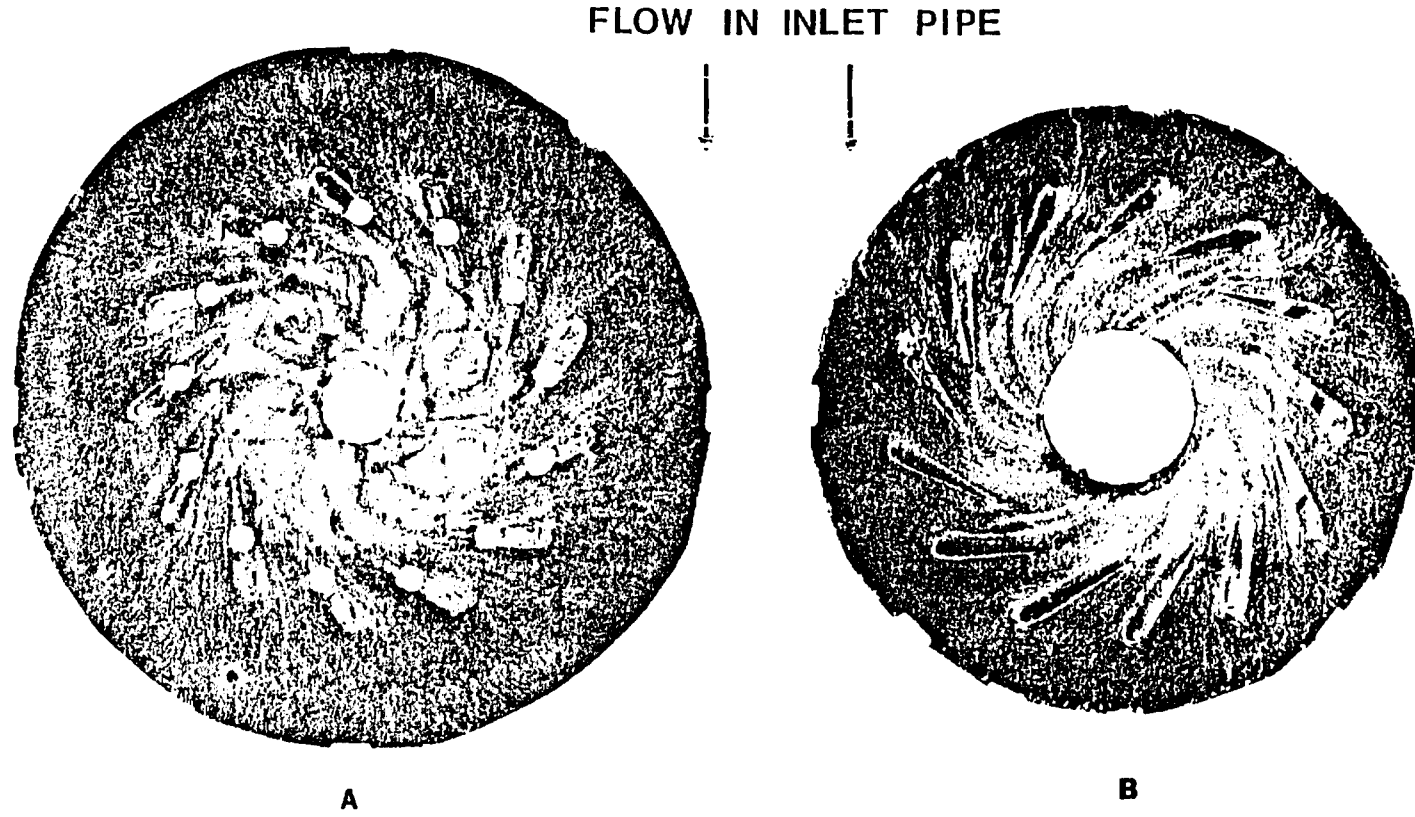


FIGURE 81 .FLOW PATTERNS IN THE TEST RIG VISUALIZED
USING LAMP BLACK AND OIL. NOZZLE ANGLE 25 DEG;
NOZZLE HEIGHT 0.148 IN. PSUPPLY 20 IN-HG,
A—PROBE HOLDER
B—SHROUD

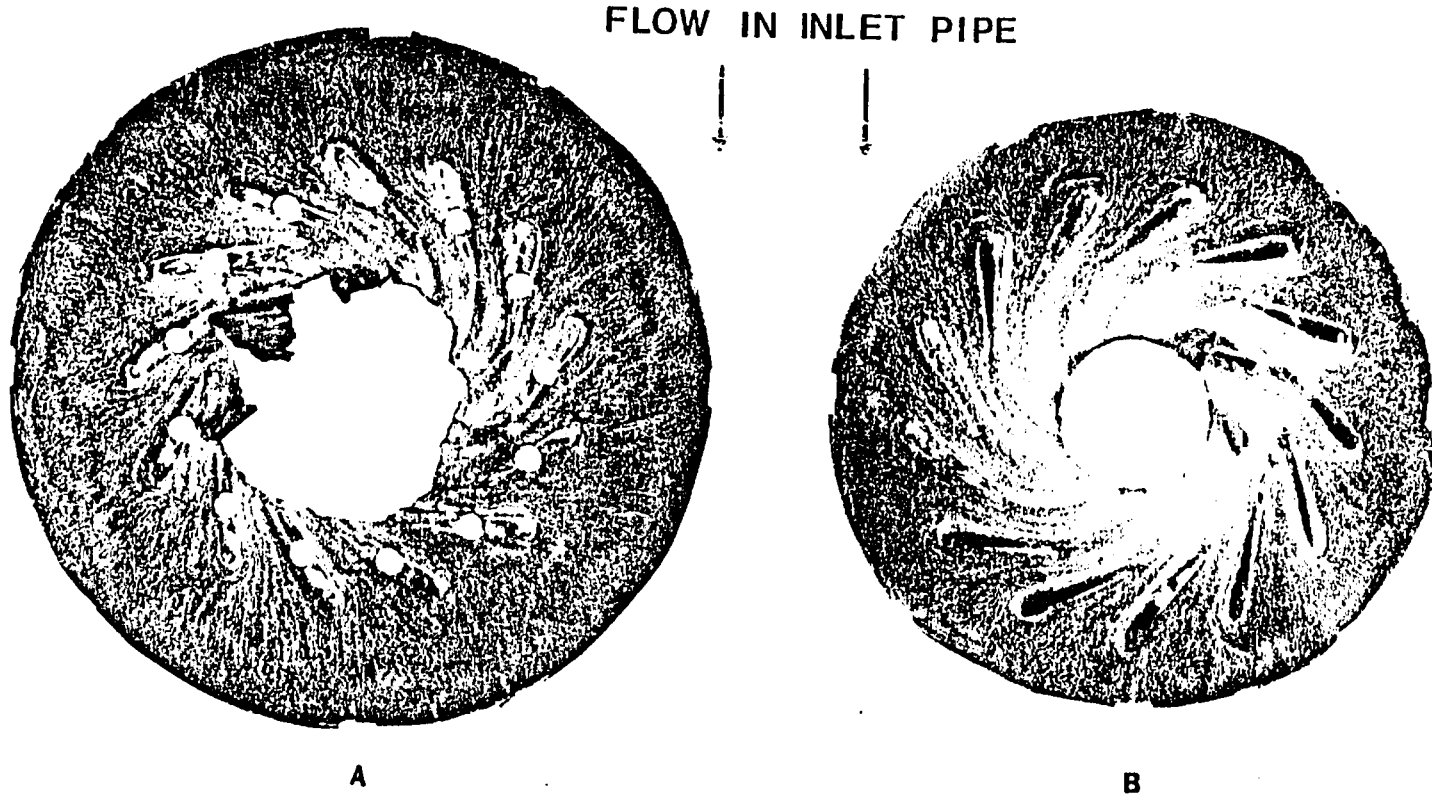


FIGURE 82 .FLOW PATTERNS IN THE TEST RIG VISUALIZED
USING LAMP BLACK AND OIL. NOZZLE ANGLE 15 DEG;
NOZZLE HEIGHT 0.148 IN. PSUPPLY 20 IN-HG,
A—PROBE HOLDER
B—SHROUD

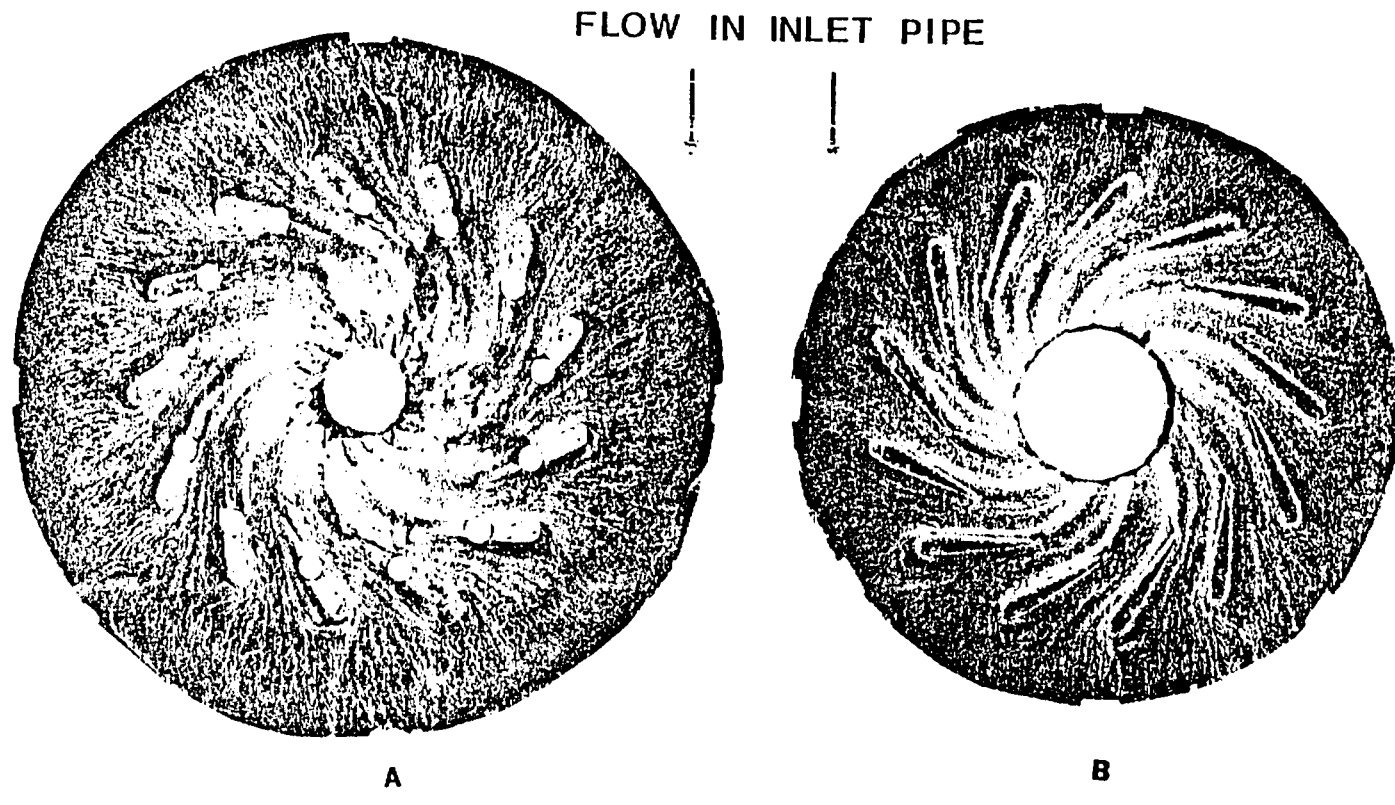


FIGURE 83 .FLOW PATTERNS IN THE TEST RIG VISUALIZED
USING LAMP BLACK AND OIL. NOZZLE ANGLE 25 DEG;
NOZZLE HEIGHT 0.148 IN. PSUPPLY 20 IN-HG,
A—PROBE HOLDER
B—SHROUD

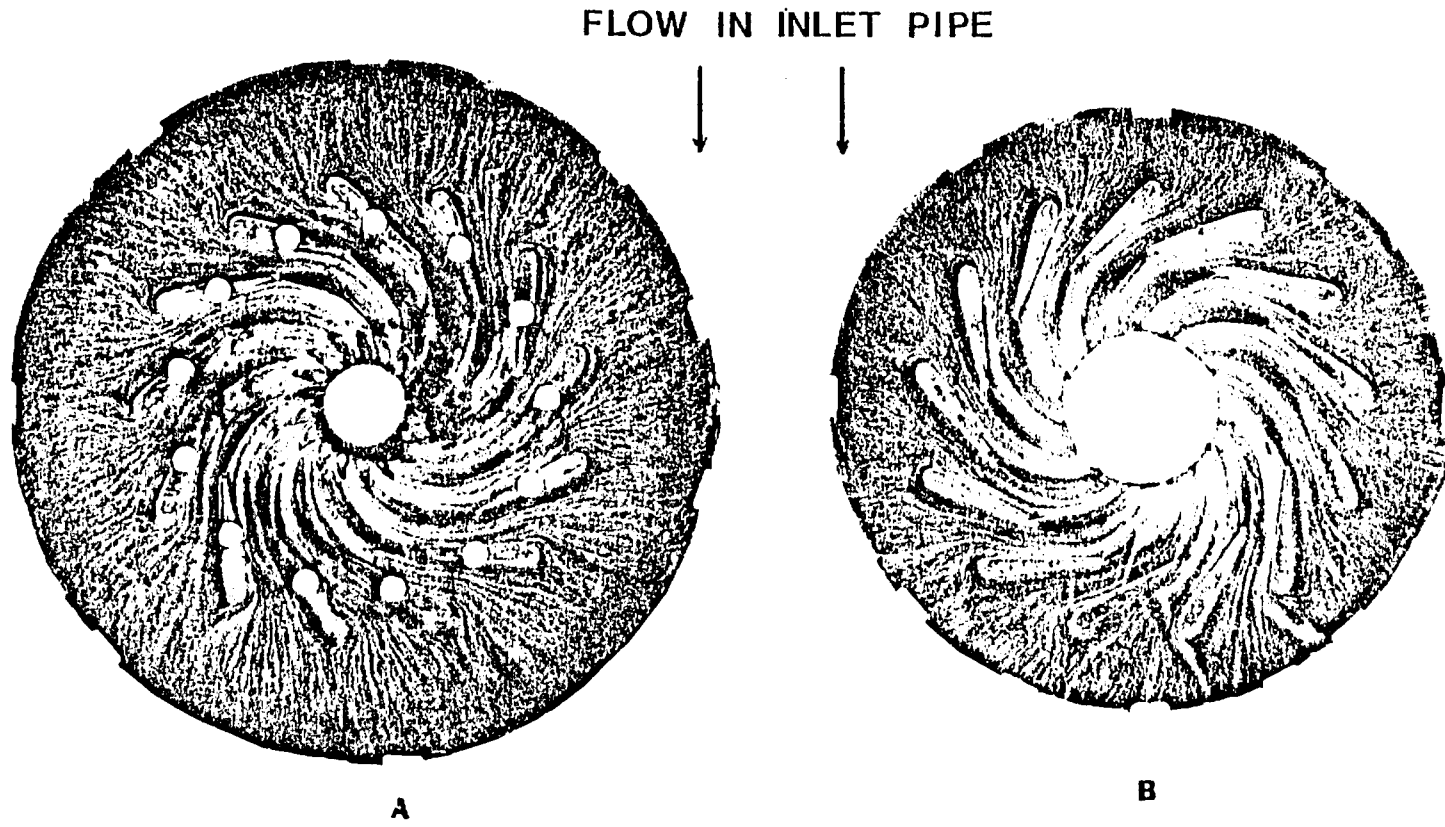


FIGURE 84 .FLOW PATTERNS IN THE TEST RIG VISUALIZED
USING LAMP BLACK AND OIL. NOZZLE ANGLE 15 DEG;
NOZZLE HEIGHT 0.148 IN. PSUPPLY 20 IN-HG,
A—PROBE HOLDER
B—SHROUD

TABLE 1
VARIATION OF TRAILING EDGE ANGLES, α_{TE} , WITH PROTRACTOR ANGLE ON THE STEEL TEST RIG

PROTRACTOR ANGLE, DEG.	0.0°	+5.0°	+10.0°	+15.0°	-5.0°	-10.0°	-15.0°
VANE NO.	α_{TE} (Deg)						
1	14.0	10.0	4.0	0.0	16.5	20.0	24.0
2	13.5	10.0	5.0	0.5	16.5	20.5	25.0
3	14.5	10.0	4.0	0.0	15.0	20.0	25.0
4	14.0	9.9	3.0	0.0	15.0	20.5	25.0
5	13.0	10.0	5.0	1.0	15.0	21.0	25.0
6	13.0	10.0	5.0	0.0	15.0	21.0	25.0
7	15.0	10.0	5.0	1.0	16.0	21.0	25.0
8	14.0	10.0	5.5	1.5	16.0	21.5	25.0
9	15.0	10.5	6.0	2.0	17.0	21.5	26.0
10	15.0	11.0	7.0	2.0	17.0	22.0	26.0
11	15.0	10.5	6.0	2.0	16.5	23.0	26.5
12	16.0	11.0	5.0	2.0	17.0	23.0	26.5
13	16.0	10.0	5.0	1.0	17.0	22.0	25.0
AVERAGE	13.46	10.22	5.04	1.0	16.11	21.31	25.31

TABLE 2
VARIATION OF NOZZLE THROAT WIDTHS WITH PROTRACTOR ANGLE ON THE TEST RIG

NOZZLE #	1 THROAT (mm)	2 THROAT (mm)	3 THROAT (mm)	4 THROAT (mm)	5 THROAT (mm)	6 THROAT (mm)	7 THROAT (mm)	PROTRACTOR ANGLE (Deg.)
1	13.20	12.31	11.14	9.74	8.12	6.83	5.30	For Column #1 = -20. ^o
2	12.80	11.91	10.82	9.36	7.84	6.54	4.99	For Column #2 = -15. ^o
3	12.82	12.07	10.90	9.47	7.91	6.57	5.04	For Column #3 = -10. ^o
4	13.02	12.26	11.07	9.70	8.12	6.81	5.28	For Column #4 = -5. ^o
5	12.81	12.21	11.01	9.61	8.05	6.81	5.28	For Column #5 = 0. ^o
6	12.98	12.37	11.16	9.75	8.24	6.97	5.40	For Column #6 = +5. ^o
7	12.89	12.34	11.16	9.75	8.20	6.86	5.33	For Column #7 = +10. ^o
8	12.94	12.34	11.21	9.84	8.26	7.03	5.53	
9	12.93	12.34	11.14	9.40	8.17	6.93	5.38	
10	12.94	12.29	11.14	9.70	8.18	6.87	5.38	
11	13.13	12.41	11.23	9.80	8.20	6.93	5.38	
12	13.12	12.33	11.23	9.84	8.30	6.98	5.45	
13	13.23	12.38	11.22	9.83	8.22	6.98	5.40	
AVERAGE	12.99	12.27	11.11	9.68	8.14	6.85	5.32	

TABLE 3

The optical test rig results for nozzle trailing edge angle of 8°.

P_T (PSIA)	P_1 (PSIA)	P_2 (PSIA)	P_3 (PSIA)	P_4 (PSIA)	M_1 ---	M_2 ---	M_3 ---	M_4 ---
21.64	19.55	19.06	18.47	18.27	0.380	0.430	0.480	0.495
29.14	24.54	23.45	22.35	21.91	0.500	0.565	0.630	0.652
35.14	29.52	27.80	25.94	25.20	0.505	0.590	0.670	0.715
41.64	34.38	32.12	29.62	28.44	0.530	0.620	0.715	0.760
47.64	39.39	36.50	33.50	31.83	0.527	0.625	0.730	0.781

TABLE 4

The optical test rig results for nozzle trailing edge angle of 18°.

P_T (PSIA)	P_1 (PSIA)	P_2 (PSIA)	P_3 (PSIA)	P_4 (PSIA)	M_1 ---	M_2 ---	M_3 ---	M_4 ---
22.64	19.65	19.06	18.47	18.32	0.460	0.505	0.550	0.555
28.64	24.51	23.43	22.25	21.61	0.475	0.545	0.613	0.650
34.64	29.42	27.80	25.98	24.81	0.570	0.570	0.655	0.705
40.64	34.29	32.22	29.82	28.15	0.590	0.590	0.680	0.745
46.64	39.30	36.90	33.84	31.39	0.592	0.592	0.690	0.774

TABLE 5

The optical test rig results for nozzle trailing edge angle 28°.

P_T (PSIA)	P_1 (PSIA)	P_2 (PSIA)	P_3 . (PSIA)	P_4 (PSIA)	M_1 ---	M_2 ---	M_3 ---	M_4 ---
18.32	19.60	19.1	18.59	18.42	0.420	0.467	0.508	0.520
21.51	24.56	23.43	22.40	21.91	0.468	0.550	0.601	0.630
24.71	29.52	27.8	26.10	25.05	0.503	0.590	0.668	0.711
27.65	34.43	32.35	30.01	28.15	0.510	0.598	0.690	0.748
29.37	37.23	34.78	32.08	29.57	0.515	0.660	0.705	0.790

References:

1. Balje, O.E., "A Contribution to the Problem of Designing Radial Turbomachines", ASME Trans., Vol. 74, May 1952, pp. 451-472.
2. Mizumachi, N., "A Study of Radial Gas Turbine", the University of Michigan Translation IP-476, 1960.
3. Knoernschild, E.M., "The Radial Turbine for Low Specific Speeds and Low Velocity Factors", ASME Trans., Journal of Engineering for Power, Vol. 83A, Jan. 1961, pp. 1-8.
4. Hiett, G.F. and Johnston, I.H., "Experimental Concerning the Aerodynamic Performance of Inward-Flow Radial Turbines", Proceedings, Inst. of Mechanical Engineer, Vol. 178, Part 3I, 1963, pp. 28-42.
5. Rodgers, C., "Efficiency and Performance Characteristics of Radial Turbines", SAE Paper No. 660754, 1966.
6. Benson, R.S. and Jackson, D.C., "Flow Studies in Radial Inflow-Turbine Interspace Between Nozzles and Rotors", Inst. of Mechanical Engineer. Conference on Heat and Fluid Flow in Steam and Gas Turbine Plant, 1973, pp. 213-223.
7. Khalil, I.M., Tabakoff, W. and Hamed, A., "Losses in Radial Inflow Turbines", ASME Paper 76-FE-9, 1976.
8. Fairbanks, F., "The Determination of Deviation Angles at Exit From the Nozzle of an Inward Flow Radial Turbine", ASME Paper 80-GT-147, 1980.
9. Dixon, S.L., "Fluid Mechanics, Thermodynamics of Turbomachinery", Third Edition 1978, Ch. 8, pp. 221-252.
10. Fluids Meters, ASME Publication, Six Edition, 1971.
11. Belih, L., "Secondary Flow in Blade Cascade of Axial Turbomachines and the Possibility of Reducing its Effects", Second International ASME Symposium, Fluid Machinery and Fluidics, Tokyo, Sept. 1972, pp. 41-49.

(References - cont.)

12. Longston, L.S., Nice, M.L., and Hooper, R.M., "Three-Dimensional Flow within a Turbine Cascade Passage", ASME Trans. J. of Engineering for Power, Vol. 99, No. 1, Jan. 1977, pp. 21-28.
13. Marchal, P.L. and Sieverding, C.H., "Secondary Flows Within Turbomachinery Bladings", in: Secondary Flows in Turbomachines, AGARD-CP-214, Paper 11, 1977.
14. Longston, L.S., "Cross Flows in a Turbine Cascade Passage", ASME Trans. J. of Engineering for Power, Vol. 102, Oct. 1980, pp. 866-874.
15. Gregory-Smith, D.G., "Secondary Flows and Losses in Axial Flow Turbines", ASME Paper 82-GT-19, 1982.

APPENDIX A

Analysis of One-Dimensional, Compressible Flow in the Vaneless Space

The Continuity Equation

$$2\pi r b \rho V_r = \text{const} \quad (1)$$

or, in differential form

$$\frac{1}{\rho} \frac{d}{dr} + \frac{1}{V_r} \frac{dV_r}{dr} + \frac{1}{b} \frac{db}{dr} + \frac{1}{r} = 0 \quad (1A)$$

The Momentum Equation in radial direction

$$V_r \frac{dV_r}{dr} - \frac{V_\theta^2}{r} = - \frac{1}{\rho} \frac{dP}{dr} - \frac{df_{r,\text{shear}}}{dm} \quad (2)$$

with

$$\begin{aligned} \frac{df_{r,\text{shear}}}{dm} &= \left[\frac{c_f \frac{\rho V^2}{2} \cos \beta r d\theta dr}{\rho r d\theta dr b} \right] 2 \\ &= c_f \frac{v^2 \cos \beta}{b} \end{aligned} \quad (3)$$

Introducing Eq. 3 into Eq. 2 yields

$$-V_r \frac{dV_r}{dr} + \frac{V_\theta^2}{r} = + \frac{1}{\rho} \frac{dP}{dr} = c_f \frac{V^2 \cos \beta}{b} \quad (4)$$

The Momentum Eq. in Tangential Direction

$$V_r \frac{dV_\theta}{dr} + \frac{V_r V_\theta}{r} = \frac{f_{\theta, \text{shear}}}{dm} \quad (5)$$

with

$$\begin{aligned} \frac{df_{\theta, \text{shear}}}{dm} &= \frac{-c_f \frac{\rho V^2}{2} \sin \beta r d\theta dr}{\rho r d\theta dr b} \\ &= -\frac{c_f V^2 \sin \beta}{b} \end{aligned} \quad (6)$$

Hence we obtain equation

$$V_r \frac{dV_\theta}{dr} + \frac{V_r V_\theta}{r} = -\frac{c_f V^2 \sin \beta}{b} \quad (7)$$

The Equation of State of an Ideal Gas reads $P = \rho RT$, or in differential form

$$\frac{1}{P} \frac{dP}{dr} = \frac{1}{T} \frac{dT}{dr} + \frac{1}{\rho} \frac{dp}{dr} \quad (8)$$

The Energy Eq. is

$$h_t = h + \frac{V^2}{2} = \text{const}, \quad (9)$$

or

$$T_t = T + \frac{V^2}{2c_p} = \text{const.} \quad (10)$$

if we assume constant specific heats.

In addition, we have equation

$$V_r = V \cos \beta \quad (11)$$

and

$$V_\theta = V \sin \beta \quad (12)$$

Equation 10 can be re-written as

$$T_t = T \left(1 + \frac{\gamma-1}{2} M^2 \right) \quad (13A)$$

or

$$\frac{dT_t}{T_t} = \frac{dT}{T} + \frac{(\gamma-1) M dM}{1 + \frac{\gamma-1}{2} M^2} = 0 \quad (13B)$$

Hence

$$\frac{1}{T} \frac{dT}{dr} = - \frac{(\gamma-1) M}{1 + \frac{\gamma-1}{2} M^2} \frac{dM}{dr} \quad (13C)$$

In addition

$$a^2 = \gamma \frac{P}{\rho} \quad (14)$$

or

$$\frac{2}{a} \frac{da}{dr} = \frac{1}{P} \frac{dP}{dr} - \frac{1}{\rho} \frac{d\rho}{dr} \quad (14A)$$

which is equivalent to Eq. 8 since $a^2 = \gamma RT$ and $\frac{2}{a} \frac{da}{dr} = \frac{1}{T} \frac{dT}{dr}$ and,
since

$$M = \frac{V}{a} \quad (15)$$

We have

$$\frac{1}{M} \frac{dM}{dr} = \frac{1}{V} \frac{dV}{dr} - \frac{1}{a} \frac{da}{dr} = \frac{1}{V} \frac{dV}{dr} - \frac{1}{2T} \frac{dT}{dr} \quad (15A)$$

Combining Equations 15A and 13C yields

$$\frac{1}{M} \frac{dM}{dr} = \frac{1}{V} \frac{dV}{dr} + \frac{\frac{\gamma-1}{2} M}{1 + \frac{\gamma-1}{2} M^2} \frac{dM}{dr}$$

and

$$\frac{1}{V} \frac{dV}{dr} = \frac{1}{M(1 + \frac{\gamma-1}{2} M^2)} \frac{dM}{dr} \quad (16)$$

Equation 1A can be re-written as

$$\begin{aligned} \frac{1}{\rho} \frac{dp}{dr} &= - \frac{1}{V_r} \frac{dV_r}{dr} - \frac{1}{b} \frac{db}{dr} - \frac{1}{r} \\ &= - \frac{1}{V \cos \beta} \frac{d(V \cos \beta)}{dr} - \frac{1}{b} \frac{db}{dr} - \frac{1}{r} \\ &= - \frac{1}{V} \frac{dV}{dr} + \tan \beta \frac{d\beta}{dr} - \frac{1}{b} \frac{db}{dr} - \frac{1}{r} \\ &= - \frac{1}{M(1 + \frac{\gamma-1}{2} M^2)} \frac{dM}{dr} + \tan \beta \frac{d\beta}{dr} - \frac{1}{b} \frac{db}{dr} - \frac{1}{r} \end{aligned} \quad (17)$$

Introducing Equations 17 and 13C into Equation 8 gives

$$\begin{aligned} \frac{1}{P} \frac{dP}{dr} &= - \frac{(\gamma-1)M}{1 + \frac{\gamma-1}{2} M^2} \frac{dM}{dr} - \frac{1}{M(1 + \frac{\gamma-1}{2} M^2)} \frac{dM}{dr} \\ &\quad + \tan \beta \frac{d\beta}{dr} - \frac{1}{b} \frac{db}{dr} - \frac{1}{r} \end{aligned}$$

or

$$\frac{1}{P} \frac{dP}{dr} = - \frac{1 + (\gamma-1) M^2}{M(1 + \frac{\gamma-1}{2} M^2)} \frac{dM}{dr} + \tan \beta \frac{d\beta}{dr} - \frac{1}{b} \frac{db}{dr} - \frac{1}{r} \quad (18)$$

Since

$$\frac{ds}{R} = - \frac{dP_t}{P_t} \quad (19)$$

and

$$P_t = P \left(1 + \frac{\gamma-1}{2} M^2\right)^{\frac{\gamma}{\gamma-1}} \quad (20)$$

$$\begin{aligned} \frac{1}{P_t} \frac{dP_t}{dr} &= - \frac{1}{R} \frac{ds}{dr} = \frac{dP}{P} + \frac{\gamma M \frac{dM}{dr}}{1 + \frac{\gamma-1}{2} M^2} \\ &= \frac{(M^2 - 1)}{M(1 + \frac{\gamma-1}{2} M^2)} \frac{dM}{dr} + \tan\beta \frac{d\beta}{dr} - \frac{1}{b} \frac{db}{dr} - \frac{1}{r} \end{aligned} \quad (21)$$

As a result, Eq. 4 can be written as

$$\begin{aligned} &- V \cos\beta \frac{d(V \cos\beta)}{dr} + \frac{V^2 \sin^2\beta}{r} \\ &= \frac{a^2}{\gamma} \left[- \frac{1+(\gamma-1)M^2}{M(1+\frac{\gamma-1}{2} M^2)} \frac{dM}{dr} + \tan\beta \frac{d\beta}{dr} - \frac{1}{b} \frac{db}{dr} - \frac{1}{r} \right] \\ &\quad + c_f \frac{V^2 \cos\beta}{b} \end{aligned} \quad (22)$$

because

$$\frac{1}{P} \frac{dP}{dr} = \frac{P}{P} \frac{1}{P} \frac{dP}{dr} = \frac{a^2}{\gamma} \frac{1}{P} \frac{dP}{dr} \quad (23)$$

while Eq. 7 can be written as

$$V \cos\beta \frac{d(V \sin\beta)}{dr} + \frac{V^2 \sin\beta \cos\beta}{r} = - c_f \frac{V^2 \sin\beta}{b}$$

or

$$\frac{\cos\beta \sin\beta}{V} \frac{dV}{dr} + \cos^2\beta \frac{d\beta}{dr} + \frac{\sin\beta \cos\beta}{r} = -c_f \frac{\sin\beta}{b}$$

or, in view of Eq. 16

$$\frac{1}{M(1+\frac{\gamma-1}{2}M^2)} \frac{dM}{dr} + \frac{\cos\beta}{\sin\beta} \frac{d\beta}{dr} + \frac{1}{r} = - c_f \frac{1}{B\cos\beta} \quad (24)$$

Eq. (22) can be re-written as

$$\begin{aligned} -\gamma M^2 \cos^2\beta \left(\frac{1}{V} \frac{dV}{dr} \right) + \gamma M^2 \cos\beta \sin\beta \frac{d\beta}{dr} + \frac{\gamma M^2 \sin^2\beta}{r} \\ = [\quad] + c_f \frac{\gamma M^2 \cos\beta}{B} \end{aligned}$$

which, the view of Eq. (16) becomes

$$\begin{aligned} -\gamma M^2 \cos^2\beta \left[\frac{1}{M(1+\frac{\gamma-1}{2}M^2)} \frac{dM}{dr} \right] + \gamma M^2 \cos\beta \sin\beta \frac{d\beta}{dr} + \gamma M^2 \frac{\sin^2\beta}{r} \\ = - \frac{1+(\gamma-1)M^2}{M(1+\frac{\gamma-1}{2}M^2)} \frac{dM}{dr} + \tan\beta \frac{d\beta}{dr} - \frac{1}{B} \frac{db}{dr} - \frac{1}{r} \\ + c_f \frac{\gamma M^2 \cos\beta}{B} \end{aligned}$$

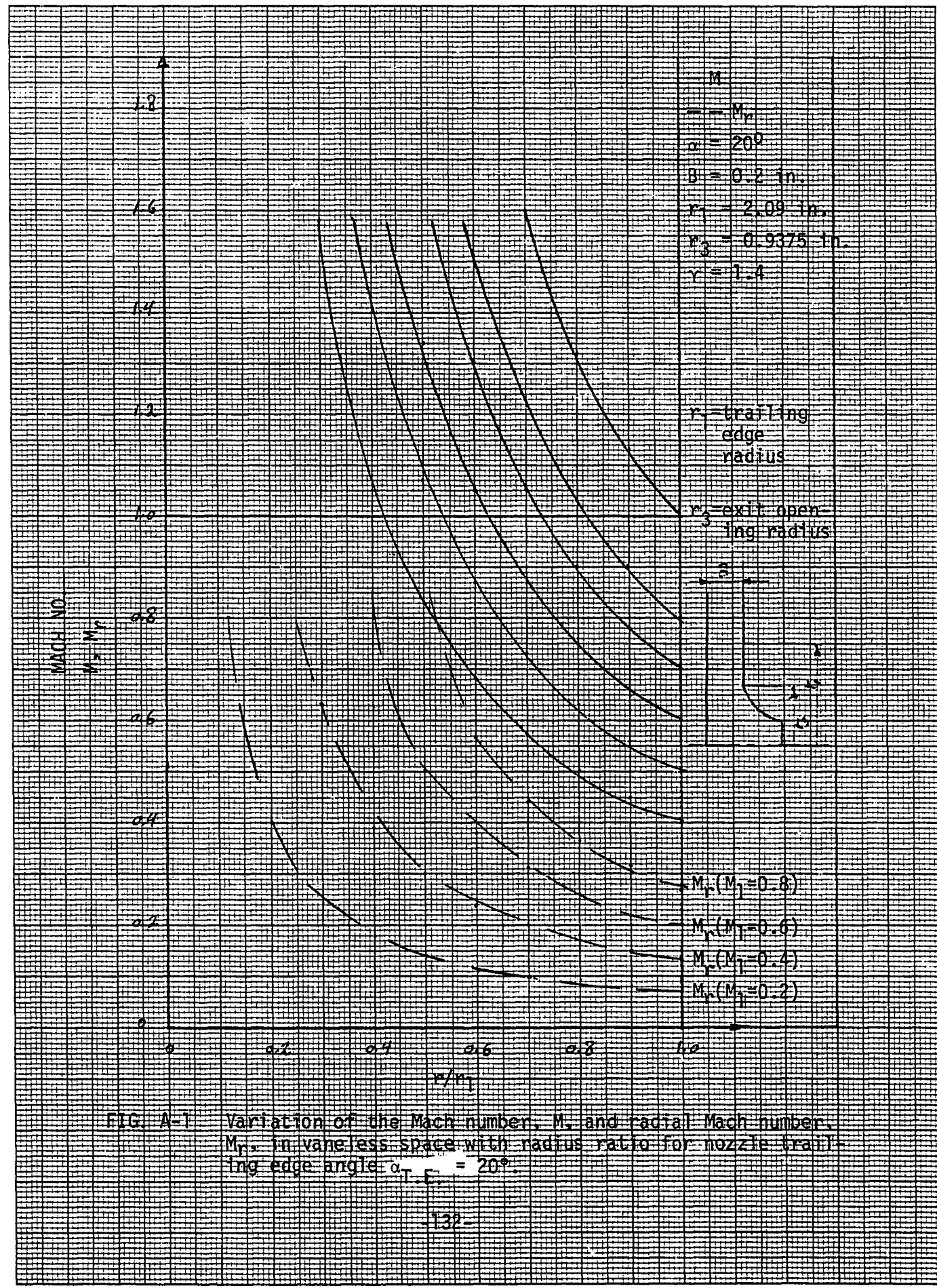
Using dimensionless variables $R = \frac{r}{r_1}$ and $B = \frac{b}{b_1}$, we can rewrite Equation 24 as

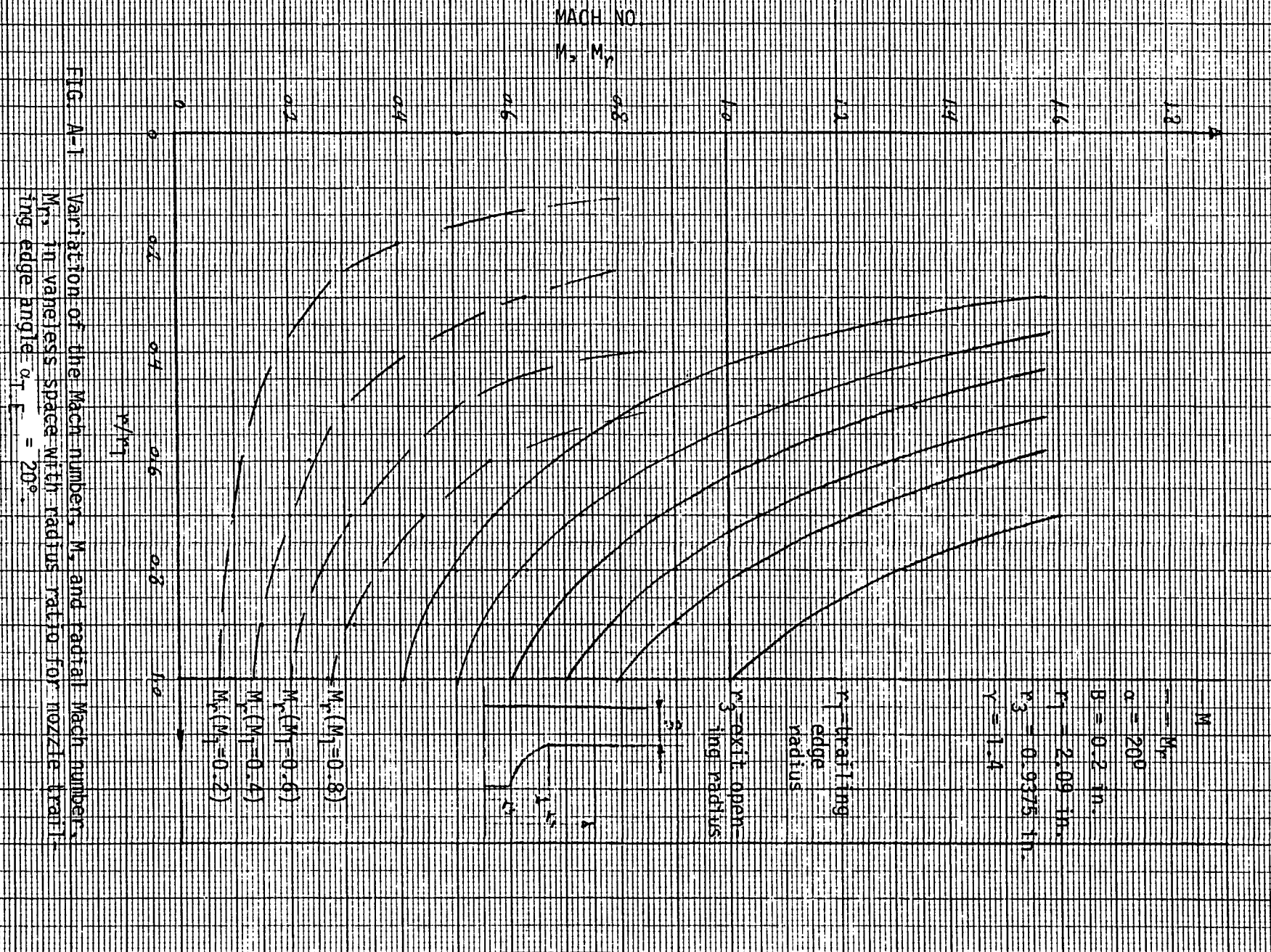
$$\frac{1}{M(1+\frac{\gamma-1}{2}M^2)} \frac{dM}{dR} = -\cos\beta \frac{d\beta}{dR} - \frac{1}{R} - c_f \frac{1}{B\cos\beta} \quad (25)$$

Eliminating the term $\frac{dM}{dR}$ from Equation 20 with the aid of Equation 24 and introducing the dimensionless variables R and B we obtain equation

$$\frac{d\beta}{dR} = \frac{\frac{M^2}{R} + \frac{1}{B} \frac{dB}{dR} - c_f \frac{1 + (\gamma-1) M^2}{B \cos \beta}}{\cot \beta \left(\frac{1}{\cos^2 \beta} - M^2 \right)} \quad (26)$$

Equations 25 and 26 can be solved for $M(r)$ and $\beta(r)$ with the friction coefficient c_f , and the variation of the vaneless space with radius, $B(r)$, known. Also the initial values of the Mach number, M , and the flow angle, β , must be given.





APPENDIX B

The calculations of the flow velocity, the Mach number, the mass flow rate, and the flow angle for nozzle height 0.148 in. and nozzle trailing edge angle 20° and for the high pressure test are given in this appendix as a sample.

The uncertainty calculations of the above values are also presented in this appendix. The following data were measured for the nozzle height 0.148 in. and the high pressure test, at probe no. 1.

$$P_{\text{sup}} = 49.72 \pm 0.06 \text{ IN-HG. (ABS)}$$

$$P = 43.28 \pm 0.06 \text{ IN-HG. (ABS)}$$

$$P_T = 49.17 \pm 0.06 \text{ IN-HG. (ABS)}$$

$$P_{\text{atm}} = 29.98 \pm 0.01 \text{ IN-HG.}$$

$$T_{\text{sup}} = 69 \pm 1 \text{ }^{\circ}\text{F} \quad \text{or} \quad 529 \pm 1 \text{ }^{\circ}\text{R}$$

$$P_{\text{sup}} - P_T = 7.45 \pm 0.05 \text{ IN-H}_2\text{O} \quad \text{or} \quad 0.5500 \pm 0.0037 \text{ IN-HG.}$$

The following equations are used to calculate the Mach number, M, temperature, T, velocity of fluid, v, density, ρ , loss coefficients, e, y_N , and ξ .

$$M = \left[\left(\frac{P}{P_T} \right)^{\frac{1-\gamma}{\gamma}} - 1 \right] \frac{2}{\gamma-1}^{\frac{1}{2}} \quad (1)$$

$$T = T_{\text{sup}} / \left(1 + \frac{\gamma-1}{2} M^2 \right) \quad (2)$$

$$V = \sqrt{\gamma RT} / M \quad (3)$$

$$\rho = \frac{P}{RT} \quad (4)$$

$$e = (P_{sup} - P_T) / P_{sup} = \frac{\Delta P_1}{P_{sup}} \quad (5)$$

$$\gamma_N = (P_{sup} - P_T) / (P_T - P) = \frac{\Delta P_1}{\Delta P_2} \quad (6)$$

$$\xi = \gamma_N / (1 + \frac{\gamma M^2}{2}) \quad (7)$$

The following equations are used to calculate errors.

$$\delta M = \left| -\frac{1}{\gamma M} X^{\frac{1-2\gamma}{\gamma}} \right| \delta X$$

where

$$X = \frac{P}{P_T} \quad (8)$$

$$\delta T = \left| \frac{\delta T_{sup}}{\left(1 + \frac{\gamma-1}{2} M^2\right)} \right| + \left| -\frac{(\gamma-1)M\delta M}{\left(1 + \frac{\gamma-1}{2} M^2\right)^2} T_{sup} \right| \quad (9)$$

$$\delta V = \left| \sqrt{R\gamma} \frac{1}{2} T^{-\frac{1}{2}} M \delta T \right| + \left| \sqrt{\gamma RT} \delta M \right| \quad (10)$$

$$\delta \rho = \left| \frac{\delta P}{RT} \right| + \left| -\frac{P}{RT^2} \delta T \right| \quad (11)$$

$$\delta e = \left| \frac{\delta \Delta P_1}{P_{sup}} \right| + \left| -\Delta P_1 \frac{\delta P_{sup}}{P_{sup}^2} \right| \quad (12)$$

$$\delta Y_N = \left| \frac{\delta \Delta P_1}{\Delta P_2} \right| + \left| -\Delta P_1 \frac{\delta \Delta P_2}{(\Delta P_2)^2} \right| \quad (13)$$

$$\delta \xi = \left| \frac{\delta Y_N}{1 + \frac{\delta M^2}{2}} \right| + \left| - \frac{Y_N \gamma^{M \delta M}}{(1 + \frac{\gamma}{2} M^2)^2} \right| \quad (14)$$

Using the value of P and P_T in equation (1) the Mach number is:

$$M = \left[\left(\frac{43.28}{49.17} \right)^{\frac{1-1.4}{1.4}} - 1 \right] \frac{2}{1.4-1}^{\frac{1}{2}} = 0.4298$$

$$X = \frac{43.28}{49.17} = 0.8802 \text{ and } \delta X = 0.0023$$

The error in calculation of Mach number, M , can be obtained from Equation 8 as follows:

$$\delta M = \left| \frac{1}{(1.4)(0.4298)} (0.8802)^{\frac{1-2.8}{1.4}} \right| (0.0023) = 0.0045$$

Temperature, T , is obtained from Equation (2) and the error in Temperature, T , calculation can be obtained from Equation (9) as follows:

$$T = 529 / \left(1 + \frac{0.4}{2} (0.4298)^2 \right) = 510.15 {}^\circ R$$

$$\begin{aligned} \delta T &= \left| \frac{1}{1 + \frac{0.4}{2} (0.4298)^2} \right| + \left| \frac{(0.4)(0.4298)(0.0045)510.15}{[1 + \frac{0.4}{2} (0.4298)^2]^2} \right| \\ &= 1.33 {}^\circ F \end{aligned}$$

To get the velocity and its error Equations 3 and 10 are used.

$$V = \sqrt{1.4 \times 53.34 \times (66.54+460) \times (32.2)} (0.4298)$$
$$= 476.51 \text{ ft/sec.}$$

$$\delta V = |\sqrt{1.4 \times 53.34 \times 32.2} [\frac{1}{2} (66.54+460)^{-\frac{1}{2}} (0.4298)(1.01) + \sqrt{(66.54+460)} (0.0045)]| = 5.53 \text{ ft/sec.}$$

$$\rho = \frac{(43.28)(144)(0.4912)}{(53.34)(460+66.54)} = 0.11244 \text{ lbm/ft}^3$$

$$\delta \rho = \left| \frac{(0.06)(0.4912)(144)}{53.34 \times (66.54+460)} \right| + \left| \frac{43.28 \times 1.01}{53.34 \times (66.54+460)} \right| = 0.0017$$

$$e = \frac{0.55}{49.72} = 0.01109$$

$$\delta e = \left| \frac{0.0037}{49.72} \right| + \left| \frac{0.55(0.06)}{49.72^2} \right| = 0.00009$$

$$\gamma_N = \frac{0.55}{(49.17-43.28)} = 0.09384, \quad \xi = \frac{0.09384}{[1 + \frac{1.4}{2} (0.4298)^2]} = 0.083095$$

$$\delta \gamma_N = \left| \frac{0.0037}{49.17-43.28} \right| + \left| \frac{0.55(0.12)}{(49.17-43.28)^2} \right| = 0.00253,$$

$$\delta \xi = \left| 0.00253 / \left[1 + \frac{1.4}{2} (0.4298)^2 \right] \right| + \left| -0.09384 \times 1.4 \times 0.4298 \times 0.0045 / \left[\left(1 + \frac{1.4}{2} (0.4298)^2 \right)^2 \right] \right|, \quad \delta \xi = 0.002440$$

Mass flow rate is obtained from orific data as follows:

$$\Delta P = 5.7 \pm 0.05 \text{ IN of S.G.} = 2.95$$

$$T_1 = 71.9 \pm 1.0 \text{ }^{\circ}\text{F}$$

$$P_1 = 82 \pm 0.5 \text{ PSIG}$$

$$P_{atm} = 29.98 \pm 0.1 \text{ IN-HG.}$$

From reference number 10 the following equation is taken to calculate mass flow rate

$$\dot{m} = 0.52502 \frac{CY d^2 Fa}{\sqrt{1-\beta^4}} \sqrt{\rho_1 \Delta P} \quad (15)$$

where the values of Y, c and Fa are also obtained from reference 10.

$$\beta = \frac{d}{D} = \frac{1.145}{2.0} = 0.5725 \quad \begin{aligned} d &= \text{orific diameter} \\ D &= \text{pipe diameter} \end{aligned}$$

$F_a = 1$ for low temperature.

$$R_d = \frac{10^6 d}{15} = (10^6)(1.145)/15 = 7.633 \times 10^5$$

For $R_d = 7.633 \times 10^5$ and $\beta = 0.5725$ from reference 10 the value of C is obtained to be $C \approx 0.6078$

$$\Delta P = \left(\frac{5.7}{12}\right)(2.95)\left(\frac{62.4}{144}\right) = 0.6072 \text{ or } = 0.6072 \pm 0.0053 \text{ (PSIA)}$$

$$T_1 = (71.9 + 460) = 531.9 \pm 1 \text{ }^{\circ}\text{R}$$

$$x = \left(\frac{\Delta P}{P_1}\right)/\gamma = \frac{0.6072}{(96.73)(1.4)} = 0.0045$$

Using reference 10 with the values of x and β the value of y is obtained to be $y \approx 1.0$.

$$\rho_1 = \frac{P_1}{RT_1} = \frac{96.73 \times 144}{(53.34)(531.9)} = 0.49095$$

$$\delta\rho_1 = \left| \frac{0.55}{53.34 \times 531.9} \right| + \left| \frac{(96.73+1.0)}{(53.34)(531.9)^2} \right| = 0.00003$$

Therefore the mass flow rate is:

$$\dot{m} = \frac{(0.52502)(0.6078)(1.145)^2(1)(1)}{\sqrt{1-0.5725^4}} \sqrt{(0.49095)(0.6072)}$$

$$= 0.24196 \text{ Ibm/sec.}$$

The uncertainty in calculation of the mass flow rate can be obtained as follows:

$$\delta\dot{m} = \frac{0.52502 \text{ cyd}^2 \text{Fa}}{\sqrt{1-\beta^4}} \left[\frac{1}{2} \sqrt{\Delta P} \rho_1^{-\frac{1}{2}} \delta P_1 + \frac{1}{2} \sqrt{\rho_1} \Delta P^{-\frac{1}{2}} \delta \Delta P \right]$$

$$\delta\dot{m} = 0.0011 \text{ for given data.}$$

The flow angle, θ , can be obtained from Equation 17 which is obtained from the continuity equation.

$$\sin(\theta) = \dot{m}/2\pi r \rho V H \quad (17)$$

$$\sin(\theta) = 0.24196/2\pi(\frac{1.44}{12})(0.11244)(476.51)(\frac{1.148}{12}) = 0.4856$$

Therefore $\theta = 29.05^\circ$.

The error calculations for flow angle can be obtained from Equation 18 or 19

$$\delta\theta = \frac{1}{\cos\theta} [|\frac{\delta\dot{m}}{2\pi r \rho V H}| + |-\frac{\dot{m}\delta\rho}{2\pi r V H \rho^2}| + |-\frac{\dot{m}\delta V}{2\pi r H \rho V^2}|] \quad (18)$$

$$\delta\theta = \tan\theta [|\frac{\delta\dot{m}}{\dot{m}}| + |-\frac{\delta\rho}{\rho}| + |-\frac{\delta V}{V}|] \quad (19)$$

$$\delta\theta = \tan(29.05) [|\frac{0.0011}{0.24196}| + |-\frac{0.00171}{0.11244}| + |-\frac{5.53}{476.51}|] = 0.02 \text{ Rad. or } 1.00^\circ$$

In summary the sample of calculation for nozzle height 0.148 m. and for the high pressure test when nozzle trailing edge is 20° can be written as follows:

Mach number	$M = 0.4298 \pm 0.0045$
Temperature	$T = 50.15 \pm 1.33^\circ F$
Velocity	$V = 476.51 \pm 5.53 \text{ ft/sec}$
density	$\rho = 0.1124 \pm 0.0017 \text{ lbm/ft}^3$
loss coefficient	$e = 0.0111 \pm 0.0001$
loss coefficient	$\gamma_N = 0.094 \pm 0.003$
loss coefficient	$\xi = 0.083 \pm 0.002$

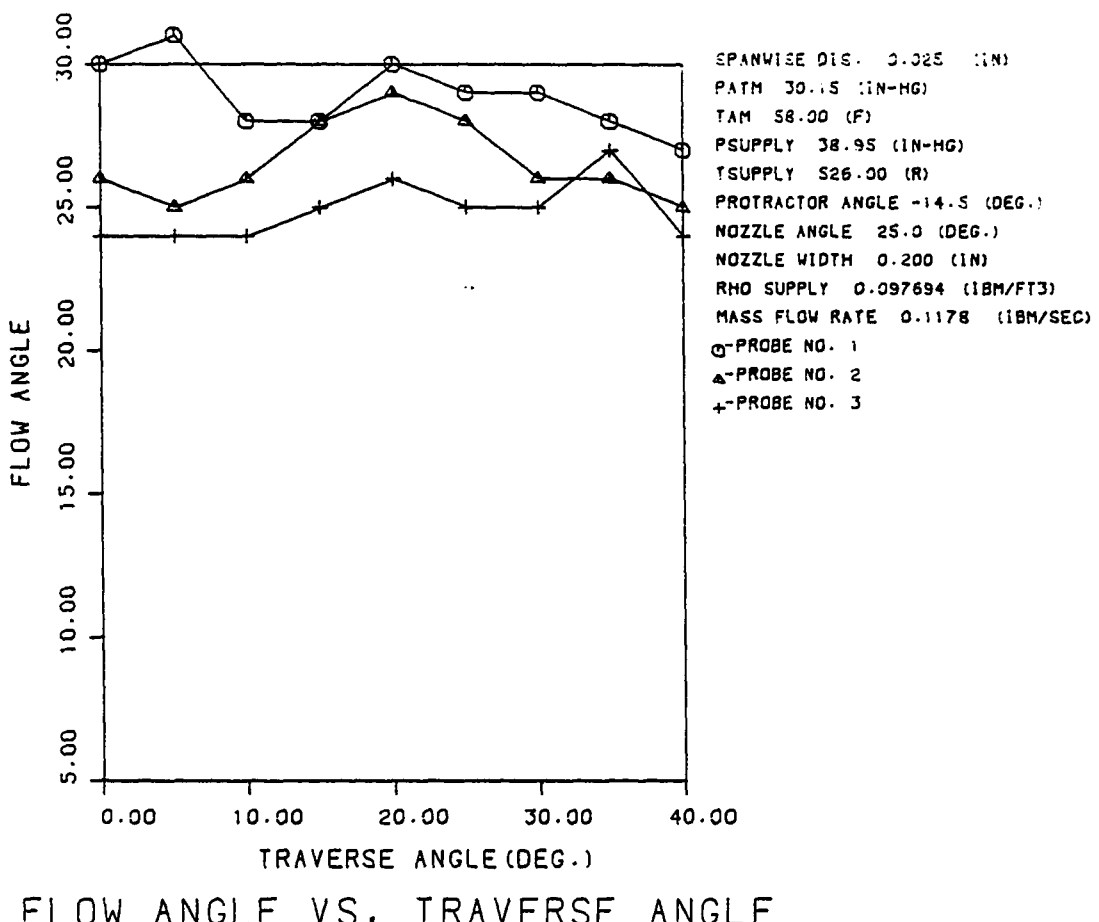
mass flow rate

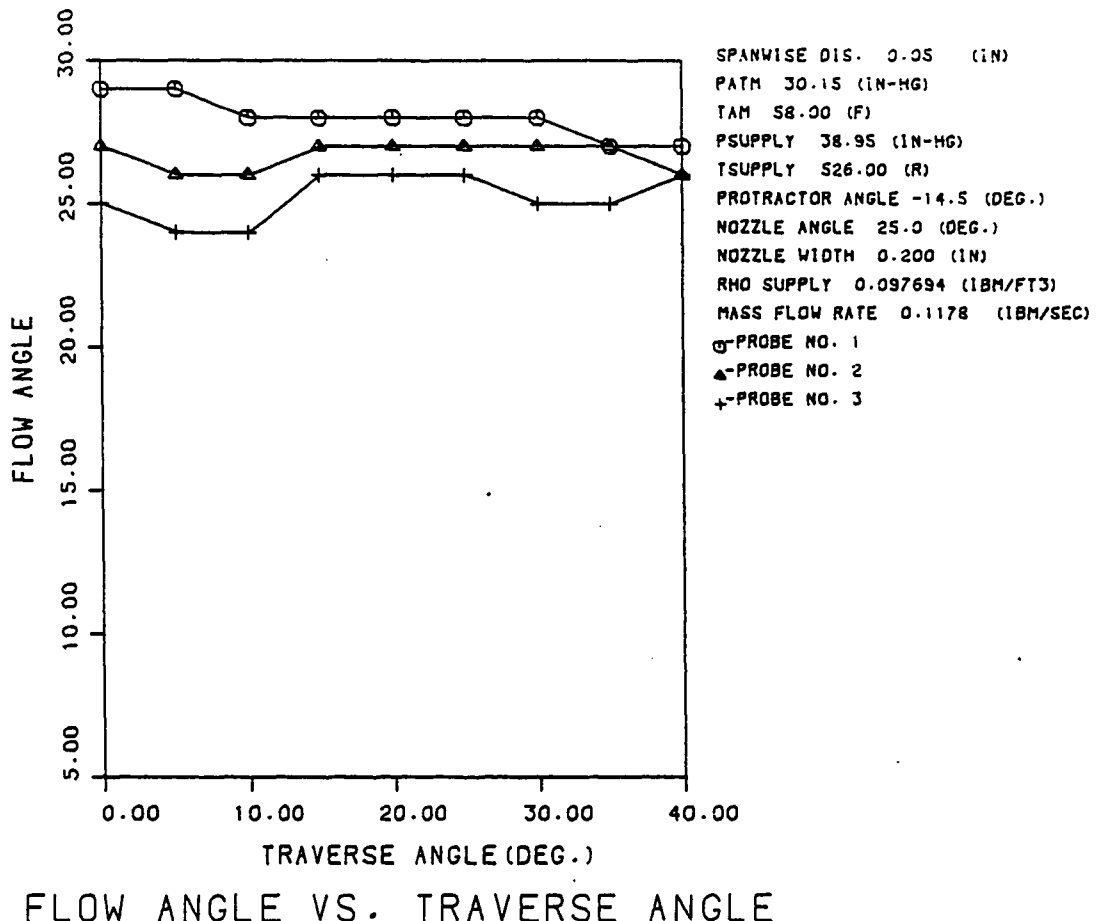
$$\dot{m} = 0.2419 \pm 0.0011 \text{ lbm/sec}$$

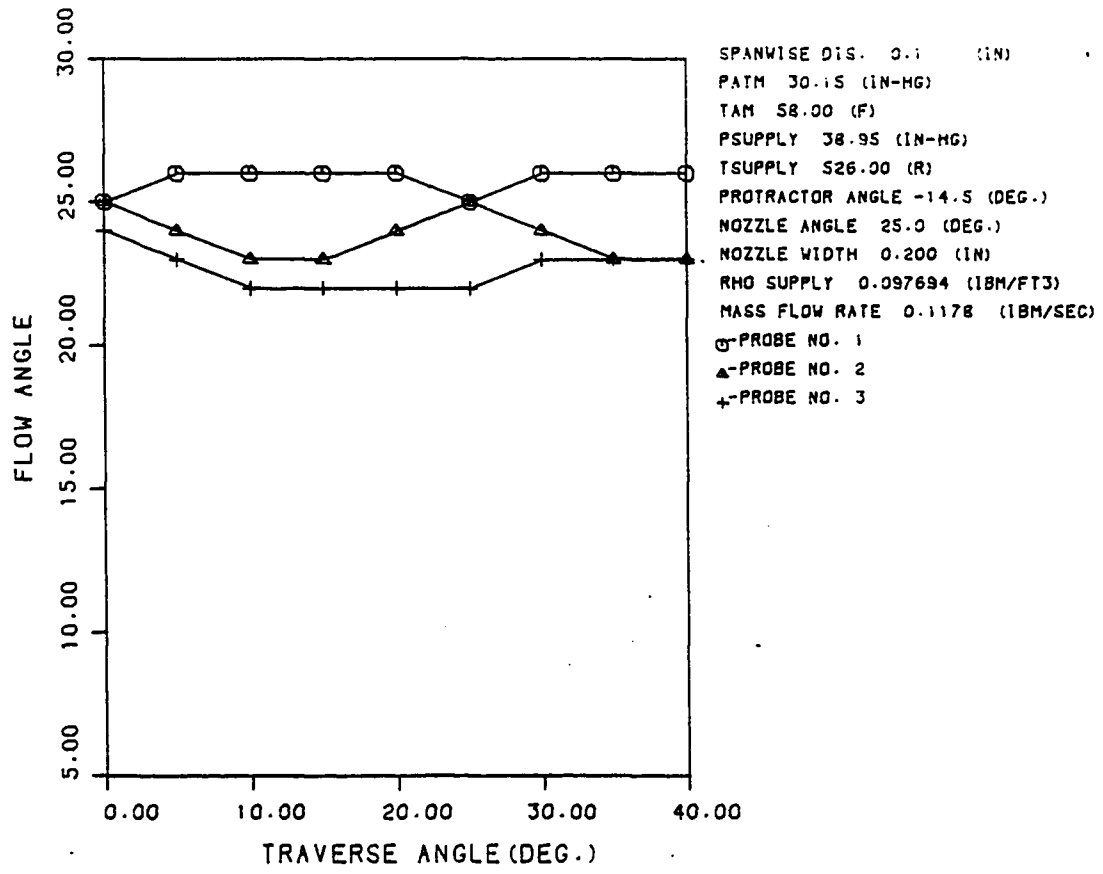
flow angle

$$\theta_M = 29.05 \pm 1.00 \text{ DEG.}$$

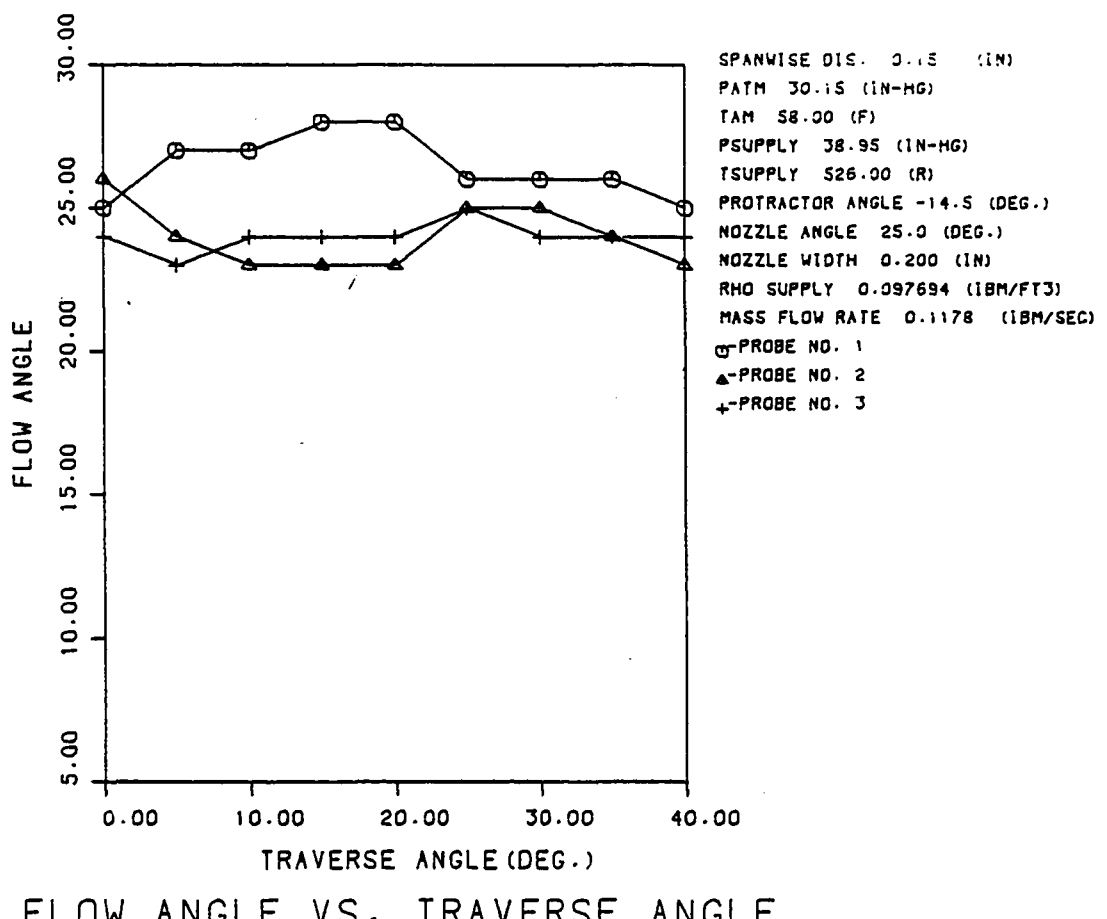
APPENDIX C
Sample of Intermediate Test Results

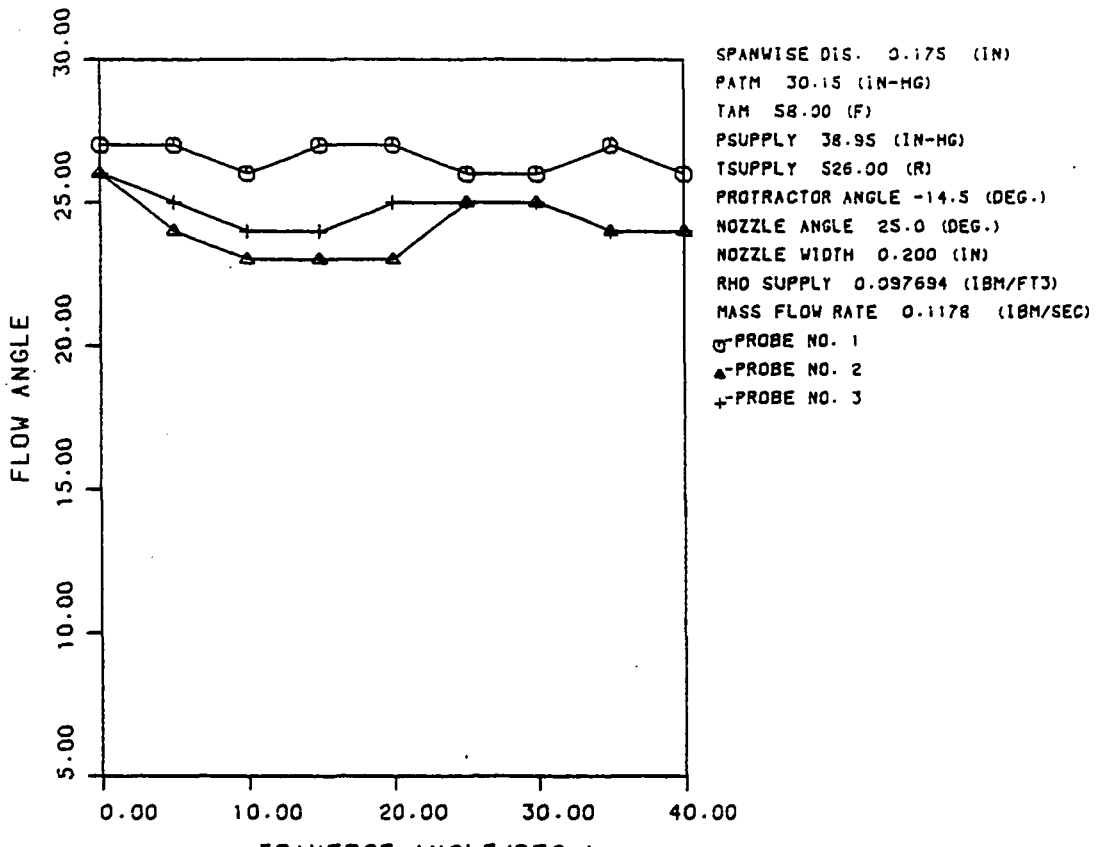




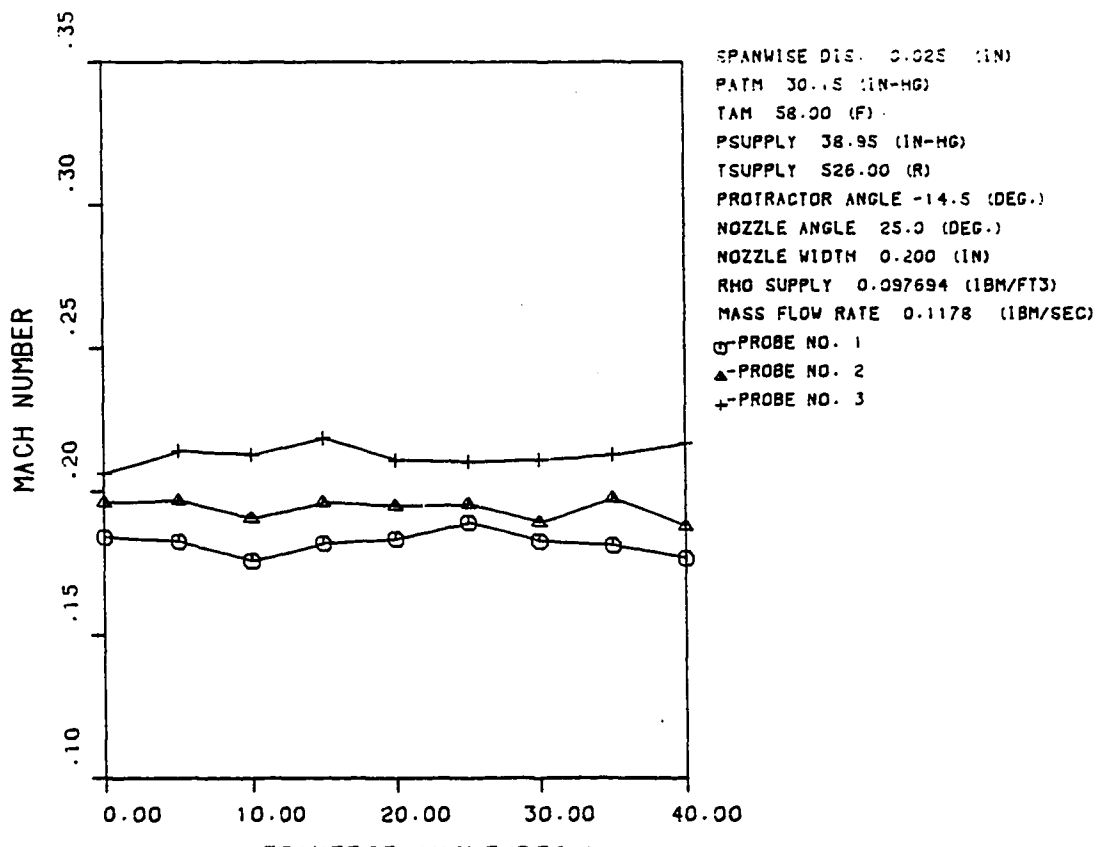


FLOW ANGLE VS. TRAVERSE ANGLE

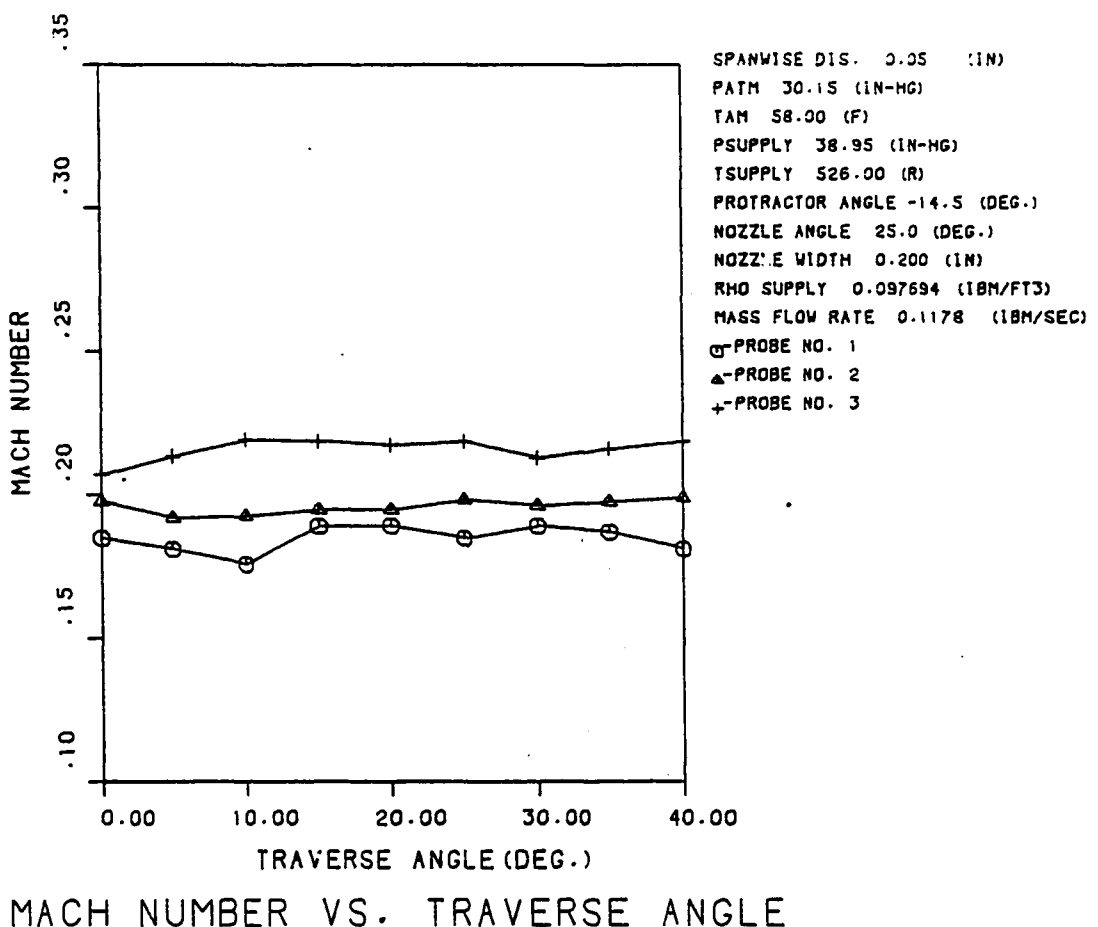


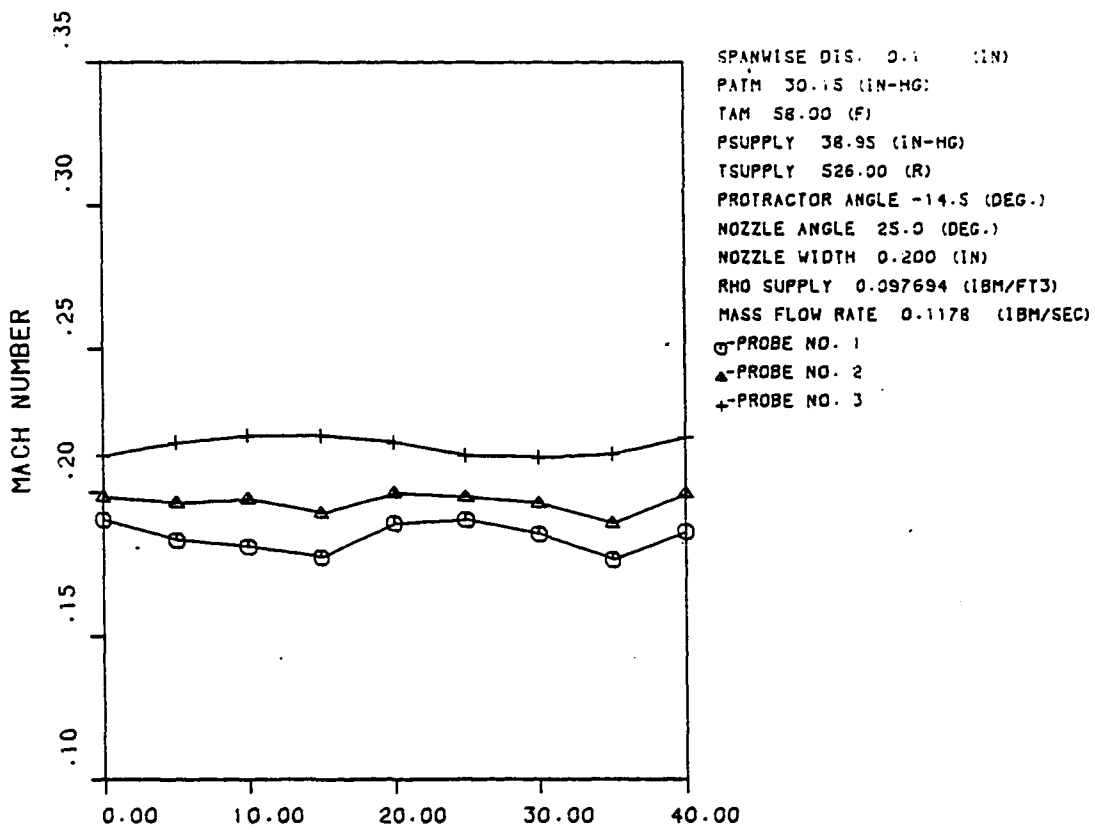


FLOW ANGLE VS. TRAVERSE ANGLE

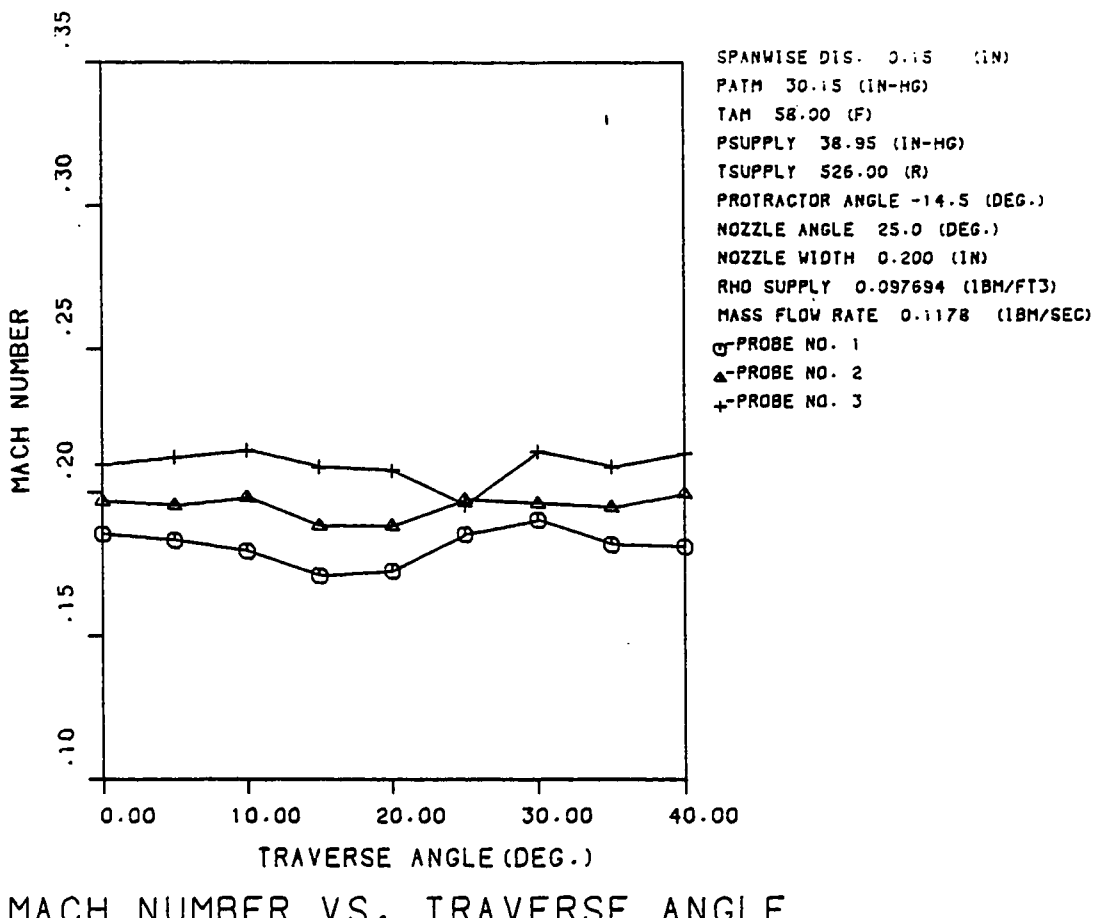


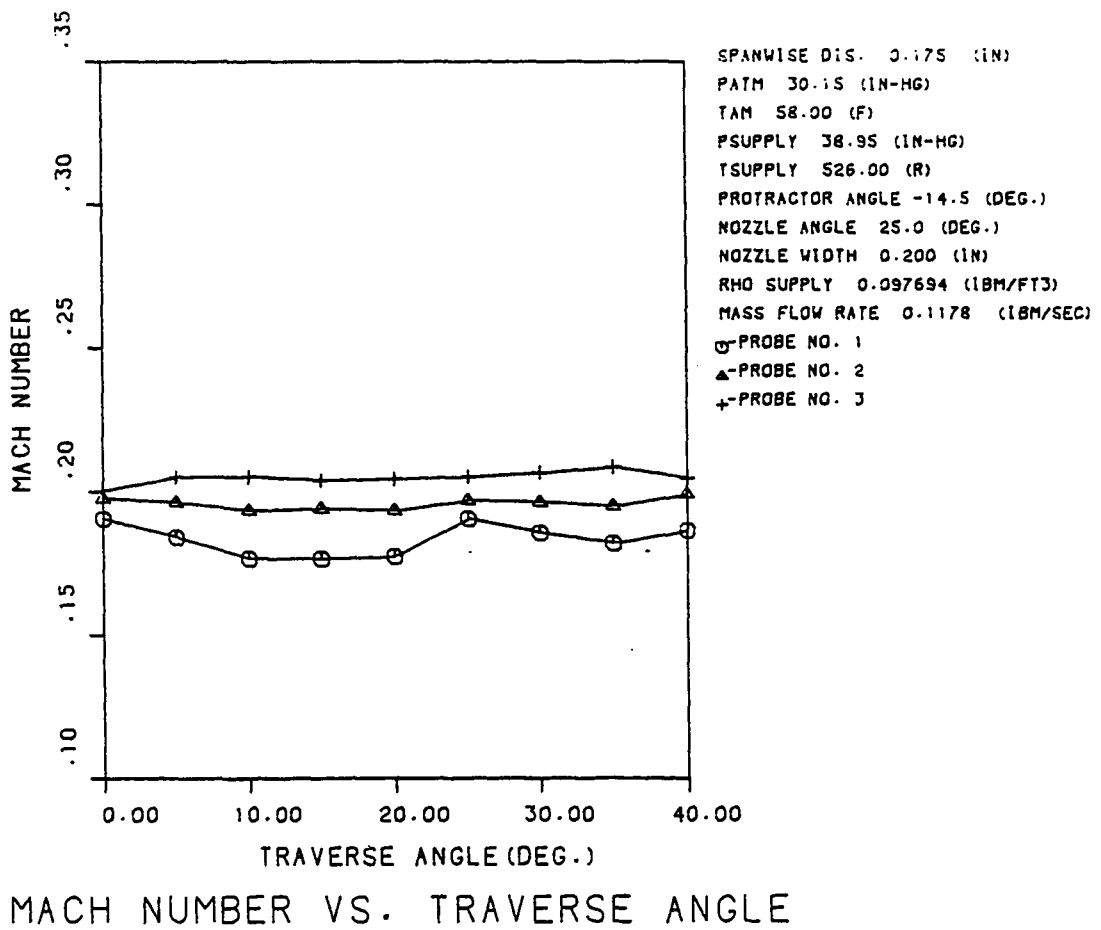
MACH NUMBER VS. TRAVERSE ANGLE

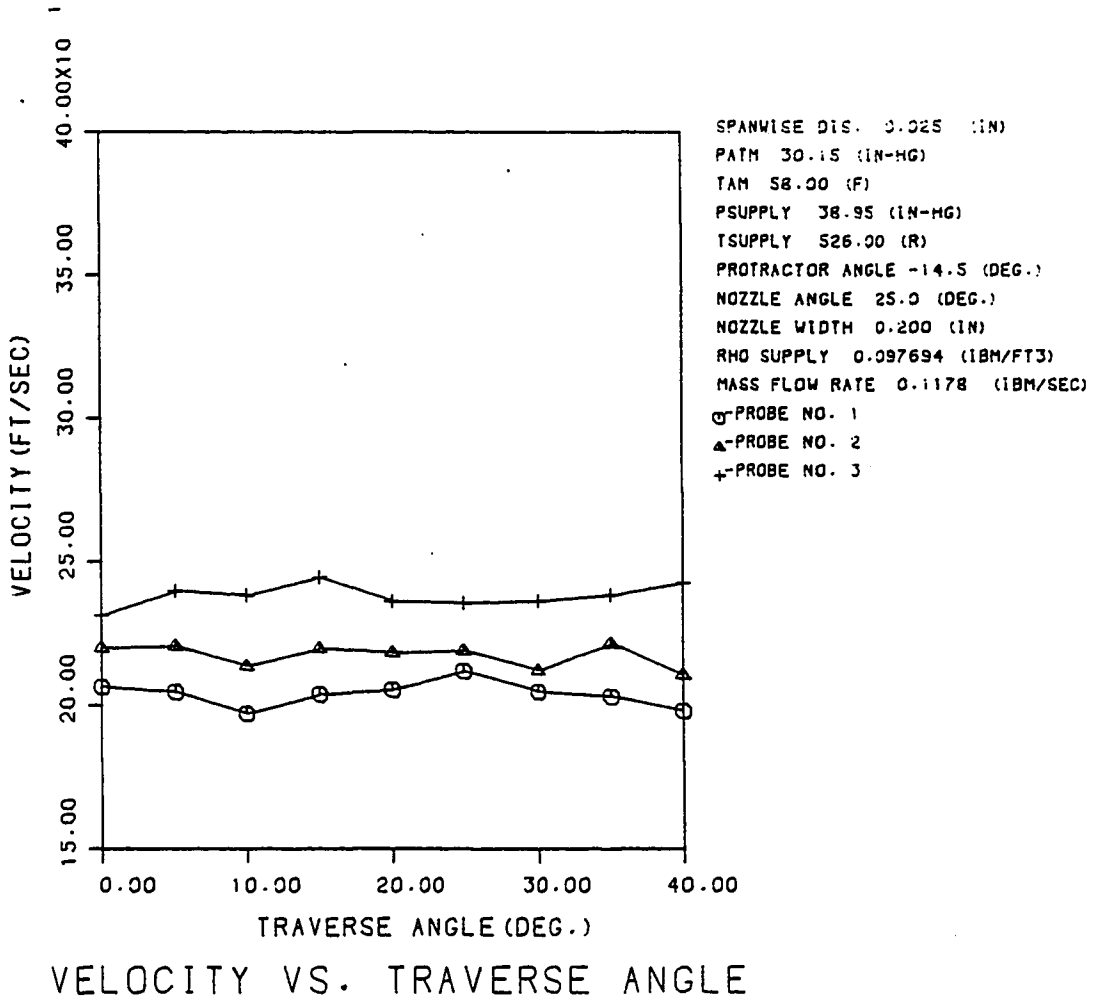


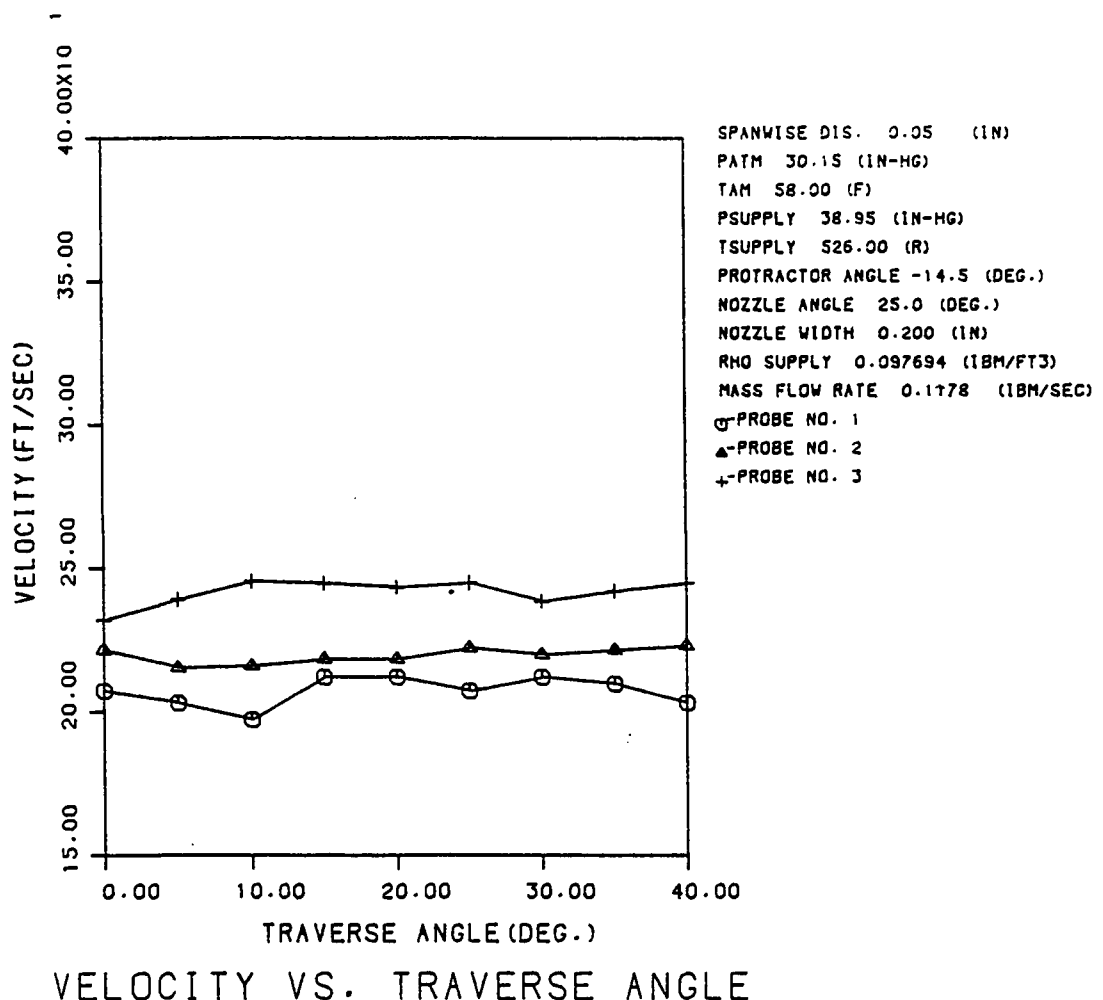


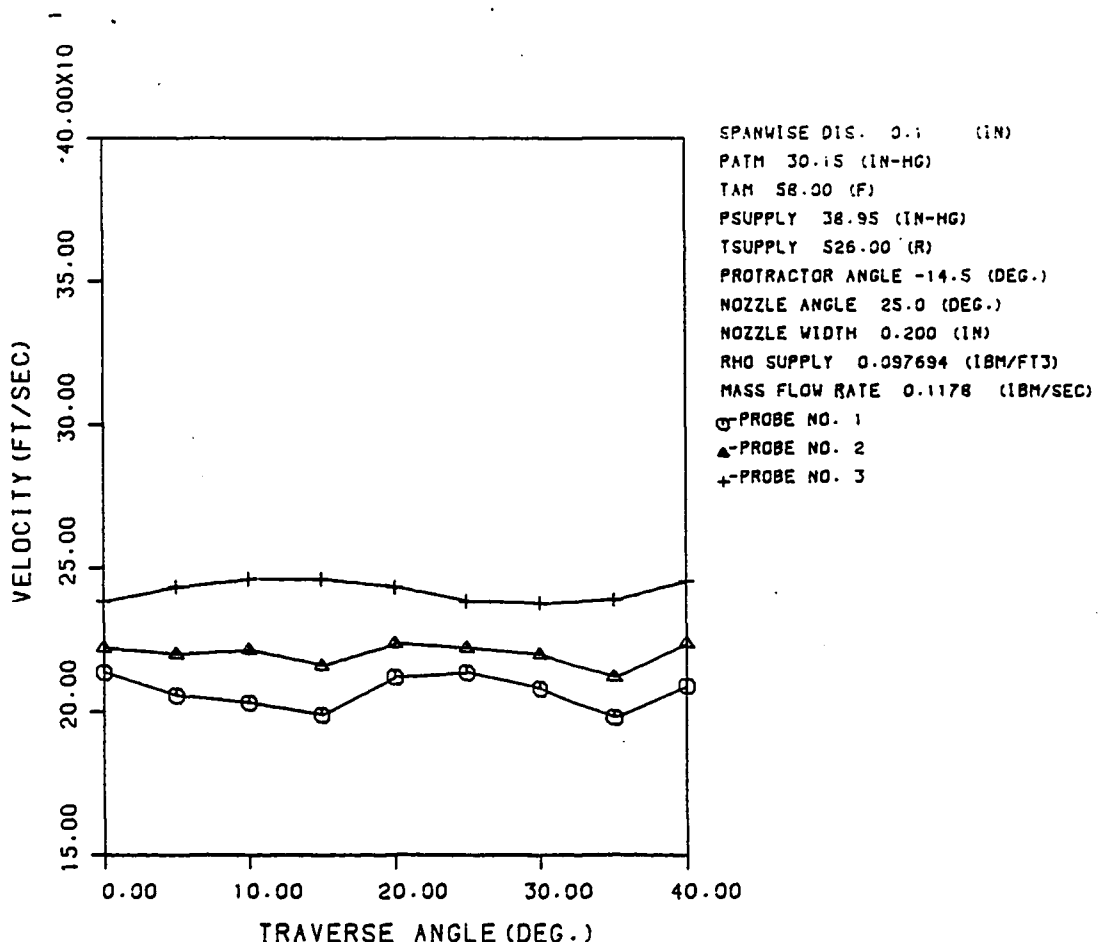
MACH NUMBER VS. TRAVERSE ANGLE



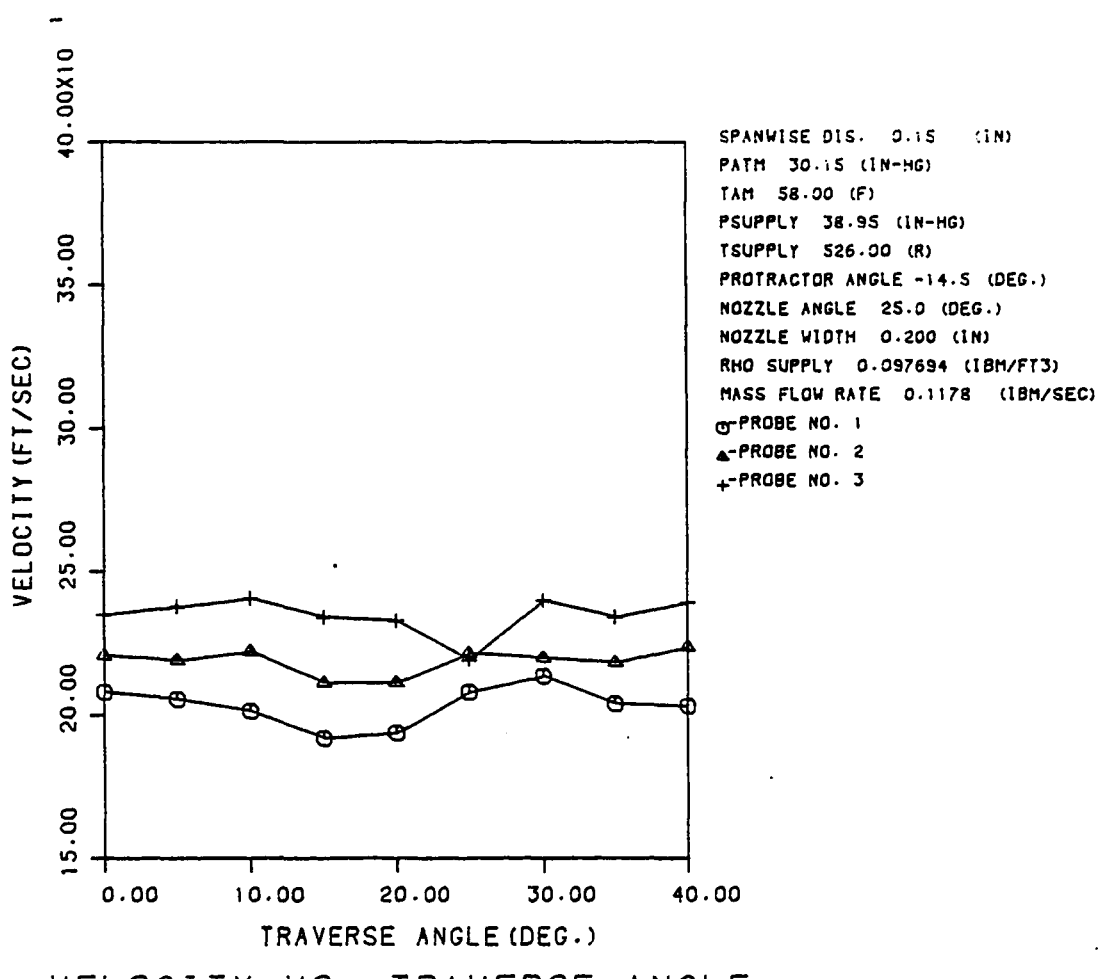




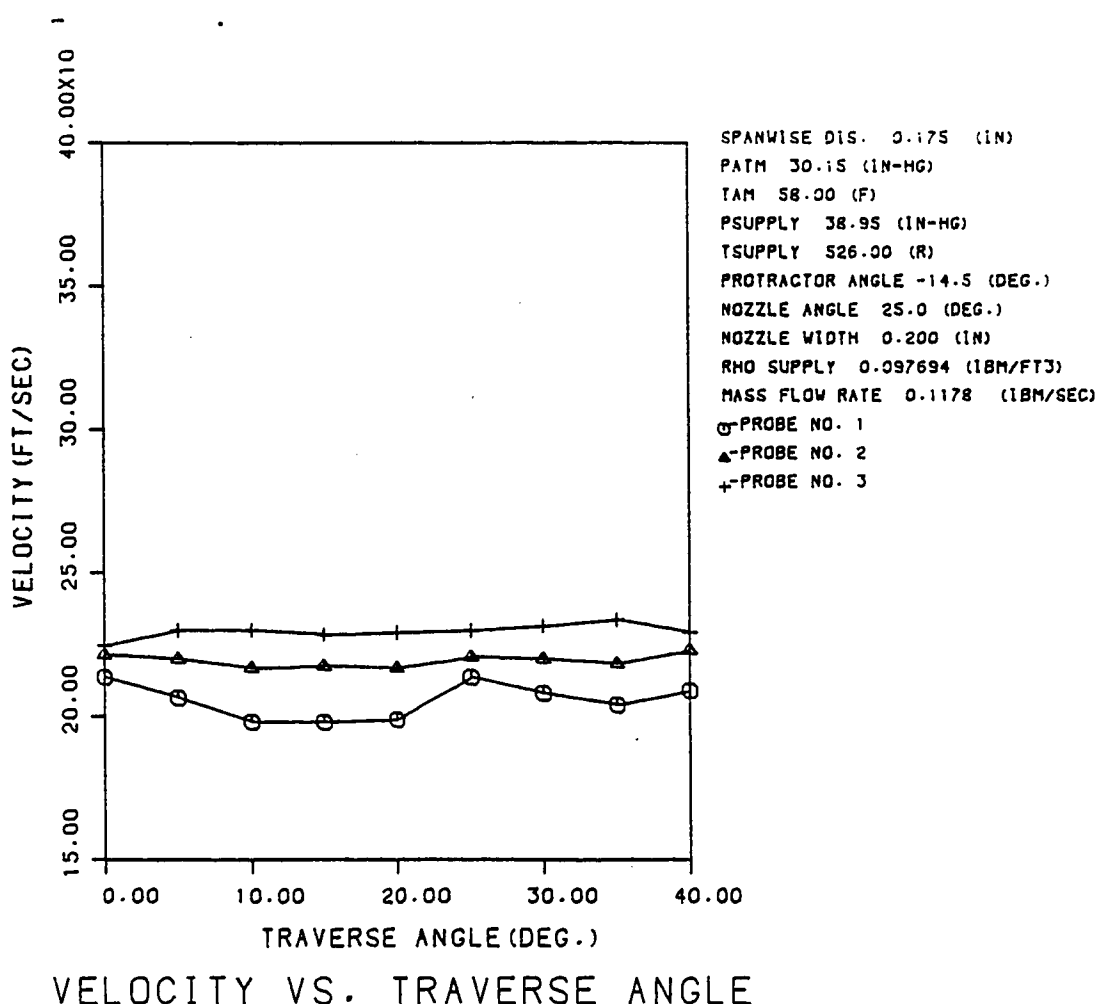


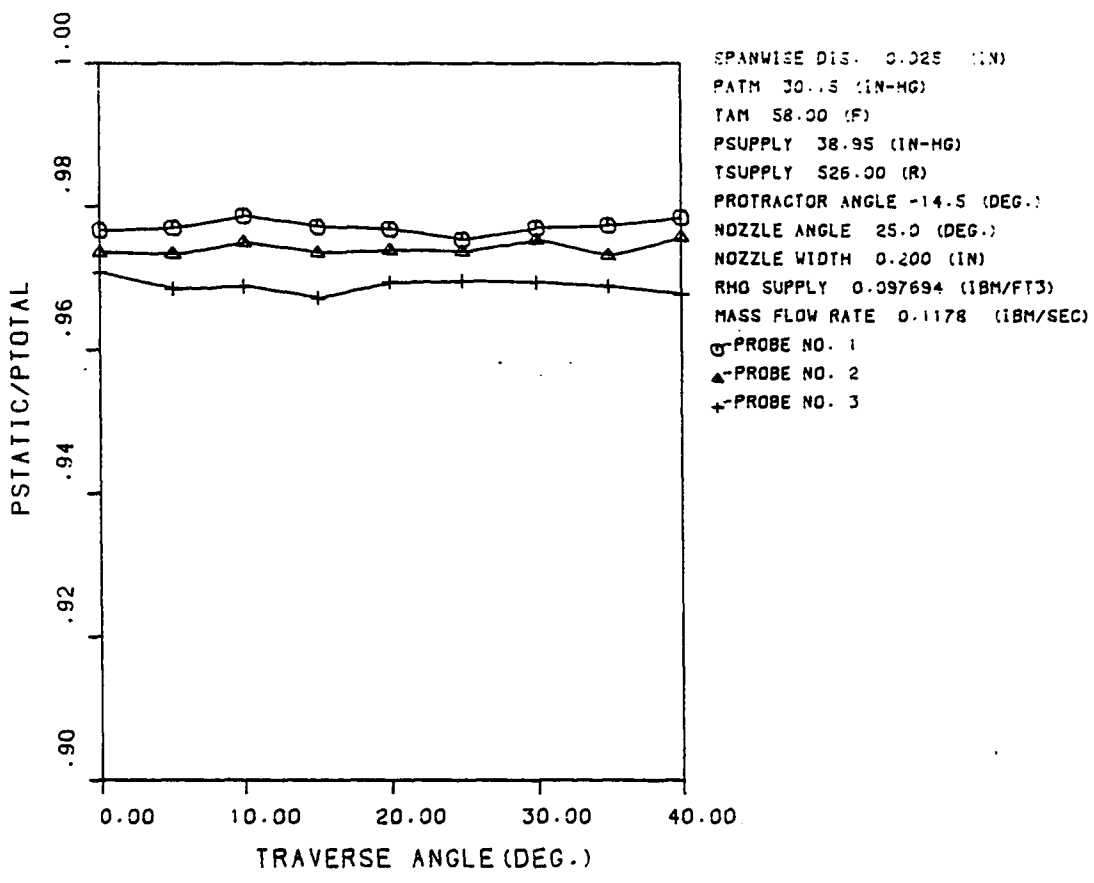


VELOCITY VS. TRAVERSE ANGLE

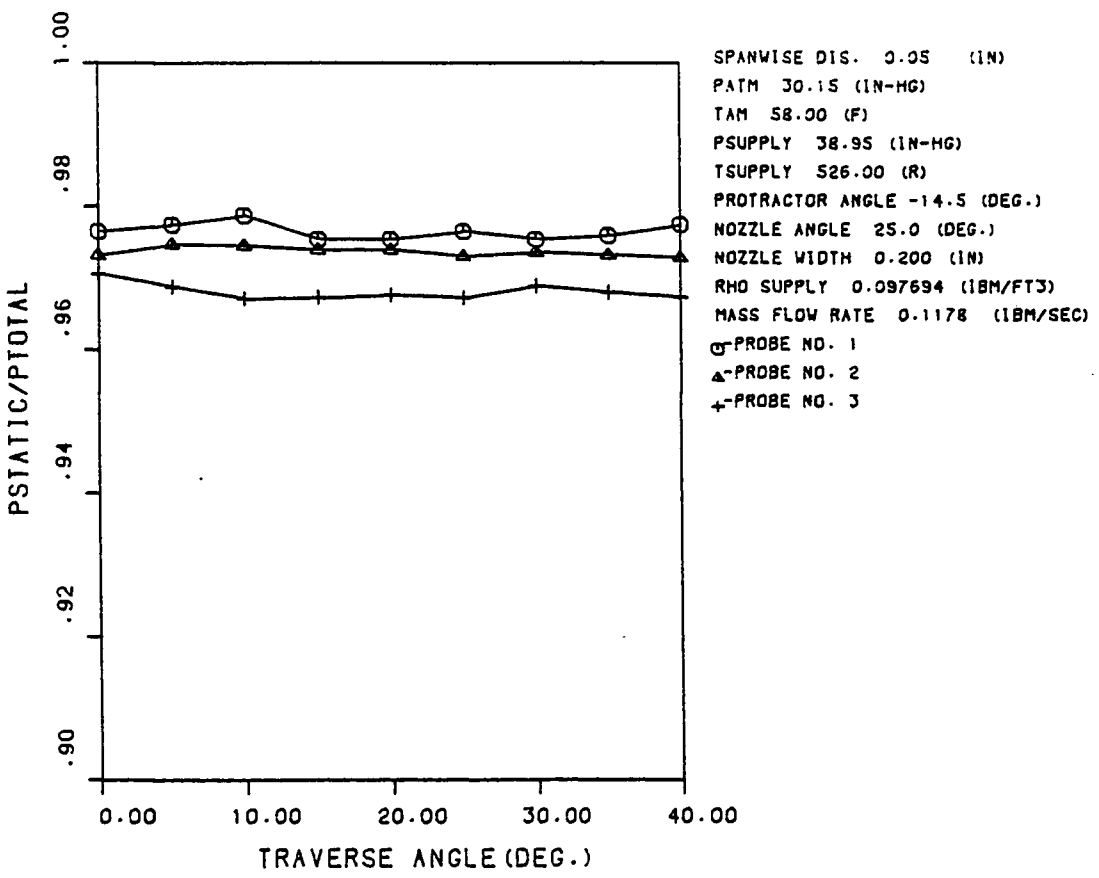


VELOCITY VS. TRAVERSE ANGLE

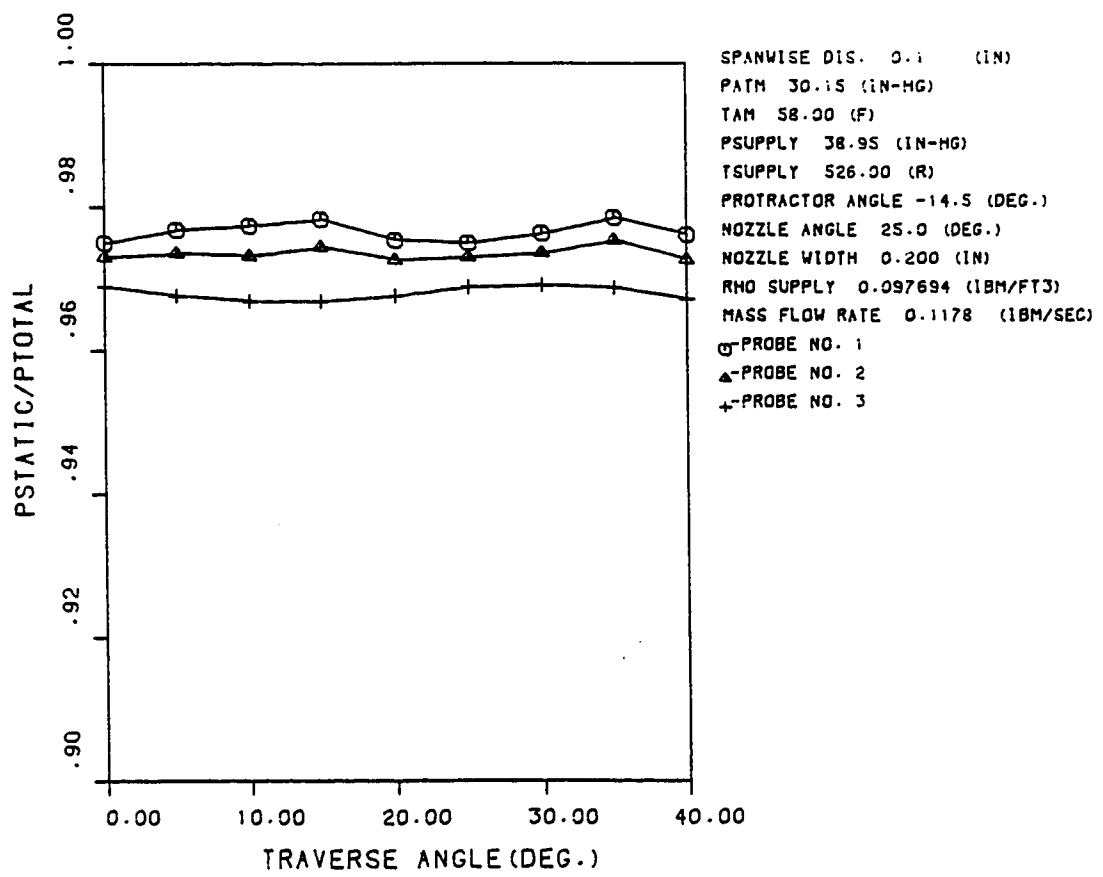




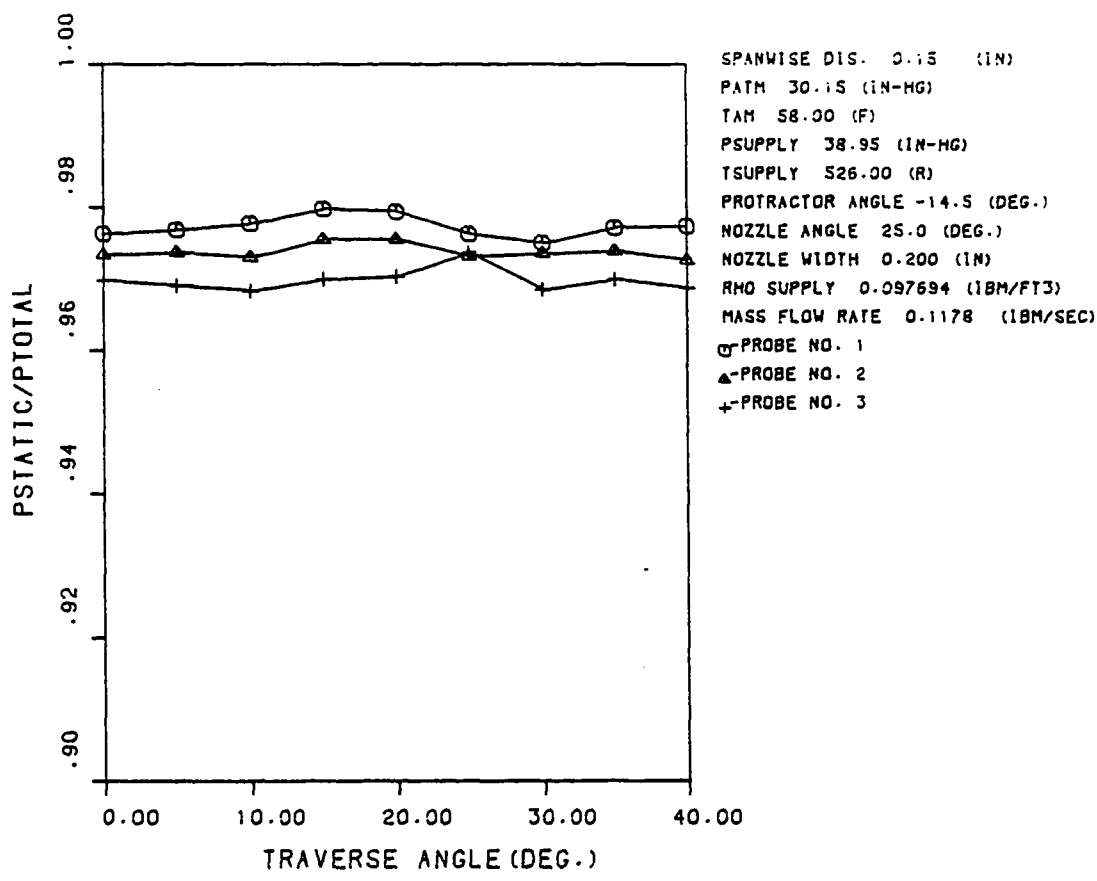
PRESS. RATIO VS. TRAVERSE ANGLE



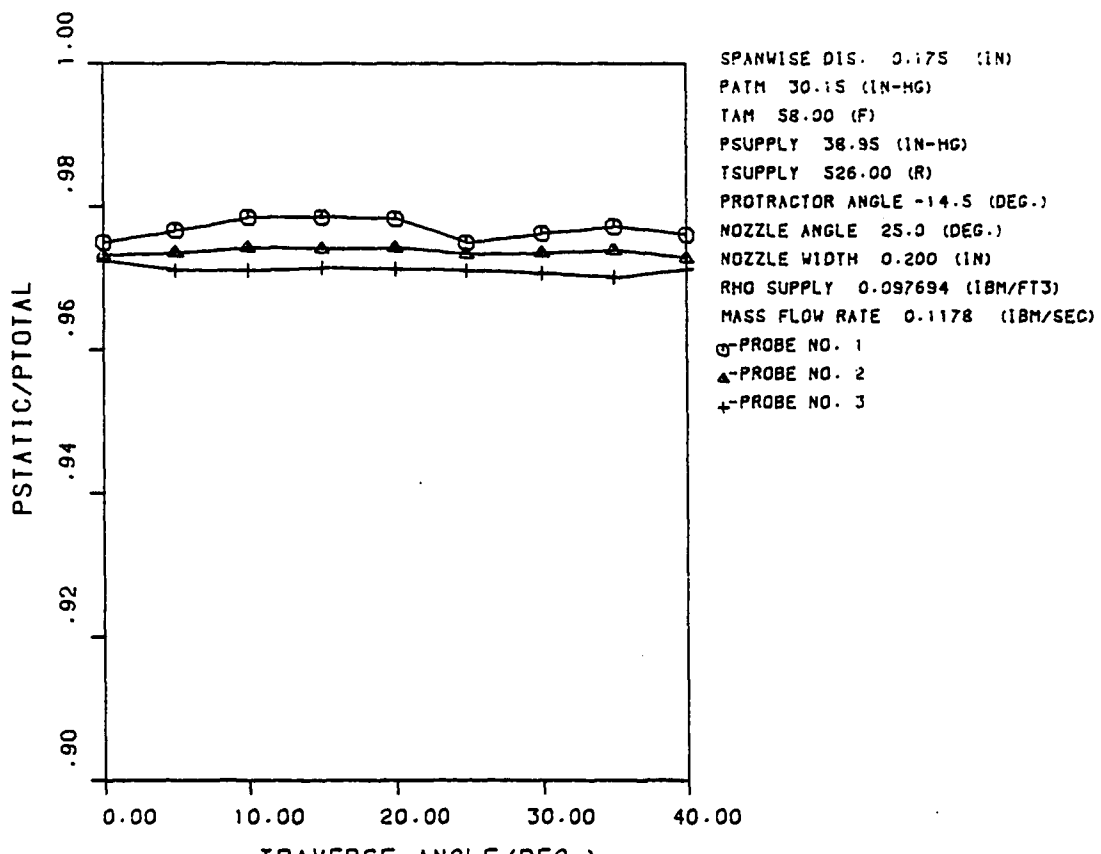
PRESS. RATIO VS. TRAVERSE ANGLE



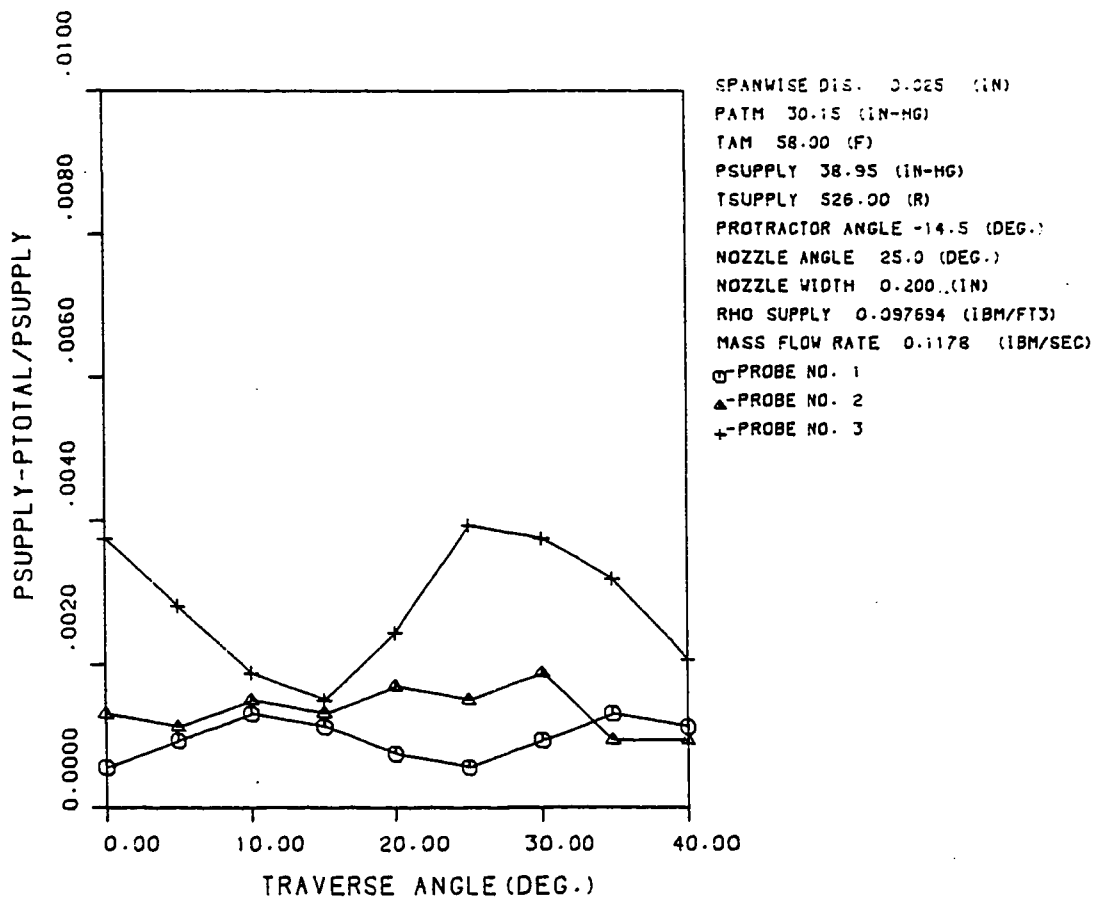
PRESS. RATIO VS. TRAVERSE ANGLE



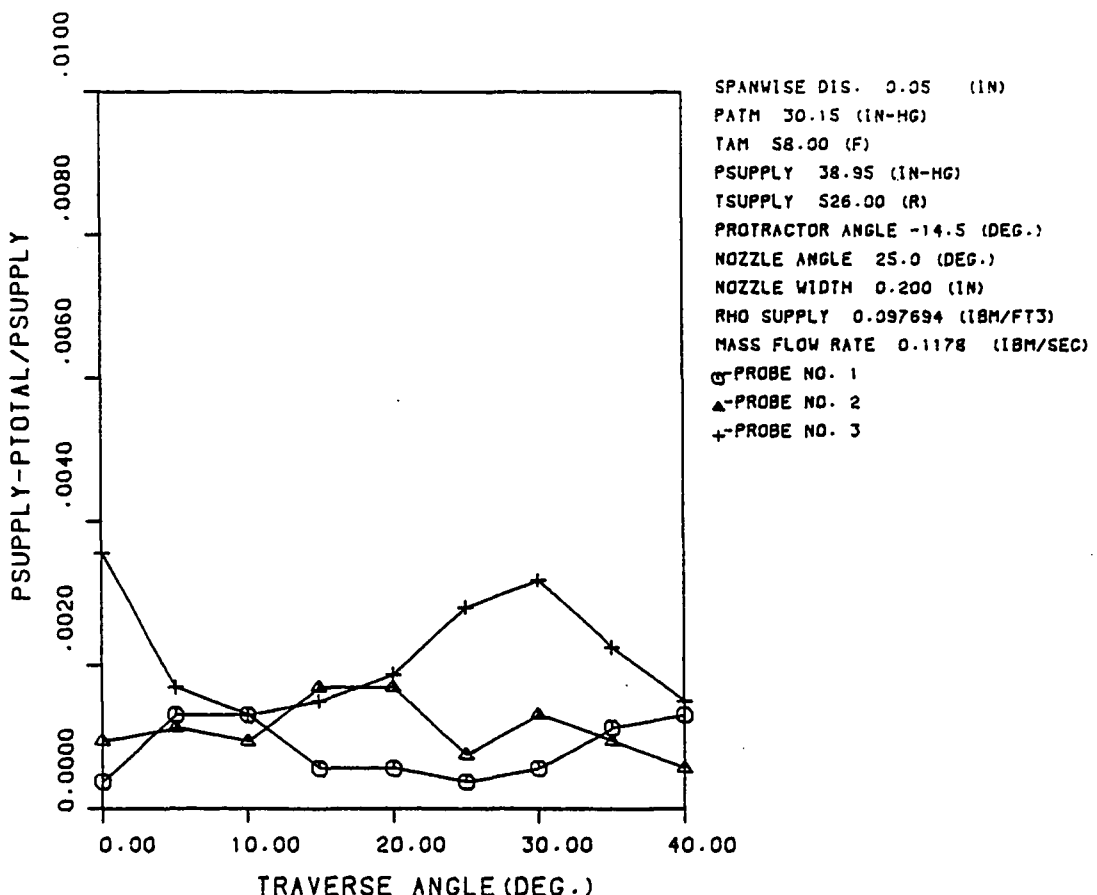
PRESS. RATIO VS. TRAVERSE ANGLE



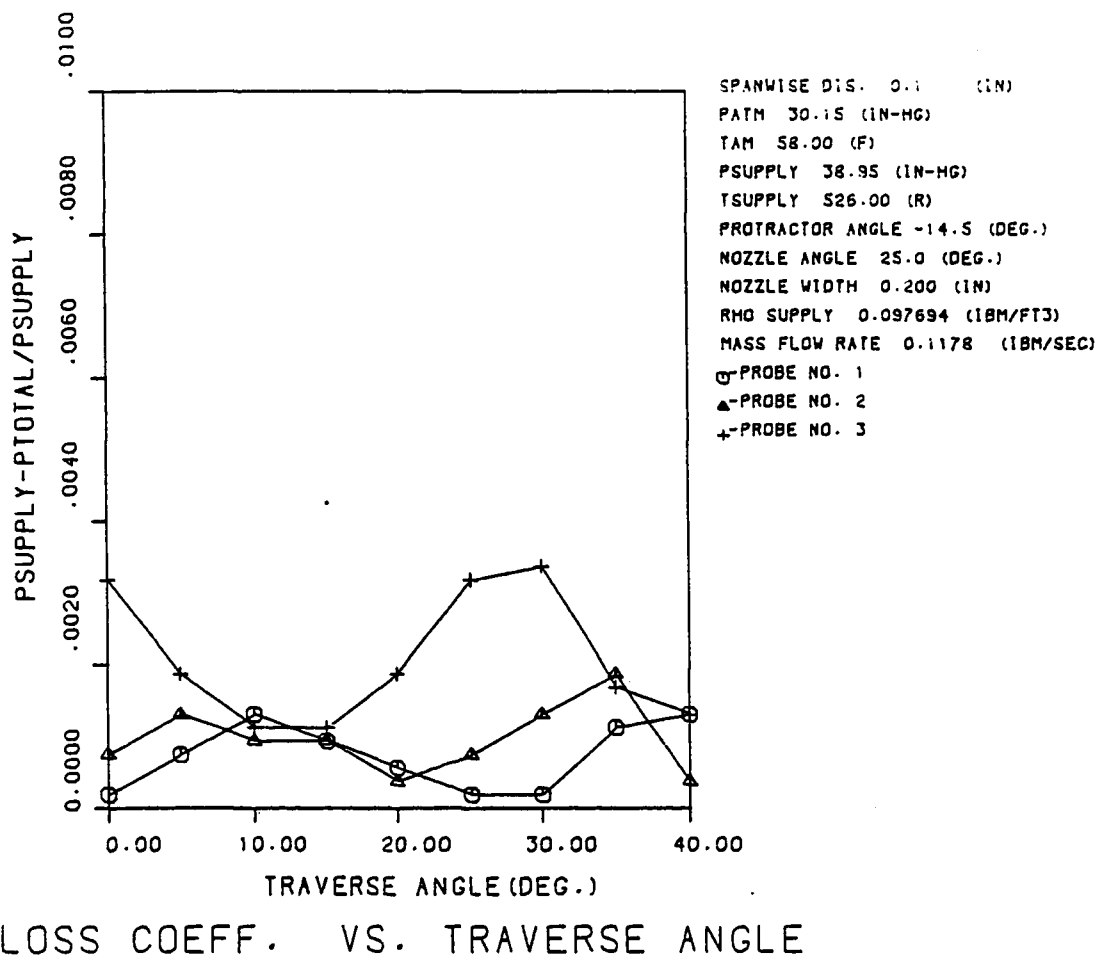
PRESS. RATIO VS. TRAVERSE ANGLE

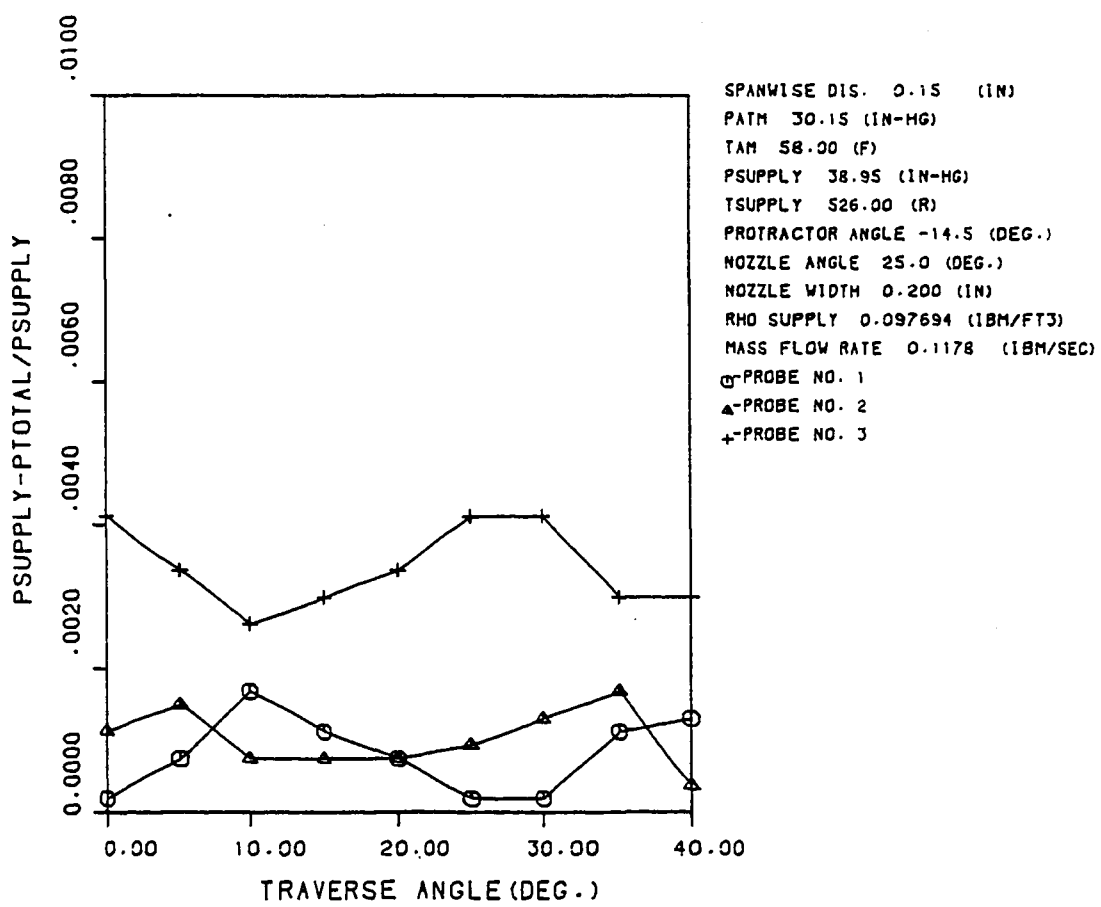


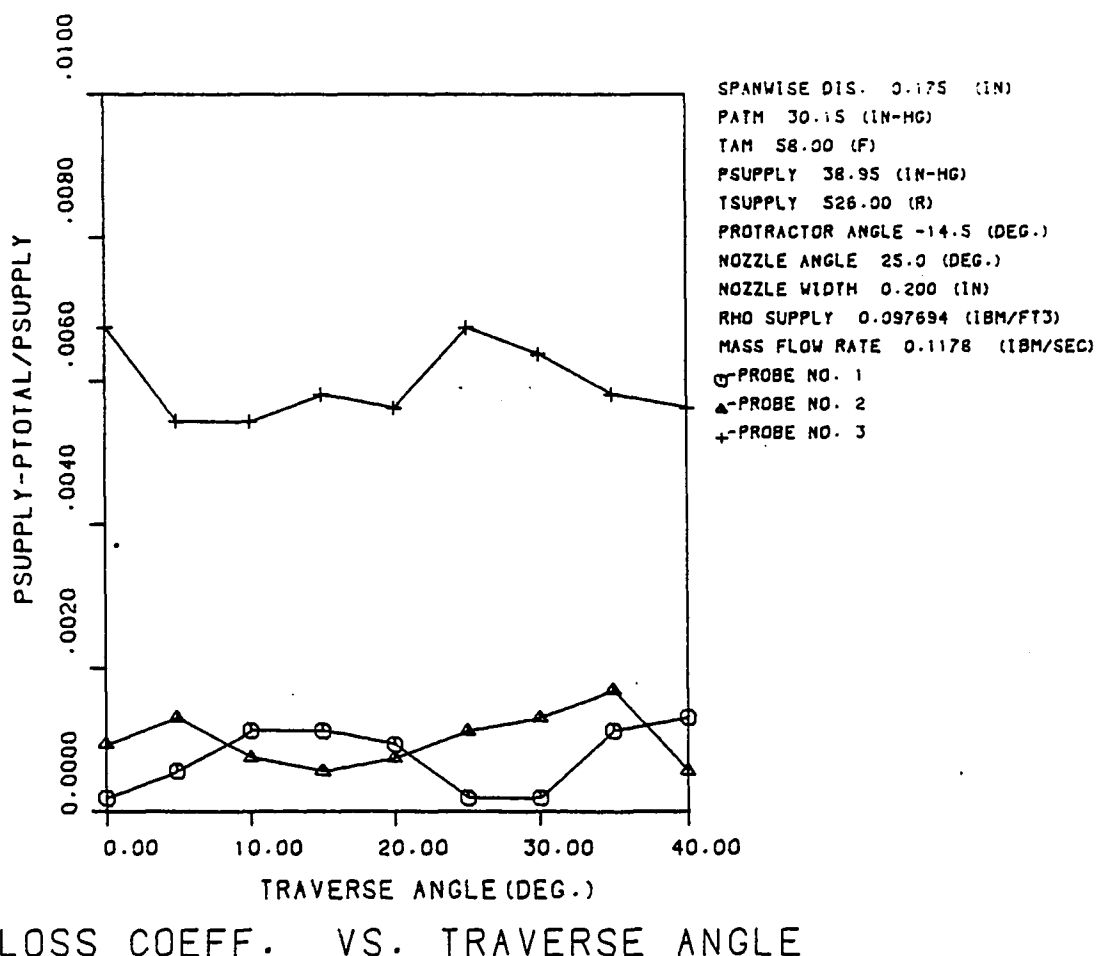
LOSS COEFF. VS. TRAVERSE ANGLE

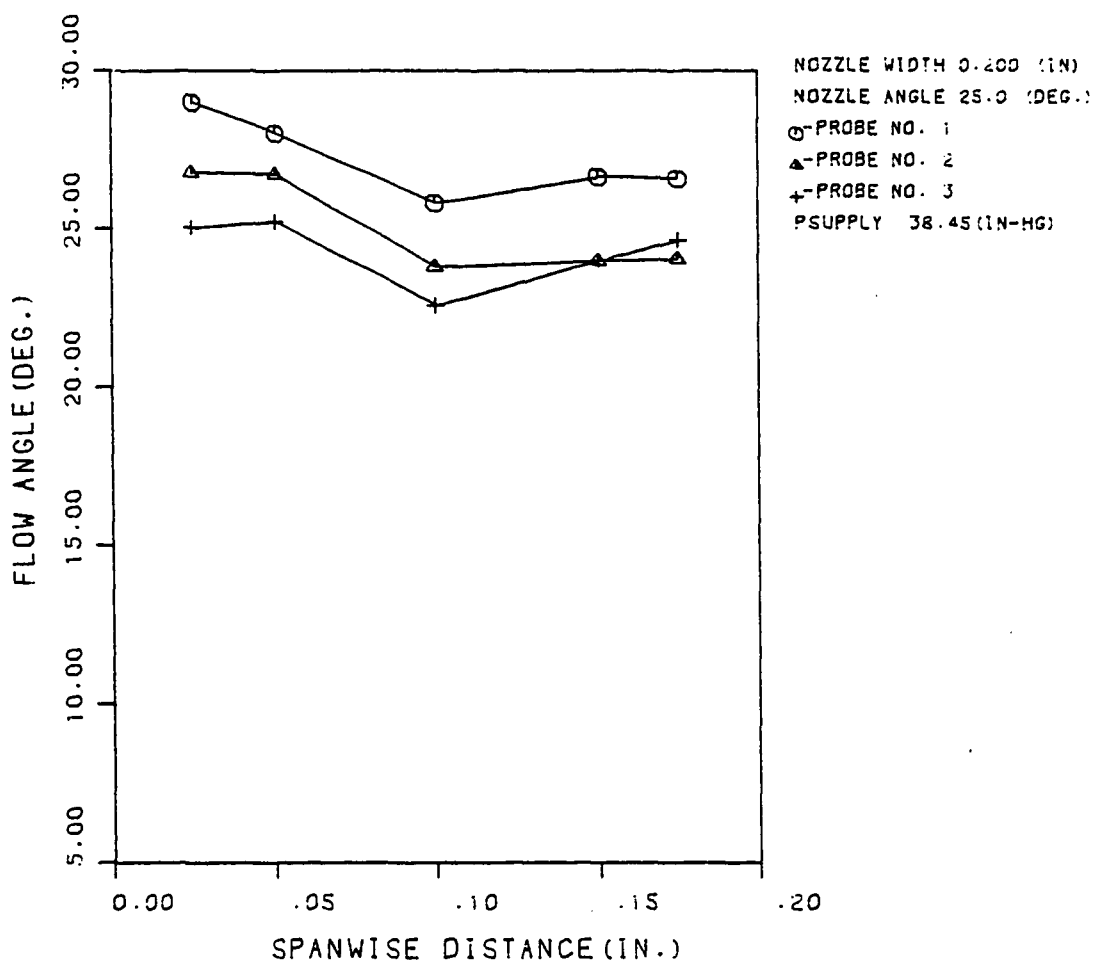


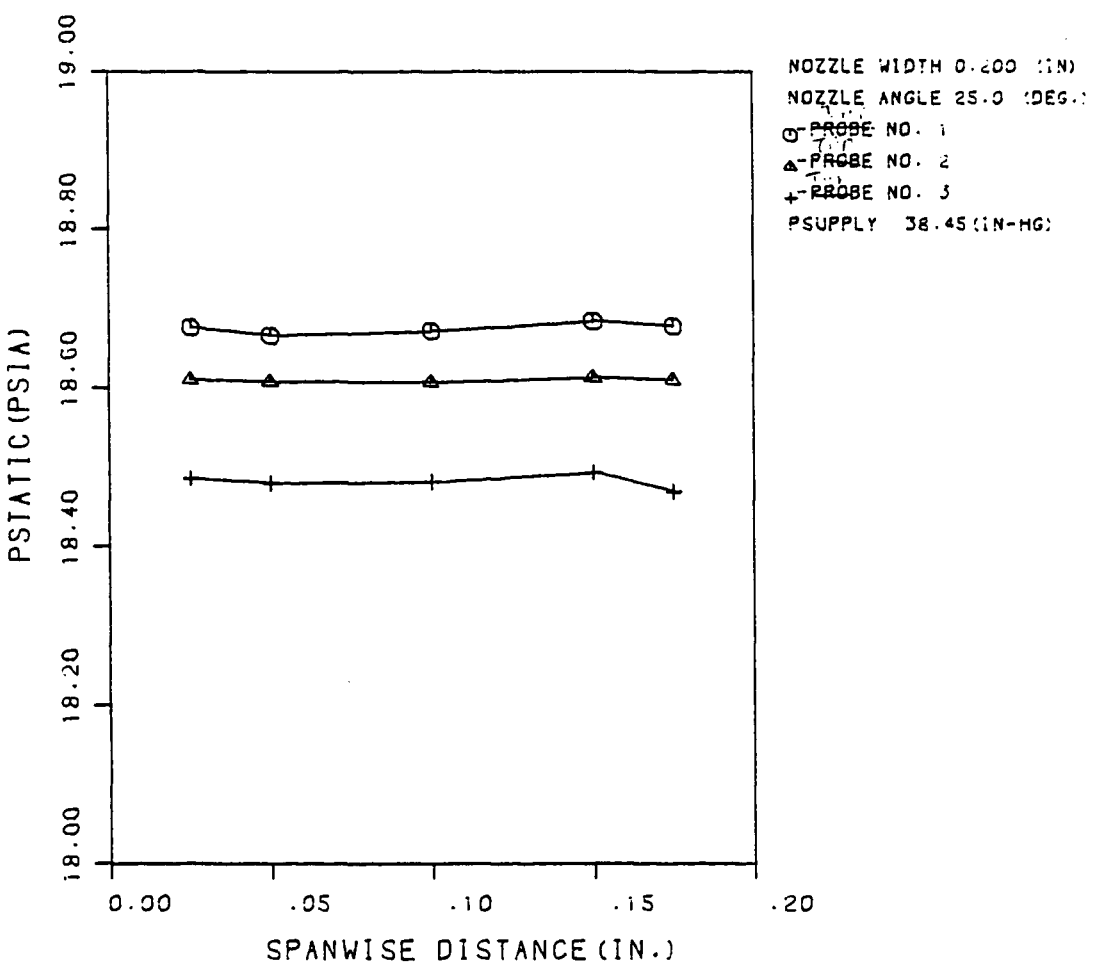
LOSS COEFF. VS. TRAVERSE ANGLE

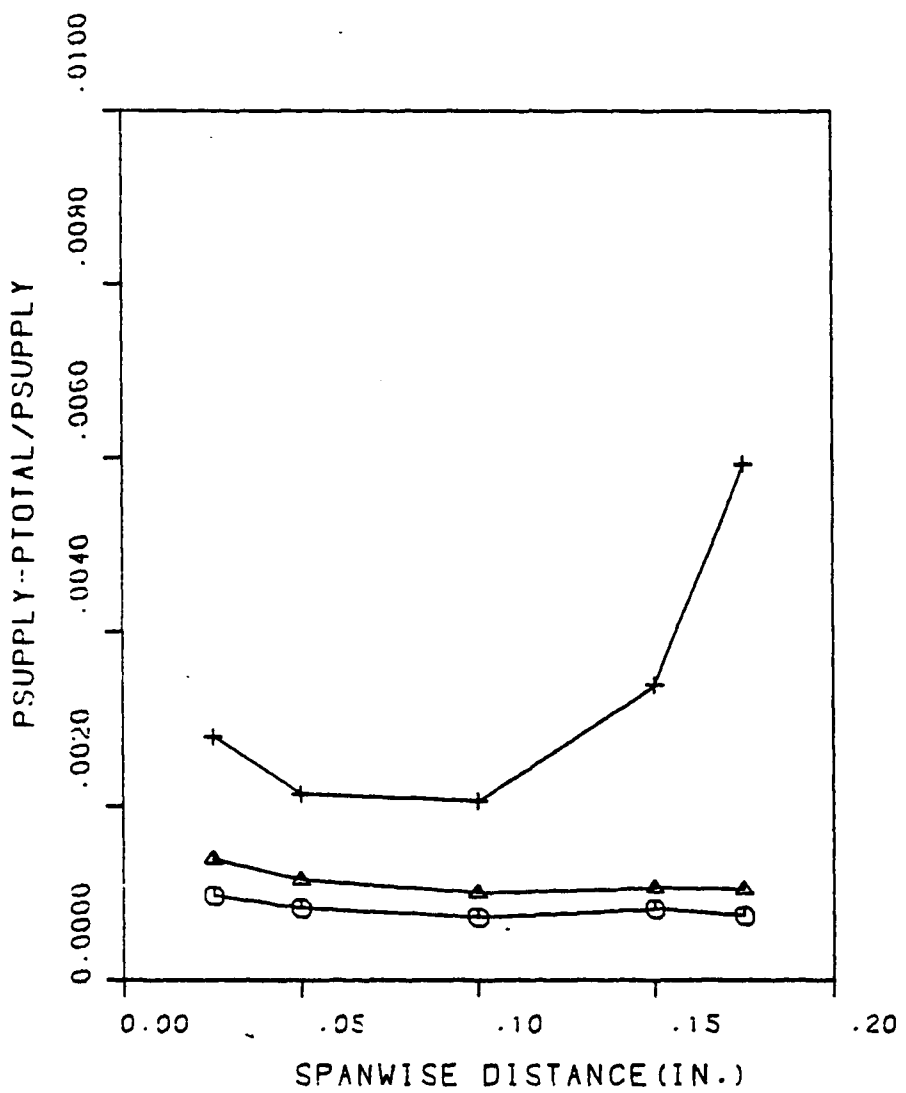


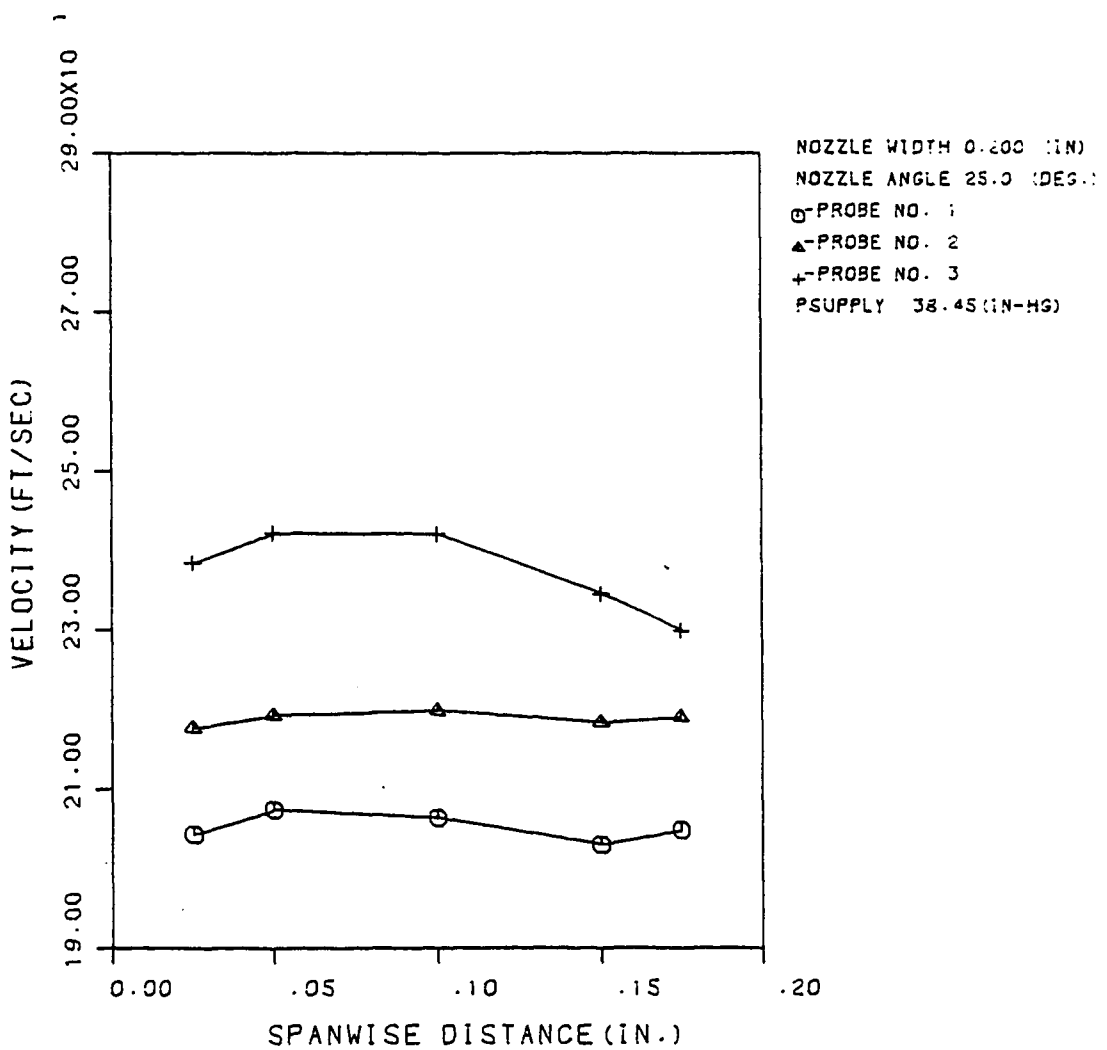


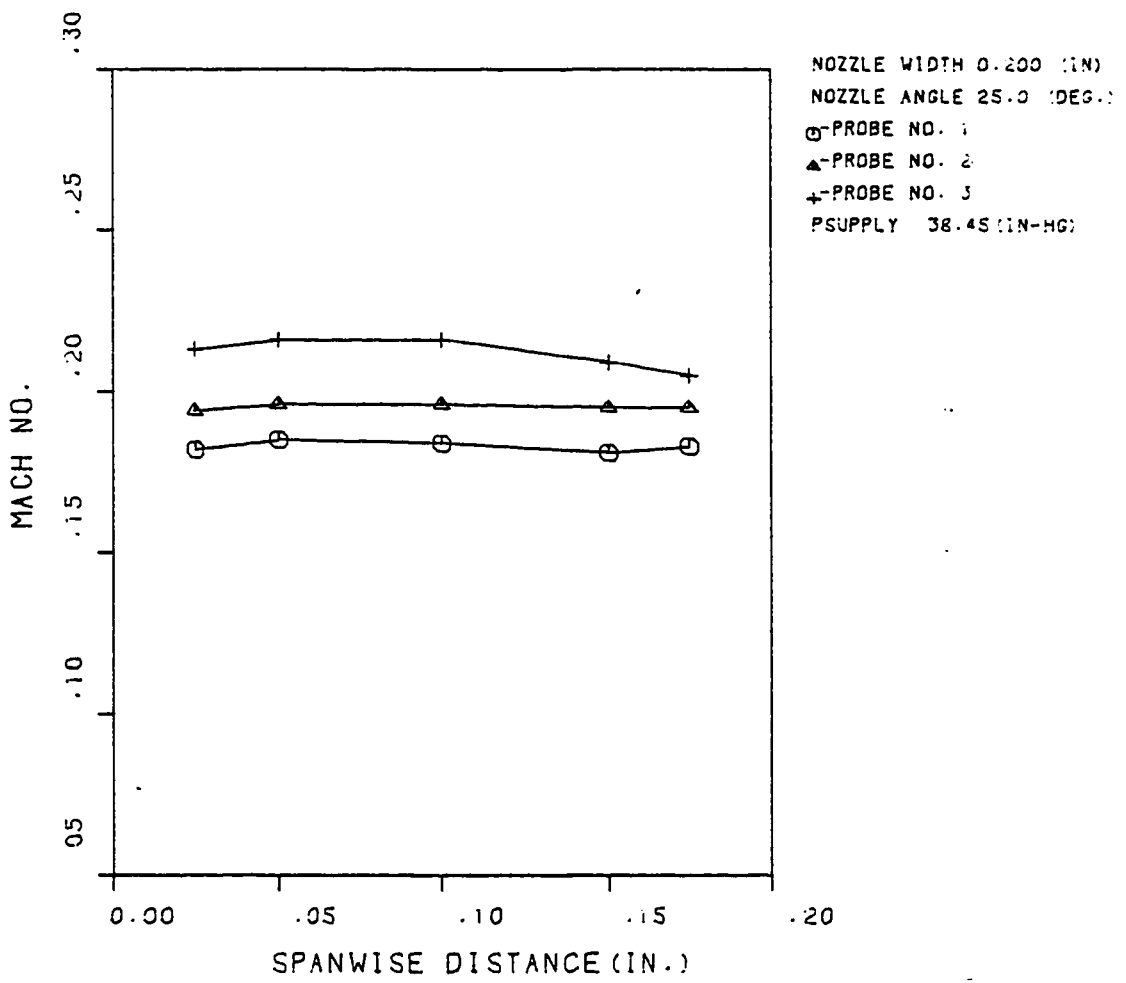


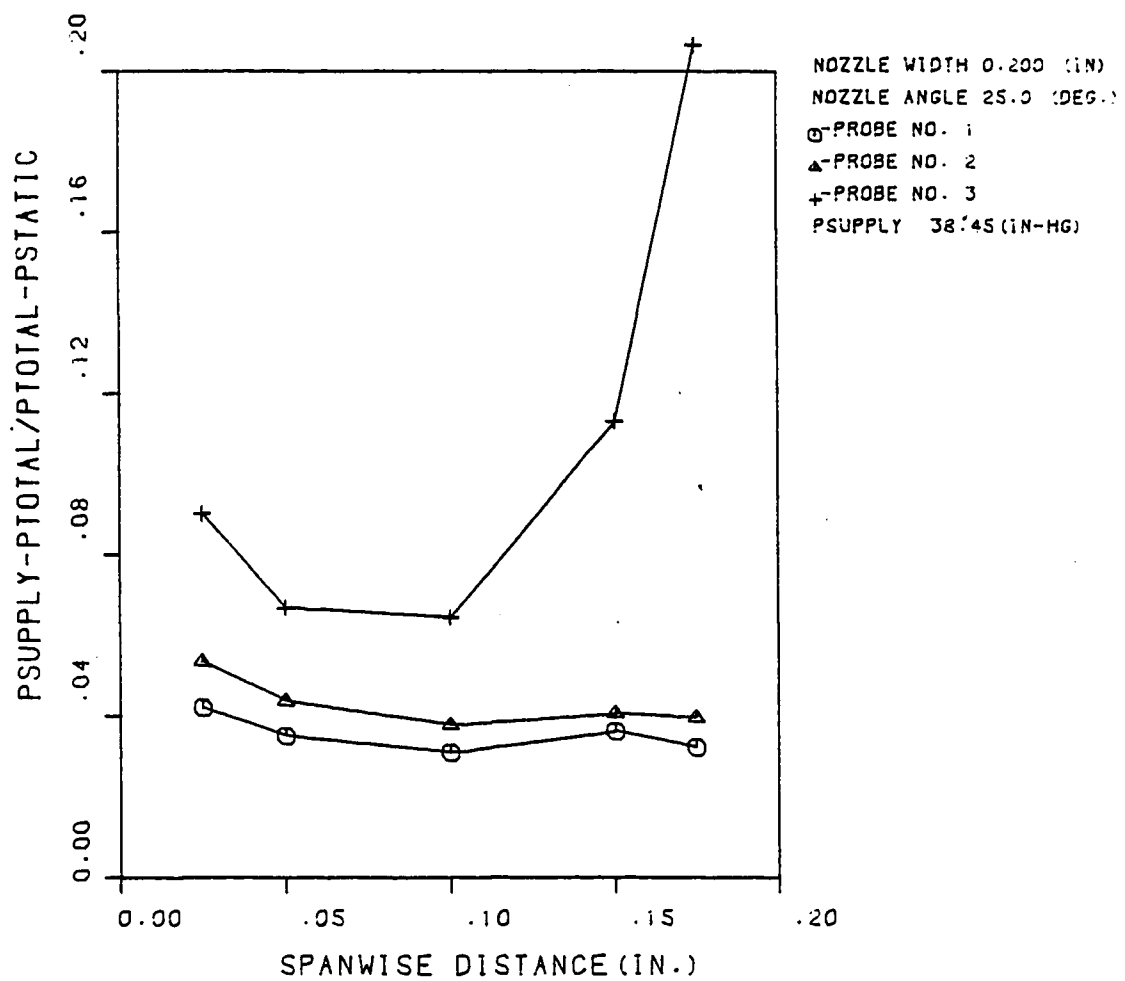












BIOGRAPHY OF AUTHOR:

Seyed Gholam Reza Hashemi was born to Miss Anis and Mr. Mortaz Hashemi in Tehran, Iran on September 29, 1957.

He finished his high school in 1976 and in fall of the same year he was admitted to the Engineering Department of the Iran College and Science University in Tehran. In spring of 1979 he came to the United States as a transfer student. First he went to the Hofstra University in Hempstead, New York, to study English and Engineering. In summer of 1979 he came to Lehigh University to study Mechanical Engineering. He received his Bachelor of Science Degree in Mechanical Engineering in the fall of 1981. In spring of 1981 he started his Master's program at Lehigh University.